THE APPLICATION OF DISCRETE DIFFUSION MONTE CARLO TO RADIATIVE TRANSFER IN HOMOLOGOUS OUTFLOW WITH NON-MONOTONIC OPACITY DEPENDENCE

by

Ryan T. Wollaeger

A dissertation submitted in partial fulfillment of
the requirements for the degree of

Doctor of Philosophy

(Engineering Physics)

at the

UNIVERSITY OF WISCONSIN-MADISON

2014

Date of final oral examination: 8/1/2014

The dissertation is approved by the following members of the Final Oral Committee:
- Gregory A. Moses, Spangler Professor, Engineering Physics
- Carl R. Sovinec, Professor, Engineering Physics
- Douglass L. Henderson, Professor, Engineering Physics
- Paul P. H. Wilson, Professor, Engineering Physics
- Daniel R. van Rossum, Research Associate, Flash Center for Computational Science, Department of Astronomy and Astrophysics, University of Chicago

ACKNOWLEDGEMENTS

I would like to thank Daniel R. van Rossum for input on the physics of Type Ia supernovae and for the considerable code development and tests. Thank you to Donald Q. Lamb and Carlo Graziani for the input on astrophysics and the guidance for the code goals. I would also like to thank Douglass L. Henderson, Todd J. Urbatsch, Jeffery D. Densmore, Allan B. Wollaber, and Jim E. Morel for sharing their expertise in transport theory. Thank you to the Los Alamos National Laboratory the summer internships of 2011 and 2012. Thank you to PRISM Computational Sciences for supporting the initial DDMC research. Thank you to Gregory A. Moses, Donald Q. Lamb for supporting and guiding this work. Many thanks to Gregory A. Moses for the opportunity to pursue radiation-hydrodynamics research.

My research is supported by: University of Chicago, Flash Center for Computational Science under NSF grant AST-0909132

Contents

1 Introduction 1
1.1 Radiative Transport 2
  1.1.1 Radiation Matter Interaction 7
  1.1.2 NLTE Transport 14
  1.1.3 LTE Transport 15
1.2 Applications of Radiation Transport Theory 19
  1.2.1 Type Ia Supernovae 20
  1.2.2 Inertial Confinement Fusion 22
1.3 Computational Transport Methods 25
  1.3.1 Deterministic Methods 26
  1.3.2 Monte Carlo Methods 31
  1.3.3 Residual Monte Carlo 38

2 Literature Review 47
2.1 IMC-DDMC Review 48
  2.1.1 Fleck and Cummings Implicit Monte Carlo (IMC) 48
  2.1.2 IMC Maximum Principles 51
  2.1.3 Gentile-Fleck Factor Modified IMC 55
  2.1.4 McClarren and Urbatsch's BDF-2 Scheme for Temporal Discretization in IMC 57
  2.1.5 Symbolic Implicit Monte Carlo (SIMC) 59
  2.1.6 Discontinuous Finite Element Transport in Diffusive Problems 63
  2.1.7 Clouet and Samba's Corner Term Analysis 68
  2.1.8 Densmore's Analysis of Spatial Discretization in IMC 72
  2.1.9 Smedley-Stevenson and McClarren's Source Tilt Reconstruction 75
  2.1.10 Random Walk in Diffusive IMC 78
  2.1.11 N'Kaoua's Monte Carlo Coupling with Diffusion via Domain Decomposition 80
  2.1.12 Discrete Diffusion Monte Carlo (DDMC) 81
  2.1.13 Multi-group IMC Diffusion (IMD) 87
  2.1.14 Multi-frequency DDMC 88
  2.1.15 Abdikamalov's Velocity-dependent Multigroup IMC-DDMC 91
2.2 Type Ia Supernovae Review 94
  2.2.1 Type Ia Explosion Model Summary 95
  2.2.2 Pinto and Eastman Grey Type Ia SN Model 99
  2.2.3 PHOENIX Code 99
  2.2.4 SEDONA Code 101
  2.2.5 ARTIS Code 102

3 SuperNu: A Radiative Transfer Code for Type Ia Supernovae 104
3.1 IMC-DDMC Method 104
  3.1.1 Multigroup Velocity Space IMC 106
  3.1.2 Asymptotic Analysis for Space and Group Boundaries 114
  3.1.3 Multigroup Velocity Space IMC-DDMC 129

3.1.4 Opacity Regrouping 138
3.2 Code Summary 141
3.3 Numerical Results 142
3.3.1 Static Grid Problems 142
3.3.2 Velocity-Dependent Problems 151
3.3.3 W7 Model of Type Ia Supernova 167

4 Conclusions **178**
4.1 Future Work 179

REFERENCES **180**

List of Figures

1 Intensity measuremant apparatus of Castor [19], where A_1, A_2, r, Δt, $\Delta \nu$, and ΔE are aperture area, detector area, distance, time span, detector frequency range, and detected energy. 3
2 Absolute magnitude of light curves fit to a template light curve with a stretch correction [87]. The parameter family allows for direct comparison between luminosity measurements and thus relative distances. 21
3 A tokamak uses toroidal and poloidal magnets to confine the plasma [1]. 24
4 An ICF reactor uses particle beam pulses to confine the plasma [4, p. 48]: 1. irradiation, 2. ablation driven implosion of fuel, 2. thermonuclear ignition, 3. explosion [33] 25
5 The stick drop simulation produces an a probability that converges to $3/\pi$ for an increasing number of samples. 33
6 Residual Monte Carlo test in a homogeneous medium. Error convergence versus total particle number simulated. 46
7 Solutions to the picket-fence opacity problem in Section 3.3.1. P_1 (dashed) and IMC-DDMC (solid) unitless material temperature profiles at two different (mean free) times plotted as a function of unitless radius (mean free paths). In Fig. 7a, with 15 cells, DDMC couples to the material and IMC streams. In Fig. 7b, with 50 cells, IMC is applied to both pickets. 147
8 IMC (solid) and IMC-DDMC (dashed) L_2 temperature error relative to the P_1 solution plotted over the number of mean free paths per cell at 600 mean free times. . . 148
9 IMC (solid blue), non-OR IMC-DDMC (dashed green), and opacity-regrouped IMC-DDMC (dot-dashed red) material temperature versus radius for the monotonic opacity regrouping problem with $\sigma_0 = 5.32345 \times 10^{18}$ $\mathrm{K}^{7/2}$/cm. 149
10 IMC (solid blue), non-OR IMC-DDMC (dashed green), and opacity-regrouped IMC-DDMC (dot-dashed red) material temperature versus radius for the monotonic opacity regrouping problem with $\sigma_0 = 5.32345 \times 10^{19}$ $\mathrm{K}^{7/2}$/cm. 150
11 IMC (solid blue), non-OR IMC-DDMC (dashed green), and opacity-regrouped IMC-DDMC (dot-dashed red) material temperature versus radius for the monotonic opacity regrouping problem with $\sigma_0 = 5.32345 \times 10^{20}$ $\mathrm{K}^{7/2}$/cm. 150

12 In Fig. 12a, manufactured (solid), standard IMC (dashed), and standard DDMC (dash-dotted) radiation temperatures (T_r) and material temperatures (T) for the quasi-manufactured problem with 1000 time steps. In Fig. 12b, manufactured (solid), modified DDMC with large time steps (dashed), and modified DDMC with small time steps. The Gentile-Fleck factor prevents the radiation and material temperatures from nearly trading places in the first time step, relative to the analytic manufactured solution. 155

13 In Fig. 13a, manufactured (dashed) and DDMC (solid, dot-solid, and dot-dashed) material temperature at three different times plotted over the velocity grid. In Fig. 13b, the manufactured source in the pure scattering group is missing. 159

14 In Fig. 14a, radiation energy density for pure IMC (solid lines) and IMC-DDMC (dashed lines) for the step source problem with $\tau_D = 3$. In Fig. 14b, the fit of Eq. (3.57), with $C_1 = 0.55$ and $C_2 = 1.25$, is implemented for IMC-DDMC. . . . 161

15 Radiation energy density for pure IMC (solid line), IMC-DDMC without a G_U factor (dotted solid line), and IMC-DDMC with G_U for the step source problem with $\tau_D = 10$. The fit of Eq. (3.57), with $C_1 = 0.6$ and $C_2 = 1.25$, is implemented for IMC-DDMC with G_U ("HMC-GU"). 162

16 In Fig. 16a, radiation energy density for pure IMC (solid lines) and IMC-DDMC (dashed lines) for the step source problem with $\tau_D = 3$; IMC-DDMC uses upwind Doppler shift. In Fig. 16b, the DDMC Doppler shift algorithm from Section 3.1.3 is employed; relative to Fig. 16a, redshift from optically thick groups is mitigated since absorption/effective scattering is dominant over Doppler correction. 163

17 Material temperature, and grouped spectra of IMC (solid), non-opacity-regrouped (non-OR) IMC-DDMC (dashed, $g_c = 0$), and opacity-regrouped IMC-DDMC (dot-solid, $g_c = 10$) at 3.5 and 5 days for the spherical step source problem. In Fig. 17a, material temperature is plotted versus velocity. In Fig. 17b, grouped luminosity is plotted versus group center. 164

18 Non-opacity-regrouped (non-OR) IMC-DDMC (solid), and opacity regrouped IMC-DDMC (dashed) L_1 error versus time step of group spectra relative to pure IMC for radiation escaping the outermost cell of the 10 group, Heaviside source problem. . 165

19 Opacity-regrouped IMC-DDMC W7 bolometric light curves for opacity mixing $\alpha_\sigma \in \{0.0, 0.5, 1.0\}$ (solid) and $\alpha_\sigma \in \{0.3, 0.8\}$ (dashed; so solid and dashed curves alternate versus α_σ) and a fixed number of subgroups, $G_g = 20$. In Figs. 19a, and 19b, group resolutions are $G = 225$, $G = 625$, respectively. 170

20 Opacity-regrouped IMC-DDMC W7 spectra for opacity mixing $\alpha_\sigma = 0.0, 0.3, 0.5$ (dotted, dashed, and solid, respectively) and a fixed number of subgroups, $G_g = 20$. In Figs. 20a, and 20b, group resolutions are $G = 225$, $G = 625$, respectively. . . . 171

21 IMC-DDMC (solid) and Gentile-Fleck factor modified IMC-DDMC (dashed) material temperatures and spectra at day 32 post-explosion with $G = 225$ and $\alpha_\sigma = 0.5$. 173

22 In Fig. 22a, bolometric light curves for `SuperNu` with 500 groups (blue), multigroup `PHOENIX` with 500 groups (green), and standard `PHOENIX` (red). In Fig. 22b, spectra at day 20 for `SuperNu` with 500 groups (blue) and standard, or high-resolution, `PHOENIX` (green). 174

23 W7 SN Ia luminosity error versus time for 225 (blue), 400 (green), and 625 (red) groups relative to the 1024 group test. The spatial and temporal grids have 256 cells and 992 time steps, respectively, in each simulation. 176
24 W7 SN Ia luminosity error versus time for 32 (blue), 64 (green), and 128 (red) cells relative to the 256 cell test. The wavelength and temporal grids have 1024 groups and 992 time steps, respectively, in each simulation. 176
25 W7 SN Ia luminosity error versus time for 124 (blue), 248 (green), and 496 (red) time steps relative to the 992 time step test. The spatial and wavelength grids have 256 cells and 1024 groups, respectively, in each simulation. 177

List of Tables

1 Fusion reactions. 23
2 Monotonic Opacity Computation Times (minutes) 151
3 Run Times for First 64 Time Steps of Heaviside Problem with $g_c \in \{0 \dots 10\}$ with 1 Core (minutes) 166
4 Total Run Times for Opacity-Regrouped HMC W7 with 24 Cores (hours) 172

1 Introduction

Type Ia supernovae (SNe Ia) are thought to result from thermonuclear explosions of carbon-oxygen white dwarf stars. The amount of energy released from fusion reactions is converted into kinetic energy that unbinds the star. The resulting fluid is ballistic and homologous within $\sim$100 seconds of the initial fusion disruption. During the span of several weeks, radioactive ^{56}Ni emits gamma rays that heat the ejecta to produce visible light. The luminosities of SNe Ia typically span a small range and are often correlated. Consequently, these events are of interest to cosmology as "standard candles" for measuring the expansion rate of the Universe.

Photon transport in Type Ia supernovae is challenging to simulate with high fidelity. The observed light curves and spectra result from the interaction of photons with millions of spectral lines of a multi-species fluid in various excitation and ionization stages. Moreover, the fluid is expanding at a semi-relativistic rate; so a photon that does not interact with a line in one part of the ejecta can transport into resonance with the same line elsewhere in the fluid. The complicated opacity spectrum and the high-velocity expansion of the fluid imply that the span of material properties over physical time scales of weeks is large. Depending on the transport method and code, high-fidelity simulations of SNe Ia can be demanding to memory and efficiency. Enough opacity data must be stored to resolve the spectrum and the transport method must be efficient in optically thick regions of the domain.

The intent of this thesis is to describe the theory of a hybrid transport-diffusion, Monte Carlo, local thermodynamic equilibrium (LTE), radiative-transfer code for Type Ia supernovae and other applications. The methods applied are Implicit Monte Carlo (IMC) for radiation transport and Discrete Diffusion Monte Carlo (DDMC) for radiation diffusion. DDMC accelerates IMC calculations where diffusion theory is applicable. The code presented, named `SuperNu`, implements IMC and DDMC in one-dimensional, spherical geometry to propagate and deposit radiation energy in either static material or ballistic, homologous fluid. The fluid velocity field does not depend on radiation momentum deposition. At the time of the writing of this thesis, novel features of `SuperNu` include:

- a Lagrangian IMC-DDMC implementation for homologous flow [104] (see Section 3.1),

- a boundary condition for high-velocity spatial cell edges that interface IMC and DDMC [104] (see item 1 of Section 3.1.2),
- a "distance to Doppler shift" for IMC and an asymptotically informed scheme that emulates continuous redshift for DDMC [103] (see item 2 of Section 3.1.2),
- a non-contiguous opacity regrouping scheme that optimizes DDMC by allowing groups to have disjoint frequency intervals [103] (see Section 3.1.4),
- and an implementation of the W7 Type Ia supernova (SN Ia) problem [76] solved with IMC-DDMC (see Section 3.3.3).

The ability of the code to solve the W7 problem efficiently is attributable to the non-contiguous opacity regrouping method. This method finds DDMC groups that are optically thick and combines them to reduce effective or physical, inelastic scattering. For the numerical tests presented in Chapter 3, only effective scattering is considered.

The outline of the thesis is as follows: in Chapter 1, the relevant theory and motivations are given for transport and transport methods; in Section 2.1, articles detailing features, limitations, and improvements of IMC and related transport methods are discussed; in Section 2.2, the physics of SNe Ia and codes used to simulate SNe Ia are reviewed; in Chapter 3, the `SuperNu` radiation transport methods and framework are presented along with numerical tests of particular features; in Section 3.3.3, IMC-DDMC simulation data for the W7 SN Ia problem are presented; and in Chapter 4, conclusions and avenues of future research are summarized.

1.1 Radiative Transport

Radiative transport is the phenomenon of photon propagation through space, time, and matter. In many cases, it is possible to accurately describe a field of photons with a distributional density profile in phase space, f_ν. The subscript, ν, indicates photon frequency or energy dependence and is often expressed as a parenthetical argument. Excluding polarization [19, p. 70], the radiation distribution, f_ν, and intensity, I_ν, depend on seven variables: three spatial dimensions, $\vec{r}$, two direction dimensions, $\hat{\Omega}$, time, t, and frequency, ν. Furthermore, f_ν and I_ν are related by (see, e.g., [86, p. 2], [73, p. 311]),

$$I_\nu = ch\nu f_\nu \ \ , \tag{1.1}$$

where c is the speed of light in a vacuum and h is Planck's constant. Briefly, $I_\nu(\vec{r}, \hat{\Omega}, t)$ is the amount of power at a time t, per differential surface neighborhood around a position $\vec{r}$, per differential solid angle around a direction $\hat{\Omega}$, per differential frequency interval about a frequency ν [73, p. 311]. Castor [19, p. 70] provides an intuitive description of radiation intensity from the standpoint of measurement from a detector in an idealized apparatus. In the set-up, radiation from an aperture open for a finite time interval streams through a vacuum to a detector that registers radiation in a finite frequency band. The amount of energy detected divided by the measurement time, the frequency band, the solid angle of the detector viewed from the aperture, and the area of the aperture gives an estimate of intensity at the aperture [19, pp. 70-72]. Figure 1 is a copy of Castor's illustration [19, p. 71].

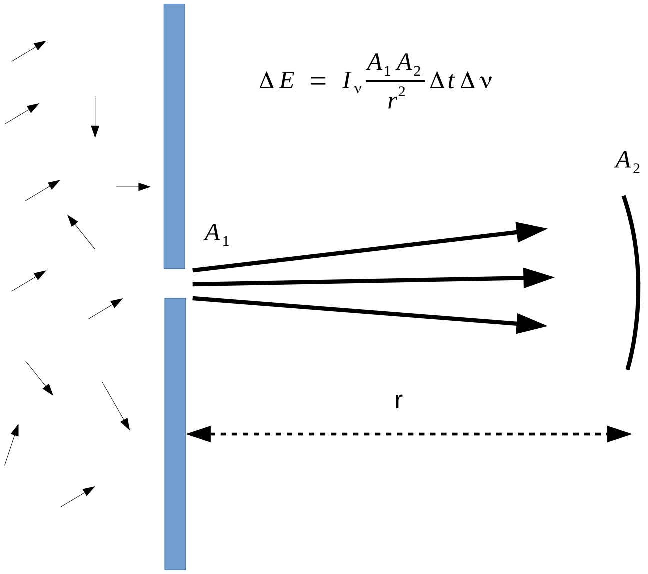

Figure 1: Intensity measuremant apparatus of Castor [19], where A_1, A_2, r, Δt, $\Delta\nu$, and ΔE are aperture area, detector area, distance, time span, detector frequency range, and detected energy.

If initial, boundary, and source conditions for a radiation field are known, then I_ν may be obtained from the radiation transport equation. The transport equation is a statement of energy conservation along a direction. For a given direction, photon particles advect at the speed, c, are removed from the direction by absorption and scattering, and are added to the direction by sources and scattering. Despite different speeds and interactions, the description for neutron transport is similar. Consequently, we summarize the derivation of the transport equation by Lewis and Miller [62] but use photon transport notation. The summary is a statement of energy balance in one inertial frame of reference. Buchler [14] provides a derivation of the transport equation in a general, comoving fluid frame that is discussed in section 1.1.1. For a small volume in phase space, $|\Delta\vec{r}|\Delta A\Delta\Omega\Delta\nu$, the change in I_ν over a small change in the local time Δt is balanced by losses from streaming and collisions and gains from emission and scattering. This balance can be expressed as [62, p. 22]

$$\begin{aligned}\frac{1}{c}(I_\nu(\vec{r},\hat{\Omega},t+\Delta t) - I_\nu(\vec{r},\hat{\Omega},t))|\Delta\vec{r}|\Delta A\Delta\nu\Delta\Omega = &\\ - (I_\nu(\vec{r}+|\Delta\vec{r}|\hat{\Omega},\hat{\Omega},t) - I_\nu(\vec{r},\hat{\Omega},t))\Delta A\Delta t\Delta\nu\Delta\Omega &\\ - \sigma_\nu(\vec{r})I_\nu(\vec{r},\hat{\Omega},t)|\Delta\vec{r}|\Delta A\Delta t\Delta\nu\Delta\Omega + \frac{q_\nu(\vec{r},\hat{\Omega},\nu,t)}{4\pi}|\Delta\vec{r}|\Delta A\Delta t\Delta\nu\Delta\Omega \quad , &\end{aligned} \tag{1.2}$$

where $|\Delta\vec{r}|$ is the distance to change position along direction $\hat{\Omega}$, ΔA is the area of a surface oriented with normal vector $\hat{\Omega}$, Δt is a finite time span, $\Delta\nu$ is a bandwidth containing ν, and $\Delta\Omega$ is a solid angle neighborhood around $\hat{\Omega}$. The “macroscopic” opacity [62, p. 4], σ_ν, dictates the amount of energy removal out of the phase space volume; the external and scattering sources, q_ν, dictate the amount of energy addition to the phase space volume. Following Lewis and Miller [62, pp. 4-5], a beam traveling along a direction is diminished proportional to the ratio of collision area to beam area. For a $|\Delta\vec{r}|$ that resolves one layer of collision centers across a beam area of ΔA, the density of collision centers for $\Delta A|\Delta\vec{r}|$ multiplied by the collisional area per center multiplied by $|\Delta\vec{r}|$ yields the loss fraction for the beam traveling $|\Delta\vec{r}|$ [62, p. 5]. Considering Eq. (1.2), σ_ν is the loss ratio per $|\Delta\vec{r}|$. Dividing Eq. (1.2) by $\Delta t|\Delta\vec{r}|\Delta A\Delta\Omega\Delta\nu$ and taking the limit of the result as Δt, $|\Delta\vec{r}| \to 0$ yields

$$\frac{1}{c}\frac{\partial I_\nu}{\partial t} + \hat{\Omega}\cdot\nabla I_\nu = \frac{q_\nu}{4\pi} - \sigma_\nu I_\nu \quad , \tag{1.3}$$

where the streaming operator, $\hat{\Omega} \cdot \nabla$, is the directional derivative along $\hat{\Omega}$. The source term q_ν can be expressed as the sum of external sources (i.e. material emission) and scattering sources. For photons of frequency ν' traveling in direction $\hat{\Omega}'$, the portion of $I_{\nu'}(\vec{r}, \hat{\Omega}', t)$ redistributed into the neighborhood of direction $\hat{\Omega}$ and the neighborhood of ν is governed by the differential scattering opacity, $\sigma_s(\vec{r}, \nu' \to \nu, \hat{\Omega}' \cdot \hat{\Omega})$. In Eq. (1.3), q_ν divides into external and scattering sources [62, p. 35],

$$q_\nu = q_{\nu,e} + \int_{4\pi} \int_0^\infty \frac{\nu}{\nu'} \sigma_s(\vec{r}, \nu' \to \nu, \hat{\Omega}' \cdot \hat{\Omega}) I_{\nu'}(\vec{r}, \hat{\Omega}', t) \, d\nu' \, d\Omega' \quad , \tag{1.4}$$

and the total opacity σ_ν is

$$\sigma_\nu = \sigma_{\nu,a} + \int_{4\pi} \int_0^\infty \sigma_s(\vec{r}, \nu \to \nu', \hat{\Omega} \cdot \hat{\Omega}') \, d\nu' \, d\Omega' \quad , \tag{1.5}$$

where $q_{\nu,e}$ and $\sigma_{\nu,a}$ are the external source and absorption opacity, respectively [86, p. 13-15]. Considering Eq. (1.1), the fraction ν/ν' conserves particle number through collision events. Castor indicates it is also possible to derive the transport equation purely from classical electromagnetism [19, p. 70].

Radiation traveling through a small aperture may diffract; in this case, geometric ray tracing for photons no longer furnishes a complete description. In transport theory, particles are assumed to be points [62, p. 3]. The point particle assumption is valid when the particle wavelength, λ, is small compared to the characteristic size of collision centers, $|\Delta\vec{r}|$, and mean free path length, $1/\sigma$. For some material, the spacing of collision locations is analogous to the aperture while mean free path length is analogous to a distance to a detector in Castor's construction. Hence, if the objective is to apply transport theory where valid, $1/\sigma$ must be large (see, e.g., [19, p. 70], [53, p. 478]) and $|\Delta\vec{r}|$ must be large enough to subtend the characteristic diffraction angle. The complimentary constraint is that diffraction angle or λ must be sufficiently small. For two rays associated with oscillatory fields initially in phase at a distance $|\Delta\vec{r}|$ apart and directed to meet at a distance $1/\sigma$ along a vector orthogonal to $\Delta\vec{r}$, the phase difference of the fields at the meeting point is

$$\Delta\phi = \frac{2\pi}{\lambda}\left\{\left(\frac{\sigma^{-1}}{\cos(\theta)}\right)\left(\left(\left(\frac{|\Delta\vec{r}|\cos(\theta)}{\sigma^{-1}}\right)^2 - \frac{2|\Delta\vec{r}|\sin(\theta)}{\sigma^{-1}} + 1\right)^{\frac{1}{2}} - 1\right)\right\} \quad , \tag{1.6}$$

where $\Delta\phi$ is the phase change and θ is the observation angle of one of the rays with respect to the axis orthogonal to $\Delta\vec{r}$. Setting $\lambda \ll |\Delta\vec{r}| \ll \sigma^{-1}$ and expanding to leading order, Eq. (1.6) implies a minimum of the diffracted intensity profile at

$$\theta \approx \frac{\lambda}{2|\Delta\vec{r}|} \quad . \tag{1.7}$$

Notably, $1/\sigma$ is not present in Eq. (1.7) and the angular span of diffraction viewing angles must diminish with decreasing wavelength or increased collision center spacing.

For a plane wave normally incident on a circular aperture of radius $|\Delta\vec{r}|$, Jackson [53, p. 492] computes the diffracted power per solid angle as

$$\frac{dP}{d\Omega} = P_i\frac{(k|\Delta\vec{r}|)^2}{4\pi}(\mu^2+\eta^2)\left|\frac{2J_1(k|\Delta\vec{r}|\sin(\theta))}{k|\Delta\vec{r}|\sin(\theta)}\right|^2 \quad , \tag{1.8}$$

where P_i is total incident power, $k = 2\pi/\lambda$, $\mu = \cos(\theta) = \hat{k}\cdot\hat{\Omega}$, $\hat{\Omega}$ is the unit normal to the aperture, $\hat{k}$ is a wave direction after transmission through the aperture, $\eta = \hat{k}\cdot\Delta\vec{r}/|\Delta\vec{r}|$ and J_1 is the first-order Bessel function of the first kind. The value $|2J_1(k|\Delta\vec{r}|\sin(\theta))/k|\Delta\vec{r}|\sin(\theta)|^2$ peaks to one at $\theta = 0$ and drops sharply to zero when $|k\Delta\vec{r}| \gg 1$ [53, p. 492]; the radiation passes through the aperture geometrically.

The radiation transport equation has been applied to compute radiation fields in astrophysical settings and high energy density experimental settings. Considering a pure Nickel-56 fluid of 2 solar masses ($M_\odot$), or ~2.8×10^{33} g, homologously expanding at $U = 2.2\times10^9$ cm/s at t =2 days with maximum radius $R = Ut$, adopting a nominal grey microscopic opacity of 0.13 cm^2/g from Pinto and Eastman [85] for Type Ia supernovae, and setting the material at 10^5 K: $|\Delta\vec{r}| \approx 5.08\times10^3$ cm, $\sigma^{-1} \approx 6.33\times10^{11}$ cm, and $\lambda \approx 10^{-5}$ cm. Thus, in the context of the early phase of thermonuclear supernovae, the result, $\lambda \ll |\Delta\vec{r}| \ll \sigma^{-1}$, roughly implies transport theory is satisfactory in predicting radiation propagation. Considering a high energy density regime with an electron density $n_e = 10^{18}$ cm^{-3}, $\sigma^{-1} = 10^{-24}T_e^3$ cm^{-1} (T_e in K), and a temperature of $T_e = 10^7$ K, the result is: $|\Delta\vec{r}| \approx 1/n_e^{1/3} = 10^{-6}$ cm, $\sigma^{-1} = 10^{-3}$ cm, and $\lambda \approx 10^{-7}$. The electron aperture and photon wavelength are small with respect to the mean free path for the estimates considered. The strength of diffraction is low for modest diffraction angles; at a 0.1 radian diffraction angle, $|2J_1(k|\Delta\vec{r}|\sin(\theta))/k|\Delta\vec{r}|\sin(\theta)|^2 \approx 0.005$, or approximately half a percent of the geometric component. The drop in power transmission with increasing diffraction angle is sharper for the astrophysical case. Pomraning [86] provides an in depth discussion of the validity of the transport equation. Since the equation for photon transport, or radiative transfer, is an equation of intensity, photon interference and diffraction are ignored by the solutions [86]. Perceiving photons as localized wave packets instead of plane waves, the width of the packets must be small compared to atomic spacing and photon separation [86].

1.1.1 Radiation Matter Interaction

Radiation interactions with material are mediated through the cross section and emission in Eq. (1.3). Three primary types of interaction for which one can compute a photon cross section are [4, p. 345]:

- Emission
  - Bremsstrahlung (free-free)
  - Radiative capture (free-bound)
  - Line emission (bound-bound)
- Absorption
  - Inverse bremsstrahlung (free-free)
  - Photo-ionization (bound-free)
  - Line absorption (bound-bound)
- Scattering
  - Compton (Thomson)
  - Pair production

The terms “bound” and “free” refer to electron states before and after a photon collision with respect to a potential field. The processes listed manifest in the quantization of the Hamiltonian for an atom in an external field [19, p. 152] (shown in Gaussian units),

$$H = -\sum_i \frac{Ze^2}{r_i} + \sum_{i<j} \frac{e^2}{r_{ij}} + \sum_i \frac{1}{2m}[\vec{p}_i - \frac{e}{c}\vec{A}(\vec{r}_i)]^2 + \int \frac{1}{8\pi}(|\vec{E}|^2 + |\vec{B}|^2)dV \quad , \tag{1.9}$$

where the terms on the right side are (left to right): potential energy due to electron interaction with atomic nucleus, electron-electron Coulomb repulsion, kinetic energy, and electromagnetic field energy. Expanding the kinetic energy term yields a radiation-matter interaction Hamiltonian [19, p. 153],

$$H_{\text{int}} = -\frac{e}{mc}\sum_i \vec{p}_i \cdot \vec{A}(\vec{r}_i) + \frac{e^2}{2mc^2}\sum_i |\vec{A}(\vec{r}_i)|^2 \quad , \tag{1.10}$$

where to first order the terms linear in vector potential, $\vec{A}$, account for absorption and emission while the terms quadratic in $\vec{A}$ account for scattering. To compute rates and cross sections associated with the different portions of the Hamiltonian from first principles, one can choose a quantum or quasi-classical (equivalently quasi-quantum) approach [4, p. 345]. One can either use the scattering matrix-propagator framework [89] or the closely related Fermi's golden rule,

$$R(i \to f) = \frac{4\pi^2}{h}|\langle f|H_{\text{int}}|i\rangle|^2 \rho_f \quad , \tag{1.11}$$

where i denotes the initial state, f denotes the final state, and ρ_f is the state density about the final state. The quantity $R(i \to f)$ is the transition probability per unit time from i to f. A cross section can be thought of as a transition probability per unit time per the photon current incident on a collision target. The probability rate is often written as a differential [89, p. 80]. With this in mind an alternative to Eq. (1.11) is

$$\frac{d\,R(i \to f)}{d\Omega} = \frac{4\pi^2}{h}|\langle f|H_{\text{int}}|i\rangle|^2 \rho'_f \quad , \tag{1.12}$$

where Ω is solid angle and ρ'_f is the state density per unit energy per unit solid angle. Then

$$\frac{d\sigma_\nu}{d\Omega} = \frac{1}{|\int_{\Omega_{\text{inc}}} \hat{\Omega} I_\nu d\,\Omega|} \frac{d\,R(i \to f)}{d\Omega} \quad , \tag{1.13}$$

where Ω_{inc} is the domain of solid angle of the intensity incident on the target particle and $d\sigma/d\Omega$ is the differential cross section for the interaction implied by the quantum state transition $i \to f$. Cross sections computed with Eq. (1.13) are important to accurately model radiative transfer in computer codes. In addition, the cross section σ is informative as to whether the diffusion equation can be used instead of (1.3) to solve for the scalar flux $\int_{4\pi} I_\nu d\Omega$. Fick's law [19, p. 84],

$$\int_{4\pi} \hat{\Omega} I_\nu d\,\Omega = -\frac{1}{3\sigma_\nu}\vec{\nabla}\int_{4\pi} I_\nu d\,\Omega = -\frac{1}{3\sigma_\nu}\vec{\nabla}\phi_\nu \quad , \tag{1.14}$$

can be derived from the lowest order terms in an asymptotic expansion of Eq. (1.3). Integrating Eq. (1.3) and incorporating Eq. (1.14) then yields

$$\frac{1}{c}\frac{\partial \phi_\nu}{\partial t} - \vec{\nabla}\cdot\left(\frac{1}{3\sigma_\nu}\vec{\nabla}\phi_\nu\right) = q_\nu - \sigma_\nu \phi_\nu \tag{1.15}$$

where it has been assumed that the scattering, absorption, and emission are isotropic.

Equations (1.12) and (1.13) indicate that the cross sections for emission, absorption and scattering can each be formulated with probabilities. For line-line interactions, the probability density functions for absorption, stimulated emission, and spontaneous emission are the Einstein coefficients $\{B_{ij}, B_{ji}, A_{ji}\}$, respectively [73, p. 329], where i represents a lower energy state and j represents the higher energy state.

For a given line profile Ξ_ν with the $i \leftrightarrow j$ transition, the rates of energy absorbed and emitted from the line per unit volume are [73, p. 329]

$$(\sigma_{\nu,a} + \tilde{\sigma}_{\nu,a})I_\nu = \frac{B_{ij}h\nu_{ij}}{4\pi} n_i \Xi_\nu I_\nu \quad , \tag{1.16a}$$

$$\tilde{\sigma}_{\nu,a} I_\nu = \frac{B_{ji}h\nu_{ij}}{4\pi} n_j \Xi_\nu I_\nu \quad , \tag{1.16b}$$

$$q_{\nu,e} = \frac{A_{ji}h\nu_{ij}}{4\pi} n_j \Xi_\nu \quad , \tag{1.16c}$$

where n_i and n_j are the population densities at state i and j, and $h\nu_{ij}$ is the energy difference between state i, j. The stimulated (or induced) emission coefficient is written as $\tilde{\sigma}_{\nu,a}$ because it is seen as a correction to the absorption. Given the symmetry of form between Eqs. (1.16a) and (1.16b), stimulated emission can be thought of as negative absorption. Bound-free and free-free interactions are discussed in 1.1.3.

In conjunction with collision type, the state of the radiation field also depends on the motion of the matter with which photons interact. At relativistic speeds, in different frames of reference the properties of a radiation field are different. For instance, a radiative emission source moving away from an observer will appear to the observer to be emitting lower frequency photons than an identical radiation source not moving with respect to the observer. Thus, it must be that relativistic effects affect the collision expressions described above by changing intensity, direction, and frequency. There are several ways to both express and derive the set of radiation hydrodynamics equations that incorporate relativity in the radiation coupling with matter. The starting point of special relativity is the acknowledgement that different inertial frames of reference observe the same speed of light. An equation that preserves light speed for each frame is

$$c^2\Delta t^2 - |\Delta\vec{r}|^2 = c^2\Delta t_0^2 - |\Delta\vec{r}_0|^2 \ \ , \tag{1.17}$$

where $(c\Delta t, \Delta\vec{r})$ and $(c\Delta t_0, \Delta\vec{r}_0)$ are the change in spacetime coordinates of two different reference frames. Eq. (1.17) implies that a transformation in reference frame must be accompanied by changes in length and time that preserve the equality. The set of transformations between frames that preserve Eq. (1.17) is the Minkowski group of three dimensional rotations along with the 4x4 hyperbolic transformation [19, p. 103]

$$\mathbf{A} = \begin{pmatrix} \gamma & \gamma\vec{U}^T/c \\ \gamma\vec{U}/c & \mathbf{I} + (\gamma-1)\vec{U}\vec{U}^T/U^2 \end{pmatrix} \ \ , \tag{1.18}$$

where $\vec{U}$, U, and $\gamma = 1/\sqrt{1-U^2/c^2}$ are the velocity, speed, and dilation factor of the frame being transformed with respect to the resulting frame. The superscript, T, indicates the transpose is taken; for a column vector, the transpose is a row vector. Without loss of generality, if one spatial direction (z) is made to align with the velocity, then the orthogonal components of $\vec{r}$ don't change between frames and $\mathbf{A}$ can be reduced to a 2x2 matrix

$$\begin{pmatrix} ct \\ z \end{pmatrix} = \mathbf{A} \begin{pmatrix} ct_0 \\ z_0 \end{pmatrix} = \gamma \begin{pmatrix} 1 & U/c \\ U/c & 1 \end{pmatrix} \begin{pmatrix} ct_0 \\ z_0 \end{pmatrix} \quad . \tag{1.19}$$

Henceforth, the terms adorned with a 0 subscript will denote quantities measured in the material fluid comoving frame while the bare quantities will denote those measured in the lab frame. A thought experiment about spatial contraction and time dilation reveals Lorentz invariant quantities. Briefly using Eq. (1.19),

$$\begin{pmatrix} 0 \\ \Delta z \end{pmatrix} = \gamma \begin{pmatrix} 1 & U/c \\ U/c & 1 \end{pmatrix} \begin{pmatrix} c\Delta t_0 \\ \Delta z_0 \end{pmatrix} \rightarrow \Delta z = \frac{1}{\gamma}\Delta z_0 \ , \tag{1.20a}$$

$$\begin{pmatrix} c\Delta t \\ \Delta z \end{pmatrix} = \gamma \begin{pmatrix} 1 & U/c \\ U/c & 1 \end{pmatrix} \begin{pmatrix} c\Delta t_0 \\ 0 \end{pmatrix} \rightarrow \Delta t = \gamma \Delta t_0 \ , \tag{1.20b}$$

where Δz is a length measured at one point in time in the lab frame, Δt is a time duration in the lab frame following a spatial point moving at $\vec{U}$. Since the orthogonal lengths do not change, it is apparent that in the differential limit of the spacetime measures

$$dt\, d^3\vec{r} = dt_0\, d^3\vec{r}_0 \quad . \tag{1.21}$$

Because any lab frame coordinate system can be rotated to align one axis with the velocity of the other inertial frame without changing the magnitude of the velocity between the frames, Eq. (1.21) must be true between any two inertial frames [19, p. 106]. The differential time parameter τ of a particle inertial frame must satisfy $c^2 d\tau^2 = c^2 dt^2 - |\vec{r}|^2$. Differentiating the spacetime vector with respect to the proper time τ yields the energy-momentum vector. Incorporating the invariance of the measure of τ along with $\frac{dt}{d\tau} \sim \nu$ into Eq. (1.21) yields [19, p. 105]

$$\nu d^3\vec{r} = \nu_0 d^3\vec{r}_0 \quad . \tag{1.22}$$

The 4x1 vector for photon energy-momentum is [19, p. 103] $\frac{h\nu}{c^2}(1, c\hat{\Omega})^T = (E/c^2, \vec{p})^T$. Hence the magnitude of the momentum scales with the energy. Pomraning [86, p. 270] defines a Jacobian matrix for the momentum volume element. With $\hat{\Omega} = (\mu_i)$, the Jacobian can be expressed as

$$\mathbf{J} = \frac{\nu}{\nu_0}\left(\frac{\partial \mu_i}{\partial \mu_{0,j}}\right) = \frac{\nu}{\nu_0}\mathbf{R} \tag{1.23}$$

where $\mathbf{R}$ is a three dimensional rotation. Given $d^3\vec{p} \sim \nu^2 d\nu d\Omega$, another invariant equation is then

$$\nu d\nu d\Omega = \nu_0 d\nu_0 d\Omega_0 \quad . \tag{1.24}$$

Equations (1.21), (1.22), and (1.24) can be used to construct the comoving frame transport equation. In the lab frame, the form of Eq. (1.3) remains unchanged while the individual terms will be affected by fluid motions of the interacting material. For instance, if the comoving scattering cross sections are isotropic, the lab frame scattering cross sections will be anisotropic. In addition, the radiation field will be affected by aberration and Doppler shift. These relations are derived by Pomraning [86, p. 156] and Castor [19, p. 102–111]. Buchler [14, p. 396] expands the proper time derivative of the photon Boltzmann distribution using a basis of 4-vectors orthogonal with respect to the Minkowski inner product. The essential result for photons can be obtained by neglecting O(U^2/c^2) in a variational (chain rule) expansion in the space-time and energy-momentum of a Lorentz invariant distribution, $\tilde{f}$,

$$\frac{d\tilde{f}}{d\tau} = \left(1 + \frac{\vec{U}\cdot\hat{\Omega}_0}{c}\right)\left(\frac{\partial \tilde{f}}{\partial t} + \vec{U}\cdot\nabla\tilde{f}\right) + c\hat{\Omega}_0\cdot\nabla\tilde{f} - \nu_0\left(\frac{1}{c}\frac{\partial \vec{U}}{\partial t} + \hat{\Omega}_0\cdot\nabla\vec{U}\right)\cdot\nabla_{\nu_0\hat{\Omega}_0}\tilde{f} \quad , \tag{1.25a}$$

$$\tilde{f} \sim \frac{I_\nu}{\nu^3} = \frac{I_{\nu_0}}{\nu_0^3} \quad , \tag{1.25b}$$

where it has been assumed that spacetime in the inertial lab frame is not curved so that one may directly apply Eq. (1.3) to get the transport solution. Equation (1.25a) is mixed in independent variables with photon energy and direction defined with respect to the comoving frame and space-time with respect to the lab frame. Equation (1.25b) results from the invariant differentials. Incorporating Eq. (1.25b) into Eq. (1.25a), multiplying through by ν_0^3 and balancing the resulting expression with $q_0/4\pi - \sigma_0 I_0$ gives Castor's equation,

$$\begin{aligned}\left(1+\frac{\hat{\Omega}_0\cdot\vec{U}}{c}\right)\left(\frac{1}{c}\frac{\partial I_0}{\partial t}+\frac{\vec{U}}{c}\cdot\nabla I_0\right)+\hat{\Omega}_0\cdot\nabla I_0-\frac{\nu_0}{c}(\vec{a}/c+\hat{\Omega}_0\cdot\nabla\vec{U})\cdot\nabla_{\nu_0\hat{\Omega}_0}I_0 \\ +\frac{3}{c}(\hat{\Omega}_0\cdot\vec{a}/c+\hat{\Omega}_0\cdot\nabla(\vec{U}\cdot\hat{\Omega}_0))I_0=\frac{q_0}{4\pi}-\sigma_0 I_0\ \ ,\end{aligned}\tag{1.26}$$

where $\vec{a} = \partial\vec{U}/\partial t$ and the ν_0 subscripts have been discarded for convenience. In practice, it is often assumed the right side of Eq. (1.26) is isotropic [19, p. 109]. Applying $\int_0^\infty\int_{4\pi} d\nu_0 d\Omega_0$ and $\int_0^\infty\int_{4\pi}\hat{\Omega}_0 d\nu_0 d\Omega_0$ to the right side of Eq. (1.26) yield radiation energy-momentum terms to couple to the Euler equations, g_0^0 and $\vec{g}_0$. The 4x1 vector given by $(g^0,\vec{g})$ is a 4-vector in the relativistic sense [19, p. 109], hence to first order

$$g^0 = g_0^0 + \frac{\vec{U}}{c^2}\cdot\vec{g}_0\ \ , \tag{1.27a}$$

$$\vec{g} = \vec{g}_0 + \vec{U}g_0^0\ \ . \tag{1.27b}$$

Neglecting other external forces, the set of coupled Euler equations are [19, p. 85]

$$\frac{\partial\rho}{\partial t} + \nabla\cdot(\rho\vec{U}) = 0\ \ , \tag{1.28a}$$

$$\frac{\partial\rho\vec{U}}{\partial t} + \nabla\cdot(\rho\vec{U}\vec{U}^T) + \nabla P = -\vec{g}\ \ , \tag{1.28b}$$

$$\frac{\partial}{\partial t}\left(\rho e + \frac{1}{2}\rho U^2\right) + \nabla\cdot\left(\rho\vec{U}(e+P/\rho) + \frac{1}{2}\rho\vec{U}U^2\right) = -g^0\ \ , \tag{1.28c}$$

where $e, \rho, \vec{U}$ and P are the internal energy, density, velocity, and pressure fields to be solved for over the given space-time domain. The mass conservation law remains unchanged with radiation coupling; there is no coupling term in Eq. (1.28a). With either Eq. (1.3) or (1.26), the resulting set of six equations (Eq. (1.28b) has one for each spatial dimension) has seven unknowns. To close the set of equations, an equation of state relating pressure to internal energy and density can be used.

A discussion of state variables such as temperature and pressure from micro-physics is available provided by Mihalas and Weibel Mihalas [73]. If a temperature field exists and the near-equilibrium state of the fluid is not perturbed by the radiation field in such a way that causes the characteristic thermalization time to become comparable in magnitude to the characteristic fluid flow time, then one may use local thermodynamic equilibrium (LTE) radiative transport with Eq. (1.28). Otherwise, one must keep track of the micro-physical energetic state of the matter to determine the nature of the vector $(g^0, \vec{g})$.

1.1.2 NLTE Transport

Non-LTE or NLTE stands for non-local thermodynamic equilibrium. In terms of radiation matter interaction, non-LTE transport accounts for the effects of the photon field on the ionization and excitation state of the matter [19, p. 179]. If material collisions (electron-ion, ion-ion, etc.) are not sufficiently frequent, the relaxation time to ascribe local temperatures may be too large to ascribe a material temperature field. In other words, one temperature may not be sufficient or accurate enough to describe the material state. In such instances, the computations of the matter radiation interaction can be resolved to the microscopic level by keeping track of atomic populations. This indexing of the atomic populations is obtained with the kinetic equation, [19, p. 180]

$$\rho \frac{D(N_{ij}/\rho)}{Dt} = \sum_k [N_{ik}(P_{kj} + C_{kj}) - N_{ij}(P_{jk} + C_{jk})] \ , \tag{1.29}$$

where N_{ij} is a number density of atoms of species i at energy j, P_{kj} is a radiative rate from energy state k to energy state j, and C_{kj} is an inelastic electron collision rate between the same states. This equation is coupled through the rate coefficients with the intensity, I_ν, so Eq. (1.29) along with Eq. (1.3) are a solvable system of equations.

For $k > j$, the values of P_{kj} and P_{jk} can be obtained from Eq. (1.16). Balancing photon transitions with atomic state [19, p. 181],

$$N_{i,k}P_{k,j} = \frac{1}{4\pi}\int_{4\pi}\int_{0}^{\infty} N_{ik}(B_{kj}I_\nu + A_{kj})\Xi_{\nu,j,k}\,d\nu\,d\Omega \ , \tag{1.30a}$$

$$N_{i,j}P_{j,k} = \frac{1}{4\pi}\int_{4\pi}\int_{0}^{\infty} N_{ij}B_{jk}I_\nu\Xi_{\nu,j,k}\,d\nu\,d\Omega \ . \tag{1.30b}$$

The values $\sigma_{\nu,a}$ and $q_{\nu,e}$ are

$$\sigma_{\nu,a} = \frac{h\nu}{4\pi}\sum_{i}\sum_{j}\sum_{k>j}(N_{ij}B_{jk} - N_{ik}B_{kj})\Xi_{\nu,j,k} \ , \tag{1.31a}$$

$$q_{\nu,e} = \frac{h\nu}{4\pi}\sum_{i}\sum_{j}\sum_{k>j}N_{ik}A_{kj}\Xi_{\nu,j,k} \ , \tag{1.31b}$$

where the contributing state transitions as well as the number of atomic species has been summed over. Though not explicitly expressed, the rates and number of energy levels delineated with the instantiations of j and k are dependent on the atomic species index, i.

1.1.3 LTE Transport

If the assumptions underlying local thermodynamic equilibrium (LTE) [73, p. 386–387] hold, then the state of the material can be partially described with a temperature field. Moreover, if radiation sources do not significantly unbalance the material state, then the spectrum of the emitted photons can be described in terms the material temperature as well. The microscopic implications have been covered by Mihalas and Weibel Mihalas [73]. With respect to Eq. (1.31), one can show the Planck function results from detailed balance of radiative processes. Detailed balance of radiation processes implies each transition $j \to k$ that absorbs a photon is exactly balanced by the inverse $k \to j$ stimulated or spontaneous emission [73, p. 387]. Another LTE assumption is complete redistribution of photon frequency in an absorption followed by an emission [19, p. 194–195]. Complete redistribution occurs when the frequency of a photon absorbed by a particular atom does not correlate with the atom's subsequent emission; correlation is tempered by atomic and electronic collisions. Because LTE hinges on material collisions occurring much more frequently than radiative processes [73, p.387], it is valid to group the assumption of complete redistribution with LTE. Balancing absorption with spontaneous and stimulated emission for one line, $k' \rightarrow j'$, and solving Eq. (1.16) for $I_\nu = S_{\nu,j',k'}$, the source intensity must be [19, p. 182]

$$S_{\nu,j',k'} = \frac{q_{\nu,e}(k' \rightarrow j')}{\sigma_{\nu,a}(j' \rightarrow k')} = \frac{N_{ik'} A_{k'j'}}{N_{ij'} B_{j'k'} - N_{ik'} B_{k'j'}} \quad . \tag{1.32}$$

From the interaction Hamiltonian, Eq. (1.10), and the relativistic invariants, Eqs. (1.21), (1.22), and (1.24), the rate coefficients can be expressed in terms of the photon frequency and degeneracy of the two atomic states to give

$$S_{\nu,k',j'} = \frac{2h\nu^3/c^2}{N_{ij'} g_{ik'} / N_{ik'} g_{ij'} - 1} \quad , \tag{1.33}$$

where $g_{ij'}$ and $g_{ik'}$ are the number of angular momentum projections of atom i at energy level j' and k', respectively [19, p. 155].

The macroscopic state of an ensemble of particles is completely specified with the internal energy, volume, and number of particles [73, p. 35]. In statistical mechanics, entropy is defined as being proportional to the logarithm of the number of possible distinct particle configurations that yield the macroscopic state [73, p. 36],

$$\mathcal{S} = k \ln(W) \quad , \tag{1.34}$$

where $\mathcal{S}$ is the entropy, k is Boltzmann's constant, and W is the number of microscopic configurations. To compute W, Mihalas assumes the state of the gas is in a classical limit [73, p. 37]. The procedure of counting divides phase space into energy cells; each energy cell having a number of phase space configurations, g_{ij}, associated with the energy level. In using g_{ij}, it has been implied that the energy bin j is associated with a particular atomic species i; hence the particles are tacit electrons for the purpose of this summary. The species index is carried through the analysis but ignored to maintain the classical assumption. Consequently W is (with a subscript i) [73, p. 38]

$$W_i(v_{ij}) = \prod_j (g_{ij})^{v_{ij}} \; / \; \prod_j (v_{ij})! \quad , \tag{1.35}$$

where v_{ij} is the number of electrons occupying a state of energy j. From the numerator of Eq. (1.35), it can be inferred that the Pauli exclusion principle has been neglected. Equation (1.35) might be reasonably applicable to a plasma with ion species i where the free energy spectrum of the electrons has been artificially discretized. Incorporating Eq. (1.35) into (1.34), applying Sterling's approximation [73, p. 39], deriving the partition function [73, p. 40], and using the first and second law of thermodynamics results in a relationship between the ratio of two atomic state densities and temperature [73, p. 41],

$$N_{ij'}/N_{ik'} = \frac{g_{ij'}}{g_{ik'}} e^{-\frac{h\nu}{kT}} \quad , \tag{1.36}$$

where $h\nu$ is the transition energy for $k' \to j'$ (j' and k' are not necessarily bound energy states) and $N_{ij'} = v_{ij'}/V$ for system volume V. So for a near-equilibrium system of radiating particles, combining Eq. (1.36) with Eq. (1.33) yields the Planck function,

$$S_{\nu,j',k'} = B_\nu = \frac{2h\nu^3/c^2}{e^{-\frac{h\nu}{kT}} - 1} \quad . \tag{1.37}$$

Considering Eq. (1.33) with Eq. (1.37), each radiative process must, as a collective component of the electron dynamics, contribute a Planckian source intensity. By construction, Eq. (1.37) must be the equilibrium radiation intensity in a thermal material. Additionally, Eq. (1.37) indicates the well known result that photons obey Bose-Einstein statistics and are thus bosons. The implication that photons are bosonic can be traced back to the interaction Hamiltonian in Eq. (1.10) and the consequent dependence of the total emission rate on I_ν.

Incorporating Eq. (1.37) into Eq. (1.3), the frequency dependent, thermal radiative transport equation is [86, p. 46]

$$\begin{aligned}\frac{1}{c}\frac{\partial I_\nu}{\partial t} + \hat{\Omega}\cdot\nabla I_\nu &= \sigma_{\nu,a}(B_\nu - I_\nu) \\ &+ \int_{4\pi}\int_0^\infty \frac{\nu}{\nu'}\sigma_s(\vec{r},\nu'\to\nu,\hat{\Omega}'\cdot\hat{\Omega}) I_{\nu'}(\vec{r},\hat{\Omega}',t)\left(1 + \frac{c^2 I_\nu(\vec{r},\hat{\Omega},t)}{2h\nu^3}\right) d\nu'\, d\Omega' \\ &- \int_{4\pi}\int_0^\infty \sigma_s(\vec{r},\nu\to\nu',\hat{\Omega}\cdot\hat{\Omega}') I_\nu(\vec{r},\hat{\Omega},t)\left(1 + \frac{c^2 I_{\nu'}(\vec{r},\hat{\Omega}',t)}{2h(\nu')^3}\right) d\nu'\, d\Omega' \quad . \end{aligned} \tag{1.38}$$

It is assumed in Eq. (1.38) that $\sigma_{\nu,a}$ is corrected for stimulated emission. In addition, the angular arguments of the scattering opacities imply that bulk material motion is not being taken into account. To do so, one needs to include additional angular arguments to the opacity and source terms to account for the relativistic anisotropies that the lab frame observes [86, p. 154]. In many practical contexts, the frequency shift of the photons from scattering is negligible [19, p. 160–161]. If it is further assumed that $\sigma_s(\vec{r}, \nu \to \nu', \hat{\Omega} \cdot \hat{\Omega}') = \sigma_s(\vec{r}, \nu' \to \nu, \hat{\Omega}' \cdot \hat{\Omega})$, then $\sigma_s(\vec{r}, \nu' \to \nu, \hat{\Omega}' \cdot \hat{\Omega}) = \sigma_{\nu,s}(\vec{r}, \hat{\Omega}' \cdot \hat{\Omega})\delta(\nu - \nu')$ and

$$\frac{1}{c}\frac{\partial I_\nu}{\partial t} + \hat{\Omega} \cdot \nabla I_\nu = \sigma_{\nu,a}(B_\nu(T) - I_\nu) - \sigma_{\nu,s} I_\nu + \int_{4\pi} \sigma_{\nu,s}(\hat{\Omega}' \cdot \hat{\Omega}) I_\nu(\vec{r}, \hat{\Omega}', t)\, d\Omega' \quad , \tag{1.39}$$

where $\sigma_{\nu,s} = \int_{4\pi} \int_0^\infty \sigma_s(\vec{r}, \nu \to \nu', \hat{\Omega} \cdot \hat{\Omega}') d\nu'\, d\Omega'$. When the material background is absent of bulk fluid flow Eq. (1.28) reduces to

$$\frac{\partial(\rho e)}{\partial t} = -\int_{4\pi} \int_0^\infty \sigma_{\nu,a}(B_\nu - I_\nu)\, d\nu\, d\Omega \quad . \tag{1.40}$$

Defining the specific heat as $c_v = \partial e/\partial T$ and $C_v = \rho c_v$, at constant density, Eq. (1.40) becomes

$$C_v \frac{\partial T}{\partial t} = \int_{4\pi} \int_0^\infty \sigma_{\nu,a}(I_\nu - B_\nu(T)) d\nu\, d\Omega \quad . \tag{1.41}$$

The Planck spectrum's dependence on the material temperature, T, is written explicitly in Eq. (1.41) and Eq. (1.39) to show the material-radiation coupling.

The above description of LTE allows for a robust treatment of photoionization, recombination, and bremsstrahlung processes. Using Saha's equation, the Maxellian distribution, and energy conservation, the photoionization probability is [73, p. 331],

$$p_\nu = \left(\frac{8\pi m_e^2 v_e^2 g_1}{h^2 g_0} \right) G(v) \quad , \tag{1.42}$$

where m_e is the electron mass, v_e is the electron velocity after collision, g_1 is the ion degeneracy weight, g_0 is atom degeneracy weight, and $G(v)$ is the induced recombination probability. Using the Einstein relations, Mihalas and Weibel Mihalas [73] write the total absorption cross section for photoionization at LTE as

$$\sigma_{\nu,a} = n_0 h\nu p_\nu (1 - e^{-h\nu/kT}) \ , \tag{1.43}$$

where n_0 is the density of atoms [73, p. 332]. The derivation of free-free absorption is similar [19, p. 168].

The theory presented is meant to be a survey of the electrodynamical physics that contribute to a theoretical foundation for subsequent sections of this thesis. Topics that have not been discussed include: polarization of light, refraction, dispersion, and fully relativistic quantum electrodynamics (QED). Detailed derivations of transport with polarized light and in refractive or dispersive media can be found in Pomraning's book on the foundations of radiation hydrodynamics [86, p. 106–153]. Finally, it is worth noting one additional argument for neglecting radiation diffraction provided by Pomraning [86, p. 47–49]. Pomraning states that the interacting material must not have crystalline regularity. The systems of interest are gases and plasmas; thus the material is not crystalline.

1.2 Applications of Radiation Transport Theory

Since equilibrium radiation energy density is proportional to the fourth power of temperature, radiation can have an important effect on material or fluid properties at high temperature. Examples where radiation transport is important to complete physical descriptions include stars, active galaxies, supernovae, high energy density experiments such as radiative shocks in Xenon, and inertial confinement fusion [19, 4]. High temperatures manifest in astrophysical and laboratory plasma contexts. Pomraning [86, p. ix] states generally that for material at temperatures on the order of thousands of degrees, radiation primarily transports energy; at temperatures on the order of millions of degrees, the radiation field may dominate the energy and momentum balance in the radiation-matter system. Consequently, multi-physics simulations of problems involving high temperature generally need to have a radiation field coupled to the material. In Sections 1.2.1 and 1.2.2, Type Ia supernovae (SNe Ia) and Inertial Confinement Fusion (ICF) are summarized, respectively. These fields motivate the radiation transport calculations presented in this thesis.

1.2.1 Type Ia Supernovae

Supernovae are the bright explosions of stars. The term, supernova, derives from the explosion appearing as a new astronomical object [52, 39]. Classifications of supernovae depend on characteristics of the observed spectra and, relatedly, the mechanism behind the explosion [83, p. 1]. If the spectrum of a supernova has hydrogen lines, it is classified as a Type II. Otherwise if there is no hydrogen in the spectrum, then the supernova is classified as a Type I.

Type Ia supernovae have been used as "standard candles" to measure the accelerated rate of expansion of the Universe (see, e.g. [90, 81]). The findings motivate the existence of dark energy. The majority of the events appear to display remarkably close peak luminosities. Moreover, the differences in the peak of the luminosity readings appear to be correlated with the duration of the events. Roughly speaking, the luminosity profiles versus time, or the light curves (LCs), of the observed events fit a one-parameter family; the parameter used by Phillips [84] is the amount of decline in the light curve magnitude in 15 days after maximum luminosity, Δm_{15}. Phillips and others found that larger decline rates corresponded to more brief, less luminous events. Additionally, the luminosity magnitudes appear to scale roughly linearly with Δm_{15} [84, 82]. Depicted in Fig., Perlmutter et al. propose a stretch factor of the time scale to fit light curves to a standard "template" LC [82, 80].

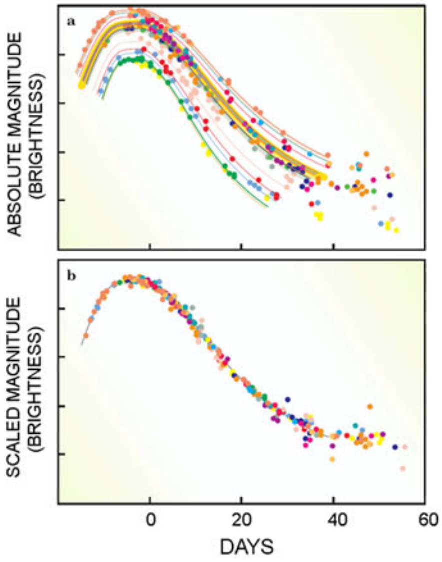

Figure 2: Absolute magnitude of light curves fit to a template light curve with a stretch correction [87]. The parameter family allows for direct comparison between luminosity measurements and thus relative distances.

SNe Ia are thought to have a thermonuclear burn phase that releases a large amount of energy and a ballistic phase. In the thermonuclear burn phase, heavier elements are synthesized in a burn wave that may become supersonic [92]. In the ballistic phase the post-explosion, high-velocity outflow emits gamma rays from radioactive decay of ^{56}Ni [98]. Evidence indicates that most observed Type Ia supernovae originate from the thermonuclear disruption of Carbon-Oxygen (C-O) white dwarf stars that have approached the Chandrasekhar mass, $\sim 1.4\,\mathrm{M}_{\odot}$ [52]. To approach the Chandrasekhar mass, it is believed that C-O white dwarfs accrete mass from a companion star; this is inferred through elimination of other candidate systems [52, 7, 92]. Gamezo [39] provides a description of what must occur as the star accretes mass to cause an explosion:

1. As the star obtains mass near $M = 1.4\,\mathrm{M}_{\odot}$, the temperature and rate of fusion reactions increase from gravitational compression.

2. The energy decrease from neutrino cooling and heat transfer is eventually less in magnitude than the energy increase from thermonuclear fusion.

3. Expansion becomes significant when thermal pressure overtakes the electron degeneracy pressure.

4. Expansion cannot cool the material enough to prevent thermonuclear burn. An energy of approximately 10^{51} ergs is released over several seconds.

During the nuclear deflagration, many SN Ia appear to produce approximately $\sim$0.6 $M_\odot$ of ^{56}Ni [52]. Seitenzahl et al. [92] present simulation results with a range of 0.3 to 1.11 $M_\odot$ of ^{56}Ni produced. For many SNe Ia, evidence of Si II, Ca II, S II appear in the line spectra around maximum luminosity [10]. The decay chain that heats the outflow is $^{56}\text{Ni}\rightarrow{}^{56}\text{Co}\rightarrow{}^{56}\text{Fe}$. For the spectra, SN Ia are characterized by an absence of Hydrogen lines and the presence of a strong Silicon line; these features constrain the nature of the possible progenitor system.

1.2.2 Inertial Confinement Fusion

The following discussion closely follows the text of Atzeni and Meyer-ter-Vehn [4]. From Einstein's mass-energy equivalence, energy release from a nuclear reaction with a change in total mass is [4, p. 2]

$$Q = \left(\sum_i m_i - \sum_f m_f \right) c^2 \ , \tag{1.44}$$

where Q is the net energy, m_i is the initial mass of a reactant, m_f is the final mass of a product, and c is again the speed of light. If the Q value is positive, the sum of the initial masses is greater than that of the final masses and the reaction is exothermic. The amount of energy released is equal to the amount of binding energy between the constituent nucleons of the products gained. Hence, reactions increasing the binding energy per nucleon are favored [4, p. 2–3]. It has been observed that fission reactions, where a nucleus splits into several smaller nuclei, occur for mass numbers greater than $A \approx 56$. At mass numbers greater than $A \approx 56$, the binding energy per nucleon begins to decreases with increasing mass number [4, p. 3]. Thus fusion reactions, where smaller nuclei collide and form larger nuclei, are more likely to occur in the mass number region below 56.

As with α-decay [55, p. 251–257], a fusion interaction involves transmission through a Coulomb potential barrier. Hence the calculation of probabilities or rates are similar in form. A rudimentary treatment of the fusion cross section calculation is given in [4]. Some important fusion reactions are given below [4, p. 11].

Table 1: Fusion reactions.

Reaction	Q (MeV)
$D + T \rightarrow \alpha + n$	17.59
$D + D \rightarrow \alpha + \gamma$	23.85
$^3He + {}^3He \rightarrow \alpha + 2p$	12.86
$p + {}^{15}N \rightarrow {}^{12}C + \alpha$	4.97

In Table 1, D is deuterium and T is tritium. The third and fourth reactions are the ends of the $p - p$ cycle and CNO cycle, respectively. In the first (DT) reaction, 14.1 MeV is carried on the neutron product [4, p. 13]. The DT reaction has the largest reactivity of all fusion reactions in any temperature interval below 400 keV [4, p. 18].

The two principle types of plasma confinement for controlled fusion experiments are inertial confinement fusion (ICF) and magnetic confinement fusion (MCF) [4, p. 31]. Both approaches are thermonuclear in that Coulomb scattering may redistribute a particle’s kinetic energy several times before it fuses with another [4, p. 32]. In addition, both fusion reactor types require temperatures of order 10 keV [4, p. 34]. The dominant form of radiation emission at temperatures of order 10 keV is bremsstrahlung which leads to a power loss per unit volume of [4, p. 32]

$$W_{ff} = 5.34 \times 10^{-24} n^2 T^{1/2} \ \frac{\text{erg}}{\text{s cm}^3} \ , \tag{1.45}$$

where W_{ff} is the free-free cooling power per cubic centimeter, n is either the electron or ion density for a fully ionized DT gas in cm^{-3}, and T is material temperature in keV. The power from fusion surpasses radiative cooling at $T \approx 4.3$ keV [4, p. 33].

Magnetic confinement employs magnetic fields to constrain the motion of the plasma. Current magnetic confinement reactors include the toroidal tokamak, stellerator and other systems.

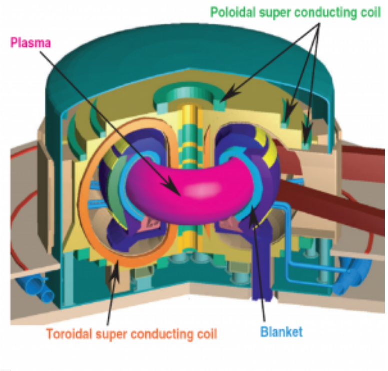

Figure 3: A tokamak uses toroidal and poloidal magnets to confine the plasma [1].

There are many introductory references on basic plasma physics in magnetically confinement reactors. One such book is by Chen [21]. One key figure of merit for MCF is the ignition ratio $P_{\text{fus}}/P_{\text{aux}}$, where P_{fus} and P_{aux} are the power produced from fusion and the auxiliary power required by the reactor to maintain equilibrated operating conditions [4, p. 35]. If the reactor achieves ignition, the fusion energy will sustain the state of the plasma; so $P_{\text{fus}}/P_{\text{aux}} = \infty$. Another key parameter is the plasma density multiplied by the confinement time, $n\tau_E$, where τ_E is the time diffusion would take to remove all thermal energy from the plasma [4, p. 36]. For a DT plasma, the Lawson criterion implies steady state reactor operation satisfies

$$n\tau_E = \frac{3kT}{(P_{\text{aux}}/P_{\text{fus}} + 0.2)\langle\sigma v\rangle Q/4 - C_b T^{1/2}} \ , \tag{1.46}$$

where k is Boltzmann's constant, T is temperature in keV, $\langle\sigma v\rangle$ is the fusion reactivity, and $C_b = 5.34 \times 10^{-24}\text{erg cm}^3\text{s}^{-1}\text{keV}^{-1/2}$ [4, p. 37]. Incorporating $P_{\text{fus}}/P_{\text{aux}} = 5$ and $T = 10$ keV into Eq. (1.46) yields $n\tau_E \approx 5 \times 10^{14}\text{s/cm}^3$. Given that densities in MCF are of order 10^{14}cm^{-3}, the time for energy loss from diffusion must be on the order of seconds or greater to obtain good reactor performance. This order of confinement time is much greater than that of typical ICF systems.

Inertial confinement employs particle inertia to implode a (typically small) volume of plasma in very short time scales when compared to magnetic fusion. Current inertial confinement reactors use laser or ion beams to drive the fuel.

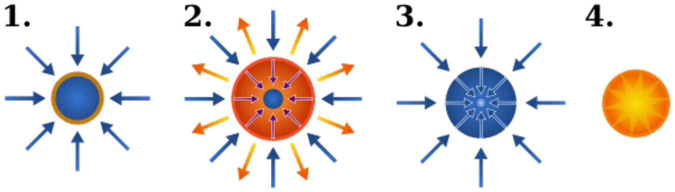

Figure 4: An ICF reactor uses particle beam pulses to confine the plasma [4, p. 48]: 1. irradiation, 2. ablation driven implosion of fuel, 2. thermonuclear ignition, 3. explosion [33]

The confinement time for the process shown in Fig. 4 is on the order of nanoseconds for typical target specifications. The solid shell of the target fuel must be compressed by a factor of $\sim$1500 [4, p. 43]. The compression ratio is derived from a fractional burn up of $\sim$0.3 of 1 mg of fuel with solid DT initially at 0.225 g/cm^3 [4, p. 43]. The irradiation can be performed directly with particle beams reaching the surface of the fuel or indirectly from X-rays produced from particle beams in a cavity surrounding the fuel. The radiation cavity used for indirect drive is often called a hohlraum. The hohlraum emits thermal radiation that is consequently isotropic; which allows for theoretically uniform fuel capsule heating [4, p. 303]. This uniformity however hinges on how the beam that impacts the hohlraum is interacting with local plasma. The key quantity of merit for ICF is the "target energy gain", $G = E_{\text{fus}}/E_d$, where E_{fus} is the energy obtained from one target and E_d is the energy transferred to the target by the beam [4, p. 35]. The target energy gain must be 30 to 100 for feasible power production of an ICF reactor. At temperatures of order $\sim$1 keV, radiation is a non-negligible component of the physics dictating how efficiently a fusion capsule may burn.

1.3 Computational Transport Methods

There exist computational methods to solve the transport equation, in order to predict properties of supernovae and high energy density experiments. In the following Sections 1.3.1 and 1.3.2, common deterministic and stochastic transport methods are briefly described.

1.3.1 Deterministic Methods

Two well researched deterministic methods for solving the transport equation are discrete ordinates and integral transport. Some features and limitations of these methods are detailed in the ensuing descriptions. Section 1.3.1 is a summary of more complete arguments and problems given by Lewis and Miller [62] as well as other texts.

A discrete ordinates method solves the transport equation for discrete directions [62, p. 116]. Eq. (1.3) becomes

$$\left(\frac{1}{c}\frac{\partial}{\partial t} + \hat{\Omega}_\kappa \cdot \nabla + \sigma_\nu\right) I_\nu(\vec{r}, \hat{\Omega}_\kappa, t) = \frac{q_\nu(\vec{r}, t, \hat{\Omega}_\kappa)}{4\pi} \tag{1.47}$$

where $\kappa \to (k'', k', k)$ is the index of a particular ray. Often the ray direction is described with three orthogonal projection cosines when in fact there are only two independent direction variables,

$$\mu_{k''} = \cos(\theta) \ , \tag{1.48a}$$

$$\eta_{k'} = (1 - \mu_{k''}^2)^{1/2} \cos(\omega) \ , \tag{1.48b}$$

$$\xi_k = (1 - \mu_{k''}^2)^{1/2} \sin(\omega) \ , \tag{1.48c}$$

where (θ, ω) are the spherical coordinates for direction κ and $\mu_{k''}^2 + \eta_{k'}^2 + \xi_k^2 = 1$. Accompanying the set $\{\hat{\Omega}_\kappa\}$ is a corresponding set of weights $\{w_\kappa\}$ that quantitatively ascribe to each ray an amount of influence on the scalar radiation field. To determine the value of each weight, the ray directions must be selected; this selection of directions and the associated weights is referred to as a quadrature set [62, p. 158].

A commonly used quadrature set for multiple dimensions is the level symmetric quadrature. Each of the three direction cosines in $(\mu_{k''}, \eta_{k'}, \xi_k)$ described in Eq. (1.48) belong to a set of $N/2$ values in $\{\Omega_k \in [0, 1] | k \in \{1 \ldots N/2\}\}$ ($N/2$ is a convention of convenience used by Lewis and Miller). So $\mu_k = \eta_k = \xi_k$ [62, p. 158]. The number of directions in the first octant is $N(N + 2)/8$. By symmetry, the number of directions for each octant then is $N(N + 2)/8$. Furthermore, Lewis and Miller show that there is only one degree of freedom in choosing the direction cosines. Given

Ω_1, [62, p. 160]

$$\Omega_k = \Omega_1 + (k-1)\frac{2(1-3\Omega_1^2)}{N-2} \quad . \tag{1.49}$$

The weights can be computed by requiring they be [62, p. 160] normalized:

$$\sum_{\kappa=1}^{N(N+2)/8} w_\kappa = 1/8 \quad , \tag{1.50}$$

equal for directions that are a permutation of the same three Ω_k, and constrained with closure equations for the remaining degrees of freedom. For the LQ$_N$ method, the constraints are [64, p. 2], along with Eq. (1.50),

$$\sum_{\kappa=1}^{N(N+2)} w_\kappa \mu_\kappa^p = \sum_{\kappa=1}^{N(N+2)} w_\kappa \eta_\kappa^p = \sum_{\kappa=1}^{N(N+2)} w_\kappa \xi_\kappa^p = \begin{cases} 0 & \text{for odd } p \\ 1/(p+1) & \text{for even } p \end{cases} \quad , \tag{1.51}$$

where p is a nonnegative integer.

Other quadrature methods may reduce the symmetry constraints to better capture aspects of a particular problem to be solved. Having obtained the quadrature set the transport problem remains to be solved. Given the scattering term in q_ν of Eq. (1.47), deterministic solutions of the transport equation are often obtained iteratively. Introducing a time index , n and an iteration per time step index, l, Eq. (1.47) can be finite differenced to

$$\left(\frac{1}{c\Delta t_n} + \hat{\Omega}_\kappa \cdot \nabla + \sigma_\nu\right) I_{\nu,n+1}^{l+1} = \frac{q_{\nu,n+1}^{l}}{4\pi} + \frac{I_{\nu,n}^{\infty}}{c\Delta t_n} \quad , \tag{1.52}$$

where $I_{\nu,n}^{\infty}$ is the fully converged solution from the previous time step. Note that as $\Delta t_n \to \infty$, Eq. (1.51) approaches steady state. The source term with discrete ordinates is [62, p. 172]

$$q_{\nu,n+1}^{l} = \sum_{\kappa=1}^{N(N+2)} w_\kappa \sigma_{\nu,s,\kappa} I_{\nu,n+1}^{l} + q_{\nu,e,n+1} \tag{1.53}$$

The spatial derivative can be discretized in one of several ways to yield a system of equations.

A limitation of discrete ordinates methods is an error referred to as ray effects. Optically thin (or generally transparent) or low scattering problems with sources localized relative to the domain size may induce these effects [62, p. 195]. Ray effects are errors that arise from an insufficient approximation of the scalar flux by the angular quadrature [62, p. 196]. Resolving the spatial grid does not reduce the error as it is intrinsic to the discretization in angle. The scalar flux profile can have spurious oscillations that do not appear for the solution with angular continuity. The peaks of the oscillation in the scalar flux are along the discrete rays pointing away from the source.

Integral transport obviates the discretization in direction by integrating over solid angle. Thus the scalar flux is the dependent variable for which to be solved. In principle, the solution should have no error due to approximation in angle. Time dependent, neutral particle, integral transport solutions have been obtained by Olson and Henderson [79]. For time dependent problems, applying the method of characteristics $\vec{r} = \vec{r}' + s\hat{\Omega}$, $t = t' + s/c$ will allow the transport equation to be expressed in a general integral form. The parameter s tracks the change in flux in space and time along a ray in the direction $\hat{\Omega}$. With $\vec{r} = \vec{r}(s)$ and $t = t(s)$ [86, p. 30]

$$-\frac{d}{ds} I_\nu(\vec{r} - s\hat{\Omega}, \hat{\Omega}, t - s/c) = \left(\frac{1}{c}\frac{\partial}{\partial t} + \hat{\Omega} \cdot \nabla \right) I_\nu(\vec{r} - s\hat{\Omega}, t - s/c) \quad . \tag{1.54}$$

Incorporating the total path derivative into Eq. (1.1) and solving for I_ν in terms of s yields [86, p. 30]

$$I_\nu(\vec{r}, \hat{\Omega}, t) = \frac{1}{4\pi} \int_0^\infty q_\nu(\vec{r} - s'\hat{\Omega}, \hat{\Omega}, t - s'/c) e^{-\int_0^{s'} \sigma_\nu(\vec{r} - s''\hat{\Omega}, \hat{\Omega}, t - s''/c) ds''} ds' \quad . \tag{1.55}$$

Recalling $\int_{4\pi} I_\nu d\Omega = \phi_\nu$,

$$\phi_\nu(\vec{r}, t) = \frac{1}{4\pi} \int_{4\pi} \int_0^\infty q_\nu(\vec{r} - s'\hat{\Omega}, \hat{\Omega}, t - s'/c) e^{-\int_0^{s'} \sigma_\nu(\vec{r} - s''\hat{\Omega}, \hat{\Omega}, t - s''/c) ds''} ds' d\Omega \quad . \tag{1.56}$$

If the source and total opacity are isotropic, Equation (1.56) can be converted into a time-dependent volume integral by noting $s'^2 ds' d\Omega = dV'$ [62, p. 212] while taking $\vec{r}' = \vec{r} - s'\hat{\Omega}$ and $t' = t - s'/c$,

$$\phi_\nu(\vec{r}, t) = \frac{1}{4\pi} \int \frac{q_\nu(\vec{r}', t')}{c^2 (t - t')^2} e^{-\tau(\vec{r}, t; \vec{r}', t')} dV' \quad , \tag{1.57}$$

where $\tau(\vec{r},t;\vec{r}',t') = \int_0^{c(t-t')} \sigma_\nu(\vec{r}-s''\hat{\Omega},t-s''/c)ds''$ and the integral is taken over all space. From here, we will make various simplifications to Eq. (1.57) to arrive at a particular equation set that would be amenable to computation.

For one dimensional planar geometry, the volume element can be expressed as a symmetric differential expanding ring, $dV' = 2\pi c^2(t-t')dx'dt'$. With $t' \in [0,t]$ and $x' \in [-\infty,\infty]$, causality implies $q_\nu(x',t')$ must have no influence on the solution if $|x-x'| > c(t-t')$. So

$$\phi_\nu(x,t) = \frac{1}{2}\int_0^t \int_{-\infty}^{\infty} \frac{q_\nu(x',t')}{(t-t')}\Theta(c(t-t')-|x-x'|)e^{-\tau(x,t;x',t')}dx'dt' \quad , \tag{1.58}$$

where $\Theta(c(t-t')-|x-x'|)$ is the Heaviside function. Equation (1.57) was derived starting from general transport with scattering as done by Bell, Glasstone [6, p. 23–25], and Pomraning. It is notable that causality is not an automatic result from the above derivation. Henderson [50] takes an alternative approach to arriving at Eq. (1.58) by deriving the single-collision transport kernel for planar geometry. In the article referenced [50], Henderson applies the Laplace transform to the planar geometry transport equation. Henderson's solution has the following form (using notation consistent with the article) [50, p. 173]:

$$\phi_\nu(x,t) = \int_0^t \int_{-\infty}^{\infty} K(x,x';t,t')q_\nu(x',t')dx'dt' \quad , \tag{1.59}$$

where $K(x,x';t,t')$ is the planar kernel. Particles can be partitioned by the number of scattering events they have undergone. Each set of particles that have undergone $j-1$ collisions are the source of the set of particles that undergo j collisions [50, p. 174]. So the single collision (or equivalently pure absorbing) kernel solution can be used to obtain the solution with scattering for the scalar flux. The multiple collision concept has a significant role as the theoretical basis of Monte Carlo transport methods in Section 1.3.2.

For Eq. (1.58), some simplifications result in a matrix equation that can be solved algebraically. For a finite slab of material, $0 \le x \le L$, with vacuum boundary conditions

$$\phi_\nu(x,t) = \frac{1}{2}\int_0^t \int_0^{L} \frac{q_\nu(x',t')}{(t-t')}\Theta(c(t-t')-|x-x'|)e^{-\tau(x,t;x',t')}dx'dt' \quad . \tag{1.60}$$

Averaging ϕ_ν over a width Δx_i and a time step Δt_n, Eq. (1.60) becomes

$$\Delta t_n \Delta x_i \phi_{\nu,i,n} = \frac{1}{2}\int_{t_{n-1}}^{t_n}\int_{x_{i-1/2}}^{x_{i+1/2}}\int_0^t\int_0^L \frac{q_\nu(x',t')}{(t-t')}\Theta(c(t-t')-|x-x'|)e^{-\tau(x,t;x',t')}dx'dt'\,dx\,dt \quad , \tag{1.61}$$

where $\Delta t_n = t_n - t_{n-1}$ and $\Delta x_i = x_{i+1/2} - x_{i-1/2}$. We may break the integral up into zones in space and time and approximate the source, $q_\nu(x',t') \approx \sigma_{\nu,s,i',n'}\phi_{\nu,i',n'} + q_{\nu,e,i',n'} = q_{\nu,i,n}$, to obtain

$$\begin{aligned}\Delta t_n \Delta x_i \phi_{\nu,i,n} = &\sum_{n'=1}^{n}\sum_{i'=1}^{I} q_{\nu,i,n}\times \\ &\int_{t_{n-1}}^{t_n} dt \int_{x_{i-1/2}}^{x_{i+1/2}} dx \int_{t_{n'-1}}^{\min(t_{n'},t)} dt' \int_{x_{i'-1/2}}^{x_{i'+1/2}} dx' \left(\frac{1}{2}\frac{\Theta(c(t-t')-|x-x'|)}{t-t'}e^{-\tau(x,t;x',t')}\right) \quad ,\end{aligned} \tag{1.62}$$

where $i, i' \in \{1\ldots I\}$, $n' \in \{1\ldots n\}$, and $n \in \{1\ldots N\}$. Setting $P_{i,n;i',n'}$ equal to $\frac{\sigma_{\nu,i,n}}{\Delta t_{n'}\Delta x_{i'}}$ multiplied by the integral term in Eq. (1.62),

$$\sigma_{\nu,i,n}\Delta t_n \Delta x_i \phi_{\nu,i,n} = \sum_{n'=1}^{n}\sum_{i'=1}^{I} P_{i,n;i',n'}\Delta t_{n'}\Delta x_{i'}(\sigma_{\nu,s,i',n'}\phi_{\nu,i',n'} + q_{\nu,e,i',n'}) \quad . \tag{1.63}$$

Equation (1.63) is the time dependent analogue of the formula presented by Lewis and Miller for the "collision probability method" [62, p. 216]. The left hand side is simply the number of collisions in time step Δt_n and spatial cell Δx_i. The $P_{i,n;i',n'}$ term can be interpreted as the probability a particle from cell and time step (i', n') will stream to (i, n) and make its first collision there. Conveniently, the identities in [62] for the collision probability method may be used here (with deletion of the per time unit):

$$f_{i,n} = \sigma_{\nu,i,n}\Delta t_n \Delta x_i \phi_{\nu,i,n} \quad , \tag{1.64a}$$

$$H_{i,n;i',n'} = \delta_{i,i'}\delta_{n,n'} - \frac{\sigma_{\nu,s,i',n'}}{\sigma_{\nu,i',n'}}P_{i,n;i',n'} \quad , \quad \tilde{s}_{i,n} = \sum_{n'=1}^{n}\sum_{i'=1}^{I} P_{i,n;i',n'}\Delta t_{n'}\Delta x_{i'} q_{\nu,e,i',n'} \quad , \tag{1.64b}$$

$$\mathbf{Hf} = \tilde{\mathbf{s}} \tag{1.64c}$$

where $\delta_{i,i'}$, $\delta_{n,n'}$ are Kronecker delta functions. Equation (1.64c) can be solved algebraically with scalar flux trivially obtained from $\mathbf{f}$. To verify the discretized scheme described here, the benchmark solutions of Olson and Henderson may be used [79].

The collision probability method is advantageous over discrete ordinates in that there is no accuracy loss due to approximation in angle. The exact treatment in angle can be inferred from Eq. (1.64). There are several drawbacks to using integral transport. The matrix $\mathbf{H}$ is generally dense and unsymmetric [62, p. 218]. These features of $\mathbf{H}$ may prohibit the method from scaling to problems on large, multidimensional spatial domains over long periods of time. Indeed, even deriving the entries of $\mathbf{H}$ for multidimensional problems requires considerable algebra.

1.3.2 Monte Carlo Methods

Before considering transport, we discuss some basic principles of Monte Carlo. Monte Carlo methods solve deterministic problems with randomly sampled independent variables. In doing so, the MC method tallies an expected value that in principle should equal the solution to the problem for an infinite number of samples (and infinite grid resolution if there is a grid). A well known tally experiment, invented by Georges-Louis Leclerc, Comte de Buffon, involves dropping a stick of length 1 on a surface with lines spaced uniformly 1 apart. The problem is to compute how likely the stick will touch one of the lines after being dropped once. The ratio of drops that result in the stick intersecting a line, N_l, to the total number of drops, N_t, converges to $1/\pi$ as $N_t \to \infty$.

Suppose instead a stick of length 1 is dropped on a uniform grid of 1×1 squares. The probability that the stick touches a square boundary is different than the probability the stick would touch one of the lines in the original experiment. Values sufficient for specifying the stick's position and orientation are the location of one of the stick's ends and the angle the stick makes with a reference axis, (x, y, θ). For this problem, it was found to be easier to calculate the probability that a stick is entirely in a square and subtract the result from 1. The coordinate (x, y) is always in a square or on a cell boundary, so $(x, y) \in [0, 1] \times [0, 1]$ can be sampled in one square without loss of generality. The probability of finding $(x, y) \in [x_1, x_2] \times [y_1, y_2]$ where $0 \leq x_1 \leq x_2 \leq 1$ and $0 \leq y_1 \leq y_2 \leq 1$ is $(x_2 - x_1)(y_2 - y_1)$. Similarly the probability of finding $0 \leq \theta_1 \leq \theta \leq \theta_2 \leq 2\pi$ is $(\theta_2 - \theta_1)/2\pi$.

So the probability density function, p, satisfies

$$p(x, y, \theta) = \frac{1}{2\pi} \quad . \tag{1.65}$$

If $0 \leq \theta \leq \pi/2$, then in order for the stick to be in the square, $0 \leq x \leq 1 - \cos(\theta)$ and $0 \leq y \leq 1 - \sin(\theta)$. If (x, y) is moved from $(0, 0)$, the constraints imply the range of angles for θ must decrease. But this is a rotationally symmetric condition for any of the four corners, so the probability a stick will be entirely in the square without touching the boundary is

$$1 - P_l = 4 \int_0^{\pi/2} \int_0^{1-\cos(\theta)} \int_0^{1-\sin(\theta)} p(x, y, \theta)\, dy\, dx\, d\theta \quad . \tag{1.66}$$

So the probability of a dropped stick touching a square boundary is

$$P_l = \frac{3}{\pi} \quad , \tag{1.67}$$

or three times as likely as a stick touching one of the uniformly spaced lines. The process of dropping N_t sticks onto a grid can be simulated with the following pseudo-code:

```
• $N_l = 0$
• For $i = 1..N_t$
    – sample $x$, $y$, $\theta$
    – If $x + \cos(\theta) \notin [0, 1]$ or $y + \sin(\theta) \notin [0, 1]$
        ∗ $N_l = N_l + 1$
    – End If
• End For
• $\tilde{P}_l = N_l / N_t$
```

Figure 5 is a plot of $|\tilde{P}_l - P_l|$ versus N_t for the above algorithm.

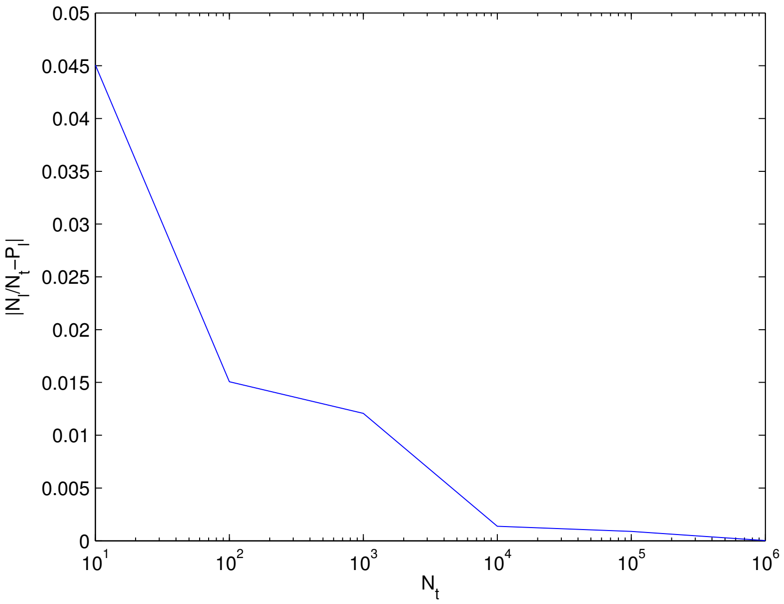

Figure 5: The stick drop simulation produces an a probability that converges to $3/\pi$ for an increasing number of samples.

The ability to numerically acquire P_l from random processes highlights an important feature of Monte Carlo algorithms:

- The solution of the integral Eq. (1.66) can be solved stochastically by ascribing a probabilistic interpretation to P_l and $p(x, y, \theta)$.

Eq. (1.66) could have been constructed without explicit reference to the stick problem, yet the stick simulation solves Eq. (1.66). Moreover, each stick can be thought of as a “particle” of the solution given it has properties x, y and θ that allow the integral quantity N_l to be incremented during the simulation.

For MC transport, the field of particles are not sticks but photon packets. Since photons are quantum particles, the transport equation is a statement of particle conservation as well. A statement of particle conservation along a direction can be obtained from substituting the right side of Eq. (1.1), $I_\nu = ch\nu f_\nu$, into the transport equation; the conservation implies that the number of particles is accounted for across the domain by balancing streaming and absorption with scattering and emission. In Monte Carlo transport, the transport equation is thought of as describing a field of discrete particles generated with varying properties from a source and interacting with the background material independently from each other. Moreover, there are features of transport that for photons are inherently stochastic in nature (e.g. thermal emission, scattering). To both invoke causality and partition the stochastic process used in tracking photon packets, we return to the concept underlying the multiple-collision method discussed in Section 1.3.1.

From Section 1.3.1, particles having undergone $j-1$ collisions can be thought of as a source for particles having undergone j collisions. The integral equation for each set of photon packets enumerated by j is [50, p. 174]

$$\phi_{\nu,j}(\vec{r},t) = \frac{1}{4\pi}\int_{4\pi}\int_0^\infty q_{\nu,j}(\vec{r}-s'\hat{\Omega},\hat{\Omega},t-s'/c)e^{-\int_0^{s'}\sigma_\nu(\vec{r}-s''\hat{\Omega},\hat{\Omega},t-s''/c)ds''}ds'd\Omega \quad , \tag{1.68}$$

where [50, p. 174]

$$q_{\nu,j}(\vec{r},\hat{\Omega},t) = \begin{cases} q_{\nu,e}(\vec{r},\hat{\Omega},t) \;\; \text{for } j=1 \quad , \\ \\ \displaystyle\int_{4\pi}\int_0^\infty \frac{\nu}{\nu'}\sigma_s(\vec{r},\nu'\to\nu,\hat{\Omega}'\cdot\hat{\Omega})I_{\nu',j-1}(\vec{r},\hat{\Omega}',t)\,d\nu'\,d\Omega' \;\; \text{otherwise} \quad , \end{cases} \tag{1.69}$$

and $\phi_{\nu,j} = \int_{4\pi} I_{\nu,j}$. Only a subset of particles in the $j-1$ class scatter into the j class, so the time integrated total of photons in $j-1$ class must be greater than or equal to the total energy of the j class over the same time span; a photon cannot unscatter unless time is reversed. This implies that the integral in Eq. (1.68) is a bounded operator and the total scalar flux ϕ_ν can be expressed as [50, p. 174]

$$\phi_\nu(\vec{r},t) = \sum_{j=0}^{\infty}\phi_{\nu,j}(\vec{r},t) \tag{1.70}$$

without diverging. From the preceding arguments, it seems that the MC process for a photon packet must be to first generate properties from the source density ($j-1=0$) and update the properties through deterministic streaming until the distance to the next collision is traversed. At this point the particle can either be absorbed (if not accounted for by deterministically lowering the particle weight) or scattered. If the particle is scattered it becomes a source for the next class $j - 1 \rightarrow j$. Additionally, we may use Eq. (1.70) to tally the scalar flux since it relates the flux to counting collisions.

We consider an external source density of photon packets $q_{\nu,e}(\vec{r}, \hat{\Omega}, t)/4\pi$ over a domain D and time span $[T_0, T]$. This source density can be converted to a probability density function for photon packets in the domain and time span with properties that allow for the integration of $q_{\nu,e}/4\pi$,

$$p_e(\vec{r}, \hat{\Omega}, t, \nu) = \frac{q_{\nu,e}(\vec{r}, \hat{\Omega}, t)}{\displaystyle\int_D dV' \int_{4\pi} d\Omega' \int_{T_0}^{T} dt' \int_0^{\infty} d\nu' q_{\nu',e}(\vec{r}', \hat{\Omega}', t')} = \frac{q_{\nu,e}(\vec{r}, \hat{\Omega}, t)}{E_e} \quad , \tag{1.71}$$

where E_e is the total energy added to the domain over the time span from the external source. If N_t photon packets are used in the integration, the expected number of packets in a parameter volume $dV\, d\Omega\, dt\, d\nu$ around a point $(\vec{r}, \hat{\Omega}, t, \nu)$ from the external source is $N_t\, p_e(\vec{r}, \hat{\Omega}, t, \nu) dV\, d\Omega\, dt\, d\nu$. As in the stick-drop-grid experiment, particles generated outside the domain and time span of interest are neglected in order to arrive at a meaningful solution. Additionally, each particle in the domain and time span can have energy $E_p = E_e/N_t$. Sources on the boundary, ∂D, can be treated in a similar manner.

With the source particles generated and the collided fluxes, $\phi_{\nu,j}$, constrained to a causal ordering, there must be no other sources for $j + 1$ until the existing particles collide. So the equation corresponding to the flux of each particle from its location and time, $(\vec{r}', t')$, is

$$\frac{1}{c}\frac{\partial I_{\nu,0}}{\partial t} + \hat{\Omega} \cdot \nabla I_{\nu,0} = 0 \tag{1.72}$$

which has the solution $I_{\nu,0}(\vec{r}, \hat{\Omega}, t) = I_{\nu,0}(\vec{r}' + s\hat{\Omega}, \hat{\Omega}, t' + s/c)$. This solution is satisfied by changing the photon packet properties in the same manner, in other words advecting the packet. But this solution only exists in this form until the characteristic parameter, s, is equal to the distance where a collision must occur. This distance can be obtained by constructing another probability density function from Beer's Law [19, p. 76] (assuming σ_ν does not vary significantly over s),

$$I_{\nu,0}(\vec{r},\hat{\Omega},t) = I_{\nu,0}(\vec{r}',\hat{\Omega},t')e^{-\sigma_\nu s} \quad , \tag{1.73}$$

which is the solution to Eq. (1.72) with non-zero opacity. Since the energy in a parameter volume $dV\,d\Omega\,d\nu = dA\,ds\,d\Omega\,d\nu$ around a point $(\vec{r}',\hat{\Omega},t',\nu')$ is $I_\nu(\vec{r}',\hat{\Omega},t')dA\,ds\,d\Omega\,d\nu/c$, the expected uncollided energy at a point $(\vec{r},\hat{\Omega},t)$ later on the characteristic for the same differential volume is reduced by a factor of $e^{-\sigma_\nu s}$. Hence the probability that a particle makes it uncollided from $s = 0$ to $s = l$ and subsequently collide in a neighborhood dl about l is $e^{-\sigma_\nu l}\sigma_\nu dl$. Then the probability of a particle colliding between 0 and d is $1 - \zeta = 1 - e^{-\sigma_\nu d}$ [62, p. 303]. Lewis and Miller show [62, p. 300–302] that ζ can be uniformly sampled between 0 and 1 to obtain a distance to collision (scattering or absorption),

$$d = -\frac{1}{\sigma_\nu}\ln(\zeta) \quad . \tag{1.74}$$

To summarize, a source particle generated from $q_{\nu,e}$ with appropriate properties is advected until $s = d$, at which point it may become part of the source for the $j = 1$ class of photon packets.

The particles that do not get absorbed during the collision event are scattered. The process for the particles generated in the $j \neq 0$ class is nearly the same as the process of the $j = 0$ class. The only difference is that $q_{\nu,e}$ is substituted with $q_{\nu,j}$. The scattering distribution is fully specified by $\sigma_s(\vec{r},\nu' \to \nu,\hat{\Omega}'\cdot\hat{\Omega})$ and the particle properties of the $j - 1$ set.

A tally for particles in a frequency range $[\nu_{g-1},\nu_g]$ may be constructed. If $p \in \{1 \ldots N_t\}$ is a particle index, $l_{p,g}$ is the total distance traversed events per particle in domain D in the time span $[0,T]$ while having a frequency in the range indexed by g, then the average scalar flux per particle may be approximated as [62, p. 311]

$$\tilde{\phi}_{p,g} = \frac{E_p l_{p,g}}{\Delta\nu_g V_D T} = \frac{E_p}{\Delta\nu_g V_D T}\sum_{j=0}^{J_{p,g}} l_{p,j,g} = \frac{E_p}{\Delta\nu_g V_D T}\sum_{j=0}^{\infty} l_{p,j,g} H(J_{p,g} - j) \quad , \tag{1.75}$$

where $l_{p,j,g}$ are the straight line distances between collisions, V_D is the volume of D, $\Delta\nu_g = \nu_g - \nu_{g-1}$, $J_{p,g}$ is the total number of collisions in g before the particle terminates (by absorption, escaping the problem bounds, or scattering indefinitely out of g) and $H(J_{p,g} - j)$ is the discrete Heaviside step function. The total scalar flux at frequency ν in the domain is

$$\tilde{\phi}_g = \sum_{j=0}^{\infty} \sum_{p} \left(\frac{E_p l_{p,j,g}}{\Delta\nu_g V_D T} \right) H(J_{p,g} - j) = \sum_{j=0}^{\infty} \tilde{\phi}_{g,j} \quad , \tag{1.76}$$

where $\tilde{\phi}_{g,j}$ is the flux contribution from particles that have collided j times. If the domain and the time span are subdivided into cells and time steps, V_i and Δt_n, as had been done for the integral collision probability method, then the scalar flux can be calculated from a tally in each zone and time step. Since particles will cross boundaries and are censused at the end of time steps, the problem of particle tracking is more complicated than the unpartitioned tally. With frequency, space, and time grids introduced, the Monte Carlo scalar intensity estimate may be written as

$$\tilde{\phi}_{g,i,n} = \sum_{j=0}^{\infty} \sum_{p} \left(\frac{E_p l_{p,j,g}(i,n)}{\Delta\nu_g V_i \Delta t_n} \right) H(J_{p,g}(i,n) - j) = \sum_{j=0}^{\infty} \tilde{\phi}_{g,j,i,n} \quad , \tag{1.77}$$

where $J_{p,g}(i,n)$ and $l_{p,j,g}(i,n)$ are the total number of collisions and the path length after collision j, respectively, for particle p in group g in cell i in time step n. By construction, $\tilde{\phi}_{g,i,n}$ is an approximation of the expectation value $\phi_{g,i,n}$. $\phi_{g,i,n}$, in turn, is the the flux averaged over a frequency group, spatial cell, and time step. In the limit as the number of particles, N_t, the number of cells I, the number of groups G, and the number of time steps N go to infinity,

$$\tilde{\phi}_{g,i,n} \to \phi_\nu(\vec{r}, t) \quad , \tag{1.78}$$

which is the scalar intensity solution for fully continuous independent variables.

The theoretical insight into Monte Carlo transport is that the integral form of the transport equation can be partitioned into an iterative series of the same integral form. Particles have to have properties that satisfy the iterated source density as a probability distribution. Advecting each photon packet deterministically to a collision location is merely a means of initializing the next iteration of a source integral. Solving the transport equation with particles is consequently equivalent to atemporally solving a series of source integrals.

1.3.3 Residual Monte Carlo

Monte Carlo transport does not only derive theoretical underpinnings from integral transport but may in fact form part of a composite solution scheme along with a collision probability approach. In particular, Wollaeger and Densmore [102] find that Monte Carlo and a collision probability matrix may be used to formulate a Residual Monte Carlo method for the spatially discrete, angularly continuous, steady state transport equation. The extension to time dependence is simple but the scheme to be described is iterative; in some time-dependent problems such a solution may be expensive. Moreover, as will be discussed, the continuous angle residual Monte Carlo transport scheme requires matrix multiplication. In one dimension this multiplication is not costly but in two dimensions or higher the matrix storage becomes problematic. The matrix is not generally sparse. If a matrix-free continuous angle residual Monte Carlo transport scheme is discovered, then there would potentially exist a means to remove statistical noise from multi-dimensional radiation-hydrodynamics calculations with Monte Carlo radiation transport with modest additional computational cost. To our knowledge, a general, continuous angle residual scheme has not been discovered. Consequently, the following derivation is a proof of principle extracted from the summary by Wollaeger and Densmore [102]. We stress that there are no novelties to the method presented here.

Residual Monte Carlo is a Monte Carlo technique that yields exponential convergence of the statistical error with respect to the number of particle histories. In contrast, standard Monte Carlo produces statistical error that converges as the inverse of the square root of the number of particle histories [62]. Due to the improved convergence rate, residual Monte Carlo is typically more efficient than standard Monte Carlo. Additionally, the exponential convergence rate of residual Monte Carlo is advantageous relative to standard Monte Carlo in the context of multiphysics calculations that treat the coupling between different physics iteratively. In such calculations, the statistical error can be reduced such that it is less than the iterative error when enough MC particles are applied. Work in exponentially convergent Monte Carlo includes the article by Booth for a continuous transport [8] and the article by Evans et al. for spatially discrete residual Monte Carlo radiation diffusion [35]. Recently, Evans et al. [34] formulated a Monte Carlo synthetic acceleration method for solving the thermal radiation diffusion equation in three spatial dimensions. The residual Monte Carlo scheme is used to accelerate a fixed point iteration [34]. Since the discrete diffusion matrix is sparce, it should not be as prohibitive to memory in 3D; we find that the transport matrix, $\mathbf{M}$ in Eq. (1.101), would be problematic even in 2D.

Wollaeger and Densmore [102] provide a scheme for applying the residual Monte Carlo technique to transport for spatially discrete, angularly continuous radiation transport problems. First the transport equation is discretized, then the resulting terms are given stochastic interpretations. Additionally the associated integral transport equation is constructed for the spatially discretized system. A source term for residual Monte Carlo particles can be obtained from the integral transport formulation so that no angular discretization is required. It is to this integral equation that residual Monte Carlo is applied.

The use of a spatial discretization in the method not only simplifies implementation but also should not be a significant disadvantage if the simulation of other physics besides radiation transport involves spatial discretizations as well. In addition, by not employing an angular discretization, the ray effects mentioned in Section 1.3.1 are avoided.

Residual Monte Carlo can be applied to a general transport problem of the form

$$\mathbf{A}x = b \quad , \tag{1.79}$$

where $\mathbf{A}$ represents an appropriate transport operator, x is the solution (for example, the angular or scalar flux), and b is the external source including boundary conditions. Standard Monte Carlo can be used to generate an estimate of the solution of Eq. (1.79), $x^{(0)}$. In residual Monte Carlo, the initial estimate is improved upon through an additive correction [102],

$$x = x^{(0)} + \delta x \quad . \tag{1.80}$$

Substituting Eq. (1.80) into Eq. (1.79) results in an equation for the additive correction, δx,

$$\mathbf{A}\delta x = r^{(0)} \quad , \tag{1.81}$$

with the residual $r^{(0)}$ given by

$$r^{(0)} = b - \mathbf{A}x^{(0)} \quad . \tag{1.82}$$

Because Eq. (1.81) is of the same form as Eq. (1.79), the same Monte Carlo procedure that yielded $x^{(0)}$ can be employed to produce an estimate of δx, $\delta x^{(0)}$, and hence an improved estimate of the solution through Eq. (1.80),

$$x^{(1)} = x^{(0)} + \delta x^{(0)} \quad . \tag{1.83}$$

This process can be generalized to an arbitrary number of iterations such that

$$r^{(n)} = b - \mathbf{A}x^{(n)} \quad , \tag{1.84}$$

$\delta x^{(n)}$ is an estimate of the solution to

$$\mathbf{A}\delta x = r^{(n)} \quad , \tag{1.85}$$

as determined by a standard Monte Carlo simulation, and

$$x^{(n+1)} = x^{(n)} + \delta x^{(n)} \quad . \tag{1.86}$$

It is generally difficult to evaluate the residual for transport problems that are continuous in, for example, space and angle. This computation would require a pointwise representation of the solution, which is typically not provided by a Monte Carlo simulation. To reiterate, the residual Monte Carlo scheme presented here employs a spatial discretization. Along with the corresponding integral equation, the residual can be calculated from only the angularly integrated value of the solution in each spatial cell.

The planar-geometry, monoenergetic, time-independent transport equation with isotropic scattering and sources is

$$\mu\frac{\partial\psi}{\partial x} + \sigma_t\psi(x,\mu) = \frac{\sigma_s\phi(x) + q(x)}{2} \quad . \tag{1.87}$$

In this expression, $0 < x < L$ is the spatial variable, $-1 < \mu < 1$ is the angular variable, $\psi(x,\mu)$

is the angular flux, $\sigma_t(x)$ is the total cross section, $\sigma_s(x)$ is the scattering cross section, and $q(x)$ is the radiation source. In addition, $\phi(x)$ here is the scalar flux,

$$\phi(x) = \int_{-1}^{1} \psi(x,\mu) d\mu \quad . \tag{1.88}$$

In prior and subsequent sections, ϕ is the scalar intensity. Scalar flux and scalar intensity are related through the (solid) angular integration of Eq. (1.1), where ψ replaces f_ν. Equation (1.87) is supplemented by boundary conditions that specify the angular flux for incoming directions,

$$\psi(0,\mu) = f(\mu) \quad , \quad \mu > 0 \quad , \tag{1.89}$$

and

$$\psi(L,\mu) = g(\mu) \quad , \quad \mu < 0 \quad , \tag{1.90}$$

where f and g are arbitrary distributions with respect to μ.

For simplicity, using step differencing, for a grid of I spatial cells, the discrete equations for cell i are [62, p. 133]

$$\mu \frac{\psi_i - \psi_{i-1}}{\Delta x_i} + \sigma_{t,i}\psi_i = \frac{\sigma_{s,i}\phi_i + q_i}{2} \quad , \quad \mu > 0 \quad , \tag{1.91}$$

and

$$|\mu| \frac{\psi_i - \psi_{i+1}}{\Delta x_i} + \sigma_{t,i}\psi_i = \frac{\sigma_{s,i}\phi_i + q_i}{2} \quad , \quad \mu < 0 \quad , \tag{1.92}$$

with

$$\psi_0(\mu) = f(\mu) \quad , \quad \mu > 0 \quad , \tag{1.93}$$

and

$$\psi_{I+1}(\mu) = g(\mu) \quad , \quad \mu < 0 \quad , \tag{1.94}$$

where Δx_i is the cell width and the subscript i otherwise denotes cell-averaged or piecewise constant quantities.

Equations (1.91)–(1.94) are amenable to Monte Carlo simulation [97]. This technique was originally developed for lumped, linear-discontinuous spatial discretizations but is much simpler to reduce to step differencing [97, 102]. It should be stated that the step differenced form does not preserve the correct discrete diffusion limit as demonstrated by Clouet [23] (and discussed in the literature review). Following this previous work, Eqs. (1.91) and (1.92) are rearranged as

$$(\mu + \sigma_{t,i}\Delta x_i)\psi_i = \frac{\sigma_{s,i}\phi_i\Delta x_i}{2} + \frac{q_i\Delta x_i}{2} + \mu\psi_{i-1} \quad , \quad \mu > 0 \quad , \tag{1.95}$$

and

$$(|\mu| + \sigma_{t,i}\Delta x_i)\psi_i = \frac{\sigma_{s,i}\phi_i\Delta x_i}{2} + \frac{q_i\Delta x_i}{2} + |\mu|\psi_{i+1} \quad , \quad \mu < 0 \quad . \tag{1.96}$$

If we note that Eqs. (1.95) and (1.96) are balance equations over cell i for positive and negative directions, respectively, their Monte Carlo interpretation becomes apparent. From the left side of these expressions, the probability that a particle will leak to the next cell (or through a problem boundary) is

$$P_{\text{leak}} = \frac{|\mu|}{|\mu| + \sigma_{t,i}\Delta x_i} \quad , \tag{1.97}$$

where whether the next cell is to the left or right is determined by the particle's direction, and the probability that a particle will instead undergo a collision is

$$P_{\text{collision}} = \frac{\sigma_{t,i}\Delta x_i}{|\mu| + \sigma_{t,i}\Delta x_i} \quad . \tag{1.98}$$

The three terms on the right sides of Eqs. (1.95) and (1.96) represent sources due to particles scattering, the usual radiation source, and particles leaking from adjacent cells [or the boundary conditions through Eqs. (1.93) and (1.94)], respectively. After the particle's initial cell and direction are sampled appropriately from the cell-averaged values of the radiation source and boundary conditions, it can either leak to the next cell, scatter isotropically, or be absorbed. This process continues until the particle is absorbed or leaks through a problem boundary. Note we do not have to track the particle continuously with advection and Beer's Law as was delineated in Section 1.3.2.

So far in Section 1.3.3, the general framework of residual methods and a simple step-discretized Monte Carlo solution have been described. It remains to write the discrete integral equations and subsequently the differential residual equations to be used to generate “correction particles.”

Solving Eqs. (1.91) through (1.94) for the spatially discrete angular flux yields

$$\psi_i(\mu) = \sum_{k=1}^{i} \left(\prod_{l=k}^{i} \frac{\mu}{\mu + \sigma_{t,l}\Delta x_l} \right) \left(\frac{\sigma_{s,k}\phi_k \Delta x_k + q_k \Delta x_k}{2\mu} \right) + \left(\prod_{k=1}^{i} \frac{\mu}{\mu + \sigma_{t,k}\Delta x_k} \right) f(\mu) \ , \qquad \mu > 0 \ , \tag{1.99}$$

and

$$\psi_i(\mu) = \sum_{k=i}^{I} \left(\prod_{l=i}^{k} \frac{|\mu|}{|\mu| + \sigma_{t,l}\Delta x_l} \right) \left(\frac{\sigma_{s,k}\phi_k \Delta x_k + q_k \Delta x_k}{2|\mu|} \right) + \left(\prod_{k=i}^{I} \frac{|\mu|}{|\mu| + \sigma_{t,k}\Delta x_k} \right) g(\mu) \ , \qquad \mu < 0 \ , \tag{1.100}$$

where the $\prod_{l=k}^{i}$ denotes a product of terms indexed with l ranging from integer k to i. Incorporating Eqs. (1.99) and (1.100) into Eq. (1.88), the following system of equations for the cell-averaged scalar flux is

$$\mathbf{M}\Phi = Q \quad . \tag{1.101}$$

This expression is the desired integral equation. Here, Φ is an array of the cell-averaged values of the scalar flux, $\mathbf{M}$ is a matrix where

$$M_{i,k} = \begin{cases} -\sigma_{s,k}\Delta x_k \displaystyle\int_0^1 \frac{1}{2\mu} \prod_{l=k}^{i} \frac{\mu}{\mu + \sigma_{t,l}\Delta x_l} \, d\mu \ , & k < i \ , \\[2ex] 1 - \sigma_{s,i}\Delta x_i \displaystyle\int_0^1 \frac{1}{\mu} \frac{\mu}{\mu + \sigma_{t,i}\Delta x_i} \, d\mu \ , & k = i \ , \\[2ex] -\sigma_{s,k}\Delta x_k \displaystyle\int_{-1}^0 \frac{1}{2|\mu|} \prod_{l=i}^{k} \frac{|\mu|}{|\mu| + \sigma_{t,l}\Delta x_l} \, d\mu \ , & k > i \ , \end{cases} \tag{1.102}$$

Q is an array defined by

$$Q_i = \sum_{k=1}^{I} \frac{1}{\sigma_{s,k}} (\delta_{i,k} - M_{i,k}) q_k + \int_0^1 f(\mu) \prod_{k=1}^{i} \frac{\mu}{\mu + \sigma_{t,k} \Delta x_k} \, d\mu$$
$$+ \int_{-1}^0 g(\mu) \prod_{k=i}^{I} \frac{|\mu|}{|\mu| + \sigma_{t,k} \Delta x_k} \, d\mu \quad , \tag{1.103}$$

and, as in Section 1.3.1, $\delta_{i,k}$ is the Kronecker delta function. The integrals in Eq. (1.102) can be evaluated analytically, while the integrals in Eq. (1.103) can be evaluated analytically for certain forms of $f(\mu)$ and $g(\mu)$.

A integral transport residual may now be constructed. Such a residual is fully discrete since an integration over angle has been taken. An estimate for $\Phi^{(0)}$ is obtained with the step-discrete Monte Carlo method described above. The scalar flux array for subsequent iterations are obtained from

$$\Phi^{(n+1)} = \Phi^{(n)} + \delta\Phi^{(n)} \quad , \tag{1.104}$$

where $\delta\Phi^{(n)}$ is an estimate of the solution to

$$\mathbf{M}\delta\Phi = R^{(n)} \quad , \tag{1.105}$$

and the residual in the current situation is

$$R^{(n)} = Q - \mathbf{M}\Phi^{(n)} \quad . \tag{1.106}$$

For the integral, or scalar, residual in Eq. (1.106), it is unclear what the set of differential Monte Carlo equations would be. Instead of treating the full residual directly with corrective Monte Carlo, Wollaeger and Densmore observe that $R^{(n)}$ is the uncollided component of the solution to Eq. (1.105). Dividing the solution into uncollided and collided parts gives

$$\delta\Phi = \delta\Phi_c + R^{(n)} \quad , \tag{1.107}$$

and substituting this expression into Eq. (1.105) shows that the collided component $\delta\Phi_c$ satisfies

$$\mathbf{M}\delta\Phi_c = (\mathbf{I} - \mathbf{M})R^{(n)} \quad , \tag{1.108}$$

where **I** is the identity matrix. The form of Eq. (1.108), along with a few manipulations involving Eq. (1.102), allows us to construct an equivalent set of equations similar to Eqs. (1.91) through (1.94):

$$\mu\frac{\delta\psi_{c,i} - \delta\psi_{c,i-1}}{\Delta x_i} + \sigma_{t,i}\delta\psi_{c,i} = \frac{\sigma_{s,i}\delta\phi_{c,i} + \sigma_{s,i}R_i^{(n)}}{2} \quad , \quad \mu > 0 \ ; \tag{1.109}$$

$$|\mu|\frac{\delta\psi_{c,i} - \delta\psi_{c,i+1}}{\Delta x_i} + \sigma_{t,i}\delta\psi_{c,i} = \frac{\sigma_{s,i}\delta\phi_{c,i} + \sigma_{s,i}R_i^{(n)}}{2} \quad , \quad \mu < 0 \ ; \tag{1.110}$$

$$\delta\psi_{c,0}(\mu) = 0 \quad , \quad \mu > 0 \ ; \tag{1.111}$$

$$\delta\psi_{c,I+1}(\mu) = 0 \quad , \quad \mu < 0 \quad . \tag{1.112}$$

Here, $\delta\phi_{c,i}$ and $R_i^{(n)}$ are the values of $\delta\Phi_c$ and $R^{(n)}$ for cell i, and $\delta\phi_{c,i}$ is related to $\delta\psi_{c,i}(\mu)$ by

$$\delta\phi_{c,i} = \int_{-1}^{1} \delta\psi_{c,i}(\mu)d\mu \quad , \tag{1.113}$$

analogous to Eq. (1.88). Therefore, Eqs. (1.109)–(1.112) are amenable to S_∞ simulation, from which we can generate an estimate of $\delta\Phi_c$ and then $\delta\Phi$ through Eq. (1.107). This above procedure constitutes the continuous angle, spatially discrete residual Monte Carlo method. Figure 6 from the summary of Wollaeger and Densmore [102] demonstrates exponential error convergence for a problem consisting of a 1 cm slab, a total opacity of $\sigma_t = 1$ cm, a scattering opacity of $\sigma_s = 0.5$ cm, a uniform source of $q = 1$ cm^{-1}s^{-1} and 400, 800, or 1600 particles per residual iteration. The error is plotted versus total number of particles used; this includes standard and error particles.

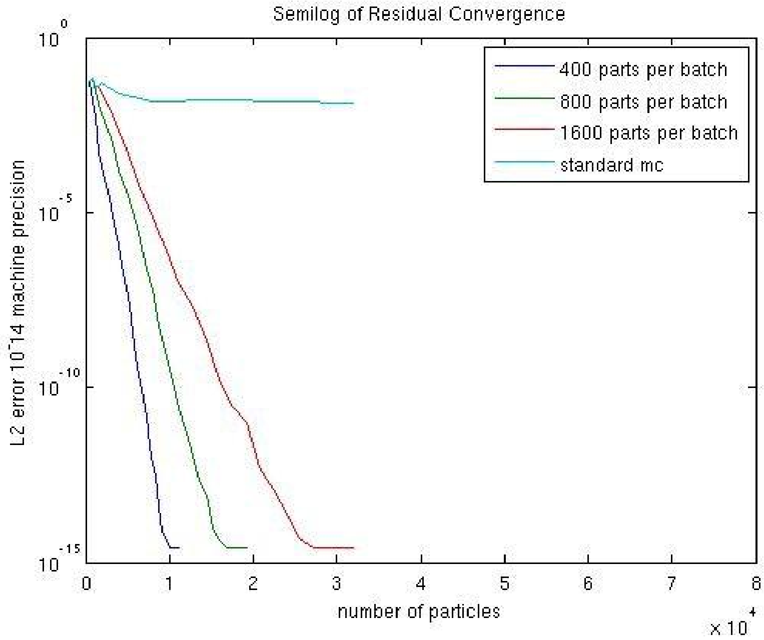

Figure 6: Residual Monte Carlo test in a homogeneous medium. Error convergence versus total particle number simulated.

By using a discrete integral transport (Section 1.3.1) to compute a residual source for Monte Carlo transport iterations (Section 1.3.2), discrete ordinates are not needed to achieve exponential convergence. The error does not saturate above machine precision and ray effects are avoided (Section 1.3.1).

2 Literature Review

Indicated in Section 1.3, there exists a field of research to develop methods to perform numerical transport and diffusion calculations. Specifically, focus is allocated to constructing methods that a computer code can execute efficiently and without exhausting memory resources. It is desirable to have the resulting program scale efficiently to many cores; thus allowing for intensive simulation in a timely manner. Efficiency must be balanced with fidelity to the underlying physical system; often high-fidelity simulations are expensive since more computational details may give rise to more computational work.

Monte Carlo (MC) methods are often useful in complicated problems where scaling to many CPUs is a concern. Monte Carlo particles are independent from one another, and hence the processes involved in their transport can be treated by independent processors. Another typical advantage, in Monte Carlo transport in particular, is that particles are somewhat agnostic of grid structure. The material-radiation interaction is dependent on cell properties, but the outline of the transport process is the same for each cell. Consequently, extending the MC component of codes to multiple dimensions often does not present the same challenge as corresponding deterministic methods might.

Relative to deterministic schemes, Monte Carlo has drawbacks as well. Because of the statistical nature of MC, Monte Carlo transport is prone to noise. Moreover, statistical noise is exacerbated by increasing grid resolution while keeping total particle number constant. However, there are techniques to reduce variance in the solution. Citing examples from Lewis and Miller, reduction techniques include: absorption suppression, Russian Roulette, and importance sampling [62, p. 329–333]. In the context of multi-physics codes that employ Monte Carlo, spurious statistical fluctuations can couple into deterministic calculations and therefore spread damaging error.

Apart from statistical quality, problem-specific domain properties may deteriorate the effectiveness of a Monte Carlo scheme that is naive to appropriate optimization. For instance, simulations with pure transport MC over optically thick, highly scattering regimes can cause particles to scatter many times before reaching the end of a time step or terminating. The larger number of Monte

Carlo steps per particle in the highly scattering domain generally leads to longer CPU times spent per particle. With domain decomposition on a strongly heterogeneous material, load imbalance may occur between a set of processors that transport particles in the optically thick regions and a set of processors that transport particles in more transparent regions. In this case, the overall computation time is rate-limited by the overtaxed cores.

Concerning fidelity to physics, in recent decades it has been demonstrated that certain deterministic and stochastic transport methods do not preserve correct diffusion behavior. Piecewise constant discretization of either the radiation field or material field through the introduction of grids lead to incorrect solutions when there are many mean free paths per cell dimension or characteristic cell size. Asymptotic analyses by various authors have demonstrated that the leading order behavior of certain spatially discrete transport schemes do not produce correct discretizations of the appropriate continuous radiation diffusion equation. In addition to error incurred from spatial grids, time-dependent MC transport has been shown to be unstable for large time steps even after measures are taken to make the transport implicit.

In the following literature review, advances in radiative transfer methods, method theory, and theory are summarized. The set of articles heading the sections are meant to provide points of reference in broader efforts associated with the method pathologies or astrophysics discussed. Thus, articles without dedicated sections are referenced throughout. In Section 2.1, findings in articles pertinent to developing IMC-DDMC code described in Chapter 3 are described. In Section 2.2, relevant articles of theory and methods for radiation transport in Type Ia supernovae are described.

2.1 IMC-DDMC Review

2.1.1 Fleck and Cummings Implicit Monte Carlo (IMC)

The Implicit Monte Carlo (IMC) method of Fleck and Cummings [37] is a Monte Carlo radiation transport method that has been explored extensively since its conception. The method is, in fact, semi-implicit in time and is prone to non-physical violations of a “maximum principle” for large time step sizes [60, 101]. The important ingredient in the treatment of the radiation-material interaction is effective scattering and absorption [37]. Despite still being prone to over-heating, IMC is an improvement over time-dependent MC transport that treat the temperature update explicitly. IMC generally can use larger time step sizes than the explicit counterpart. An absurd instance of over-heating in an explicit MC treatment would be to model a time-dependent transport problem with one optically thick spatial cell and one time step. If emission is not captured in some manner during the time step, then many photon packets would be absorbed and no emission would ever occur. If instead we have one spatial cell, two time steps, and a source spatially localized in the cell, uniformly sampling emission in the subsequent time step would induce a loss of information on the thermal profile; as if packet energy had teleported across the domain of the cell. These pathologies are discussed more in following sections.

IMC works against the pathologies to some extent through effective scattering, where a fraction of an absorbed particle is instantaneously re-emitted in a way that resembles inelastic scattering. In the original article by Fleck and Cummings, they consider both grey and multi-frequency transport in one dimensional, planar geometry under LTE conditions. As for many of the subsequent papers discussed, they exclude real scattering since it does not add any novel complication to the description of the method [37]. The grey equations are

$$\frac{1}{c}\frac{\partial I}{\partial t} + \mu\frac{\partial I}{\partial x} + \sigma I = \frac{1}{2}\sigma a c T^4 \ , \tag{2.1a}$$

$$\frac{\partial U_m}{\partial t} = \sigma\left(\int_{-1}^{1} I\, d\mu' - acT^4\right) + S \ , \tag{2.1b}$$

where $I = 2\pi\int_0^\infty I_\nu d\nu$, T is the material temperature, U_m is the material energy density, S is an external material source, σ is a frequency independent absorption opacity, (x,t) is the space-time coordinate, μ is the x-component of the direction, and $a = 8\pi^5k^4/15c^3h^3$ is the radiation constant [37]. Adding an external source to Eq. (2.1a) does not inform the IMC discretization procedure. For convenience, $U_r = aT^4$ and $\beta = \partial U_m/\partial U_r$ are introduced to give

$$\frac{1}{c}\frac{\partial I}{\partial t} + \mu\frac{\partial I}{\partial x} + \sigma I = \frac{1}{2}\sigma c U_r \ , \tag{2.2a}$$

$$\frac{\partial U_r}{\partial t} = \beta\sigma\left(\int_{-1}^{1} I\, d\mu' - cU_r\right) + \beta S \ . \tag{2.2b}$$

The material equation, Eq. (2.2b), is integrated over a time step and a time-centering parameter, α, is introduced. Accordingly, Eq. (2.2b) becomes

$$U_{r,n+1} - U_{r,n} = \Delta t_n \beta \sigma \left(\int_{-1}^{1} I d\mu' - c(\alpha U_{r,n+1} + (1-\alpha) U_{r,n}) \right) + \beta \Delta t_n S \ \ , \tag{2.3}$$

where $\Delta t_n = t_{n+1} - t_n$, and β, σ, S, and I are assumed to be appropriately time-centered [37].

For a perfect gas, $\beta = 4aT^3/C_v$, where C_v is constant. The opacity is generally dependent on temperature as well, $\sigma = \sigma(T)$. Because the temperature at the end of the time step isn't known, β and σ are typically evaluated at the beginning of the time step. The approximations $\beta = \beta_n$ and $\sigma = \sigma_n$ are the reason for categorizing IMC as a semi-implicit numerical method. With Eq. (2.3), $\bar{U}_r = \alpha U_{r,n+1} + (1-\alpha) U_{r,n}$ can be expressed in terms of U_n and I as

$$\bar{U}_r = \frac{(1-f_n)}{c} \int_{-1}^{1} I \, d\mu' + f_n U_{r,n} + \frac{(1-f_n)}{c\sigma} S \ \ , \tag{2.4}$$

where

$$f_n = \frac{1}{1 + \alpha \beta_n c \Delta t_n \sigma_n} \tag{2.5}$$

is termed the Fleck factor [37, p. 324] in subsequent literature on or related to IMC.

Replacing U_r with $\bar{U}_r$, β with β_n, and σ with σ_n in Eq. (2.1) yields the grey, differential IMC equations

$$\frac{1}{c}\frac{\partial I}{\partial t} + \mu \frac{\partial I}{\partial x} + \sigma_n I = \frac{1}{2}(1-f_n)\sigma_n \int_{-1}^{1} I \, d\mu' + \frac{1}{2} f_n \sigma_n c U_{r,n} + \frac{1}{2}(1-f_n) S \ \ , \tag{2.6a}$$

$$\frac{\partial U_m}{\partial t} = f_n \sigma_n \left(\int_{-1}^{1} I \, d\mu' - c U_{r,n} \right) + f_n S \ \ . \tag{2.6b}$$

Integrating Eq. (2.6a) over μ and adding the result to Eq. (2.6b) gives

$$\frac{1}{c}\frac{\partial \phi}{\partial t} + \frac{\partial F}{\partial x} = -\frac{\partial U_m}{\partial t} \ \ , \tag{2.7}$$

where $\phi = \int_{-1}^{1} I d\mu$ and $F = \int_{-1}^{1} \mu I d\mu$. Equation (2.7) is the correct statement of energy conservation for the original system of equations, (2.1). Applying a similar procedure, Fleck and Cummings subsequently arrive at that the non-grey, differential IMC equations,

$$\frac{1}{c}\frac{\partial I_\nu}{\partial t} + \mu\frac{\partial I_\nu}{\partial x} + \sigma_{\nu,n} I_\nu = \frac{1}{2}(1-f_n)\frac{\sigma_{\nu,n} b_{\nu,n}}{\sigma_{P,n}} \int_{-1}^{1}\int_0^\infty \sigma_{\nu',n} I_{\nu'}\, d\nu'\, d\mu' + \frac{1}{2} f_n \sigma_{\nu,n} b_{\nu,n} c U_{r,n} + \frac{1}{2}(1-f_n)\frac{\sigma_{\nu,n} b_{\nu,n}}{\sigma_{P,n}} S \ , \tag{2.8a}$$

$$\frac{\partial U_m}{\partial t} = f_n \int_0^\infty \int_{-1}^{1} \sigma_{\nu,n} \left(I_\nu - 2\pi B_{\nu,n}\right) + f_n S \ , \tag{2.8b}$$

where $b_{\nu,n} = 4\pi B_{\nu,n}/cU_{r,n}$ is the normalized Planck function, $\sigma_{P,n} = \int_0^\infty b_{\nu,n}\sigma_{\nu,n}$ is the Planck opacity at the beginning of time step n, and $2\pi I_\nu \to I_\nu$.

In Eqs. (2.6) and (2.8), setting the control parameter, α, to 0 yields fully explicit equation sets with the usual Monte Carlo interpretation. Setting $\alpha = 1$ leads to a Monte Carlo method that is less prone to the unphysical heating error mentioned above. Fleck and Cummings realized that Eq. (2.8a) is amenable stochastic interpretation after the IMC discretization procedure. Since $\sigma_\nu = f_n\sigma_\nu + (1-f_n)\sigma_\nu$, $(1-f_n)\sigma_\nu$ is interpreted as an artificial scattering opacity and $f_n\sigma_\nu$ is an artificial absorption opacity. The first terms on the right sides of Eqs. (2.6a) and (2.8a) are scattering sources; the effective scattering source in Eq. (2.8a) is inelastic.

Despite the increased stability of the the $\alpha \neq 0$ IMC equations over explicit coupled transport, IMC is observed to be prone to over-heating instability. In the following section, Section 2.1.2, the theoretical source of IMC instability is discussed. Recent schemes for mitigating over-heating are reviewed in Sections 2.1.3 and 2.1.4.

2.1.2 IMC Maximum Principles

The semi-implicit nature due to the linearization within time steps has been mathematically proven to still allow for nonphysically large heating to occur for large time steps by Larsen and Mercier [60]. The "Maximum Principle" for the thermal transport equations is [60]:

- For a domain D, let $0 \leq T_L < T_U$ be fixed constants.

- Let I_ν, T, and $I_{\nu,b}$ (the boundary intensity) satisfy

$$B_\nu(T_L) \le I_\nu(\vec{r}, \hat{\Omega}, 0) \le B_\nu(T_U) \ \ , \tag{2.9a}$$

$$T_L \le T(\vec{r}, 0) \le T_U \ \ , \tag{2.9b}$$

$$B_\nu(T_L) \le I_{\nu,b}(\vec{r}, \hat{\Omega}, t) \le B_\nu(T_U) \ \ , \ \ \vec{r} \in \partial D, \ \hat{\Omega} \cdot \vec{n} < 0 \tag{2.9c}$$

  where $\vec{n}$ is the unit outward normal vector at $\vec{r}$ on ∂D.

- Then, for all $\vec{r} \in D$ and $t > 0$,

$$B_\nu(T_L) \le I_\nu(\vec{r}, \hat{\Omega}, t) \le B_\nu(T_U) \ \ , \tag{2.10a}$$

$$T_L \le T(\vec{r}, t) \le T_U \ \ . \tag{2.10b}$$

Larsen proves a statement analogous to the one listed above but for the IMC equations [60]. The proof is not given here, but the statement may be summarized as follows:

- For a domain D, let $0 \le T_L < T_U$ be fixed constants.
- Let I_ν, T, and $I_{\nu,b}$ satisfy Eq. (2.9).
- Additionally, for all time steps n, let Δt_n satisfy

$$\zeta_1 = \sup_{T_L < T < T_U} \left(\frac{16\pi\alpha}{C_v(T)} \int_0^\infty \sigma_\nu(T) \left(\frac{B_\nu(T_U) - B_\nu(T)}{T_U - T} - \frac{B_\nu(T)}{T} \right) \right) \ \ , \tag{2.11a}$$

$$\varsigma(T_L, T, T_U) =$$

$$\max \left(\int_{4\pi} \int_0^\infty \sigma_\nu(T) \frac{B_\nu(T_U) - B_\nu(T)}{U_m(T_U) - U_m(T)} d\nu \, d\Omega \ \ , \right. \tag{2.11b}$$

$$\left. \int_{4\pi} \int_0^\infty \sigma_\nu(T) \frac{B_\nu(T) - B_\nu(T_L)}{U_m(T) - U_m(T_L)} d\nu \, d\Omega \right) \ \ , \tag{2.11c}$$

$$\zeta_2 = \sup_{T_L < T < T_U} \left(\varsigma(T_L, T, T_U) - \alpha\beta(T)\sigma_P(T) \right) \ \ , \tag{2.11d}$$

$$\Delta t_n \max(\zeta_1, \zeta_2) \le 1 \ \ . \tag{2.11e}$$

- Then, for all $\vec{r} \in D$ and $t > 0$,

$$B_\nu(T_L) \leq I_\nu(\vec{r}, \hat{\Omega}, t) \leq B_\nu(T_U) \ , \tag{2.12a}$$

$$T_L \leq T_n(\vec{r}) \leq T_U \ . \tag{2.12b}$$

Larsen and Mercier prove the condition by induction of the time steps. In other words, if Eq. (2.11) is satisfied for all time steps, then $T_L \leq T_n \leq T_U$ and $B_\nu(T_L) \leq I_\nu(\vec{r}, \hat{\Omega}, t \in [t_{n-1}, t_n]) \leq B_\nu(T_L)$ imply $T_L \leq T_{n+1} \leq T_U$ and $B_\nu(T_L) \leq I_\nu(\vec{r}, \hat{\Omega}, t \in [t_n, t_{n+1}]) \leq B_\nu(T_U)$ [60]. Ultimately, the maximum principle for the continuous IMC equations is a sufficient but not necessary condition to avoid over-heating. In practice, IMC can often perform well for time step sizes that are larger than the maximum principle constraint predicts.

Recently, Wollaber et al. [101] formulated a discrete maximum principle for the IMC equations that includes a spatial grid in the derivation. They further demonstrate the discrete maximum principle is a better predictor of time step induced over-heating. The development of the discrete maximum principle is communicated in the context of a one dimensional, semi-infinite medium, Marshak wave problem with a Planckian source at a temperature T_U on the finite boundary of the medium [101]. To form the inequality and hence the conditions, Wollaber et al. constrain the leftmost piecewise-constant temperature to be less than or equal to T_U after the first time step update. The resulting inequality for the time step size is written as [101]

$$\Delta t_0 < \frac{C_{v,0}(T_U - T_0)}{R(\Delta x_1, \Delta t_0) - f_0 \sigma_{P,0} a c T_0^4} \ , \tag{2.13}$$

where $R(\Delta x_1, \Delta t_0)$ is the average effective deposition rate density in the leftmost cell for the first time step, $n = 0$. The authors both introduce approximate procedures to obtain an estimate of R and rigorously bound R to provide *both* necessary and sufficient conditions for Δt_n.

The separate necessary and sufficient conditions are realized by using modified transport equations to obtain analytic solutions to substitute for R in Eq. (2.13). For the necessary condition, a false radiation intensity, $\breve{I}$, and false updated discrete material temperature, $\breve{T}_1$, are solved from [101]

$$\frac{1}{c}\frac{\partial \breve{I}_\nu}{\partial t} + \mu\frac{\partial \breve{I}_\nu}{\partial x} + \sigma_{\nu,0}\breve{I}_\nu = \sigma_{\nu,0} f_0 2\pi B_\nu(T_0) \ , \tag{2.14a}$$

$$C_{v,0}\frac{\breve{T}_1 - T_0}{\Delta t_0} = \frac{1}{\Delta t_0 \Delta x_1}\int_0^{\Delta x_1}\int_0^{\Delta t_0}\int_0^{\infty}\int_{-1}^{1} \sigma_{\nu,0} f_0(\breve{I}_\nu - 2\pi B_\nu(T_0)) d\mu d\nu dt dx \ , \tag{2.14b}$$

$$\breve{I}_\nu(x,\mu,0) = 2\pi f_0 B_0 \ , \ 0 \le x < \infty, -1 \le \mu \le 1 \ , \tag{2.14c}$$

$$\breve{I}_\nu(0,\mu,t) = B_\nu(T_U) \ , \ t > 0, 0 < \mu \le 1 \ , \tag{2.14d}$$

where effective scattering is removed [101]. It should be noted that $\sigma_{\nu,0}$ indicates a lab frame, frequency-dependent opacity evaluated at the beginning of the first time step while σ_{0,ν_0} frequency dependent comoving opacity. Thus subscript ordering is conserved to prevent conflicting notation with later sections. The authors prove that $T_1 > \breve{T}_1$ is always true; hence if Δt_0 admits a $\breve{T}_1 > T_U$, then $T_1 > T_U$. Ergo, it is necessary that Eq. (2.13) not allow for $\breve{T}_1 > T_U$ [101]. After considerable analysis, Wollaber et al. arrive at a necessary deposition rate, R, that has distinct formula for the cases $c\Delta t_0 \le \Delta x_1$ and $c\Delta t_0 > \Delta x_1$; the former case allows for radiation from the $x = 0$ boundary to escape before time step completion so the formulae are distinct.

The analysis for the sufficient condition is similar, with the false intensity being set to [101]

$$\hat{I}_\nu = \begin{cases} 2\pi(B_\nu(T_U) + B_\nu(T_0)) \ , \ x < ct \ , \\ 2\pi B_\nu(T_0) \ , \ x \ge ct \ , \end{cases} \tag{2.15a}$$

$$C_{v,0}\frac{\hat{T}_1 - T_0}{\Delta t_0} = \frac{1}{\Delta t_0 \Delta x_1}\int_0^{\Delta x_1}\int_0^{\Delta t_0}\int_0^{\infty}\int_{-1}^{1} \sigma_{\nu,0} f_0(\hat{I}_\nu - 2\pi B_\nu(T_0)) d\mu d\nu dt dx \ . \tag{2.15b}$$

It turns out $\hat{T}_1 > T_1$ is always true; thus a time step that has $\hat{T}_1 < T_U$ is sufficient.

Wollaber et al. [101] subsequently employ the diffusion approximation for the grey and multi-frequency cases to get thresholds that estimate the maximum principle boundary. The plots demonstrate close agreement between the derived discrete maximum principle and experimentally obtained over-heating for 1D Marshak wave problems. The continuum condition of Larsen and Mercier appears conservative compared even to the sufficient condition derived by Wollaber et al. Thus, the inclusion of spatial grid effect appears to be essential in explaining why the condition of Larsen and Mercier is sufficient but often much too conservative [60, 101].

In the next section, we review Gentile's modified IMC method that mitigates over-deposition of radiation [42]. In other words, the method reduces the R value of Wollaber et al. to relax the constraint on time step size.

2.1.3 Gentile-Fleck Factor Modified IMC

Gentile explores a higher order discretization of the material temperature equation. The result, along with approximations, is a "Gentile-Fleck" factor that has the standard Fleck factor as a lower bound [42]. The procedure involves linear expansions in opacity and the Planck function [42]. Thus Gentile commences with the transport and material temperature equation written as

$$\frac{1}{c}\frac{\partial I_\nu}{\partial t} + \hat{\Omega}\cdot\nabla I + \left(\sigma_{\nu,n} + \Delta T_n \frac{\partial \sigma_{\nu,n}}{\partial T}\right) I = \left(\sigma_{\nu,n} + \Delta T_n \frac{\partial \sigma_{\nu,n}}{\partial T}\right)\left(B_{\nu,n} + \Delta T_n \frac{\partial B_{\nu,n}}{\partial T}\right) \quad , \tag{2.16}$$

and

$$\begin{aligned} C_{v,n}\frac{\Delta T_n}{\Delta t_n} = &\int_0^\infty \int_{4\pi} \left(\sigma_{\nu,n} + \Delta T_n \frac{\partial \sigma_{\nu,n}}{\partial T}\right) I_\nu d\Omega d\nu \\ &- \int_0^\infty \int_{4\pi} \left(\sigma_{\nu,n} + \Delta T_n \frac{\partial \sigma_{\nu,n}}{\partial T}\right)\left(B_{\nu,n} + \Delta T_n \frac{\partial B_{\nu,n}}{\partial T}\right) d\Omega d\nu \quad , \end{aligned} \tag{2.17}$$

where $\Delta T_n = T_{n+1} - T_n$ and $B_{\nu,n} = B_\nu(T_n)$ [42]. Gentile solves Eq. (2.17) for $\Delta T_n/\Delta t_n$ to get

$$C_{v,n}\frac{\Delta T_n}{\Delta t_n} = g\left(\int_0^\infty \int_{4\pi} \sigma_{\nu,n}(I_\nu - B_{\nu,n}) d\Omega d\nu\right) \quad , \tag{2.18}$$

where [42]

$$g_n \equiv \frac{1}{1 + \frac{\Delta t_n}{C_{v,n}} \int\int (\sigma_{\nu,n}\partial B_{\nu,n}/\partial T - (I_{\nu,n} - B_{\nu,n})\partial \sigma_{\nu,n}/\partial T) d\Omega d\nu} \tag{2.19}$$

is the naive form of the Gentile-Fleck factor. According to Gentile, the form for ΔT_n can be incorporated into the linear expansions in Eq. (2.16) and terms of order ΔT_n^2 can be neglected. The transport equation that results has effective emission and scattering terms with probability distribution functions that are dependent on $B_{\nu,n}$, $\sigma_{\nu,n}$ *and* $\partial B_{\nu,n}/\partial T$, $\partial\sigma_{\nu,n}/\partial T$ and I_n. The Gentile-Fleck factor, g_n, takes the role of the Fleck factor, f_n from standard IMC. To avoid having to sample direction-dependent probability densities, Gentile reduces the probability densities to the standard IMC distributions. The argument provided is that direction-dependent sampling is susceptible to statistical noise [42]. Equation (2.19) can yield negative values of g_n. Evidently, arguments provided by Gentile indicate this is physical; negative effective absorption removes energy from the material and adds to the radiation field [42]. To avoid negative material temperature, g_n is constrained to be positive and less than or equal to the Fleck factor [42],

$$g_n = \frac{1}{1 + \beta_n c\sigma_{P,n}\Delta t_n - \min\{(E - aT^4)\partial\sigma_{P,n}/\partial T, 0\}} \leq f_n \quad . \tag{2.20}$$

By replacing f_n with g_n in IMC, Gentile demonstrates the new MC scheme avoids a "temperature flip" [41, 42] over-heating pathology of standard IMC for opacity inversely proportional to the fifth power of temperature. For coarse time steps, within the first time step, a high radiation temperature and low material temperature causes large and immediate over-deposition. The material temperature jumps roughly to the initial radiation temperature while the radiation temperature abruptly drops to the initial material temperature. For the given form of opacity, emission drops as $1/T$ to make the error persist across computed times [42]. Despite the improvement, the Gentile-Fleck factor also induces more effective scatters per IMC particle. To mitigate the additional computational expense, Gentile couples IMC to Random Walk (RW). The RW method is discussed in Section 2.1.10. In our implementation of the Gentile-Fleck factor, we have IMC-DDMC which similarly mitigates the cost of increase in effective scattering.

In Chapter 3, we briefly touch on a compressed derivation of the Gentile-Fleck factor as well as a simple optimization for intensive opacity calculations. We apply the Gentile-Fleck factor to IMC-DDMC in the W7 model of Type Ia supernovae and verify it counteracts the "temperature flip" pathology in the context of high-velocity fluid.

An alternative to encapsulating higher order in a modified Fleck factor is to increase the order of the time discretization of the material temperature equation. A review of the second order backward difference formula (BDF-2) for time integration, developed by McClarren and Urbatsch, is also seen to mitigate over-heating. The BDF-2 approach is discussed in the next review, Section 2.1.4.

2.1.4 McClarren and Urbatsch's BDF-2 Scheme for Temporal Discretization in IMC

In the absence of external sources, taking $\alpha = 1$ in the material IMC equation, Eq. (2.3), yields

$$\frac{U_{r,n+1} - U_{r,n}}{\Delta t_n} = \beta\sigma\left(\int_{-1}^{1} I d\mu' - cU_{r,n+1}\right) \quad . \tag{2.21}$$

If $\beta \neq \beta_{n+1}$ and $\sigma \neq \sigma_{n+1}$, then the integral over intensity I is computed from a tally of particles whose energy is determined from values computed in a time step preceding $n+1$. Hence $\int_{-1}^{1} I d\mu'$ would be algorithmically independent of $U_{r,n+1}$. Regardless of the conditions on β, σ, or I, Eq. (2.21) can be interpreted as a backward differenced formula (BDF) of O(1),

$$\frac{U_{r,n+1} - U_{r,n}}{\Delta t_n} = g(U_{r,n+1}) \quad , \tag{2.22}$$

where g can be an arbitrary function. For the purposes of thermal transport, it is the right hand side of Eq. (2.21). McClarren and Urbatsch apply a method that replaces Eq. (2.22) with a second order BDF formula (BDF-2) [71, p. 502],

$$\frac{3U_{r,n+1} - 4U_{r,n} + U_{r,n-1}}{3\Delta t_n} = \frac{2}{3} g(U_{r,n+1}) \quad . \tag{2.23}$$

Defining $U_{r,n+1/2} = (4U_{r,n} - U_{r,n-1})/3$ and evaluating β, σ, and indirectly I at $U_{r,n+1/2}$ linearizes Eq. (2.23) in $U_{r,n+1}$. Then [71]

$$U_{r,n+1} = mU_{r,n+1/2} + (1-m)\frac{1}{c}\int_{-1}^{1} I d\mu' \quad , \tag{2.24}$$

where

$$m = \frac{1}{1 + \frac{2}{3}\beta_{n+1/2} c\sigma_{n+1/2}\Delta t_n} \quad . \tag{2.25}$$

McClarren and Urbatsch use a different form for β described by

$$\beta C_v \frac{\partial T}{\partial t} = \frac{1}{\sigma(T)} \frac{\partial(\sigma(T) a T^4)}{\partial t} \quad . \tag{2.26}$$

Then it must be that [71]

$$\beta = \frac{a}{C_v} \left(4T^3 + T^4 \frac{d}{dT} \ln(\sigma) \right) \quad . \tag{2.27}$$

Now if σ and β are taken to be constants at $T = T_{n+1/2}$, Eqs. (2.24) and (2.25) are still satisfied, but with $\beta_{n+1/2}$ equal to Eq. (2.27) evaluated at $T = T_{n+1/2}$. It was further found that setting

$$m = \frac{1}{1 + \theta \beta_{n+1/2} c \sigma_{n+1/2} \Delta t_n} \quad , \tag{2.28}$$

where $\theta \in [2/3, 1]$, gave more robust results for some certain numerical experiments [71].

The quantity m takes the place of the Fleck factor in IMC (along with $\sigma = \sigma_{n+1/2}$) after incorporating $U_{r,n+1}$ into the transport equation. With several infinite medium tests [71], McClarren and Urbatsch show that the BDF method can suffer some oscillation effects, but these effects can be reduced by setting $\theta = 1$. The BDF-2 scheme apparently mitigates the "temperature flip" phenomenon without having the opacity derivative with respect to temperature in the β term. Thus the method should not be much more expensive than standard IMC in regimes where g_n from Section 2.1.3 is significantly smaller than f_n.

Including Section 2.1.4, the preceding reviews have described the IMC maximum principles and means of preventing violation of the maximum principles. The unifying theme has been over-deposition due to large time steps or small cell sizes. Another IMC pathology exists in the regime of small time steps and large, or optically thick cell, cell sizes. For both Symbolic Implicit Monte Carlo (SIMC) and IMC, small time steps in optically thick spatial cells allows radiation energy to propagate across cells faster than may be permitted by causality. An attempt to treat the numerical energy "teleportation" error in SIMC is discussed in Section 2.1.5. SIMC should not suffer maximum principle violations since the method is fully implicit. In Sections 2.1.6, 2.1.7, 2.1.5, 2.1.8, and 2.1.9, theoretical explanations for the manifestation of error from spatial discretization are discussed. The underlying theme is that certain discretizations for transport methods generally do not preserve correct diffusion behavior for optically thick spatial cells.

2.1.5 Symbolic Implicit Monte Carlo (SIMC)

Symbolic Implicit Monte Carlo (SIMC) is a realization of the stochastic interpretation of the collision probability matrix described in the introduction. By not assigning each particle an explicit weight, one can solve the material coupled transport equation implicitly without introducing effective scattering [11]. The method was developed by recognizing that the particle transport did not depend on the weight of the particle [11]. The independence of the transport process from the particle weights allows one to solve the updated material state from a matrix equation with matrix coefficients determined from collision probability tallies. Problems that would have much effective scattering due to a small Fleck factor ($f_n << 1$) in IMC do not suffer effective scattering in SIMC.

The equations of Brooks [11] are the time dependent equations for a NLTE, two state material in slab geometry. SIMC can be used to solve steady state problems as Clouet and Samba show with Eq. (2.55). The physical scattering in Φ in Eq. (2.55) is not modeled directly by introducing ansatz $\varphi_{l,i}(\vec{r})$ and $I_{l,i}(\vec{r},\hat{\Omega})$. Monte Carlo may then be directly applied to Eq. (2.57a) to directly obtain the matrix element $a_{l,i;l',i'}$. To elaborate on a previous statement, the analysis be Samba and Clouet is useful for IMC because the derivations are translatable under the mapping $\sigma \to \sigma_a$, $\sigma_a \to f\sigma_a$, $\sigma_s \to (1-f)\sigma_a$, where f is an equilibrium Fleck factor. This mapping is similar but not identical to that of Densmore's equilibrium model problem [25].

The LTE SIMC of N'Kaoua also avoids effective scattering [75, 28]. From the summary of Densmore, the appropriate equations are [28]

$$\frac{1}{c}\frac{\partial I}{\partial t} + \hat{\Omega}\cdot\nabla I + \sigma_n I = \frac{1}{4\pi}\sigma_n acT_{n+1}^4 \quad , \tag{2.29a}$$

$$\frac{\partial U_m}{\partial t} = \sigma_n \int_{4\pi} I\, d\Omega - \sigma_n acT_{n+1}^4 \quad . \tag{2.29b}$$

It is discernible that the material properties are evaluated at the end of the previous time step. The radiation particles censused from a previous time step have packets of known energy, since presumably, the cell-centered material temperature, $T_{n,i}$, has been solved. So the censused particles' motions are governed by [28]

$$\frac{\partial I_{\text{cen}}}{\partial t} + \hat{\Omega} \cdot \nabla I_{\text{cen}} + \sigma_n I_{\text{cen}} = 0 \ , \tag{2.30}$$

where I_{cen} is the portion of radiation intensity that had been censused on the previous time step. With the naive piecewise discretization of the method observables, radiation generated in a cell i is governed by [28]

$$\frac{\partial I_{D_i}}{\partial t} + \hat{\Omega} \cdot \nabla I_{D_i} + \sigma_n I_{D_i} = \frac{\sigma_n c \varphi_i}{4\pi} \ , \tag{2.31}$$

where φ_i is one in cell i and zero everywhere else in the domain D and I_{D_i} is intensity in the domain originating from the subdomain (cell) D_i. The birth cell index of a photon packet can be stored as a property of the packet in order to assign a numeric weight between time steps. Making the assumption of the material being a perfect gas, the discrete material equation becomes [28, p. 183]

$$\begin{aligned} C_v(T_{n+1} - T_n) = \frac{1}{V_i} \int_{t_n}^{t_{n+1}} \int_{4\pi} \int_{D_i} \sigma_{n,i} I_{\text{cen}} d^3\vec{r} d\Omega dt + \\ \frac{1}{V_i} \sum_{i'=1}^{I} a T_{n+1,i'}^4 \int_{t_n}^{t_{n+1}} \int_{4\pi} \int_{D_i} \sigma_{n,i} I_{D_{i'}} d^3\vec{r} d\Omega dt - \sigma_{n,i} \Delta t_n a c T_{n+1,i}^4 \end{aligned} \tag{2.32}$$

where V_i and $\sigma_{n,i}$ are the volume and cell-centered opacity of cell i, respectively. Equation (2.32) describes a system of equations over the spatial domain for each time step. The matrix may be both dense and lacking in symmetry since it is tallied stochastically. One might expect issues to occur for scalability to problems with large, highly resolved, multi-dimensional spatial domains given Eq. (2.32) is a stochastic analogue to the time dependent collision probability method derived in section 1.3.1.

With piecewise constant φ_i sources, SIMC has been observed to produce Marshak waves that propagate too quickly [72]. As a remedy for the teleportation error, Brooks et al. [12] incorporate trial space discretizations for the material temperature equation. These discretizations are self-consistent.

Brooks et al. [12] unify N'Kaoua's method and Clouet and Samba's [23] SIMC trial space extension to both a discontinuous and continuous finite element formulation of SIMC for thermal radiative transport. A material state variable is discretized over a linear trial space; this variable is either the material temperature, $T(\vec{r},t)$, or the equilibrium radiation energy density, aT^4 for the difference formulation of the thermal transport equations [12],

$$\frac{1}{c}\frac{\partial \delta I_\nu}{\partial t}+\mu\frac{\partial \delta I_\nu}{\partial x}=-\sigma_{\nu,a}\partial I_\nu-\frac{1}{2c}\frac{\partial B_\nu(T)}{\partial t}-\frac{\mu}{2}\frac{\partial B_\nu}{\partial x}\quad , \tag{2.33a}$$

$$\frac{\partial U_m}{\partial t}=\int_0^\infty\int_{-1}^1\sigma_{\nu,a}\delta I_\nu+S\quad , \tag{2.33b}$$

where $\delta I_\nu = I_\nu - B_\nu(T(x,t))/2$ as in the IMC section, the azimuthal component of the direction has been integrated out of I_ν and $B_\nu/4\pi$, and S is an external source expressed in the material energy balance. The frequency may be sampled without knowing T^{n+1}. The SIMC frequency distribution is separated from the Planck functions on the right hand side of Eq. (2.33a) [12]:

$$\frac{1}{c}\frac{\partial B_\nu(T)}{\partial t}-\mu\frac{\partial B_\nu}{\partial x}=-\frac{1}{ca}\frac{\partial B}{\partial T^4}\left(aT^3\frac{\partial T}{\partial t}+\mu caT^3\frac{\partial T}{\partial x}\right)\quad , \tag{2.34}$$

where $(1/ac)\partial B/\partial T^4$ can be a probability distribution function in frequency since it integrates to one. SIMC without the difference formulation apparently suffers inhibitive noise effects for optically thick materials [12].

For either state variable considered, the expansions in $T(x,t)$ or $aT(x,t)^4$ are made to be algebraically self-consistent [12]. According to Brooks [12], expanding in aT^4 makes for a simpler sampling distribution than expanding the trial functions in material temperature. Unfortunately with the constraint of consistency, incorporating a linear expansion in aT^4 causes T to be non-linear at the sub-cell level. Making a linear expansion in the material temperature allows for more straightforward coupling to other physics [12] but sampling MC particles becomes more complicated. In either case the basis functions for the linear discontinuous component of the analysis are [12]

$$\varphi_{i,1} = \begin{cases} \frac{x_{i+1/2}-x}{\Delta x_i} & \text{for } x \in [x_{i-1/2}, x_{i+1/2}] \ , \\ 0 & \text{otherwise} \end{cases} \ , \tag{2.35a}$$

$$\varphi_{i,2} = \begin{cases} \frac{x-x_{i-1/2}}{\Delta x_i} & \text{for } x \in [x_{i-1/2}, x_{i+1/2}] \ , \\ 0 & \text{otherwise} \end{cases} \ . \tag{2.35b}$$

Instead of reviewing the equations here, we will paraphrase an outline of the solutions scheme [12, p. 474] and discuss some of the features in the derivation.

- The material state variable is a superposition of trial space functions with time dependent coefficients.
- Space, angle and frequency sampling distributions are known at the beginning of a time step while per SIMC the source strengths are undetermined.
- The particle advance is made to tally the collision probability matrix (or the matrix that resulted from the inner products of the intensity field with the trial functions).
- The collision probability matrix is incorporated into the nonlinear material state equations.
- The equations are solved (Brooks uses a Newton-Raphson iteration [12]).

The discontinuous linear T and T^4 trial spaces tested by Brooks et al. [12] appear to have some difficulty solving a Marshak wave with a steep gradient for large cells. Specifically, the temperature profiles are able to become non-monotonic for large cells at early time. Otherwise, the self-consistent SIMC trial space formulation significantly mitigates teleportation error relative to the ancestral piecewise constant method.

To understand why a higher order representation is required to obtain robust solutions in optically thick cells, it is informative to review Adam's article on finite element solutions [3]. In Adam's article on discontinuous finite element schemes for transport, requirements are put on trial spaces so that a transport method can correctly solve optically thick problems. The article only considers discrete ordinate systems; this does not detract from the generality of the conclusions. We cover a small portion of Adam's article in Section 2.1.6 and subsequently consider a similar analysis for continuous-angle transport in Section 2.1.7. Additionally in Section 2.1.7, we discuss the asymptotic derivation of the fully continuous diffusion equation from the fully continuous transport equation.

2.1.6 Discontinuous Finite Element Transport in Diffusive Problems

Finite elements have been applied to transport problems in both deterministic and Monte Carlo methods. In particular, a trial space approach has been explored for SIMC; this is reviewed in the previous section, Section 2.1.5. Adams [3] provided analysis and testing of discontinuous finite element methods (DFEMs) applied to optically thick transport problems. Discontinuous finite elements can in some problems help capture sharp changes in material properties at boundaries contained by spatial cell surfaces [3]. The analysis follows the approach of asymptotic analysis elaborated by Larsen and Keller [59] and explored by others (see, e.g. [44, 67, 25]) but considers discretization and discrete ordinates. Larsen et al. [61] have applied asymptotic analysis to the discrete ordinate transport equations previously for different discretizations in planar geometry.

Adams determines conditions of the discontinuous elements that need to be met in order for the discrete leading order solution to be a correct discretization of the diffusion equation [3]. Adams outlines all the conditions required for good code performance and recovery of the correct diffusion solution:

- Resolution: transport methods must have at least one degree of freedom per spatial vertex devoted to allow for the scheme to emulate the correct discrete diffusion behavior.
- Continuity: the solution should be continuous or approach continuity in optically thick domain interiors.
- Robustness: it is desirable that the DFEM method not allow for spurious oscillations in space or negative flux.

- Accuracy: grid resolution in an optically thick domain should furnish a method solution close to the corresponding resolved diffusion solution.
- Boundary condition: the DFEM should reproduce the asymptotic diffusion-limit boundary condition [44, 67] when the boundary layer is not resolved by the spatial grid.

We focus the discussion here on "resolution" and "continuity" since these conditions are critical to correct solutions of transport in optically thick media and affect results in other pertinent articles.

One issue in an FEM transport method that uses discontinuous elements is that the leading order discrete, asymptotic solution may not be continuous at cell edges [3]. Adams appears to circumvent this issue by applying lumping in the finite element matrix for cell interfaces [3]. The article poses arguments general enough to be applied to multiple grid geometries and topologies. The portion discussed here is only a brief summary of Adam's article. The equation solved is the steady state, grey transport equation in discrete ordinates [3],

$$\left(\hat{\Omega}_\kappa \cdot \nabla + \sigma(\vec{r})\right) I(\vec{r}, \hat{\Omega}_\kappa) = \frac{1}{4\pi}(\sigma_s(\vec{r})\phi(\vec{r}) + q_e(\vec{r}))\ ,\ \text{for}\ \vec{r} \in D\ \ , \tag{2.36a}$$

$$\phi(\vec{r}) = \sum_{\kappa=1}^{K} w_\kappa I(\vec{r}, \hat{\Omega}_\kappa)\ \ , \tag{2.36b}$$

$$I(\vec{r}, \hat{\Omega}) = I_b(\vec{r}, \hat{\Omega})\ ,\ \text{for}\ \vec{r} \in \partial D\ ,\ \vec{n}(\vec{r}) \cdot \hat{\Omega} < 0\ \ . \tag{2.36c}$$

Adams then defines several quantities for the subsequent manipulations:

- $D_i =$ domain of cell i,
- $L_i =$ number of faces of cell i,
- $\partial D_{i,l} =$ face $l \in \{1 \dots L_i\}$ of cell i,
- $\partial D_i =$ boundary of cell i, $\partial D_i = \cup_l^{L_i} \partial D_{i,l}$,

for non overlapping cells [3]. The generality of Adams' approach even admits non-planar spatial cell faces which each have average outward normal vectors [3],

$$\vec{n}_{i,l} = \frac{\int_{\partial D_{i,l}} \vec{n}(\vec{r}) d^2\vec{r}}{\int_{\partial D_{i,l}} d^2\vec{r}} \quad , \tag{2.37}$$

as well as weight functions enumerated by cell [3],

$$\varphi_{i,j}(\vec{r}) = 0 \ \text{ for } \vec{r} \notin \ \text{cell } i \quad , \tag{2.38}$$

where $j \in \{1 \dots J_i\}$ and J_i are the number of weight functions in cell i. In performing the weak formulation of the transport equation, Adam applies Green's theorem (the divergence theorem on $\nabla \cdot (I\hat{\Omega}\varphi_{i,j})$ is equivalent) to the streaming operator as Samba and Clouet do in the transport "corner term" (CT) derivation [23]. In contrast to Samba and Clouet's analysis, Eq. (2.36) is discretized in angle, and the postulated leading order weak variation solution, in orders of a small parameter ϵ, can be obtained without corner terms. The resulting equation in our notation is [3, p. 301]

$$\int_{\partial D_i} \vec{n} \cdot \hat{\Omega} \varphi_{i,j} I \, d^2\vec{r} + \int_{D_i} (\varphi_{i,j}\sigma I - I\hat{\Omega} \cdot \nabla\varphi_{i,j}) d^3\vec{r} = \frac{1}{4\pi} \int_{D_i} \varphi_{i,j}(\sigma_s \phi + q_e) \tag{2.39}$$

where $d^2\vec{r}$ and $d^3\vec{r}$ are differential surface and volume elements, respectively. By using calculus identities, the surface of each cell is explicitly incorporated into the finite element analysis. Adams also discriminates between weight functions described above and basis functions [3], $b_{i,j}$, where $i \in \{1 \dots I\}$ is the spatial cell index and $j \in \{1 \dots J_i\}$ so that a solvable system of equations is obtained for each cell i (i.e. the number of basis functions in each cell must equal the number of weight functions). So for cell i,

$$I(\vec{r}, \hat{\Omega}) \approx \sum_{j}^{J_i} I_{i,j}(\hat{\Omega}) b_{i,j}(\vec{r}) \quad . \tag{2.40}$$

Equation (2.40) is then inserted into the volume integral on the left hand side of Eq. (2.39). The boundary condition is discretized in streaming direction to ensure particle properties correspond to the cell they are coming from (in Monte Carlo, this is an explicit condition on quantities associated with packets crossing a surface [31]) [3]. The discontinuous finite element equations in fully general matrix form are [3]

$$\hat{\Omega}_{\kappa} \cdot (\mathbf{L}_{b,i}\vec{I}_{b,i} + \mathbf{L}_{i}\vec{I}_{i}) + \mathbf{T}_{i}\vec{I}_{i} = \frac{1}{4\pi}\mathbf{S}_{i}\vec{\phi}_{i} + \frac{1}{4\pi}\vec{q}_{e,i} \quad , \tag{2.41}$$

where $\mathbf{L}_{b,i}$, $\mathbf{L}_{i}$, $\mathbf{T}_{i}$, and $\mathbf{S}_{i}$ are the $J_i \times J_i$ inner product matrices approximating operators of streaming at the cell surface, streaming in the cell interior, the total opacity, and the scattering opacity, respectively, for cell i. Additionally, $\vec{I}_{b,i}$, $\vec{I}_{i}$, $\vec{\phi}_{i}$ and $\vec{q}_{e,i}$ are $J_i \times 1$ arrays approximating intensity at the cell boundary, cell interior intensity, scalar intensity, and external sources, respectively.

After examining discontinuous finite elements for a two dimensional Cartesian grid using bilinear finite elements, Adam discusses "mass-matrix" lumping. For transport equations where σ and σ_s are constant within cells, lumping the mass matrix $\mathbf{M}_{i} = \mathbf{T}_{i}/\sigma_i$ constrains collisions to be cell-local [3]. After introducing a new concept termed "surface lumping", which essentially diagonalizes $\mathbf{L}_{b,i}$ by evaluating the basis function of each entry (j, j') at the point where $b_{i,j'}$ is maximum (referred to as the support point $\vec{r}_{i,j}$; in practical terms, these are cell vertices) [3].

Adams applies asymptotics first to the un-lumped discontinuous FEM (DFEM) system and demonstrates that there is no requirement on the leading order solution (the scalar flux) to be pointwise continuous at the boundaries of cells [3]. Although pointwise continuity is not necessarily obtained from a general DFEM, weak continuity is preserved [3],

$$\sum_{l=1}^{L_i} \left(\frac{2 \displaystyle\sum_{\kappa | \vec{n}_{i,l}\cdot\hat{\Omega}_{\kappa} > 0} w_{\kappa}\vec{n}_{i,l}\cdot\hat{\Omega}_{\kappa}}{\displaystyle\sum_{\kappa | \vec{n}_{i,l}\cdot\hat{\Omega}_{\kappa} > 0} w_{\kappa}} \right) \int_{\partial D_{i,l}} \varphi_{i,j}(\vec{r})(\phi^{(0)}(\vec{r}^{\,-}_{i,l}) - \phi^{(0)}(\vec{r}^{\,+}_{i,l}))\, d^2\vec{r} = 0 \quad , \tag{2.42}$$

where $\vec{r}^{\,-}_{i,l}$ is a point in D_i immediately on the interior of the surface i, l and $\vec{r}^{\,+}_{i,l}$ is presumably the reflection of $\vec{r}^{\,-}_{i,l}$ about a plane tangent to the cell surface at $\vec{r_{i,l}}$, the closest point on the surface to $\vec{r}^{\,-}_{i,l}$. The value $\phi^{(0)}(\vec{r})$ is the lowest order scalar flux from the usual expansion in ϵ. With surface lumping over weight functions that have "locality", where $\varphi_{i,j}(\vec{r}) = 0$ for $\vec{r} \in \partial D_{i,l}$ and $l \notin \{l_j\}$

[3], Eq. (2.42) becomes [3]

$$\sum_{l_j=1}^{L_{i,j}} \left(\frac{2 \displaystyle\sum_{\kappa | \vec{n}_{i,l_j} \cdot \hat{\Omega}_\kappa > 0} w_\kappa \vec{n}_{i,l_j} \cdot \hat{\Omega}_\kappa}{\displaystyle\sum_{\kappa | \vec{n}_{i,l_j} \cdot \hat{\Omega}_\kappa > 0} w_\kappa} \right) (\phi^{(0)}(\vec{r}_{i,j}^{\,-}) - \phi^{(0)}(\vec{r}_{i,j}^{\,+})) \int_{\partial D_{i,l_j}} \varphi_{i,j}(\vec{r})\, d^2\vec{r} = 0 \ , \qquad (2.43)$$

where $r_{i,j}$ is the support point (vertex) of a weight function $\varphi_{i,j}$, $r_{i,j}^{\pm}$ are the immediate exterior and interior (boundary layer) points about the support point, respectively. Equation (2.43) implies that the scalar flux at the vertex j must be equal for all spatial cells meeting j from the set of cells adjacent to faces of i. The set $l_j \in \{1 \ldots L_{i,j}\}$ enumerates faces of cell i that touch vertex j. But this must ensure pointwise continuity at cell boundaries. Adams rephrases the condition as a matrix equation [3]

$$\mathbf{M} \underline{\phi}_{i,j}^{(0)} = 0 \ , \qquad (2.44)$$

where $\mathbf{M}$ is a symmetric, singular matrix with $M_{i,i} = -\sum_{i' \neq i} M_{i,i'}$. The matrix exists for each vertex, j, and the cell index, i, covers the range of cells that have vertex j. Given the properties of $\mathbf{M}$, to solve Eq. (2.44) for each j, $\phi_{i,j}^{(0)}$ for all i must be equal [3].

Adam's use of surface-matrix lumping at the cell bounds constrains the leading order scalar flux to be continuous at cell bounds. The continuity for the leading order solution arises despite the use of discontinuous trial spaces. Without surface lumping, the continuity condition is a weighted integral, Eq. (2.42).

The portion of Adam's article that includes the asymptotic analysis is not provided here. The review consequently is a small portion of the article's contents. We have highlighted the equations that indicate weak and strong continuity of the leading order solution at cell boundaries. An equation similar to Eq. (2.44) manifests in the asymptotic work of Clouet and Samba [23] for Symbolic IMC (SIMC). In these references, a symmetric, singular matrix equation of the scalar fluxes gives rise to incorrect solutions when the explicit or implicit trial space applied does not satisfy the "resolution" requirement of Adams [3]. In other words, there are not enough degrees of freedom for the continuity constraint to yield a reasonable solution. In one dimension a concrete example of no resolution is the piecewise constant representation over a finite planar domain. If the boundary conditions prescribe zero scalar flux at the boundaries, then since each interior cell profile is uniform the entire leading order interior solution must be zero [23].

In the following section, the approach to asymptotically analyze the continuous transport equation is described. For continuous-angle transport over arbitrary grids, Clouet and Samba apply asymptotic analysis with "corner terms" that decay to zero as the domain gets optically thick [23]. With vanishing corner terms in the weak formulation of the angularly integrated transport equation, if the external and scattering sources are piecewise constant, then the leading order equation is a false discrete diffusion equation that has the properties of $\mathbf{M}$ [23].

2.1.7 Clouet and Samba's Corner Term Analysis

Here, the corner term analysis of Clouet and Samba [23] is discussed. Also referenced is the work of Larsen and Keller [59] and Habetler and Matkowski [44], which are early examples of the utility of asymptotic analysis. If there exists a small parameter ϵ in a set of equations with boundary conditions, asymptotic analysis allows for the derivation of an approximate interior solution and an approximate "boundary layer" solution. So the intensity is often expressed as $I_\nu = I_{\nu,b} + I_{\nu,i}$ where $I_{\nu,b}$ is the solution near the boundary and $I_{\nu,i}$ is the interior solution. Early time values of I_ν may be considered a boundary layer in time, so the solution may be further subdivided to $I_\nu = I_{\nu,b} + I_{\nu,i} + I_{\nu,b,0} + I_{\nu,i,0}$ where $I_{\nu,b,0}$ is the solution at early time near a boundary and $I_{\nu,i,0}$ is the interior solution at early times [59]. The notions "early" and "near" correspond to time $t \sim \epsilon T$ and position $|\vec{r} - \vec{r}_b| \sim \epsilon L_D$ where T is on the order of the observational time scale of the problem and L_D is a typical length scale of the domain D. Considering a plane parallel system and setting, $\epsilon = 1/\sigma L_D$, $\tilde{x} = x/L_D$, and $\tilde{t} = |\vec{U}|t/L_D$ the grey transport equation with isotropic scattering and no external sources can be rewritten as [44]

$$\epsilon \left(\frac{|\vec{U}|}{c} \frac{\partial I}{\partial \tilde{t}} + \mu \frac{\partial I}{\partial \tilde{x}} \right) + I = \frac{\sigma_s}{2\sigma} \phi \ , \tag{2.45}$$

where σ_s is a grey scattering opacity and $\vec{U}$ is a velocity. For many problems of interest, one may assume that a typical macroscopic velocity is O(ϵ), so

$$K\epsilon^2\frac{\partial I}{\partial \tilde{t}} + \mu\epsilon\frac{\partial I}{\partial \tilde{x}} + I = \frac{\sigma_s}{2\sigma}\phi \ \ , \tag{2.46}$$

where K is O(1) [44]. Incorporating $I = \sum_{j=0}^{\infty} I^{(j)}\epsilon^j$ and $\chi = \sigma_s/\sigma = \sum_{p=0}^{\infty}\chi^{(p)}\epsilon^p$ into Eq. (2.46) and matching terms with coefficients ϵ^j yield a set of recursive equations [44],

$$I^{(j)} = \frac{1}{2}\chi^{(j)}\phi^{(j)} \ \text{ for } j = 0 \ \ , \tag{2.47a}$$

$$K\frac{\partial I^{(j-2)}}{\partial \tilde{t}} + \mu\frac{\partial I^{(j-1)}}{\partial \tilde{x}} + I^{(j)} = \frac{1}{2}\chi^{(0)}\phi^{(j)} + \frac{1}{2}\sum_{p=1}^{j}\chi^{(p)}\phi^{(j-p)} \ \text{ otherwise } \ . \tag{2.47b}$$

So $\chi^{(0)}$ must be one. Reducing Eq. (2.47) for $j \in \{0, 1, 2\}$ in terms of the scalar flux coefficients yields

$$\frac{K}{2}\frac{\partial\phi^{(0)}}{\partial\tilde{t}} + \mu\frac{\partial}{\partial\tilde{x}}\left(\frac{\phi^{(1)}}{2} - \frac{\mu}{2}\frac{\partial\phi^{(0)}}{\partial\tilde{x}}\right) + I^{(2)} = \frac{1}{2}\phi^{(2)} + \frac{1}{2}\chi^{(2)}\phi^{(0)} \ \ . \tag{2.48}$$

Finally, integrating over μ yields a diffusion equation for $\phi^{(0)}$,

$$K\frac{\partial\phi^{(0)}}{\partial\tilde{t}} - \frac{1}{3}\frac{\partial^2\phi^{(0)}}{\partial\tilde{x}^2} - \chi^{(2)}\phi^{(0)} = 0 \ \ , \tag{2.49}$$

where $\sigma(1+\epsilon^2\chi^{(2)}) \approx \sigma_s \rightarrow \chi^{(2)} \approx -\sigma_a/\epsilon^2\sigma$ and σ_a is the absorption opacity. Substituting the dimensional coordinates into Eq. (2.49) introduces the recognizable radiation diffusion equation,

$$\frac{1}{c}\frac{\partial\phi}{\partial t} - \frac{1}{3\sigma}\frac{\partial^2\phi}{\partial x^2} + \sigma_a\phi = 0 \ \ , \tag{2.50}$$

where the 0 subscript has been dropped to give ϕ the interpretation as an approximation of scalar flux. Incorporating higher asymptotic moments, $j > 2$, would give improvements over diffusion theory [44].

Fick's law follows from Eq. (2.50). The formula $I = \phi/2 + 3\mu F/2$ where $F = \int_{-1}^{1}\mu I d\mu$ satisfies Fick's law and the diffusion equation. The linearity of I in μ admits a simple boundary condition for flux into the domain,

$$4\int_0^1 \mu' I(x_b,\mu',t)\,d\mu = \phi(x_b,t) - \frac{2}{3\sigma}\frac{\partial\phi}{\partial x}\bigg|_{x=x_b} \quad . \tag{2.51}$$

The plane parallel formulation of Eq. (2.51) can readily be generalized by making the boundary a tangent plane to a more arbitrary surface ∂D with unit normal vector field $\vec{n}(\vec{r}_b)$ such that $\vec{r}_b \in \partial D$,

$$4\int_{\hat{\Omega}'\cdot\vec{n}(\vec{r}_b)<0} |\hat{\Omega}'\cdot\vec{n}(\vec{r}_b)| I_b\,d\mu' = \phi(\vec{r}_b,t) + \frac{2}{3\sigma}\vec{n}(r_b)\cdot\nabla\phi\bigg|_{\vec{r}=\vec{r}_b} \quad , \tag{2.52}$$

where $I_b = I(\vec{r}_b,\mu',t)$. Equation (2.52) is often referred to as the Marshak boundary condition [27]. The incoming flux can be described with Chandrasekhar's H-function [20, p. 77]. Chandrasekhar starts the derivation with discrete ordinates incident on a surface of the domain to obtain the solution of transmitted radiation immediately on the interior of the domain [20, p. 77],

$$\sum_{j=1}^{N/2} w_j = 1 \quad , \tag{2.53a}$$

$$1 = \sum_{j=1}^{N/2} \frac{w_j}{1-\mu_j^2 k_p^2} \quad , \quad p \in \{1\dots N/2-1\} \quad , \tag{2.53b}$$

$$H(\mu) = \frac{1}{\mu_1\cdots\mu_{N/2}} \frac{\prod_{i=1}^{N/2}(\mu+\mu_i)}{\prod_{p=1}^{N/2-1}(1+k_p\mu)} \quad , \tag{2.53c}$$

$$\frac{\phi(\vec{r}_b,t)}{2} = \frac{\sqrt{3}}{2}\left(\sum_{\kappa=1}^{N/2} w_\kappa \mu_\kappa I_\kappa\right) H(\mu) \quad , \tag{2.53d}$$

where k_p is is an eigenvalue from separations of variables, $H(\mu)$ is the H-function that describes diffuse reflection (or equivalently "darkening" of transmitted radiation). The continuous form Clouet and Samba employ is [23]

$$\frac{\phi(\vec{r}_b,t)}{2} = \frac{\sqrt{3}}{2}\int_0^1 \mu H(\mu) I_b d\mu \quad , \tag{2.54}$$

where $\mu = |\hat{\Omega}\cdot\vec{n}|$ and $\hat{\Omega}\cdot\vec{n} < 0$.

Clouet and Samba demonstrate that the leading order continuous transport solution with piecewise constant sources does not discretize to the solution of a discretization of Eq. (2.50). The result is for Symbolic Implicit Monte Carlo method but motivates similar analysis for IMC. The equations used are in steady state as adding time dependence does not modify the implication of the proofs [23]. So,

$$\hat{\Omega} \cdot \nabla I + \sigma I = \sigma \Phi \tag{2.55}$$

where $\sigma\Phi = (\sigma_s \phi + q_e)/4\pi$. Introducing basis functions $\varphi_{l,i}(\vec{r})$ for each cell i over a domain, Samba and Clouet approximate $\Phi(\vec{r}) = \sum_l \sum_i \Phi_{l,i}\varphi_{l,i}(\vec{r})$. The weak formulation of the solution Φ satisfies [23]

$$\int_D (\sigma\Phi - (\sigma\phi + q_e)/4\pi)\varphi_{l,i}(\vec{r})dV = 0 \ \ , \tag{2.56}$$

where D again is the domain. If $I(\vec{r},\hat{\Omega}) = \sum\sum \Phi_{l,i} I_{l,i}(\vec{r},\hat{\Omega})$, the resulting system of equations can be further modified to

$$\hat{\Omega} \cdot \nabla I_{l,i} + \sigma I_{l,i} = \sigma \varphi_{l,i} \ \ , \tag{2.57a}$$

$$\sum_i \sum_l (b_{l,i;l',i'} - a_{l,i;l',i'})\Phi_{l,i} = \frac{1}{4\pi}\int_D q_e \varphi_{l',i'} dV \ \ , \tag{2.57b}$$

$$I_{l,i}(\vec{r},\hat{\Omega}) = 0 \ \ , \vec{r} \in \partial D, \ \hat{\Omega} \cdot \vec{n} < 0 \tag{2.57c}$$

where $b_{l,i;l',i'} = \int_D \sigma \varphi_{l,i}\varphi_{l',i'} dV$, $a_{l,i;l',i'} = (4\pi)^{-1}\int_D \sigma_s \phi_{l,i}\varphi_{l',i'} dV$ and $\phi_{l,i} = \int_{4\pi} I_{l,i} d\Omega$. The corner term is defined as [23]

$$\mathrm{CT}(\epsilon) = \int_{\partial D_i} d^2\vec{r} \int_{D_\Omega} d\Omega Q(\vec{r},\hat{\Omega}) e^{-\frac{\sigma L(\vec{r},\hat{\Omega})}{\epsilon}} \ \ . \tag{2.58}$$

where ∂D_i is the surface of cell i and D_Ω is a subset of the directions. The functions $Q(\vec{r},\hat{\Omega})$ and $L(\vec{r},\hat{\Omega})$ are non-negative and bounded over ∂D_i and D_Ω. Samba and Clouet prove a two part lemma for Eq. (2.58) that shows [23]: $\lim_{\epsilon \to 0}$CT(ϵ)$\to$ 0 exponentially for 1D problems if there exists a constant lower bound of $L(\vec{r},\hat{\Omega})$ and CT(ϵ) $= C(\epsilon/\sigma)^{d-1}$+O($\epsilon^d$) for some constant C and dimension d if $L(\vec{r}_0,\hat{\Omega}) = 0 \to L(\vec{r},\hat{\Omega}) \approx C_0(\hat{\Omega})|\vec{r} - \vec{r}_0|$ when $\vec{r}$ is close to $\vec{r}_0$. With the CT properties, performing the asymptotic expansion over Eq. (2.57) and $\varphi_{l,i}(\vec{r}) = \delta_{i,i'}$, one can prove that the lowest order ϕ_i in the ϵ satisfies a discretization consistent with [23]

$$-\frac{\partial^2 \phi}{\partial x^2} = \frac{K}{4\pi} q_e \quad , \tag{2.59}$$

in one dimension, where $K = 4 \lim_{\epsilon \to 0, \Delta x_i \to 0} (\epsilon / \Delta x_i)$. Eq. (2.59) is of course not the same equation as Eq. (2.50). The piecewise constant representation of the scalar flux does not produce the correct asymptotic limit of transport. If instead a piecewise (bi)linear set of basis functions $\varphi_{l,r}$ are employed, one regains an asymptotic limit to a discretization of the correct diffusion equation. The functions $F(\vec{r}, \hat{\Omega})$ and $L(\vec{r}, \hat{\Omega})$ manifest in the corner term as coefficients and path length in an exact solution to Eq. (2.57a), respectively.

Samba and Clouet's analysis is an example of the importance of the quantities that are discretized for Monte Carlo tallies in the transport equation. Similar to Adams [3], the article highlights the utility of asymptotic analysis in determining discretization effects on transport methods. While the treatment of radiation is continuous in the IMC scheme of Fleck and Cummings, temperature is discrete in space and time. The effects of the spatial and temporal grid are shown by Densmore [25] to have a non-trivial effect on the quality of the solution through an asymptotic analysis similar to that of Clouet and Samba.

2.1.8 Densmore's Analysis of Spatial Discretization in IMC

Densmore [25] performs an asymptotic analysis on three time scalings for IMC where the spatial sub-cell representation of the artificial emission source is either constant or piecewise-linear. One motivation for these sub-cell representations is the ubiquitous application of "source tilting" methods in IMC. Source tilting attempts to mitigate numerical teleportation error in IMC by sampling particle emission locations from a non-constant temperature profile (for LTE) within a spatial zone (cell). The sub-cell material temperature profile is often constructed with temperatures from adjacent cells. In one dimension, for example, a cell i may use the temperature values in cells $i-1$ and $i+1$ to construct a linear slope. This slope is used as a probability density function for particles generated in a time step.

The three time scalings for the asymptotic analysis Densmore uses are [25]:

1. a time step on the order of mean free times,
2. a time step at the Courant limit of the problem,
3. a scaling independent time step.

Solving Eqs. (2.6) or Eqs. (2.8) with IMC requires both a spatial grid and temporal grid. The IMC equations with spatial discretization in planar geometry for grey transport with isotropic scattering and without external sources are [37], [25, p. 1117],

$$\frac{1}{c}\frac{\partial I}{\partial t} + \mu\frac{\partial I}{\partial x} + \sigma_{n,i} I = \frac{1}{2}(1 - f_{n,i})\sigma_{n,i}\int_{-1}^{1} I \, d\mu' + \frac{1}{2} f_{n,i}\sigma_{n,i} c U_{r,n,i} \quad , \tag{2.60a}$$

$$\frac{\partial U_{m,i}}{\partial t} = f_{n,i}\sigma_{n,i}\left(\frac{1}{\Delta x_i}\int_{x_{i-1/2}}^{x_{i+1/2}}\int_{-1}^{1} I \, d\mu' - c U_{r,n,i}\right) \quad , \tag{2.60b}$$

where $x_{1/2} < x_{3/2} < \ldots < x_{I+1/2}$ and $t_0 < t_1 < \ldots < t_N$. The Fleck factor is

$$f_{n,i} = \frac{1}{1 + \alpha\beta_{n,i}\sigma_{n,i} c \Delta t_n} \tag{2.61}$$

where $\beta_{n,j} = 4aT^3_{n.i}/C_{v,n,i}$. Incorporating a linear tilt in the thermal emission source of Eq. (2.60a), the transport equation becomes

$$\frac{1}{c}\frac{\partial I}{\partial t} + \mu\frac{\partial I}{\partial x} + \sigma_{n,i} I = \frac{1}{2}(1 - f_{n,i})\sigma_{n,i}\int_{-1}^{1} I \, d\mu' + \frac{1}{2}(1 + m_{n,i}(x - x_i)) f_{n,i}\sigma_{n,i} c U_{r,n,i} \quad , \tag{2.62}$$

where Densmore uses

$$m_{n,i} \approx \frac{1}{T^4_{n,i}} \left.\frac{\partial T^4}{\partial x}\right|_{n,i} \quad , \quad |m_{n,i}| \leq \frac{2}{\Delta x_i} \quad , \tag{2.63}$$

and $x_i = (x_{i+1/2} + x_{i-1/2})/2$ [25, p. 1118]. The probability distribution then must be [36, 25],

$$p_{n,i} = \frac{1 + m_{n,i}(x - x_i)}{\Delta x_i} \quad . \tag{2.64}$$

Instead of applying an asymptotic analysis to the IMC equations, Densmore constructs [25,

p. 1119] an equivalent model problem from the steady state Eq. (2.55),

$$\mu\frac{\partial I}{\partial x}+\sigma I=\frac{(1-f)\sigma_s}{2}\int_{-1}^{1}I(x,\mu')d\mu'+\frac{f\sigma_s}{2}\frac{1+m_i(x-x_i)}{\Delta x_i}\int_{x_{i-1/2}}^{x_{i+1/2}}\int_{-1}^{1}I(x',\mu')d\mu'dx'+\frac{q_e}{2}\quad, \tag{2.65}$$

where f represents the Fleck factor. Instead of dividing a physical absorption opacity into fictitious scattering and absorption opacities, Eq. (2.65) separates a physical scattering into fictitious scattering, absorption and discrete emission over the prescribed grid. But if $\sigma_s \rightarrow \sigma_a = \sigma$, then Eq. (2.65) is the steady state version of Eq. (2.62).

In the diffusive regime, $\sigma_s \approx \sigma >> \sigma_a = \sigma - \sigma_s$. The introductory derivation in Section 2.1.7 suggests mapping $\sigma \rightarrow \sigma/\epsilon$ and $\sigma_a \rightarrow \epsilon\sigma_a$ to renormalize the quantities σ, σ_s and σ_a to O(1). Additionally, the external source and speed of light are renormalized to O(1) with $q_e \rightarrow \epsilon q_e$ and $c \rightarrow c/\epsilon$ [25]. Densmore introduces these scaling into Eq. (2.65) and the Fleck factor. If $\beta_{n,i}$ and α are of O(1), then the Fleck factor [25],

$$f_{n,i}=\frac{\epsilon^2}{\epsilon^2+C_{n,i}\Delta t_n}\quad, \tag{2.66}$$

where $C_{n,i}$ is an O(1) quantity. Supposing $f_{n,i}=\sum_{j=0}^{\infty}f^{(j)}\epsilon^j$, the three scalings listed above then imply the following list in order:

1. if $\Delta t_n \sim$mean free time, $f_{n,i} \approx f^{(0)}$,
2. if $\Delta t_n \sim \min_{1\leq i\leq I}(\Delta x_i/c)$, $f_{n,i} \approx f^{(1)}\epsilon$ and $f^{(0)} = 0$,
3. if $\Delta t_n \sim$O(1), then $f_{n,i} \approx f^{(2)}\epsilon^2$ and $f^{(0)} = f^{(1)} = 0$,

where $f^{(0)}$, $f^{(1)}$ and $f^{(2)}$ are of O(1). Along with the other specified scalings in ϵ, the equations $f = \epsilon^j f^{(j)}$ for $j \in \{0, 1, 2\}$ are used in Eq. (2.65) to obtain recursive equations of angular and scalar flux [25] in the boundary layer and interior of each spatial cell. Like the analysis by Clouet and Samba, if the lowest order solution obeys a discrete form of the correct diffusion equation, or Eq. (2.50) with source q added to the right hand side, then the method is robust in the diffuse regime of transport problems.

The conclusion of the analysis is that for the piecewise-constant IMC thermal emission source, or equivalently $m_i = 0$ for all $i \in \{1 \ldots I\}$, only $f = \epsilon^2 f^{(2)}$ results in a discretization of the proper diffusion equation [25]. The small scaling of the Fleck factor for piecewise-constant emission sources implies fictitious scattering must dominate the emission process, which in turn indicates a lower bound on Δt for simulations that do not employ source tilting techniques. The observed consequence of not employing source tilting is teleportation error. We have not observed teleportation errors in simulations that directly solve the diffusion equation either stochastically or deterministically; this finding is supported by a remark from Adams [3], who indicates that obtaining the correct leading order diffusion behavior can be achieved by directly applying diffusion in optically thick regimes.

A high-level conclusion of Densmore's considerable analysis is that discontinuous source tilting, where the m_i slopes in Eq. (2.62) do not enforce continuity at cell edges, may furnish a transport solution that discretizes to the correct diffusion equation; source tilt slopes that are constructed accurately should not return absurd results. In Section 2.1.9, we conclude the source tilt, finite element, and asymptotic analysis discussion with a survey of the unifying work of Smedley-Stevenson and McClarren [93]. Instead of discontinuous tilt accuracy, following a rigorous analysis, they enforce absolute continuity at cell bounds.

2.1.9 Smedley-Stevenson and McClarren's Source Tilt Reconstruction

Smedley-Stevenson and McClarren propose continuous source tilting based on asymptotic analyses for thermal radiation transport schemes that have linear discontinuous representations of material *reconstructed from cell-centered temperatures*. Consequently, in contrast to the discontinuous finite element approach, the work presented in the article assumes there are not enough inherent degrees of freedom per spatial cell for the methods to produce good diffusion behavior unless a non-uniform subcell temperature profile is heuristically incorporated. This constraint is made so that the transport calculation only needs cell-centered quantities from a hydrodynamics calculation [93].

Both spatially continuous and spatially discrete transport are asymptotically analyzed. In both systems, the leading order diffusion equation has spurious sources, referred to as “jump terms,” that arise from cell edge temperature profile discontinuities. The analysis is in one dimensional, planar coordinates. Considering continuous transport with pure absorption and discrete material, the cell-centered energy balance, for a cell i, is written as [93]

$$\Delta x_i \left(C_{v,i} \frac{\partial T_i}{\partial t} + \frac{1}{c} \frac{\partial \phi_i}{\partial t} \right) = \int_{x_{i-1/2}}^{x_{i+1/2}} \int_{-1}^{1} \mu \frac{\partial I}{\partial x} d\mu \, dx = F(x_{i+1/2}) - F(x_{i-1/2}) \ , \tag{2.67}$$

where F is the radiation flux; it is the flux terms that give rise to jump terms after asymptotic analysis [93]. Smedley-Stevenson and McClarren neglect coupling from cells that are not adjacent to i in estimating $F(x_{i\pm 1/2})$. In the context of the analysis, this approach is supported by the more rigorous corner term system developed by Clouet and Samba [23]. Only coupling to adjacent cells, if i is on the interior of the problem domain, Eq. (2.67) is written as

$$\begin{aligned} \Delta x_i \left(C_{v,i} \frac{\partial T_i}{\partial t} + \frac{1}{c} \frac{\partial \phi_i}{\partial t} \right) = -\tau_i(\phi_{i,L} L_{i,L\to i-1} + \phi_{i,R} L_{i,R\to i-1}) + \\ \tau_{i+1}(\phi_{i+1,L} L_{i+1,L\to i} + \phi_{i+1,R} L_{i+1,R\to i}) - \tau_i(\phi_{i,L} L_{i,L\to i+1} + \phi_{i,R} L_{i,R\to i+1}) + \\ \tau_{i-1}(\phi_{i-1,L} L_{i-1,L\to i} + \phi_{i-1,R} L_{i-1,R\to i}) \ , \end{aligned} \tag{2.68}$$

where $\tau_i = \sigma_i \Delta x_i$ is both the absorption and total number of mean free paths across cell i,

$$\phi(x) = \phi_{i,L} \varphi_{i,1} + \phi_{i,R} \varphi_{i,2} \ , \tag{2.69}$$

the φ are defined in Eq. (2.35), $L_{i,L\to i-1} = L_{i,R\to i+1}$, $L_{i,L\to i+1} = L_{i,R\to i-1}$, and the L values are obtained solving the steady state equation with the linear source [93]. Thus, I is solved in terms of $\phi(x)$ as though $\phi(x)$ is a source in the Swarzchild-Milne problem [19, 93]. For $\tau_i \gg 1$,

$$L_{i,L\to i-1} = L_{i,R\to i+1} \approx \frac{1}{4\tau_i} - \frac{1}{6\tau_i^2} \ , \tag{2.70a}$$

$$L_{i,L\to i+1} = L_{i,R\to i-1} \approx \frac{1}{6\tau_i^2} \ . \tag{2.70b}$$

Incorporating Eq. (2.70) into Eq. (2.68),

$$\Delta x_i \left(C_{v,i} \frac{\partial T_i}{\partial t} + \frac{1}{c} \frac{\partial \phi_i}{\partial t} \right) = \frac{\phi_{i+1,L} - \phi_{i,R}}{4} - \frac{\phi_{i,L} - \phi_{i-1,R}}{4} + \frac{\phi_{i+1,R} - \phi_{i+1,L}}{6\tau_{i+1}} - \frac{\phi_{i,R} - \phi_{i,L}}{6\tau_i} - \frac{\phi_{i-1,R} - \phi_{i-1,L}}{6\tau_{i-1}} \ . \quad (2.71)$$

No small parameter, ϵ, was used to rescale terms in the transport and material equations. The first two terms on the right side of Eq. (2.71) are the non-physical jump terms. They appear to be artificial surface sources at cell edges. Enforcing continuity implies $\phi_{i,L} = \phi_{i-1,R}$ and $\phi_{i,R} = \phi_{i+1,L}$. Hence, regardless of the choice of source tilting procedure, if the source tilting procedure is continuous at cell edges, then the artificial sources in the leading order equilibrium diffusion equation always vanish. Equation (2.71) is then a physical discretization. The pure absorption approximation is meant to emulate the case where IMC has very resolved time steps [93]. When the time step is small enough, it follows that the IMC Fleck factor $f_n \approx 1$. A Fleck factor of 1 without physical scattering produces the purely absorbing, coupled transport equations. When time steps are small in IMC, teleportation error is generally seen to increase.

Smedley-Stevenson and McClarren also examine the case when effective scattering is significant. The formulae for the jump terms are somewhat more complicated, but ultimately as effective scattering increases, the jump terms diminish [93]. The result agrees with the notion that increasing time step sizes both increases effective scattering and decreases teleportation error in IMC. An increase in effective scattering implies more absorption and emission are modeled as instantaneous particle events where the information on absorption location at the sub-spatial-cell (subcell) level is conserved.

For the spatially discrete transport analysis, Smedley-Stevenson and McClarren rescale the equations with a small parameter, $\epsilon \ll 1$. For the discretized system, the result is similar to Eq. (2.71), with non-physical jump terms that vanish when continuity is enforced. The difference is that flux from $i \pm 2$ affects the solution for cell i [93]; this does not affect the non-physicality of the jump terms.

Continuous source tilting schemes are proposed, including:

- averaging over the discontinuous values, obtained from a standard linear discontinuous tilt, at cell edges, $\phi_{i,R} = \phi_{i+1,L} = (\phi_i + \phi_{i+1})/2 + (\Delta\phi_i - \Delta\phi_{i+1})/4$. This approach is seen to suffer from a "saw-tooth" instability where energy in adjacent cells can decouple [93],
- and sub-dividing the source tilt profile at an inflection point taken to be $\bar{x}_i = (x_{i-1/2} + x_{i+1/2})/2$ to have two subcell linear profiles.

With either continuous source tilting approach, the cell-average value implied by the subcell profile does not in general match the true cell-centered scalar intensity [93]. The tilt scheme described in the second item in the above list does not succumb to spurious saw-tooth oscillations and mitigates teleportation error [93].

As discussed by Adams [3], a discrete form of the diffusion equation can be solved directly in optically thick regions so long as care is taken to select the regions. Teleportation error, which results from the inability of a time-dependent transport scheme coupled to discrete sources to produce a correct diffusion solution, can be at least partially avoided when diffusion theory is applied in optically thick cells and small time steps. For the remainder of the IMC-DDMC review elaborated in this section, Section 2.1, we describe some diffusion transport hybrid schemes that form precursors to the method described in Chapter 3.

2.1.10 Random Walk in Diffusive IMC

Symbolic Implicit Monte Carlo eludes the effective scattering of IMC by simulating particle histories without numerical weights and then solving a system of equations for material state over a grid. An alternative to applying pure transport without any artificial scattering in diffuse regions is to apply pure transport with artificial scattering in thin regions and diffusion in thick regions. In optically thin regions, the effective scattering is not computationally taxing. For the regions where diffusion is applied, the solution should be accurate if there are enough mean free paths over a characteristic spatial cell length.

It seems Fleck and Canfield were among the first to devise a diffusion transport hybrid method that incorporates the random walk (RW) method for diffusion and IMC for transport [36]. Incidentally, Fleck and Canfield's article appears to be the first to mention the source tilting method, reviewed in preview sections. The version of pure IMC described is otherwise the same as the original method [36]. For random walk, a particle or packet propagates in a sequence of isotropic scattering events with effective scattering opacity $(1-f)\sigma_\nu$ [36]. If $\vec{r}(N_c)$ is the vector displacement of a particle, then for random walk [36]

$$\vec{r}(N_c) = \sum_{p=1}^{N_c} \vec{R}_p \ \ , \tag{2.72}$$

where the scattering collision path vectors, $\vec{R}_p$, are independent from one another [36]. With Eq. (2.72), the expected squared displacement is

$$\langle r^2(N_c) \rangle = N_c \langle R^2 \rangle \ \ , \tag{2.73}$$

where R is a characteristic distance between scattering events. For IMC, Fleck and Canfield find

$$\langle r^2 \rangle = \frac{2N_c}{(1-f)^2 \sigma_P \sigma_R} \ \ , \tag{2.74}$$

where σ_P and σ_R are Planck and Rosseland opacities, respectively, and the probability density function,

$$p_d(\vec{r}, t) = \frac{e^{-3r^2/2\langle r^2 \rangle}}{(2\pi \langle r^2 \rangle / 3)^{3/2}} \ \ . \tag{2.75}$$

The diffusion coefficient for RW was found to be $c/3(1-f)\sigma_R$ [36, p. 516]. A particle's location becomes the center of a sphere whose radius is determined by the nearest cell bound if it does not stream out of the domain. If the radius is R_0, then if $R_0 > 1/\sigma_R$ and $d_{\text{col}} = -\ln(\zeta)/(1-f)\sigma_P < R_0$, then the particle may be advanced randomly to a point a distance R_0 away. The solution of the diffusion equation can be used to compute a probability that the particle will travel a net distance R_0 before the end of the time step is reached [36, p. 518].

Particle weight is reduced with a multiplication factor [36]

$$\langle W \rangle = e^{(1-f)\ln(1-f)\sigma_P ct} \quad . \tag{2.76}$$

Random walk has been found to increase the speed of IMC where IMC uses optically thick cells. One unfortunate feature of RW is that particles in optically thick cells that are sufficiently close to a cell bound will not take large diffusion steps. This occurs since a sufficient diffusion radius would allow position updates to points past the cell boundary. Thus, these particles may rate-limit certain IMC-RW simulations.

2.1.11 N'Kaoua's Monte Carlo Coupling with Diffusion via Domain Decomposition

The leading order, nonlinear equilibrium diffusion equation can be obtained asymptotically using the prescription described at the beginning of Section 2.1.7 or in Densmore and Larsen's analysis of time-dependent thermal transport methods. The equation is [28]

$$\frac{\partial U_m}{\partial t} + \frac{1}{c}\frac{\partial \phi}{\partial t} = \nabla \cdot \frac{1}{3\sigma_R}\nabla\phi \quad , \tag{2.77}$$

where $\phi = caT^4$ is the correct limiting condition on the scalar flux [28], and σ_R is the grey Rosseland opacity defined by [75]

$$\frac{1}{\sigma_R(T)} = \left(\int_0^\infty \frac{\partial B_\nu}{\partial T}\,d\nu\right)^{-1} \int_0^\infty \frac{1}{\sigma_\nu(T)}\frac{\partial B_\nu}{\partial T}\,d\nu \quad . \tag{2.78}$$

The scalar flux solution of N'Kaoua's thermal SIMC equation has been shown to have the equilibrium condition under asymptotic scaling [28].

N'Kaoua performs an implicit finite difference of Eq. (2.77) to yield

$$U_{m,n+1} - U_{m,n} = \mathbf{D}\underline{\phi}_{n+1} \quad , \tag{2.79}$$

and uses the Marshak boundary condition to couple the transport and diffusion domains. The transport region of the discretized material energy balance has

$$U_{m,n+1} - U_{m,n} = \mathbf{M}\underline{\phi}_{n+1} + S \ . \tag{2.80}$$

The collision probability matrix including coupling matrices is [75, p. 517]

$$\begin{pmatrix} \mathbf{M} & \mathbf{C_1} \\ \mathbf{C_2} & \mathbf{D} \end{pmatrix} \ , \tag{2.81}$$

where $\mathbf{C_1}$ and $\mathbf{C_2}$ signify energy exchange between the SIMC transport region and the diffusion region. The diffusion component of Eq. (2.81) is deterministic [75].

The diffusion component can be both stochastic and discrete [40, 31]. Such an approach may be simpler to implement, since the description of the radiation field uses MC particles entirely. Discrete Diffusion Monte Carlo (DDMC) [31, 27, 2] or Implicit Monte Carlo Diffusion (IMD) [40, 22], are methods that simulate diffusion Monte Carlo particles with discrete events. The particle position is not tracked at the subcell level; thus the rate-limiting pathology associated with IMC-RW is avoided. Since the spatial propagation of DDMC and IMD are discrete, the sampling procedures somewhat resemble the residual Monte Carlo scheme elaborated in Chapter 1.

2.1.12 Discrete Diffusion Monte Carlo (DDMC)

Discrete Diffusion Monte Carlo (DDMC) is a Monte Carlo method for radiation diffusion that tracks particle histories in discrete steps over spatial cells [31]. DDMC is distinct from random walk in important ways. While also taking large steps in place of many physical or effective scattering events, random walk still resolves particle motion at the subcell level. Numerical results of Densmore et al. [27] indicate RW is less efficient than DDMC; this is supported by the theoretical differences in the construction of the methods. However, the formulae of DDMC are dependent on grid geometries; for certain grids, random walk may be more viable. In practical implementation, DDMC is often directly coupled to Implicit Monte Carlo to produce a method that yields accurate results for heterogeneous materials [31, 27, 30]. To accurately couple IMC to DDMC, Densmore et al. [31]

incorporate the asymptotic diffusion-limit boundary condition in order to better capture the effects of anisotropy of incident radiation on an optically thick domain.

As for IMC particles, the time variable of each DDMC packet is continuous [31]. In leaving time tracking continuous, DDMC avoids ambiguities in causality that may occur at the interface of a diffusion method that discretizes time and a fully continuous IMC region. A fully stochastic diffusion-transport hybrid allows for the radiation field to be treated entirely with particles. The Implicit Monte Carlo Diffusion (IMD) method developed by Gentile converts IMC particles to IMD particles by either transporting the IMC particle in the diffusive region until census is taken after which the particle is converted or allowing the particle to undergo several scattering events to thermalize with the neighboring material [40].

The theory underlying the asymptotic diffusion limit boundary condition is considerable. Habetler and Matkowski [44] appear to be the first to have derived the condition. Malvagi and Pomraning [67] generalize the analysis to include effects of surface curvature and opacity variation at the boundary. The derivation scheme for the boundary condition requires both asymptotics and singular eigenvalue theory to the linear transport equation. On the interior of the domain, the diffusion equation is the leading order description of radiation propagation, as summarized in section 2.1.7. The boundary layer, which is of the order of a mean free path into the diffusion domain [3], is treated as a distinct region from the interior. If boundary layer physics occurs in a ϵ-fraction of the domain distance, then a rescaling of the spatial variable is necessary to arrive at an appropriate equation set for the different asymptotic orders in the boundary layer. Making a change of variable $\tilde{y} = \tilde{x}/\epsilon$, setting the time derivative to zero in Eq. (2.45), and asymptotically expanding I in ϵ yields

$$\mu\frac{\partial I^{(j)}}{\partial \tilde{y}} + I^{(j)} = \frac{1}{2}\int_{-1}^{1} I^{(j)}\,d\mu \;\; \text{for } j = 0, 1 \;\; , \tag{2.82}$$

where we have made use of $\chi \approx 1+\chi^{(2)}\epsilon^2$. The index $j \in 0, 1$ unless otherwise stated. Considering a solution of the form $I^{(j)} = \phi_\lambda(\mu)e^{-\tilde{y}/\lambda}$ gives an integral equation for $\phi_\lambda(\mu)$,

$$\phi_\lambda(\mu) = \frac{\lambda/2}{\lambda-\mu}\int_{-1}^{1}\phi_\lambda(\mu')\,d\mu' \;\; . \tag{2.83}$$

For $\lambda \notin [-1, 1]$ if $\int_{-1}^{1} \phi_\lambda(\mu')d\mu' = 1$, then it follows

$$\frac{\lambda_\pm}{2} \ln\left(\frac{\lambda_\pm + 1}{\lambda_\pm - 1}\right) = \lambda_\pm \tanh^{-1}\left(\frac{1}{\lambda_\pm}\right) = 1 \quad , \tag{2.84}$$

where $\lambda_\pm$ are the two discrete eigenvalues that satisfy Eq. (2.84) [18]. For $\lambda \in [-1, 1]$, the integral in Eq. (2.83) contains a singularity. To satisfy the presumed normalization condition, the Cauchy principal value can be used to "tune" the eigenfunction for some λ. The principal value P of the integral over ϕ_λ is

$$P : \frac{\lambda}{2} \int_{-1}^{1} \frac{d\mu'}{\lambda - \mu'} = \frac{\lambda}{2} \int_{-1}^{1} P : \frac{1}{\lambda - \mu'} d\mu' = \lim_{\delta\lambda \to 0} \left(\ln\left(\frac{1+\lambda}{\delta\lambda}\right) + \ln\left(\frac{\delta\lambda}{1-\lambda}\right) \right) \quad . \tag{2.85}$$

For continuous eigenvalues λ, the angular eigenfunction can be expressed as [44, p. 849]

$$\phi_\lambda(\mu) = \frac{\lambda}{2} P : \frac{1}{\lambda - \mu} + \delta(\lambda - \mu)(1 - \lambda \tanh^{-1}(\lambda)) \quad . \tag{2.86}$$

With $\lambda_+ = -\lambda_- = \lambda_0$, Case proves the general solution to Eq. (2.82) must be [18]

$$I^{(j)}(x, \mu) = A_{\lambda_0,(j)} \phi_{\lambda_0} e^{-\tilde{y}/\lambda_0} + A_{-\lambda_0,(j)} \phi_{-\lambda_0} e^{\tilde{y}/\lambda_0} + \int_{-1}^{1} A_{(j)}(\lambda) \phi_\lambda e^{-\tilde{y}/\lambda} d\lambda \quad . \tag{2.87}$$

But by inspection of Eq. (2.82), a linear function in μ and $\tilde{y}$ is also a solution. $C_{(j)} + B_{(j)}(\tilde{y} - \mu)$ is such a solution and according to Habetler and Matkowski it must also represent the discrete portion of the eigenvalue spectrum [44]. So

$$I^{(j)}(x, \mu) = C_{(j)} + B_{(j)}(\tilde{y} - \mu) + \int_{-1}^{1} A_{(j)}(\lambda) \phi_\lambda e^{-\tilde{y}/\lambda} d\lambda \quad . \tag{2.88}$$

Assuming a left boundary condition that scales as a source $g(\mu) = \epsilon g^{(1)}(\mu)$, the $j = 1$ coefficients in Eq. (2.88) must satisfy

$$g^{(1)}(\mu) = C_{(1)} - B_{(1)}\mu + \int_{0}^{1} A_{(1)}(\lambda) \phi_\lambda(\mu) \, d\lambda \quad . \tag{2.89}$$

It would be conducive to determining $C_{(1)}$, $B_{(1)}$ and $A_{(1)}$ if there is a half space condition [44]

$$\int_0^1 \phi_\lambda(\mu)\gamma(\mu)d\mu = 0 \ \ \forall\lambda \in [0,1] \ \ , \tag{2.90}$$

where $\gamma(\mu)$ is a weight function that only depends on μ. It turns out there exist such a function [44]. So

$$\int_0^1 g^{(1)}(\mu)\gamma(\mu)\,d\mu = C_{(1)}\int_0^1 \gamma(\mu)\,d\mu + B_{(1)}\int_0^1 \gamma(\mu)\mu\,d\mu \ \ . \tag{2.91}$$

Case and Zweifel find

$$\gamma(\mu) = \frac{3}{2}\mu(1+\mu)e^{-\frac{1}{\pi}\int_0^1 \frac{1}{\mu'+\mu}\tan^{-1}\left(\frac{\pi\mu'/2}{1-\mu'\tanh^{-1}(\mu')}\right)d\mu'} \ \ , \tag{2.92}$$

where the form of $\gamma(\mu)$ comes from complex analysis of the eigenfunction properties for a semi-infinite medium. The integral coefficients of $C_{(1)}$ and $B_{(1)}$ are 1 and $\gamma_1 = 0.7104$, respectively. $C_{(1)}$ and $B_{(1)}$ can be found with asymptotic matching between the boundary layer and interior solutions. Recalling from section 2.1.7, the equation interior intensity near $\tilde{x} = 0$ to order ϵ is [44]

$$I(\tilde{x}) \approx I^{(0)}(\tilde{x}) + \epsilon\left(\frac{\phi^{(1)}}{2} - \mu\frac{\partial I^{(0)}}{\partial\tilde{x}}\right) \approx I^{(0)}(0) + \frac{\epsilon}{2}\left(\phi^{(1)} + (\tilde{y}-\mu)\frac{\partial\phi^{(0)}}{\partial\tilde{x}}\right) \ \ , \tag{2.93}$$

where a Taylor expansion of the leading order flux is performed and inserted into the order ϵ expression through the identity $\tilde{y} = \tilde{x}/\epsilon$. Taking $\tilde{y} \to \infty$ in Eq. (2.88) makes it clear that $2C_{(1)} = \phi^{(1)}$ and $2B_{(1)} = \partial\phi^{(0)}/\partial\tilde{x}$. Then

$$2\int_0^1 g^{(1)}(\mu)\gamma(\mu)\,d\mu = \phi^{(1)}(0) - \gamma_1 \left.\frac{\partial\phi^{(0)}}{\partial\tilde{x}}\right|_{\tilde{x}=0} \ \ . \tag{2.94}$$

Exchanging $\gamma(\mu)$ with $W(\mu)$, $g(\mu)$ with I_b gives the boundary condition for planar geometry in one dimension at $x = 0$ as it is expressed for DDMC,

$$2\int_0^1 W(\mu)I_b(\mu)d\mu = \phi(0) - \frac{\gamma_1}{\sigma}\left.\frac{\partial\phi}{\partial x}\right|_{x=0} \ \ . \tag{2.95}$$

For the Marshak condition, Eq. (2.52), $W(\mu)$ (or $\gamma(\mu)$) is approximated as 2μ. Hence the value of $\gamma_1 = 2\int_0^1 \mu^2 = 2/3$ for the Marshak boundary condition. The DDMC method sets $W(\mu) = \mu + 3\mu^2/2$ or $0.91\mu + 1.635\mu^2$ [31].

Equation (2.95) is the theoretical foundation for coupling IMC and DDMC across spatial boundaries. Densmore et al. [31] incorporate Eq. (2.95) into the discretization procedure of the governing DDMC equations. The governing equations for grey DDMC in planar geometry are [31]

$$\frac{1}{c}\frac{\partial \phi}{\partial t} + \frac{\partial}{\partial x}\frac{1}{3\sigma_n}\frac{\partial \phi}{\partial x} + f_n\sigma_n\phi = f_n\sigma_n acT^4 \quad , \tag{2.96a}$$

$$C_v\frac{\partial T}{\partial t} = \int_{-1}^{1} \sigma_n I \, d\mu - acT^4 \quad , \tag{2.96b}$$

where f_n has its usual meaning as the Fleck factor. Densmore et al. [31] proceed to discretize the equations for interior DDMC cells (optically thick cells surrounded entirely by other optically thick cells) [31],

$$\begin{aligned}\frac{1}{c}\frac{d\phi_i}{dt} + (\sigma_{L,i} + \sigma_{R,i} + f_{n,i}\sigma_{n,i})\phi_i = f_{n,i}\sigma_{n,i}acT^4_{n,i} + \\ \frac{1}{\Delta x_i}(\sigma_{L,i+1}\phi_{i+1}\Delta x_{i+1} + \sigma_{R,i-1}\phi_{i-1}\Delta x_{i-1}) \quad ,\end{aligned} \tag{2.97}$$

where $\sigma_{L,i}$ and $\sigma_{R,i}$ are the left and right "leakage opacities" for cell i given by [31]

$$\sigma_{L,i} = \frac{2}{3\Delta x_i}\frac{1}{\sigma^+_{n,i-1/2}\Delta x_i + \sigma^-_{n,i-1/2}\Delta x_{i-1}} \quad , \tag{2.98a}$$

$$\sigma_{R,i} = \frac{2}{3\Delta x_i}\frac{1}{\sigma^-_{n,i+1/2}\Delta x_i + \sigma^+_{n,i+1/2}\Delta x_{i+1}} \quad , \tag{2.98b}$$

where $\Delta x_i = x_{i+1/2} - x_{i-1/2}$ is a cell length and, except for temperature, the $+$ $(-)$ superscripting the opacities indicates that the opacity is calculated with material properties on the right (left) of the cell edge. The leakage opacities are obtained through discretizing Eq. (2.96) and quantify the likelihood a particle will leak left or right. If the DDMC region of the domain has I adjacent cells, Eq. (2.97) is valid over $i \in \{2 \ldots I-1\}$ [31]. To incorporate the boundary cells 1 or I, the leakage opacity corresponding to escaping the DDMC region and conversely the probability an IMC particle is admitted into the DDMC region are solved with the boundary condition. For $i = 1$, the DDMC equation is [31]

$$\begin{aligned}\frac{1}{c}\frac{d\phi_1}{dt} + (\sigma_{L,1} + \sigma_{R,1} + f_{n,1}\sigma_{n,1})\phi_1 = f_{n,i}\sigma_{n,i}acT_{n,i}^4 + \\ \frac{1}{\Delta x_i}(\sigma_{L,2}\phi_2\Delta x_2 + \int_0^1 P(\mu)\mu I_b\, d\mu) \quad , \quad (2.99)\end{aligned}$$

where

$$\sigma_{L,1} = \frac{1}{\Delta x_1}\frac{2}{3\sigma_{n,1}\Delta x_1 + 6\lambda} \quad , \quad (2.100a)$$

$$P(\mu) = \frac{4}{3\sigma_{n,1}\Delta x_1 + 6\lambda}\left(1 + \frac{3}{2}\mu\right) \quad . \quad (2.100b)$$

Densmore, Davidson, and Carrington [26] devise a more robust formula for $P(\mu)$ and $\sigma_{L,1}$ that considers emissivity at cell boundaries. The improved boundary condition produces more accurate solutions at the IMC-DDMC boundaries for optically thick interface cells [26, 31].

A grey DDMC particle either leaks from a cell or is absorbed. Consequently, the particle tracking routine does not need to update position or angle [31]. One can only resolve a DDMC particle location to what cell it inhabits between leakage events. While the position and direction of an IMC particle become unknown when it begins propagating via DDMC, the particle history time is kept continuous to ensure causality. Setting the right side of Eq. (2.97) to zero, the solution of the resulting equation can be thought of as a probability density that a particle will make it into a neighborhood of time dt about a time t without being absorbed or leaked. So the important time update is the time to the next collision, which Densmore writes as

$$\delta t_D = -\frac{1}{c}\frac{1}{\sigma_{L,i} + \sigma_{R,i} + f_{n,i}\sigma_{n,i}}\ln(\zeta) \quad , \quad (2.101)$$

where $\zeta \in [0, 1]$ is a uniformly sampled random variable [31]. If the value δt_D is less than the time to census for a particle it will sample either a leakage or absorption from a histogram distribution of the opacities.

For multiple simulations and tests, it has been observed that DDMC can provide orders of magnitude speed-up for problems in optically thick domains when compared to either the RW hybrid previously discussed or pure IMC [31]. The high efficiency of DDMC is partly due to the absence of effective scattering in the particle histories. The absence of effective scattering in grey DDMC is a result of integrating the transport equation in both angle and frequency; which causes the scattering terms in the transport equation to cancel. To expand the base of application for DDMC, it is desirable to develop a multi-frequency approach that is not significantly detrimental to the advantageous property of not having to simulate fictitious scattering directly.

2.1.13 Multi-group IMC Diffusion (IMD)

Multifrequency and multigroup radiation transport methods are needed to solve transport problems where particles compose a spectrum and interact with matter in a manner dependent on particle location in the spectrum. Diffusion methods provide a means of optimizing multifrequency radiation transport methods that solve problems with optically thick ranges of frequency in the spectrum. One such method was developed by Cleveland, Gentile and Palmer [22] as an extension to Gentile's IMD for LTE materials. Incorporating Fick's Law into the frequency-dependent IMC Eqs. (2.8) after angular integration gives (generalizing in dimensions) [22]

$$\frac{1}{c}\frac{\partial \phi_\nu}{\partial t} - \nabla\cdot\frac{1}{3\sigma_{\nu,n}}\nabla\phi_\nu + \sigma_{\nu,n}\phi_\nu = \frac{\sigma_{\nu,n}b_{\nu,n}}{\sigma_{P,n}}\int_0^\infty \sigma_{\nu',n}\phi_{\nu'}\,d\nu' + f_n\sigma_{\nu,n}b_{\nu,n}cU_{r,n} \quad , \tag{2.102a}$$

$$\frac{\partial U_m}{\partial t} = f_n\int_0^\infty \sigma_{\nu',n}\phi_{\nu'}d\nu' - f_n cU_{r,n} \quad , \tag{2.102b}$$

where physical scattering and external sources have been neglected. In frequency-dependent IMD as well as frequency-independent IMD, both the diffusion equation and the temperature equation are forward differenced in time,

$$\begin{aligned}\frac{1}{c}\frac{\phi_{\nu,n+1}-\phi_{\nu,n}}{\Delta t_n} - \nabla\cdot\frac{1}{3\sigma_{\nu,n}}\nabla\phi_{\nu,n+1} + \sigma_{\nu,n}\phi_{\nu,n+1} = \\ \frac{\sigma_{\nu,n}b_{\nu,n}}{\sigma_{P,n}}\int_0^\infty \sigma_{\nu',n}\phi_{\nu',n+1}\,d\nu' + f_n\sigma_{\nu,n}b_{\nu,n}cU_{r,n} \quad ,\end{aligned} \tag{2.103a}$$

$$\frac{U_{m,n+1}-U_{m,n}}{\Delta t_n} = f_n\int_0^\infty \sigma_{\nu',n}\phi_{\nu',n+1}d\nu' - f_n cU_{r,n} \quad . \tag{2.103b}$$

Following spatial discretization of the flux divergence term, Cleveland obtains a set of time step dependent coefficients of the scalar flux that can be interpreted as probabilities. The feature of time step size dependence of particle probabilities in IMD is not shared with DDMC. Another difference between IMD and DDMC is IMD's additional probability for census. In DDMC, the continuity of each particle's time implies a deterministic knowledge of the amount of time each particle has left in Δt_n.

2.1.14 Multi-frequency DDMC

Densmore [29, 30] extends grey DDMC to couple to multigroup or multifrequency IMC. Consequently, in addition to IMC-DDMC spatial interfaces [31], IMC particles may scatter or effectively scatter into DDMC groups or vice versa. A threshold or cutoff frequency is used in each spatial cell [30]. Under the cutoff frequency, grey DDMC is applied to the radiation with an additional leakage opacity for escaping the group and transitioning to IMC. If a DDMC particle effectively scatters out of the lower group, the particle scatters into some IMC frequency or group. The space and direction variables of the resulting IMC particle must be sampled. The derivation of the method is for arbitrary dimensions; a discretization is not specified so the equations are applicable to arbitrary spatial grids.

The scalings for light speed and heat capacity are $c \rightarrow c/\epsilon$ and $C_v \rightarrow \epsilon C_v$, respectively [30]. For opacity [30]

$$\sigma_\nu \rightarrow \begin{cases} \dfrac{\sigma_\nu}{\epsilon} \;, & \nu < \nu_c \;, \\ \epsilon^2\sigma_\nu \;, & \nu > \nu_c \;, \end{cases} \tag{2.104}$$

for some cut-off frequency, ν_c. Multiplying Eq. (2.104) by the normalized Planck function and integrating over all frequency, the Planck opacity is [30],

$$\sigma_P = \frac{1}{\epsilon}\sigma_P^{(-1)} + \epsilon^2 \sigma_P^{(2)} \quad , \tag{2.105}$$

where $\sigma_P^{(-1)} = \int_0^{\nu_c} \sigma_\nu b_\nu d\nu$, $\sigma_P^{(2)} = \int_{\nu_c}^{\infty} \sigma_\nu b_\nu d\nu$. The scalings of C_v, c, and Eq. (2.104), lead to the Fleck factor,

$$f_n = \epsilon^2 f_n^{(2)} + O(\epsilon^4) \quad , \tag{2.106}$$

where $f_n^{(2)}$ does not depend on ϵ. Incorporating the scalings into the transport equation with $\nu < \nu_c$, expanding intensity in orders of ϵ, and integrating over $\nu \in [0, \nu_c]$ and all solid directions, Densmore et al. [30] obtain a leading order diffusion equation,

$$\begin{aligned} \frac{1}{c}\frac{\partial \phi_G}{\partial t} - \nabla \cdot \frac{1}{\sigma_{R,n,G}} \nabla \phi_G + \left((1-\gamma_{n,G})(1-f_{n,G}) + f_n\right) \sigma_{P,n,G}\phi_G = \\ \gamma_{n,G} \int_{4\pi}\int_{\nu_c}^{\infty} (1-f_n)\sigma_{\nu,n} I_\nu d\nu d\Omega + \gamma_{n,G} f_n \sigma_{P,n} ac T_n^4 \quad , \end{aligned} \tag{2.107}$$

where quantities subscripted with G have been integrated over the lower frequency interval and

$$\sigma_{R,n,G} = \left(\int_0^{\nu_c} \frac{b_{\nu,n}}{\sigma_{\nu,n}} d\nu\right)^{-1} \int_0^{\nu_c} b_{\nu,n} d\nu \quad , \tag{2.108a}$$

$$\sigma_{P,n,G} = \left(\int_0^{\nu_c} b_{\nu,n} d\nu\right)^{-1} \int_0^{\nu_c} b_{\nu,n}\sigma_{\nu,n} d\nu \quad , \tag{2.108b}$$

$$\gamma_{n,G} = \frac{1}{\sigma_{P,n}} \int_0^{\nu_c} b_{\nu,n}\sigma_{\nu,n} d\nu \quad . \tag{2.108c}$$

For $\nu > \nu_c$, the opacity is small and the transport equation is

$$\begin{aligned} \frac{1}{c}\frac{\partial I_\nu}{\partial t} + \hat{\Omega}\cdot\nabla I_\nu + \sigma_{\nu,n} I_\nu = \frac{1}{4\pi}\frac{b_{\nu,n}\sigma_{\nu,n}}{\sigma_{P,n}} \int_{4\pi}\int_{\nu_c}^{\infty} (1-f_n)\sigma_{\nu',n} I_{\nu'}(\vec{r},\hat{\Omega}',t) d\nu' d\Omega' + \\ \frac{1}{4\pi}\frac{b_{\nu,n}\sigma_{\nu,n}}{\sigma_{P,n}} \sigma_{P,n,G}\phi_G + \frac{1}{4\pi}\frac{b_{\nu,n}\sigma_{\nu,n}}{\sigma_{P,n}} f_n \sigma_{P,n} ac T_n^4 \quad . \end{aligned} \tag{2.109}$$

The temperature equation couples material to both frequency domains,

$$C_v \frac{\partial T}{\partial t} = f_n \sigma_{P,n,G} \phi_G + \int_{4\pi} \int_{\nu_c}^{\infty} f_n \sigma_{\nu,n} I_\nu d\nu d\Omega - f_n \sigma_{P,n} a c T_n^4 \ . \tag{2.110}$$

The boundary condition between IMC and DDMC spatial regions depends on the threshold frequencies in the interfacing cells. The spatial boundary condition for radiation incident on the domain in the range $\nu \in [0, \nu_c]$ is found to be [30]

$$2 \int_{\hat{\Omega} \cdot \vec{n} < 0} \int_0^{\nu_c} W(|\hat{\Omega} \cdot \vec{n}|) I_{\nu,b} d\nu d\Omega = \phi_G + \frac{\lambda}{\sigma_{R,n,G}} \vec{n} \cdot \nabla \phi_G \ , \tag{2.111}$$

where $\vec{n}$ is a unit normal vector at a point on the surface. The DDMC equation is obtained from spatially discretizing Eq. (2.107) with a finite volume approach [30]. The last case of IMC-DDMC coupling presented by Densmore et al. [30] is that of a DDMC cell with one neighboring cell, i', that has a cutoff frequency, $\nu_c' < \nu_c$, and hence requires a composite leakage opacity, $\tilde{\sigma}_{i \to i'}$, that allows for leakage to the IMC portion or DDMC portion of the lower frequency interval. Additionally, the diffusion must be balanced by all possible sources; this includes IMC radiation in the range $\nu \in [\nu_c', \nu_c]$ that transmits through the cell edge shared by i and i', denoted $b(i, i')$. The frequency threshold in the remaining adjacent cells, i'', have the same frequency threshold. On an arbitrary spatial grid, the result is [30]

$$\begin{aligned}
\frac{1}{c} \frac{\partial \phi_{i,G}}{\partial t} + \left[\sum_{i'' \neq i'} \sigma_{i \to i''} + \tilde{\sigma}_{i \to i'} + (1 - \gamma_{n,i,G})(1 - f_{n,i}) \sigma_{P,n,i,G} + f_{n,i} \sigma_{P,n,i,G} \right] \phi_{i,G} \\
= \frac{1}{V_i} \sum_{i''} \sigma_{i'' \to i} \phi_{i'',G} V_{i''} + \frac{1}{V_i} \int_{A_{b(i,i')}} \int_{\nu_c'}^{\nu_c} P_{b(i,i')}(|\hat{\Omega} \cdot \vec{n}|) |\hat{\Omega} \cdot \vec{n}| I_\nu d\nu d\Omega d^2\vec{r} + \\
\frac{\gamma_{n,i,G}}{V_i} \int_{V_i} \int_{4\pi} \int_{\nu_c}^{\infty} (1 - f_{n,i}) \sigma_{\nu,n,i} I d\nu d\Omega d^3\vec{r} \ ,
\end{aligned} \tag{2.112}$$

where $\sigma_{i \to i''}$ are DDMC-to-DDMC leakage opacities,

$$\tilde{\sigma}_{i \to i'} = \frac{\int_0^{\nu_c'} b_{\nu,n,i} d\nu}{\int_0^{\nu_c} b_{\nu,n,i} d\nu} \sigma_{i \to i'} + \frac{\int_{\nu_c'}^{\nu_c} b_{\nu,n,i} d\nu}{\int_0^{\nu_c} b_{\nu,n,i} d\nu} \sigma_{b(i,i')} \ , \tag{2.113}$$

$\sigma_{b(i,i')}$ is the DDMC-to-IMC leakage opacities, V_i is the volume of cell i, $A_{b(i,i')}$ is the surface area shared between i and i', and $P_{b(i,i')}$ is the IMC-to-DDMC transition probability for i' to i [30]. Notwithstanding the use of only one cell to construct a mixed interface, Eqs. (2.112) and (2.113) prescribe a method for diffusion-transport over a domain with spatially varying threshold frequency. When a DDMC particle leaks according to $\tilde{\sigma}_{i\to i'}$, it can transmit to IMC with probability [30]

$$P_{\text{DDMC}\to\text{IMC}} = \frac{1}{\tilde{\sigma}_{i\to i'}} \frac{\int_{\nu_c'}^{\nu_c} b_{\nu,n,i} d\nu}{\int_0^{\nu_c} b_{\nu,n,i} d\nu} \sigma_{b(i,i')} \quad , \tag{2.114}$$

or remain a DDMC particle with probability

$$P_{\text{DDMC}\to\text{DDMC}} = \frac{1}{\tilde{\sigma}_{i\to i'}} \frac{\int_0^{\nu_c'} b_{\nu,n,i} d\nu}{\int_0^{\nu_c} b_{\nu,n,i} d\nu} \sigma_{i\to i'} \quad . \tag{2.115}$$

Numerical results for the hybrid multifrequency method of Densmore et al. [30] indicate significant speed-up relative to pure IMC for problems with opacity monotonically dependent on frequency and varying levels of optical thickness. The threshold frequency approach is implemented indirectly in a multigroup setting by lumping groups that have a number of mean free paths greater than or equal to a mean free path threshold per cell, τ_D. Densmore et al. [30] choose $\tau_D = 5$; this seems to be a reasonable number of mean free paths per cell to apply a discrete diffusion theory.

2.1.15 Abdikamalov's Velocity-dependent Multigroup IMC-DDMC

Abdikamalov et al. [2] develop an IMC-DDMC method for neutrino radiation transport. The particular application of interest is in core-collapse supernovae. The approach is multigroup, and the authors apply DDMC to a cell-group where there is a sufficient number of mean free paths; so the method permits DDMC to be applied in groups that are not adjacent to lower groups. In other words, the method permits DDMC to be applied to high frequency groups that have enough mean free paths per cell.

Neutrinos are fermions and have different types [2], so the material coupling is somewhat different than that of photons. Unlike photons, neutrinos have anti-neutrinos; these are included in the type index in Eqs. (2.116) and (2.117). In addition to affecting temperature, neutrinos can change the electron fraction, Y_e [2]. For each neutrino type, indexed by j, the material equations are [2]

$$\frac{\partial U_m}{\partial t} = \sum_j \int_{4\pi} \int_0^\infty \sigma_{\nu,a}(I_{j,\nu} - B_{j,\nu}) d\nu d\Omega + \sum_j S_j \ , \tag{2.116}$$

and

$$\rho N_A \frac{\partial Y_e}{\partial t} = \sum_j s_j \int_{4\pi} \int_0^\infty \frac{\sigma_{\nu,a}}{\nu}(I_{j,\nu} - B_{j,\nu}) d\nu d\Omega \ , \tag{2.117}$$

where $I_{j,\nu}$ is the angular intensity for neutrinos of type j with energy $h\nu$, $B_{j,\nu}$ is the Fermi-Dirac thermal emission function for Type j, N_A is Avogardro's number, ρ is material density, and s_j =1, -1, and 0 for electron neutrinos, electron anti-neutrinos, and any type of heavy neutrino [2]. Abdikamalov et al. [2] operator split the transport of the different neutrinos; thus the transport of the different neutrino species occurs independently of one another *within a time step*. Coupling of neutrino species occurs at material update. Using thermodynamic relations, the authors follow the temporal discretization procedure of Fleck and Cummings [37] but for neutrinos instead of photons. The "leptonic" Fleck factor is

$$f_n = \frac{1}{1 + \alpha c \Delta t_n \bar{\gamma}_F} \ , \tag{2.118}$$

where the bar variable heading indicates time-centering, $\bar{\gamma}_F = \bar{\beta}\bar{\sigma}_F + \bar{\xi} s_j \bar{\chi}_F$, σ_F is the "Fermi" opacity weighted by the normalized Fermi-Dirac function (analogous to the Planck opacity), χ_F is a Fermi-Dirac weighted integral of $\sigma_{\nu,a}/\nu$,

$$\beta = \frac{1}{C_v}\left(\frac{\partial U_r}{\partial T}\right)_{\rho,Y_e} \ , \tag{2.119}$$

U_r is the equilibrium neutrino energy density, and

$$\xi = \frac{1}{N_A \rho}\left[\left(\frac{\partial U_r}{\partial Y_e}\right)_{\rho,T} - \frac{1}{C_v}\left(\frac{\partial U_m}{\partial Y_e}\right)_{\rho,T}\left(\frac{\partial U_r}{\partial T}\right)_{\rho,Y_e}\right] \ . \tag{2.120}$$

We do not reproduce the derivation of Eqs. (2.119) and (2.120) here. The material update for temperature and electron number has terms corresponding to effective absorption, emission, and scattering [2]. Without physical scattering and external material sources, the neutrino IMC equations are

$$\frac{1}{c}\frac{\partial I_{j,\nu}}{\partial t} + \hat{\Omega}\cdot\nabla I_{j,\nu} + \bar{\sigma}_{\nu,a} I_{j,\nu} = \frac{1}{4\pi} c f_n \bar{\sigma}_{\nu,a} U_{r,n} b_{j,\nu} + \frac{1}{4\pi}\frac{(1-f_n)\sigma_{\nu,a} b_{j,\nu}}{\bar{\gamma}_F}\int_{4\pi}\int_0^{\infty}\frac{\bar{\sigma}_{\nu,a}}{\nu} I_{j,\nu}\, d\nu\, d\Omega \quad , \tag{2.121}$$

$$\frac{\partial U_m}{\partial t} = \sum_j \left[f_n \int_{4\pi}\int_0^{\infty} \bar{\sigma}_{\nu,a} I_j\, d\nu\, d\Omega - c f_n \bar{\sigma}_F U_{r,n} + \int_{4\pi}\int_0^{\infty}\left(\bar{\kappa}_{es,l} - \frac{\bar{\sigma}_F}{\chi_F}\bar{\chi}_{es,l}\right) I_{j,\nu}\, d\mu\, d\Omega \right] \quad , \tag{2.122}$$

and

$$\frac{\partial Y_e}{\partial t} = \frac{1}{\rho N_A}\sum_j s_j \left[f_n \int_{4\pi}\int_0^{\infty} \frac{\bar{\sigma}_{\nu,a}}{\nu} I_j\, d\nu\, d\Omega - c f_n \bar{\chi}_F U_{r,n} + \int_{4\pi}\int_0^{\infty}\left(\bar{\chi}_{es,e} - \frac{\bar{\chi}_F}{\sigma_F}\bar{\kappa}_{es,e}\right) I_{j,\nu}\, d\mu\, d\Omega \right] \quad , \tag{2.123}$$

where $\kappa_{es,l} = (1-f_n)\bar{\xi} s_i \bar{\chi}_F \sigma_{\nu,a}/\bar{\gamma}_F$, $\chi_{es,l} = (1-f_n)\bar{\xi} s_i \bar{\chi}_F \sigma_{\nu,a}/\nu\bar{\gamma}_F$, $\kappa_{es,e} = (1-f_n)\bar{\beta}\bar{\sigma}_F \sigma_{\nu,a}/\bar{\gamma}_F$, and $\kappa_{es,e} = (1-f_n)\bar{\beta}\bar{\sigma}_F\sigma_{\nu,a}/\nu\bar{\gamma}_F$, and $b_{j,\nu}$ is the normalized Fermi-Dirac distribution. The authors show the neutrino IMC equations conserve energy and lepton number [2].

The authors then formulate the multigroup DDMC scheme [2]. Apart from the time discretization, neutrinos transport similarly to photons. Hence, in optically thick regimes, neutrinos should obey a diffusion equation. In particular, incorporating Fick's Law into Eq. (2.121) and discretizing in space yields a DDMC equation with similar stochastic interpretations as for the photonic case [2]. The procedure is similar to prior DDMC publications but the discretization is over a spherically symmetric grid. Both IMC and DDMC are described for coupling with relativistic flow. For IMC, the process involves transporting particles in the lab frame and converting the properties into local fluid frames when collisions are sampled. For DDMC, the first order, O(U/c), relativistic diffusion equation is considered [19, p. 112]. The O(U/c) diffusion equation is discusses in the texts on radiation hydrodynamics by Mihalas and Weibel Mihalas [73] and Castor [19]. Abdikamalov et al. [2] operator split the equation into one for static diffusion,

$$\frac{1}{c}\frac{\partial \phi_{0,\nu_0}}{\partial t} + \nabla \cdot \vec{F}_{0,\nu_0} + \sigma_{0,\nu_0,a}\phi_{0,\nu_0} = f_n \sigma_{0,\nu_0,a} b_{j,0} U_{r,n} + (1-f_n)\frac{\sigma_{0,\nu_0,a} b_{j,0}}{\sigma_F}\int_0^\infty \sigma_{0,\nu_0',a}\phi_{0,\nu_0'} d\nu_0' \ , \tag{2.124}$$

$$\frac{1}{c}\frac{\partial \phi_{0,\nu_0}}{\partial t} + \frac{\nu_0}{3c}\frac{\partial \phi_{0,\nu_0}}{\partial \nu_0}\frac{D\ln(\rho)}{Dt} = 0 \ , \tag{2.125}$$

$$\frac{1}{c}\frac{\partial \phi_{0,\nu_0}}{\partial t} + \frac{1}{c}\nabla \cdot (\vec{U}\phi_{0,\nu_0}) \ , \tag{2.126}$$

where quantities subscripted with 0 here are evaluated in the comoving frame. Equation (2.124) can be solved with the static DDMC method described by Densmore et al. [31]. Equation (2.125) has the Doppler correction term [73, 19] and can be solved like an advection equation over frequency. Equation (2.126) can be solved by moving DDMC particles. The work presented in Chapter 3 follows this operator split DDMC procedure but for a Lagrangian "velocity grid" instead of Eulerian coordinates. Lagrangian and Eulerian hydrodynamic schemes are discussed by Castor [19, pp. 41–68]. Briefly, in Eulerian methods the grid is fixed and velocity is a property of the fluid solved for each spatial cell [19, p. 49]. In Lagrangian methods, the grid moves with the fluid; hence a constant mass can be ascribed to cells and the evolution of the fluid may be tracked with respect to a mass coordinate [19, p. 49]. In the Lagrangian frame, between transport steps, IMC particles have to move while DDMC particle positions remain unchanged.

2.2 Type Ia Supernovae Review

We briefly review pertinent literature for radiation transport in astrophysical settings with particular emphasis on Type Ia supernovae (SNe Ia). This portion of the literature review is intended to provide a summary of explosion mechanisms/calculations and radiation transport methods/ codes for SNe Ia. It is not an exhaustive survey of all research associated with SNe Ia or supernovae in general.

Type Ia supernovae have historically been difficult to simulate. Incorporation and resolution of different physical features may be demanding to codes that are not optimized for the problem.

2.2.1 Type Ia Explosion Model Summary

Type Ia supernovae have seen extensive application as “standard candles” to calculate the local expansion rate of the Universe (see, e.g. [90, 81]). SNe Ia are useful objects for distance determination due to the homogeneity in their luminosity. Furthermore, intrinsic differences in the peak luminosity of many observed SNe Ia are correlated with the duration of the event; thus the duration of the event can be used to find the intrinsic luminosity [84]. However, some events are intrinsically subluminous [9, 52].

The observed luminosity is referred to as an “apparent magnitude” while the distance-independent, intrinsic luminosity is referred to as an “absolute magnitude.” Branch [9] indicates the absolute magnitude can be obtained either from the correlations of the event properties or by using “Cepheid-based” distances to the galaxies hosting the SN Ia. Cepheids are pulsating stars that have a relationship between luminosity and period [74].

Nearby events have been observed by the Calán/Tololo survey; these supernovae are used as calibration for more distant and more redshifted events [10, 52] as well as further resolution on the value of the Hubble constant [9, 52]. The Supernovae Cosmology Project [81] and the High-z Supernova Search Team [90] have collected data at higher redshift, or further back in time, to conclude there is an energy pervading the universe that manifests as negative pressure [52]. This conclusion was drawn by both teams since the distant supernovae were systematically dimmer than they should have been without accelerating expansion.

There are several approaches to fitting the supernovae to correlated families; a simple parameter obtained by Phillips [84] is the change in magnitude over 15 days starting from peak luminosity. The steeper the decline in luminosity over the 15 day span, the dimmer the intrinsic light of the Type Ia event; moreover, the correlation is roughly linear [84]. Perlmutter [82] applies a stretch parameter to fit SNe Ia to a template light curve; the stretched apparent magnitude and the absolute magnitude template allow for a determination of distance. The supernovae that fit the parameter families, roughly $\sim 85\%$ according to Hillebrandt and Niemeyer [52] fall into this “normal” category, are believed to satisfy the correlations by explosion strength.

The luminous events are believed to originate from the thermonuclear explosions of carbon-oxygen (C-O) white dwarf stars that are near the Chandrasekhar mass, ~ 1.4 $M_\odot$ [52]. Hillebrandt and Niemeyer [52] provides a summary of the history of observations of SNe Ia. Briefly, it was realized around the middle of the twentieth century that supernovae could be classified by the absence, "Type I," or presence, "Type II," of hydrogen lines in the observed spectrum [10, 52]. Subsequently, events without hydrogen and with a strong singly-ionized silicon (Si II) line in the spectra were designated a subclass of Type I, denoted Type Ia [52]. SNe Ia also have lines of Ca II, S II, neutral oxygen (O I), and Mg II around maximum light [9]. Forbidden line emissions from iron and cobalt ions are observable some time after peak luminosity [9].

Type Ia supernovae are thought to have two phases, the initial explosion involving significant C-O fusion, and a subsequent ballistic phase where radioactive ^{56}Ni generates gamma rays that thermalize with the fluid to generate visible light. According to Hillebrandt, observation constraints on the progenitor system must be made indirectly; white dwarf stars are not supposedly very luminous relative to other progenitor systems [52]. Given the absence of prominent hydrogen features in the spectrum, the explosion must not contain more than roughly 0.1 $M_\odot$ of hydrogen. The peak velocities of the ejecta are inferred from properties of the spectrum to be on the order of 10,000 to 30,000 km/s [76, 52]. The radii of the progenitors are thought to be less than or approximately equal to 10,000 km [52]. In the explosion, roughly half a solar mass of radioactive ^{56}Ni is thought to be generated in the ejecta [52]. White dwarf progenitors are thought to accrete mass from a companion in a binary system [52].

Explosions can be modelled with numerical methods in codes; the results can then be coupled to radiation transport codes as initial conditions. Equations to solve include conservation of mass, momentum, energy, and some equation of state (EOS) along with effects of chemical composition, gravitational binding, and viscosity [52]. The `FLASH` code [38, 16] applies adaptive mesh refinement to solve reactive hydrodynamics problems; the code has been used for high energy density experiment validation and astrophysics. The `FLASH` code solves nuclear deflagration and detonation in neutron stars and white dwarfs [38]. The modularity and use of Message-Passing Interface (MPI) in the code makes it capable of solving multiple physics problems with a range of complexity [38]. In the hydrodynamics section of the paper by Fryxell et al. the listed governing equations are [38]

$$\frac{\partial \rho}{\partial t} + \nabla \cdot (\rho \vec{U}) = 0 \ , \tag{2.127a}$$

$$\frac{\partial \rho \vec{U}}{\partial t} + \nabla \cdot (\rho \vec{U} \vec{U}^T) + \nabla P = \rho \tilde{\mathbf{g}} \ , \tag{2.127b}$$

$$\frac{\partial}{\partial t}\left(\rho e + \frac{1}{2}\rho U^2\right) + \nabla \cdot \left(\rho \vec{U}(e + P/\rho) + \frac{1}{2}\rho \vec{U} U^2\right) = \rho \vec{U} \cdot \tilde{\mathbf{g}} \ , \tag{2.127c}$$

$$P = \left(\frac{C_p}{C_v} - 1\right)\rho e \ , \tag{2.127d}$$

$$\frac{\partial X_j}{\partial t} + \nabla \cdot (\rho X_j \vec{U}) = 0 \ , \tag{2.127e}$$

$$\sum_j X_j = 1 \ , \tag{2.127f}$$

where Eq. (2.127a) is the mass conservation equation from Eq. (1.28a) from Chapter 1, Eqs. (2.127b) and (2.127c) are momentum and energy equations similar to those in Eq. (1.28) but with a gravitational acceleration $\tilde{\mathbf{g}}$ instead of acceleration due to radiation momentum deposition. Equation (2.127d) is the EOS for an ideal gas, where C_p is the heat capacity at constant pressure. The last two subequations characterize the advection and conservation of the different mass fractions, where ρX_j is the partial density for species j [38]. The `FLASH` code solves Eqs. (2.127) with a high-order version of the Godunov method, where discontinuities in fluid properties between adjacent spatial cells are solved with the Riemann shock problem [19, pp. 52–56]. The reconstruction of properties at cell interfaces is more sophisticated than simply applying cell average values at the discontinuity locations [38]; in particular, the Piecewise Parabolic Method (PPM) of Colella and Woodward [24] along with additional algorithmic constraints is implemented. Seitenzahl et al. [92] apply a PPM hydrodynamic solver to explore different delayed-detonation models for SNe Ia.

Hillebrandt [52] summarizes the possible explosion mechanisms. Provided here is an outline of some of the mechanisms [52]:

1. Chandrasekhar Mass Models: the majority of observed normal SNe Ia are assumed to be exploding C-O white dwarves at around 1.4 $M_\odot$.

    (a) Prompt detonation: the thermonuclear combustion commences as a detonation wave.

    The resulting nuclei are around the atomic mass of iron and there is not a significant amount of mass elements below Ni, Co, and Fe in atomic mass [52].

    (b) Pure turbulent deflagration: instabilities in the fusion burn wave induce turbulence that either is quenched or eventually leads to a supersonic wave. Models indicate that fast deflagration, yet subsonic, deflagration waves may be sufficient in producing the compositions observed in the spectra [76, 52]. The most successful 1D deflagration model is the W7 model described by Nomoto et al. [76].

    (c) Delayed detonation: a subsonic nuclear fusion front may transition to a supersonic wave. The deflagration phase "pre-expands" the star and the detonation to supersonic burn velocity produces the high-velocity, intermediate-mass elements [52].

2. Sub-Chandrasekhar Mass Models: the white dwarf accretes a helium layer from the companion star; the He layer detonates and drives a shock into the white dwarf which, in turn, ultimately induces a carbon detonation [52]. Sub-Chandrasekhar mass models are potential explanations for subluminous SNe Ia [52].

3. Merging White Dwarfs: due to gravitational wave emission, companion white dwarfs are, in principle, capable of merging into a "double-degenerate" explosion [52]. Such an explosion mechanism would explain the absence of H lines in the observed spectra [52]. However, it is also possible the binary system collapses to form a neutron star [52].

To have candidacy as a progenitor for Type Ia supernovae, a mechanism must satisfy the constraints outlined in Section 1.2.1; at least this must be the case for the normal SNe Ia. We now turn to a review of the ballistic phase of Type Ia supernovae, where radiation transport occurs in a setting with millions of lines that requires relativistic corrections [54]. In Section 2.2.2, the analytic diffusion model developed by Pinto and Eastman [85] that allows for study of basic effects of explosion structure on luminosity is reviewed. In Sections 2.2.3, 2.2.4, and 2.2.5, the deterministic SN Ia code `PHOENIX`, the SN Ia MC codes `SEDONA` and `ARTIS` are discussed. These codes illustrate approaches to overcome certain difficulties associated with accurately modelling radiation transport over the diverse material specifications of SNe Ia.

2.2.2 Pinto and Eastman Grey Type Ia SN Model

Pinto and Eastman [85] developed an analytic solution for the Type Ia supernova problem for grey absorption. The computed light curves are similar to those of more expensive calculations [85]. The analytic model provides evidence for the luminosity-duration correlations being partly attributable to differing masses [85].

According to the authors, on the time scale the fluid evolves, it is permissible to remove time and velocity dependent terms from the first moment, comoving transport equation [85]; this leaves Fick's law. The diffusion equation is non-dimensionalized and separation of variables is used in a manner that reflects the nature of Type Ia supernovae. With given gamma ray source deposition profiles, the problem is recast as an eigenvalue problem in the separated variables.

The article provides a calibrated, grey opacity for the analytic solution [85],

$$\sigma_0 = 0.13\rho \ , \tag{2.128}$$

where the opacity, σ_0, is in cm^{-1}. The thermal kinetic energy equation is [85]

$$\rho e_{\text{kin}} = \frac{3\rho N_A}{2A}(l+1)kT \sim 0.4\left(\frac{\rho}{10^{-12}}\right)\left(\frac{A}{56}\right)\left(\frac{T}{2\times10^4}\right) \ , \tag{2.129}$$

where A is the mean mass per nucleon, l is the average ionization, e_{kin} is in erg/g, T is in K, and ρ is in g/cm^3.

2.2.3 PHOENIX Code

The `PHOENIX` code [46, 47, 48, 98] is a deterministic, one dimensional, radiation transport code. Recently, it was extended to calculate gas temperature in a manner that is consistent with the radiation field [98]. To do so, a new method of *radiation energy balance* is introduced that does not depend on numerically unstable radiation-matter heating and cooling rates [98].

The transport method of `PHOENIX` is based on the short characteristic method of Olson and Kunasz [78] and implemented for fully relativistic, spherically symmetric transport by Hauschildt and Baron [47]. Hauschildt and Baron present the scalar intensity in an integral form as equal to a Λ operator operating on sources due to scattering and emission in the comoving frame [47],

$$\phi_{0,\nu_0} = c\Lambda_{\nu_0} S_{0,\nu_0} \quad , \tag{2.130}$$

where S_ν is the source function due to scattering or emission. Since S_{0,ν_0} depends on ϕ_{0,ν_0}, iteration can be used to obtain ϕ_{0,ν_0} from Eq. (2.130). The form of S_{0,ν_0} considered is

$$cS_{0,\nu_0} = (1-\varepsilon)\phi_{0,\nu_0} + \varepsilon B_{0,\nu_0} \quad , \tag{2.131}$$

where ε is a thermal coupling parameter and B_{ν_0} is the Planck function [47]. It turns out the largest eigenvalue for the Λ_{ν_0} matrix is close to 1 for optically thick, highly scattering problems [47], so fixed point iteration is a poor choice for certain problems. Consequently, the Λ_{ν_0} operator is operator split to give [47]

$$\phi_{0,\nu_0,*} = c\Lambda_{\nu_0} S_{0,\nu_0,\text{old}} \quad , \tag{2.132a}$$

$$(1 - c\Lambda^*_{\nu_0}(1-\varepsilon))\phi_{0,\nu_0,\text{new}} = \phi_{0,\nu_0,*} - c\Lambda^*_{\nu_0}(1-\varepsilon)\phi_{0,\nu_0,\text{old}} \quad , \tag{2.132b}$$

where the new operator, Λ^*, may be constructed to yield iterations with faster convergence [78, 47].

For a homologous outflow, van Rossum constructs a “target flux” equation,

$$r^2 F_{0,\nu_0,tg} = \int_0^r \left(-\frac{\rho r^2}{c}\frac{\partial}{\partial t}\frac{\phi_{0,\nu_0}}{\rho} - \frac{r^2}{ct}\phi_{0,\nu_0} + \frac{r^2 \rho\varepsilon}{4\pi} \right) \quad , \tag{2.133}$$

where spherically symmetric coordinates have been used and $F_{0,\nu_0,tg}$ is along the radial direction. The radiation energy balance uses the difference between the target flux and actual flux to approximate temperature corrections and converge iteratively [98]. The temperature iteration scheme is found to require 3 to 10 iterations [98].

2.2.4 SEDONA Code

Kasen et al. [54] have developed a three dimensional Monte Carlo code for time-dependent radiation transport in supernovae. The transport scheme incorporates polarization into the calculation as well. The three dimensionality allows for the code to be applied to aspherical progenitor systems. Similar to the `PHOENIX` code, the 3D MC transport code, called `SEDONA`, solves radiation transport for homologous outflow. The structure of the transport code is enumerated in a list [54]:

1. A 3D gamma ray transfer routine calculates energy deposition.
2. Opacities are computed.
3. Optical photon particles are transported and tallied.
4. A material temperature is computed by setting thermal emission rates per cell equal to the tallied absorption for both gamma photons and optical photons.
5. Opacities must be recomputed and the optical photon transfer is redone.
6. Spectra and light curves (LCs) are obtained from the converged result.

Apart from homologous expansion, the Solobev approximation [19, pp. 122-130] is applied to treat line transfer. The Solobev approximation assumes the frequency derivative of the intensity is much larger than the space and time derivatives. Such a condition occurs when there exist bound-bound transitions that have narrow line width, in velocity, compared to changes in other ejecta properties [19, 54]. With the narrow line assumption, the Solobev equation is [19, p. 124]

$$-\frac{1}{c}\hat{\Omega}_0 \cdot \nabla\vec{U} \cdot \hat{\Omega}_0 \nu_0 \frac{\partial I_{0,\nu_0}}{\partial \nu_0} = \frac{q_{0,\nu_0}}{4\pi} - \sigma_{0,\nu_0} I_{0,\nu_0} \ , \tag{2.134}$$

where quantities subscripted with 0 are evaluated in the comoving frame. For one line, or two levels, the opacity has the form [54]

$$\sigma_{0,\nu_0} = \frac{\pi \mathrm{e}^2}{m_\mathrm{e}} f_{lu} N_l \frac{c}{\nu_0^2} \left(1 - \frac{N_u g_l}{N_l g_u}\right) \Xi(\nu_0) = K_{lu} \Xi(\nu_0) \ , \tag{2.135}$$

where e is electron charge, m_{e} is electron mass, l (u) is the lower (upper) population state, f_{lu} is the oscillator strength [19, p. 157], N_l (N_u) is the number density of the lower (upper) atomic state, g_l (g_u) is the statistical weight of the lower (upper) atomic state, and Ξ is the line profile. Equations (2.134) and (2.135) can be used to obtain the Solobev optical depth [19, p. 125],

$$\tau_S = \frac{K_{lu}\nu_0}{|\hat{\Omega}_0 \cdot \nabla\vec{U} \cdot \hat{\Omega}_0|} \ \ , \tag{2.136}$$

which for homologous expansion simplifies to [54]

$$\tau_S = K_{lu}t\nu_0 \ \ , \tag{2.137}$$

where t is the time since the initial explosion, or the expansion time. If a particle streams to a line center, then the probability the photon bundle will interact with the line is $1 - e^{-\tau_s}$ [54]. If a line interaction occurs, the interacting particle can either be scattered, absorbed, or fluoresce; at least these are the interactions the authors consider [54].

To track MC particles over the grid, Kasen exploits the homologous relationship between velocity and space. Since the velocity field does not change from the Lagrangian perspective, particles are tracked with “velocity distances.” There is velocity distance to line centers, velocity distance to continuum interactions, velocity distance to census, and velocity distance to cell boundary [54].

To incorporate polarization, each particle has a Stokes vector that is normalized to a magnitude of one [19, p. 218]. Thus the approach allows for coherence and coherent scattering of the radiation field.

2.2.5 ARTIS Code

Similar to `SEDONA`, the `ARTIS` code described by Kromer and Sim [56] also performs Monte Carlo radiation transport in three dimensions. The code is based on the approach to astrophysical transport described by Lucy [66] and applies the Solobev approximation along with the assumption of homologous outflow. The authors map the explosion ejecta to a 3D Cartesian grid and material properties are taken to be piecewise constant [56]. The code does not introduce free parameters;

in other words, the calculation is from first principles [56]. The authors use the “macro-atom” approach of Lucy [66] to treat atomic internal energy. According to Kromer and Sim, the macro-atom approach allows for generalized treatment of radiation-matter interactions.

The calculation at early stages of the supernovae is sped up with a grey approximation [56]. Similar to DDMC, the activation of the grey scheme is determined by a threshold optical depth; the optical depth is threshold is for Thomson scattering. The optimization produces a factor of ~ 10 speed-up for the calculations considered by the authors [56].

To demonstrate the applicability of the `ARTIS` code to asymmetric progenitor systems, the authors implement an ellipsoidal toy model [56]. With the total mass and composition adopted from the W7 model, the ellipsoid model has the maximum velocities along the minor axes set to half the maximum velocity in the direction of the major axis. In this asymmetric model, the luminosity down the minor axis is significantly higher than the luminosity down the major axis [56]. Thus, the toy model asymmetry has a non-trivial effect on the emitted light.

3 SuperNu: A Radiative Transfer Code for Type Ia Supernovae

In this chapter, theoretical and practical aspects of a radiative-transfer code, `SuperNu`, for thermonuclear supernovae, are described. As in the literature review, time steps are indexed with $n \in \{1 \dots N\}$, space and velocity cells are indexed with $i \in \{1 \dots I\}$, and frequency groups are indexed with $g \in \{1 \dots G\}$. Depending on the nature of the group, group indexes may be subscripted to indicate type or a sub-index for the set $\{1 \dots G\}$.

3.1 IMC-DDMC Method

Here, we describe the novel features of an IMC-DDMC method for high-velocity, homologous, Lagrangian coordinates. The discussion of the theory and algorithms closely follow the articles of Wollaeger et al. [104] and Wollaeger and van Rossum [103].

The method described is similar to that of Abdikamalov et al. [2] for neutrino transport in core collapse supernovae discussed in Section 2.1.15. In contrast to the work of [2], velocity is treated linearly at the spatial subcell level and IMC particles are tracked with velocity distances [54] (see Section 2.2.4); the grid is Lagrangian and distinct advection schemes are required; only first-order relativistic corrections are applied to IMC and DDMC processes; methods for non-uniform group structuring are provided; asymptotic analyses are employed to obtain a boundary condition for high-velocity interfaces and to motivate a Doppler shift method; and an algorithm for collapsing non-contiguous groups of sufficient optical thickness in DDMC is implemented and tested [104, 103].

From Sections 1.1 and 1.1.1, the radiative-transfer and fluid equations are

$$\frac{1}{c}\frac{\partial I_\nu}{\partial t} + \hat{\Omega}\cdot\nabla I_\nu + \sigma_{\nu,a}I_\nu = \sigma_{\nu,a}B_\nu - \sigma_{\nu,s}I_\nu + \int_{4\pi}\int_0^\infty \frac{\nu}{\nu'}\sigma_s(\vec{r},\nu'\to\nu,\hat{\Omega}'\to\hat{\Omega})I_{\nu'}(\vec{r},\hat{\Omega}',t)d\nu' d\Omega' \quad , \tag{3.1}$$

$$\frac{\partial\rho}{\partial t} + \nabla\cdot(\rho\vec{U}) = 0 \quad , \tag{3.2}$$

$$\frac{\partial(\rho\vec{U})}{\partial t} + \nabla\cdot(\rho\vec{U}\vec{U}) + \nabla P = -\vec{g} \quad , \tag{3.3}$$

and

$$\frac{\partial}{\partial t}\left(\rho e + \frac{1}{2}\rho U^2\right) + \nabla\cdot\left(\rho\vec{U}(e+P/\rho) + \frac{1}{2}\rho\vec{U}U^2\right) = -g^{(0)} \quad , \tag{3.4}$$

where $\vec{r}$ is the spatial coordinate, $\hat{\Omega}$ is a unit direction, t is time, ν is frequency, c is the speed of light, I_ν is the radiation intensity, and B_ν is the lab frame thermal emission. The variables e, ρ, $\vec{U}$, and P are the specific internal energy, density, velocity, and pressure of the fluid in the lab frame, or with respect to one inertial frame of reference. We have dropped the transpose superscript, T, from the Kronecker product of vectors used in Chapter 1. If no operational symbol is present between vectors, then a Kronecker product is assumed; for instance, $\vec{U}\vec{U}$ is a matrix consisting of each product between any two elements of $\vec{U}$. The 4-vector $(g^{(0)}, \vec{g})$ is the radiation energy-momentum coupling [19, p. 109] discussed in Section 1.1.1. If the fluid is static, then $B_\nu(\hat{\Omega}) = B_{0,\nu_0}$ is the Planck function [86, p. 156]. Relativistically induced anisotropy, as described by Pomraning [86], is assumed in Eq. (3.1). Following Castor [19, pp. 5-10], the Lagrangian form of Eq. (3.4) is written as

$$\rho\frac{De}{Dt} + P\nabla\cdot\vec{U} = -g^{(0)} \quad , \tag{3.5}$$

where the operator $D/Dt = \partial/\partial t + \vec{U}\cdot\nabla$. In a homologous outflow, $\nabla\cdot\vec{U} = 3/t_n$ where t_n is the fluid expansion time. The ratio of the rate of adiabatic, ideal gas cooling to the thermal radiation deposition rate is approximately $\Lambda = \frac{3N_A k}{M_A a T^3}\frac{\rho/c\sigma_P}{t_n}$ where N_A, k, M_A, T, and σ_P are Avogadro's number, Boltzmann's constant, molar mass, temperature, and Planck opacity, respectively [54]. For an outflow of Nickel with $T = 12{,}000$ K, $\sigma_P = 0.1\rho$ cm^{-1}, and $t_n = 10$ days, the ratio is approximately $\Lambda \approx 1.3\times 10^{-7}$. As Kasen et al. [54] argue, Λ remains small over the times of interest in light curve and spectra observation for SNe Ia. For all velocity-dependent calculations considered, the value Λ will be very small. So for the remainder of the analysis, the gas pressure, and hence the adiabatic cooling rate, $P\nabla\cdot\vec{U}$, is neglected. Pinto and Eastman [85] provide supporting arguments for this approximation in the context of SNe Ia as well. We also make the assumption of homologous outflow as in the codes `PHOENIX` [98], `SEDONA` [54], and `ARTIS` [56]; these codes are briefly reviewed in Section 2.2. The homologous outflow equation for the coordinates are [54]

$$\vec{r} = \vec{U}t \approx \vec{U}t_n \quad , \tag{3.6}$$

where the approximate equality assumes the transport time and expansion time both start at the same initial time value and time step size is not detrimentally large. The Lagrangian momentum equation is [19, p. 9]

$$\rho\frac{D\vec{U}}{Dt} + \nabla P = -\vec{g} \quad . \tag{3.7}$$

Because P is neglected and the of Eq. (3.6) implies $D\vec{U}/Dt = 0$, Eq. (3.7) implies that the momentum coupling vector, $\vec{g} \approx 0$. A negligible momentum coupling vector agrees with the analysis of Pinto and Eastman [85]. The time-component of the momentum 4-vector, $g_0^{(0)} = g^{(0)} - \vec{U}\cdot\vec{g}/c^2$; this implies the comoving radiation-matter coupling term, $g_0^{(0)}$, can reasonably replace the lab frame term, $g^{(0)}$, in the Lagrangian-coordinate material energy equation, Eq. (3.5). If C_v is the heat capacity at constant volume for a fluid parcel, then Eq. (3.5) may be written as

$$\begin{aligned} C_v\frac{DT}{Dt} = -g_0^{(0)} = -g_{0,a}^{(0)} - g_{0,s}^{(0)} = \int_{4\pi}\int_0^\infty \sigma_{0,\nu_0,a}(I_{0,\nu_0} - B_{0,\nu_0})d\nu_0 d\Omega_0 \\ + \int_{4\pi}\int_0^\infty \sigma_{0,\nu_0,s} I_{0,\nu_0} d\nu_0 d\Omega_0 - \\ \int_{4\pi}\int_0^\infty\int_{4\pi}\int_0^\infty \frac{\nu_0}{\nu_0'}\sigma_{0,s}(\vec{r},\nu_0' \to \nu_0, \hat{\Omega}_0'\cdot\hat{\Omega}_0) I_{0,\nu_0'} d\nu_0' d\Omega_0' d\nu_0 d\Omega_0 \quad , \end{aligned} \tag{3.8}$$

where the coupling due to inelastic scattering, $g_{0,s}^{(0)}$ has been written in the form presented by Szőke and Brooks [96]. The total scattering opacity is dependent on the differential scattering opacity,

$$\sigma_{0,\nu_0,s} = \int_{4\pi}\int_0^\infty \sigma_{0,s}(\vec{r},\nu_0 \to \nu_0', \hat{\Omega}_0\cdot\hat{\Omega}_0') d\nu_0' d\Omega_0' \quad . \tag{3.9}$$

3.1.1 Multigroup Velocity Space IMC

Equation (3.8) is amenable to the IMC temporal discretization [37] or the more recent discretization procedures of Gentile [42], McClarren and Urbatsch [71], or Abdikamalov et al. [2]. For each possibility, the coupling term in Eq. (3.8) is in the comoving frame while Eq. (3.1) is in the lab frame. The resulting comoving IMC equations, in differential form, are

$$C_v \frac{DT}{Dt} = f_n \left(\int_{4\pi} \int_0^{\infty} \sigma_{0,\nu_0,a,n} I_{0,\nu_0} d\nu_0 d\Omega_0 - \sigma_{P,n} a c T_n^4 \right) - g_{0,s}^{(0)} \tag{3.10}$$

and

$$\begin{aligned}\left(1 + \hat{\Omega}_0 \cdot \frac{\vec{U}}{c}\right) \frac{1}{c} \frac{DI_{0,\nu_0}}{Dt} + \hat{\Omega}_0 \cdot \nabla I_{0,\nu_0} - \frac{\nu_0}{c} \hat{\Omega}_0 \cdot \nabla \vec{U} \cdot \nabla_{\nu_0 \hat{\Omega}_0} I_{0,\nu_0} + \frac{3}{c} \hat{\Omega}_0 \cdot \nabla \vec{U} \cdot \hat{\Omega}_0 I_{0,\nu_0} \\ + (\sigma_{0,\nu_0,s,n} + \sigma_{0,\nu_0,a,n}) I_{0,\nu_0} = \frac{f_n}{4\pi} \sigma_{0,\nu_0,a,n} b_{0,\nu_0,n} a c T_n^4 \\ + \frac{b_{0,\nu_0,n} \sigma_{0,\nu_0,a,n}}{4\pi \sigma_{P,n}} (1 - f_n) \int_{4\pi} \int_0^{\infty} \sigma_{0,\nu_0',a,n} I_{0,\nu_0'} d\nu_0' d\Omega_0' \\ + \int_{4\pi} \int_0^{\infty} \frac{\nu_0}{\nu_0'} \sigma_{0,s,n}(\vec{r}, \nu_0' \to \nu_0, \hat{\Omega}_0' \cdot \hat{\Omega}_0) I_{0,\nu_0'} d\nu_0' d\Omega_0' \quad ,\end{aligned} \tag{3.11}$$

where the integer subscript n denotes quantities evaluated at the beginning of a time step. The expansion time, t_n, is also the time at the beginning of the time step, n. The radiation-matter coupling by inelastic scattering, $g_{0,s}^{(0)}$, has been excluded from the IMC temporal discretization. In Eqs. (3.10) and (3.11), the opacities are evaluated in the comoving frame. The value b_{0,ν_0} is the frequency-normalized Planck function in the comoving frame, and the Fleck factor f_n [37], as derived by Fleck and Cummings, is

$$f_n = \frac{1}{1 + \alpha \beta_n \sigma_{P,n} c \Delta t_n} \quad . \tag{3.12}$$

Thus, the algebraic form of the Fleck factor, with the assumptions given, is the same as the static grid form. Later in Section 3.1, a compressed derivation of the Gentile-Fleck factor (see Section 2.1.3) is presented and optimized for the code. The Lagrangian time step size, Δt_n, is constrained to be the same as the Eulerian time step size; only one time step is used for the outflow calculations. The expansion time $t_n = t_1 + \sum_{n'=1}^{n-1} \Delta t_{n'}$. The comoving differential effective scattering opacity, $(1 - f_n) \frac{b_{0,\nu_0,n} \sigma_{0,\nu_0,a,n} \sigma_{0,\nu_0',a,n} \nu_0'}{4\pi \sigma_{P,n} \nu_0}$, is separable in ν_0 and ν_0'. Consequently the new frequency of a photon undergoing effective scattering is probabilistically independent of the old frequency [73,

p. 327].

The fully relativistic form of Eq. (3.11) could be obtained by a similar procedure. However, depending on the intended simulations, the assumptions used to obtain the material coupling, and consequently Eq. (3.12), may no longer hold. Here, only first order relativistic effects are considered; higher order effects can be implemented in MC codes [2]. The typical maximum outflow speed of SNe Ia is approximately $U_{\max} = 30,000$ km/s, so $(U_{\max}/c)^2 \approx 0.01$.

Equation (3.12) implies Monte Carlo particles effectively scatter in the comoving frame in the same manner as they do for static material transport. Thus the process of transforming particles from the lab frame into the comoving frame, resampling particle properties according to local fluid properties and transforming the particle properties back into the lab frame applies to both physical and effective scattering [2]. Neglecting all terms of order U^2/c^2 or higher, the frequency and direction transformations are [19, p. 103]

$$\nu = \nu_0 \left(1 + \frac{\hat{\Omega}_0 \cdot \vec{U}}{c} \right) \quad , \tag{3.13}$$

which accounts for Doppler shift in IMC, and

$$\hat{\Omega} = \frac{\hat{\Omega}_0 + \vec{U}/c}{1 + \hat{\Omega}_0 \cdot \vec{U}/c} \quad , \tag{3.14}$$

which accounts for aberration in IMC, respectively [66]. According to The radiation hydrodynamics texts by Pomraning [86, p. 156] and Castor [19, p. 104], the opacity in the lab frame is

$$\sigma_\nu = \frac{\nu_0}{\nu} \sigma_{0,\nu_0} = \left(1 - \hat{\Omega} \cdot \frac{\vec{U}}{c} \right) \sigma_{0,\nu_0} \quad . \tag{3.15}$$

The second equality in Eq. (3.15) allows for a frequency independent transformation of grouped opacities.

Following Kasen [54], MC particles are tracked in velocity space. Thus, the grid itself is logically unchanging and velocity acts as a Lagrangian coordinate. IMC particles translate "velocity distances," denoted with a lower case u. Corresponding to the physical distances in standard IMC [37], there is a velocity to a cell boundary u_b, a velocity to collision u_{col}, and a velocity distance to census at the end of a time step u_{cen}. To continuously Doppler shift IMC particles in the presence of a frequency grid, a distance to Doppler shift between groups is incorporated, u_{Dop} [104]. This distance is analogous to a distance to a spatial boundary, but requires the presence of a spatially nonuniform velocity field. Using Eq. (3.6), the velocity to a boundary can be calculated with the same formula as the physical distance and is consequently dependent on grid geometry. To write the formulae for Doppler shift and boundary distances, the group index, g, and spatial index, i, are introduced. The frequency grid is treated as an invariant in the comoving frame; thus each fluid parcel has the same local group structure. If fluid parcel 1 is moving relative to fluid parcel 2, then parcel 2 would not appear to have the same group structure from the perspective of parcel 1. The velocity distances are

$$u_{\text{col}} = \frac{-\ln(\xi)}{t_n(1-\hat{\Omega}_p\cdot\vec{U}_p/c)\sigma_{0,\nu_{0,p},n}} \quad , \tag{3.16}$$

$$u_{\text{cen}} = c\left(\frac{t_n+\Delta t_n - t_p}{t_n}\right) \quad , \tag{3.17}$$

$$u_b = \begin{cases} |(U_{i-1/2}^2-(1-\mu_p^2)U_p^2)^{1/2}+\mu_p U_p| & \text{if } \mu_p < -\sqrt{1-(U_{i-1/2}/U_p)^2} \quad , \\ \\ (U_{i+1/2}^2-(1-\mu_p^2)U_p^2)^{1/2}-\mu_p U_p & \text{otherwise} \quad , \end{cases} \tag{3.18}$$

and

$$u_{\text{Dop}} = c\left(1-\frac{\nu_{g+1/2}}{\nu_p}\right)-\vec{U}_p\cdot\hat{\Omega}_p \quad , \tag{3.19}$$

where ν_p, $\nu_{0,p}$, t_p, $\vec{U}_p$, and $\hat{\Omega}_p$ are the lab frequency, comoving frequency, time, velocity position, and lab direction of particle p, respectively. In Eq. (3.16), $\xi \in (0,1]$ is a uniformly sampled random variable. Additionally, $\mu_p = \hat{\Omega}_p \cdot \vec{U}/|\vec{U}|$. Equation (3.18) is the distance to boundary formula for a 1D spherical grid; this is the chosen grid for the numerical results that follow. For a geometry in which the inner most cell has $U_{1/2}=0$, the second case in Eq. (3.18) must be applied for the innermost cell, $i=1$, and $\mu_p \in [-1,1]$. Equation (3.19) is obtained from conserving lab frame frequency while having comoving frequency shift from $\nu_{0,p}$ down to $\nu_{g+1/2}$. Frequency (wavelength) is taken to decrease (increase) with increasing g. Effective absorption can be alternatively calculated with implicit capture [62, p. 332]. If implicit capture is used to reduce statistical noise in the tallies, the velocity distance to effective scattering of particle p [37] is

$$u_{\text{col}} = \frac{-\ln(\xi)}{t_n(1-\hat{\Omega}_p\cdot\vec{U}_p/c)(1-f_n)\sigma_{0,\nu_{0,p},a,n}} \quad . \tag{3.20}$$

The energy of a particle in the lab frame is reduced by $E_p \to E_p e^{-f_n\sigma_{\nu_p,a,n}ut_n}$.

IMC particle position in velocity space must be updated to have its physical position unchanged. The censused position is maintained with

$$\vec{U}_{p,\text{new cen}}(t_n+\Delta t_n) = \vec{U}_{p,\text{old cen}}t_n = \vec{r}_{p,\text{cen}} \quad , \tag{3.21}$$

where $\vec{U}_{p,\text{old cen}}$ is particle velocity position after transport, $\vec{U}_{p,\text{new cen}}$ is the final censused velocity position after completion of the time step, and $\vec{r}_{p,\text{cen}}$ is the IMC particle position at the end of a time step. The value, $\vec{U}_{p,\text{new cen}}$, is the IMC particle velocity location at the beginning of the $n+1$ time step. Equation (3.21) does not have to be solved directly. We introduce a time centering parameter, $\alpha_2 \in [0,1]$, to split the velocity position shift before and after transport. The following enumeration summarizes the steps taken in IMC velocity position shift:

1. $\vec{U}_{p,*\,\text{cen}}(t_n+\alpha_2\Delta t_n) = \vec{U}_{p,\text{old cen}}t_n$.
2. IMC: $\vec{U}_{p,*\,\text{cen}} \to \vec{U}_{p,*}$.
3. $\vec{U}_{p,\text{new cen}}(t_n+\Delta t_n) = \vec{U}_{p,*}(t_n+\alpha_2\Delta t_n)$,

where $\vec{U}_{p,*\,\text{cen}}$ is the intermediate velocity position after completion of IMC transport.

The opacity dependence on frequency is assumed to be piecewise constant and constant within group intervals, $\nu_0 \in [\nu_{g+1/2}, \nu_{g-1/2}]$, for all groups, $g \in \{1\ldots G_i\}$, for all cells $i \in \{1\ldots I\}$, where G subscripted with i allows for different cells to have different total numbers of groups. For

$\nu_0 \in [\nu_{g+1/2}, \nu_{g-1/2}]$,

$$\sigma_{0,\nu_0,a,n} = \sigma_{a,g,n} \quad , \tag{3.22a}$$

$$\sigma_{0,\nu_0,s,n} = \sigma_{s,g,n} \quad , \tag{3.22b}$$

where $\sigma_{a,g,n}$ ($\sigma_{s,g,n}$) is the comoving absorption (scattering) opacity that is constant for each group, g, over comoving frequency, ν_0. Integrating the comoving IMC transport equation over the comoving frequency range of group g in cell i,

$$\begin{aligned}\left(1+\hat{\Omega}_0\cdot\frac{\vec{U}}{c}\right)\frac{1}{c}\frac{DI_{0,g}}{Dt} + \hat{\Omega}_0\cdot\nabla I_{0,g} + \frac{4}{c}\hat{\Omega}_0\cdot\nabla\vec{U}\cdot\hat{\Omega}_0 I_{0,g} - \frac{1}{c}\hat{\Omega}_0\cdot\nabla\vec{U}\cdot(\mathbf{I}-\hat{\Omega}_0\hat{\Omega}_0)\cdot\nabla_{\hat{\Omega}_0} I_{0,g} \\ - \frac{1}{c}\hat{\Omega}_0\cdot\nabla\vec{U}\cdot\hat{\Omega}_0\left(\nu_{g-1/2}I_{0,\nu_{g-1/2}} - \nu_{g+1/2}I_{0,\nu_{g+1/2}}\right) + (\sigma_{s,g,n}+\sigma_{a,g,n})I_{0,g} = \\ \frac{f_n}{4\pi}\sigma_{a,g,n}b_{0,g,n}acT_n^4 + \frac{b_{0,g,n}\sigma_{a,g,n}}{4\pi\sigma_{P,n}}(1-f_n)\sum_{g'=1}^{G_i}\int_{4\pi}\sigma_{a,g',n}I_{0,g'}d\Omega'_0 \\ + \sum_{g'=1}^{G_i}\int_{4\pi}\int_{\nu_{g+1/2}}^{\nu_{g-1/2}}\int_{\nu_{g'+1/2}}^{\nu_{g'-1/2}}\frac{\nu_0}{\nu'_0}\sigma_{0,s,n}(\vec{r},\nu'_0\to\nu_0,\hat{\Omega}'_0\cdot\hat{\Omega}_0)I_{0,\nu'_0}d\nu'_0 d\nu_0 d\Omega'_0 \quad ,\end{aligned} \tag{3.23}$$

where

$$I_{0,g} = \int_{\nu_{g+1/2}}^{\nu_{g-1/2}} I_{0,\nu_0}d\nu_0 \quad , \tag{3.24a}$$

$$b_{0,g,n} = \int_{\nu_{g+1/2}}^{\nu_{g-1/2}} b_{0,\nu_0,n}d\nu_0 = \int_{\nu_{g+1/2}}^{\nu_{g-1/2}} b_{0,\nu_0}(T_n)d\nu_0 \quad , \tag{3.24b}$$

and $\mathbf{I}$ is the identity matrix. Equation (3.23) makes use of Castor's division of the Doppler and aberration corrections from the photon momentum gradient. The term with $I_{0,\nu_{g\pm1/2}}$ on the left side of Eq. (3.23) indicates that Doppler shifting will cause MC particles to leak between groups. Considering Eq. (3.6), $\hat{\Omega}_0\cdot\nabla\cdot\hat{\Omega}_0 = 1/t_n$; in this case the Doppler shift coefficients of $I_{0,\nu_{g\pm1/2}}$ are isotropic. If $\vec{U}$ is constant in space, $\nabla\vec{U} = 0$, and the Doppler and aberration corrections vanish; in this case, all the fluid parcels are in the same reference frame, so streaming across the fluid flow does not induce change in comoving direction and frequency.

IMC (and DDMC) particles are generated each time step if there is a source. For IMC particles generated by thermal emission, we apply a standard, linear tilt in equilibrium radiation energy density, or T_n^4, to mitigate teleportation error [72]. Numerical teleportation error and source tilting are reviewed in Sections 2.1.5, 2.1.8, and 2.1.5. Tracking IMC particles in the lab frame and transforming into the comoving frame for all radiation-matter interactions is a means of solving Eq. (3.23). Otherwise, Eq. (3.23) may be solved directly with Monte Carlo; the additional velocity-dependent terms must then be explicitly accounted for in the particle processes.

Before turning to IMC-DDMC, we present a brief derivation of the Gentile-Fleck factor and, with the grey form of the maximum principle of Larsen and Mercier [60], provide some justification for its use in SN Ia simulations. The multigroup form of Eq. (3.8) is

$$C_v \frac{DT}{Dt} = \sum_{g=1}^{G} \int_{4\pi} \sigma_{a,g} I_{0,g} d\Omega_0 - c\sigma_P a T^4 - g_{0,s}^{(0)} \quad . \tag{3.25}$$

Defining

$$E_* = \frac{1}{c\Delta t_n \bar{\sigma}_P} \int_{t_n}^{t_{n+1}} \sum_{g=1}^{G} \int_{4\pi} \sigma_{a,g} I_{0,g} d\Omega_0 dt \quad , \tag{3.26}$$

where $\bar{\sigma}_P$ is time centered, Equation (3.25) may be stated as

$$\frac{1}{\sigma_P \tilde{\beta}} \frac{D}{Dt}[\sigma_P(aT^4 - E_*)] = \sum_{g=1}^{G} \int_{4\pi} \sigma_{a,g} I_{0,g} d\Omega_0 - c\sigma_P a T^4 - g_{0,s}^{(0)} \quad , \tag{3.27}$$

where

$$\tilde{\beta} = \frac{1}{C_v} \left[4aT^3 + (aT^4 - E_*) \frac{1}{\sigma_P} \frac{\partial \sigma_P}{\partial T} \right] \quad . \tag{3.28}$$

Evaluating $\sigma_P \tilde{\beta}$ on the left hand side of Eq. (3.27) at the beginning of a time step, integrating Eq. (3.27) with respect to time, setting $\int_{t_n}^{t_{n+1}} \sigma_P a T^4 = \Delta t_n[\alpha \sigma_{P,n+1} a T_{n+1}^4 + (1-\alpha)\sigma_{P,n} a T_n^4]$, setting $\bar{\sigma}_P = \alpha \sigma_{P,n+1} + (1-\alpha)\sigma_{P,n}$, and setting $\Lambda_{a,n} = \sigma_{P,n}(aT_n^4 - E_*)$ give

$$\Lambda_{a,n+1} - \Lambda_{a,n} = c\Delta t_n \sigma_{P,n} \tilde{\beta}_n \left(-\alpha \Lambda_{a,n+1} - (1-\alpha)\Lambda_{a,n} - \bar{g}_{0,s}^{(0)} \right) \quad . \tag{3.29}$$

From Section 2.1.3, the Gentile-Fleck factor is defined as [42]

$$\tilde{f}_n = \frac{1}{1+\alpha\tilde{\beta}_n c\Delta_t \sigma_{P,n}} \quad , \tag{3.30}$$

where g_n has been substituted with $\tilde{f}_n$ for clarity. The time centered emission term is found to be

$$\alpha\sigma_{P,n+1}aT_{n+1}^4 + (1-\alpha)\sigma_{P,n}aT_n^4 = \\ \tilde{f}_n\sigma_{P,n}aT_n^4 - (1-\tilde{f}_n)\bar{g}_{0,s}^{(0)} + \bar{\sigma}_P\left(1-\frac{\sigma_{P,n}}{\bar{\sigma}_P}\tilde{f}_n\right)E_* \quad . \tag{3.31}$$

The next simplification is $\sigma_{P,n}/\bar{\sigma}_P$ in the last term on the right hand side of Eq. (3.31). The procedure may then follow the standard IMC derivation. To ensure $f_n \geq \tilde{f}_n \geq 0$, the approximation of Gentile [42], described in Section 2.1.3, for $\tilde{f}_n$ is incorporated (see Eq. (2.20)). For certain transport problems, such as the W7 SN Ia problem of Nomoto [76], calculating the derivative of the opacity with respect to temperature is computationally expensive since two opacity calculations are required. In our implementation, we compute the opacity twice using the initial temperature and an offset temperature at the first time step, $n = 1$; then for $n > 1$,

$$\frac{\partial\sigma_{P,n}}{\partial T} \approx \frac{\sigma_{P,n} - (\rho_n/\rho_{n-1})\sigma_{P,n-1}}{T_n - T_{n-1}} \quad . \tag{3.32}$$

In Eq. (3.32), if there is no change to the microscopic opacity but density changes, then the derivative vanishes. Consequently, the effect of expansion alone is not coupled into the calculation of the Gentile-Fleck factor.

The maximum principle of Larsen and Mercier [60] can provide some indication of whether it is possible to have temperature instabilities or overheating in an SN Ia simulation. For $\sigma_P/\rho = 0.13$ cm^2/g, $C_v/\rho = 2.0 \times 10^7$ erg/K/g, $T_U = 100000$ K, and $T_L = 10000$ K, the grey maximum principle gives $\Delta t_n \leq 0.6$ milliseconds. For a range of input near the values considered, the maximum principle predicts sufficient time steps that are very small for LTE SN Ia simulations. However, as Wollaber et al. [101] demonstrate, the over-heating pathology in IMC is also dependent on the spatial grid. In general, the continuous-space maximum principle is not necessary to achieve physical radiative-transfer results. In practice, for the W7 SN Ia model, we use quarter-day time steps sizes.

3.1.2 Asymptotic Analysis for Space and Group Boundaries

Coupling IMC and DDMC in a high-velocity grid requires some consideration of asymptotic diffusion theory. In this section, an attempt is made to motivate development of:

1. a treatment of IMC particles at high-velocity spatial method interfaces,
2. a treatment of DDMC particle Doppler shift that emulates continuous Doppler shift corrections.

1. We start with the first item in the enumeration above and see how a high-velocity interface cell edge affects the asymptotic diffusion-limit boundary condition at the cell edge. The following asymptotic analysis is based on a prescription by Malvagi and Pomraning for incorporating curvature and opacity variations into the asymptotic diffusion-limit boundary condition [67] and is extracted from the IMC-DDMC paper by Wollaeger et al. [104]. The grey O(U/c) radiative transfer equation is considered,

$$\frac{1}{c}\frac{\partial I_0}{\partial t}+\hat{\Omega}_0\cdot\nabla I_0+\sigma_{t,0}I_0+\frac{\vec{U}}{c}\cdot\nabla I_0-\frac{1}{c}\hat{\Omega}_0\cdot\nabla\vec{U}\cdot(\mathbf{I}-\hat{\Omega}_0\hat{\Omega}_0)\cdot\nabla_{\hat{\Omega}_0}I_0+\frac{4}{c}\hat{\Omega}_0\cdot\nabla\vec{U}\cdot\hat{\Omega}_0 I_0=j_0 \ \ , \tag{3.33}$$

where $I_0 = \int_0^\infty I_{0,\nu_0}d\nu_0$, j_0 is the total frequency integrated source due to scattering events and emission and $\sigma_{t,0} = \sigma_{s,0} + \sigma_{a,0}$ is a total opacity. Supposing there exists some spatial surface denoted by b, we now make use of the homologous outflow assumption to obtain

$$\frac{1}{c}\frac{\partial I_0}{\partial t} + \mu\frac{\partial I_0}{\partial z} + \mathcal{L}I_0 + (\hat{\Omega}_0\cdot\nabla)_\perp I_0 + \sigma_{t,0}I_0 + \frac{\vec{r}}{ct_f}\cdot\nabla I_0 + \frac{4}{ct_f}I_0 = j_0 \ \ , \tag{3.34}$$

where μ is the projection of the comoving angle onto an axis z aligned orthogonal to a plane tangent to surface b, the linear operator $\mathcal{L}$ accounts for the change in the directional derivative, $\hat{\Omega}_0\cdot\nabla$, due to non-trivial coordinate curvature, $(\hat{\Omega}_0\cdot\nabla)_\perp$ is the projection of the directional derivative orthogonal to z [67], and the "fluid time" $t_f = t_n$ upon implementation. The expansion of the streaming operator is taken from Malvagi and Pomraning. The next step is to postulate a parameter $\varepsilon \ll 1$ that is the ratio of mean free path length to domain length [44]. We choose to scale the variables with respect to ε as follows:

$$c \to c/\varepsilon \ , \tag{3.35a}$$

$$\sigma_{t,0} \to \sigma_{t,0}/\varepsilon \ , \tag{3.35b}$$

$$\sigma_{a,0} \to \varepsilon\sigma_{a,0} \ , \tag{3.35c}$$

$$t_f \to t_f/\varepsilon \ , \tag{3.35d}$$

$$\vec{r}_b \to \vec{r}_b/\varepsilon \ , \tag{3.35e}$$

$$s = z/\varepsilon \ , \tag{3.35f}$$

$$\vec{U}(\vec{r}, t_f) \approx \vec{U}(\vec{r}_b, t_f) \ , \tag{3.35g}$$

where $\vec{r}_b$ is a location on surface b and the rescaling in Eq. (3.35) permits treating the parameters as O(1). In terms of ε, the surface coordinate and characteristic fluid time are large in Eqs. (3.35d) and (3.35e). If $\hat{r}_b$ and $\hat{z}$ are unit vectors of the surface coordinate and z, respectively, then incorporating Eq. (3.35) into Eq. (3.34) gives

$$\frac{\varepsilon^2}{c}\frac{\partial I_0}{\partial t} + \left[\mu + \varepsilon(\hat{r}_b \cdot \hat{z})\frac{r_b}{ct_f}\right]\frac{\partial I_0}{\partial s} + \varepsilon\left[\mathcal{L} + \varepsilon\frac{r_b}{ct_f}\mathcal{L}_{\hat{r}}\right]I_0 + \\ \varepsilon\left[(\hat{\Omega}_0 \cdot \nabla)_\perp + \varepsilon\frac{r_b}{ct_f}(\hat{r}_b \cdot \nabla)_\perp\right]I_0 + \sigma_{t,0}I_0 + \frac{4\varepsilon^2}{ct_f}I_0 = \varepsilon j_0 \tag{3.36}$$

and

$$j_0 = \left(\frac{\sigma_{t,0}}{\varepsilon} + \varepsilon\sigma_{a,0}\right)\frac{1}{4\pi}\int_{4\pi} I_0 d\Omega_0 + \varepsilon q \ , \tag{3.37}$$

where q is external or thermal sources, $r_b = |\vec{r}_b|$, and the opacities have been assumed isotropic. We have defined $\hat{r}_b \cdot \nabla = (\hat{r}_b \cdot \hat{z})\partial/\partial z + (\hat{r}_b \cdot \nabla)_\perp + \mathcal{L}_{\hat{r}}$ as a means of tracking the change with respect to the ballistic fluid trajectories through curved coordinates in a fashion analogous to the streaming term for photon trajectories. At least for spherical symmetry, Eq. (3.35e) implies $\mathcal{L} \to \varepsilon\mathcal{L}$, or spatial curvature has a small effect. Incorporating Eq. (3.37) into Eq. (3.36) and grouping O(ε^2) terms on the right hand side,

$$\left[\mu + \varepsilon(\hat{r}_b \cdot \hat{z})\frac{r_b}{ct_f}\right]\frac{\partial I_0}{\partial s} + \varepsilon\mathcal{L}I_0 + \varepsilon(\hat{\Omega}_0 \cdot \nabla)_\perp I_0 + \sigma_{t,0}I_0 = \frac{\sigma_{t,0}}{4\pi}\int_{4\pi} I_0 d\Omega_0' + O(\varepsilon^2) \quad . \tag{3.38}$$

Equation (3.35) prescribes scalings that make changes in I_0 from curvature and surface variation along the ballistic fluid parcel trajectories at surface b an O(ε^2) effect. Only O(ε) effects are considered in the derivation of the diffusion-limit boundary condition. Consequently, we can neglect surface variations and curvature in the following analysis as these conditions have been thoroughly examined by Malvagi and Pomraning [67]. Following prior authors, we also separate I_0 into a boundary layer solution, $I_{0,b}$, and an interior solution, $I_{0,i}$ such that $I_0 = I_{0,b} + I_{0,i}$ and $\lim_{s\to\infty} I_{0,b} = 0$ [44, 67]. For $I_{0,b}$, Eq. (3.38) then reduces further to

$$\left[\mu + \varepsilon(\hat{r}_b \cdot \hat{z})\frac{r_b}{ct_f}\right]\frac{\partial I_{0,b}}{\partial s} + \sigma_{t,0}I_{0,b} = \frac{\sigma_{t,0}}{4\pi}\int_{4\pi} I_{0,b} d\Omega_0' + O(\varepsilon^2) \quad . \tag{3.39}$$

The boundary and interior solutions may be expanded in the small parameter ε. As described in Section 2.1.7, the expansions are written as $I_{0,(b,i)} = \sum_{m=0}^{\infty} I_{0,(b,i)}^{(m)}\varepsilon^m$. Incorporating the ε-expansion into Eq. (3.39), balancing ε^0 and ε^1 coefficients, and integrating over the azimuthal angle about z, the O(1) and O(ε) equations are

$$\mu\frac{\partial \tilde{I}_{0,b}^{(0)}}{\partial s} + \sigma_{t,0}\left(\tilde{I}_{0,b}^{(0)} - \frac{1}{2}\int_{-1}^{1}\tilde{I}_{0,b}^{(0)}(\mu')d\mu'\right) = 0 \quad , \tag{3.40}$$

and

$$\mu\frac{\partial \tilde{I}_{0,b}^{(1)}}{\partial s} + \sigma_{t,0}\left(\tilde{I}_{0,b}^{(1)} - \frac{1}{2}\int_{-1}^{1}\tilde{I}_{0,b}^{(1)}(\mu')d\mu'\right) = -(\hat{r}_b \cdot \hat{z})\frac{r_b}{ct_f}\frac{\partial \tilde{I}_{0,b}^{(0)}}{\partial s} \quad , \tag{3.41}$$

where $\tilde{I}_{0,(b,i)}^{(m)} = \int_0^{2\pi} I_{0,(b,i)}^{(m)} d\omega$ and ω is the azimuthal angle. Where Malvagi and Pomraning have O(ε) curvature and spatial variations, we have a velocity term from the advection component of the Lagrangian time derivative in the original equation, Eq. (3.33). Supposing the boundary intensity at

$s = 0$ is known, matching the asymptotic orders gives [67]

$$\tilde{I}^{(0)}_{0,b}(s = 0, \mu, t) = F(\vec{r}_b, \mu, t) - \frac{1}{2}\phi^{(0)}_{0,i}(\vec{r}_b, t) \tag{3.42}$$

and

$$\tilde{I}^{(1)}_{0,b}(s = 0, \mu, t) = -\frac{1}{2}\left(\phi^{(1)}_{0,i}(\vec{r}_b, t) - \frac{\mu}{\sigma_{0,t}}\left.\frac{\partial\phi^{(0)}_{0,i}}{\partial z}\right|_{\vec{r}_b}\right) \tag{3.43}$$

as boundary conditions, where $\mu > 0$ is the magnitude of the angular projection into the diffusive domain along axis z, $\phi^{(m)}_{0,(b,i)} = \int_{4\pi} I^{(m)}_{0,(b,i)} d\Omega_0$ and $F(\vec{r}_b, \mu, t) = \int_0^{2\pi} I_0(\vec{r}_b, \hat{\Omega}_0, t)d\omega$. Eq. (3.40) along with Eq. (3.42) is a form of the standard half-space albedo problem examined by Case [18] and Larsen and Habetler [58]. The solution to Eq. (3.40) is [67]

$$\tilde{I}^{(0)}_{0,b} = k^{(0)}_{+} + \int_0^1 k^{(0)}(\varpi)\varphi_{\varpi}(\mu)e^{-\sigma_{t,0}s/\varpi}d\varpi \quad , \tag{3.44}$$

where $k^{(0)}_{+}$ is a constant, ϖ is an eigenvalue of the singular eigenfunction $\varphi_{\varpi}(\mu)$ (the eigenfunction is formally a distribution), and $k^{(0)}(\varpi)$ is a function determined by the orthogonalities, Eqs. (3.47) and (3.48) below [44]. The constant, $k^{(0)}_{+}$, constitutes the "discrete" component of the solution [44] and is the limiting behavior of a more general discrete eigenvalue solution having taken $\sigma_{0,a} \ll \sigma_{0,s}$ with ε. The distribution, $\varphi_{\varpi}(\mu)$, is given by

$$\varphi_{\varpi}(\mu) = \frac{\varpi}{2}P : \frac{1}{\varpi - \mu} + \lambda(\varpi)\delta(\varpi - \mu) \quad , \tag{3.45}$$

where $\delta(\varpi - \mu)$ is the Dirac delta function and $\lambda(\varpi) = 1 - \varpi \tanh^{-1}(\varpi)$ ensures a normalization of $\int_{-1}^{1} \varphi_{\varpi}(\mu)d\mu = 1$ for all $\varpi \in [0, 1]$. As in Section 2.1.7, the P : is a notational device to indicate the principal value is taken upon integration [44, 18]. Case [18] rigorously proves that a function, $H(\mu)$, may be found such that

$$\int_0^1 \mu H(\mu)\varphi_{\varpi}(\mu)d\mu = 0 \tag{3.46}$$

when $\tilde{I}^{(0)}_{0,b}$ satisfies a Hölder condition. It turns out $H(\mu)$ is Chandrasekhar's H-function [67]. Making use of the Poincaré-Bertrand formula [45] and Eq. (3.46), the orthogonalities [67]

$$\int_{-1}^{1} \mu \varphi_{\varpi'}(\mu)\varphi_{\varpi}(\mu) d\mu = N(\varpi)\delta(\varpi - \varpi') \tag{3.47}$$

and

$$\int_{0}^{1} \mu H(\mu)\varphi_{\varpi'}(\mu)\varphi_{\varpi}(\mu) d\mu = N(\varpi)H(\varpi)\delta(\varpi - \varpi') \ \ , \tag{3.48}$$

where $N(\varpi) = \varpi(\lambda(\varpi)^2 + (\pi\varpi/2)^2)$, must hold. Incorporating Eq. (3.45) into Eq. (3.44) and Eq. (3.44) into the boundary condition Eq. (3.42), Eqs. (3.46) and (3.48) indicate that multiplying the result by $\mu H(\mu)$ or $\mu H(\mu)\varphi_{\varpi'}(\mu)$ and integrating over $\mu \in [0, 1]$ yields

$$k^{(0)}_{+} = \frac{\sqrt{3}}{2}\int_{0}^{1} \mu H(\mu) F(\vec{r}_b, \mu) d\mu - \frac{1}{2}\phi_{0,i}(\vec{r}_b) \ \ , \tag{3.49}$$

or

$$k^{(0)}(\varpi) = \frac{1}{N(\varpi)H(\varpi)}\int_{0}^{1} \mu H(\mu)\varphi_{\varpi}(\mu) F(\vec{r}_b, \mu) d\mu \ \ , \tag{3.50}$$

respectively [67], where $\int_0^1 \mu H(\mu) = 2/\sqrt{3}$. As $s \to \infty$, Eq. (3.41) becomes homogeneous; then as $s \to \infty$, the O(ε) solution $\tilde{I}^{(1)}_{0,b}$ must tend to some constant, $k^{(1)}_{+}$, as well. Now using the boundary condition (3.44), $k^{(1)}_{+}$ may be found in a similar manner to $k^{(0)}_{+}$ as

$$k^{(1)}_{+} = \frac{\sqrt{3}}{2}\int_{0}^{1} \mu H(\mu) \left[-\frac{1}{2}\left(\phi^{(1)}_{0,i}(\vec{r}_b) - \frac{\mu}{\sigma_{0,t}} \left.\frac{\partial \phi^{(0)}_{0,i}}{\partial z}\right|_{\vec{r}_b} \right)\right] d\mu - \int_{0}^{\infty}\int_{-1}^{1} \beta(s,\mu)(\hat{r}_b \cdot \hat{z}) \frac{r_b}{ct_f}\frac{\partial \tilde{I}^{(0)}_{0,b}}{\partial s} d\mu\, ds \ \ , \tag{3.51}$$

where a considerable variational analysis by [67] gives

$$\beta(s,\mu) = 1 + \frac{3}{2}(\mu + \sigma_{0,t}s) - \left(1 + \frac{3}{2}\mu\right) e^{-\sigma_{0,t}s/\mu}\Theta(-\mu) \ \ , \tag{3.52}$$

and Θ is the Heaviside function. Roughly speaking, to obtain Eq. (3.52), Malvagi and Pomraning [67] construct a linear functional for $k_+^{(1)}$ with Lagrange multipliers as an estimate to $k_+^{(1)}$, find an adjoint transport solution [62, p. 47] and μ times the adjoint solution as the appropriate multipliers, and incorporate constants as trial functions for $\tilde{I}_b^{(1)}$ and the adjoint solution. With the boundary layer constraint, $\lim_{s\to\infty}\tilde{I}_{0,b}=0$, $k_+^{(0)}$ and $k_+^{(1)}$ must vanish. Equations (3.51) becomes [67]

$$\phi_{0,i}^{(1)}(\vec{r}_b)+\frac{\lambda}{\sigma_t}\hat{z}\cdot\nabla\phi_{0,i}^{(0)}= \\ 2(\hat{r}_b\cdot\hat{z})\frac{r_b}{ct_f}\int_0^\infty\left(\int_{-1}^1\beta(\eta,\mu)\int_0^1\frac{1}{\varpi}k(\varpi)\varphi_\varpi(\mu)e^{-\eta/\varpi}d\varpi\,d\mu\right)d\eta\quad, \tag{3.53}$$

where $\lambda=\sqrt{3}\int_0^1\mu^2H(\mu)d\mu/2$ and $\sigma_{t,0}s=\eta$. The eigenvalue form of $\tilde{I}_{0,b}^{(0)}$ has been incorporated into Eq. (3.53). Multiplying Eq. (3.53) by ε, adding the result to $\phi_{0,i}^{(0)}=\sqrt{3}\int_0^1\mu H(\mu)F(\vec{r}_b,\mu)d\mu$, reintroducing the interior solution $\phi_{0,i}=\phi_{0,i}^{(0)}+\varepsilon\phi_{0,i}^{(1)}+O(\varepsilon^2)$, and reverting the ε-scalings from Eq. (3.35) gives

$$\phi_{0,i}(\vec{r}_b,t)+\frac{\lambda}{\sigma_{t,0}}\hat{z}\cdot\nabla\phi_{0,i}= \\ 2(\hat{r}_b\cdot\hat{z})\frac{r_b}{ct_f}\int_0^\infty\left(\int_{-1}^1\beta(\eta,\mu)\int_0^1\frac{1}{\varpi}k(\varpi)\varphi_\varpi(\mu)e^{-\eta/\varpi}d\varpi\,d\mu\right)d\eta \\ +\sqrt{3}\int_0^1\mu H(\mu)F(\vec{r}_b,\mu,t)d\mu\quad, \tag{3.54}$$

which should be correct to O(ε^2). We find

$$\int_0^\infty\int_{-1}^1\beta(\eta,\mu)\varphi_\varpi(\mu)e^{-\eta/\varpi}d\mu d\eta= \\ \varpi\left(1+\frac{3}{2}\varpi\right)-\frac{\varpi^2}{2}(1+3\varpi)\ln\left(\frac{1+\varpi}{\varpi}\right)+\frac{\varpi^2}{2(1+\varpi)}\left(\frac{5}{2}+3\varpi\right) \\ \equiv\varpi h(\varpi)\quad, \tag{3.55}$$

so

$$\int_0^1\frac{k^{(0)}(\varpi)}{\varpi}\int_0^\infty\int_{-1}^1\beta(\eta,\mu)\varphi_\varpi(\mu)e^{-\eta/\varpi}\,d\mu\,d\eta\,d\varpi=\int_0^1 h(\varpi)k^{(0)}(\varpi)d\varpi\quad. \tag{3.56}$$

Incorporating Eq. (3.50), using $\sqrt{3}\mu H(\mu) \approx 2W(\mu)$ which is a corollary of the variational derivation of $\beta(s,\mu)$ by Malvagi and Pomraning [67], and defining

$$G_U(\mu) = 1 + \frac{2}{c}\hat{z}\cdot\vec{U}(\vec{r}_b,t_f)\int_0^1 \frac{h(\varpi)\varphi_\varpi(\mu)}{(2+3\varpi)N(\varpi)}d\varpi \quad , \tag{3.57}$$

Eq. (3.54) becomes

$$\phi_{0,i}(\vec{r}_b,t) + \frac{\lambda}{\sigma_{t,0}}\hat{z}\cdot\nabla\phi_{0,i} = 2\int_0^1 W(\mu)G_U(\mu)F(\vec{r}_b,\mu,t)d\mu \quad . \tag{3.58}$$

To evaluate the integral in Eq. (3.58), we incorporate Eq. (3.45) for $\varphi_\varpi(\mu)$ to obtain

$$\begin{aligned}\int_0^1 \frac{h(\varpi)\varphi_\varpi(\mu)}{(2+3\varpi)N(\varpi)}d\varpi = \lambda(\mu)\frac{h(\mu)}{(2+3\mu)N(\mu)} + \\ \frac{1}{2}\int_0^1\left(\varpi\frac{h(\varpi)}{(2+3\varpi)N(\varpi)} - \mu\frac{h(\mu)}{(2+3\mu)N(\mu)}\right)\frac{d\varpi}{(\varpi-\mu)} \\ + \frac{\mu}{2}\frac{h(\mu)}{(2+3\mu)N(\mu)}\ln\left(\frac{1-\mu}{\mu}\right) \quad ,\end{aligned} \tag{3.59}$$

where, following [67], we have converted the principal value integration to a nonsingular form amenable to quadrature.

Equation (3.59) along with the form of the functions $\lambda(\mu)$, $N(\mu)$, and $h(\mu)$ reveal the leading order behavior of the angular dependence in G_U. For the case of $\mu \to 0$: $\lambda(\mu) \to 1$, $N(\mu) \to \mu$ and $h(\mu) \to 1$. Hence, the first term on the right side of Eq. (3.59) tends to $0.5/\mu$ as $\mu \to 0$. From the last term on the right side of Eq. (3.59), the next order of divergence as $\mu \to 0$ is logarithmic. The remaining terms tend to a bounded integral over ϖ as $\mu \to 0$. We find that the behavior in μ of Eq. (3.59) is well approximated by $C_1/\mu - C_2\mu$ where C_1 and C_2 are positive constants. In Section 3.3.2, we test $0.5c(G_U - 1)/(\hat{z}\cdot\vec{U}) = 0.55/\mu - 1.25\mu$ for a three mean free path threshold between IMC and DDMC and $0.5c(G_U - 1)/(\hat{z}\cdot\vec{U}) = 0.6/\mu - 1.25\mu$ for a ten mean free path threshold between IMC and DDMC. These choices are approximations to the quadrature expressed in Eq. (3.59).

In Eq. (3.58), replacing $\hat{z}$ with $\vec{n}$, dropping the subscript i, replacing μ with $|\hat{\Omega}_0 \cdot \vec{n}|$, and adding a group index yields

$$\phi_{0,g}(\vec{r}_b, t) + \left(\frac{\lambda}{\sigma_{a,g,n} + \sigma_{s,g,n}}\right) \vec{n} \cdot \nabla\phi_{0,g}(\vec{r}_b, t) = \\ 2\int_{\hat{\Omega}_0 \cdot \vec{n} < 0} \int_{\nu_{g+1/2}}^{\nu_{g-1/2}} W(|\hat{\Omega}_0 \cdot \vec{n}|) G_U(|\hat{\Omega}_0 \cdot \vec{n}|) I_{0,\nu_0}(\vec{r}_b, \hat{\Omega}_0, t) d\nu_0 d\Omega_0 \quad . \tag{3.60}$$

When $\vec{U} = 0$, the standard diffusion-limit boundary condition is recovered.

2. The next analysis considers Doppler corrections in the diffusion limit. The frequency is treated in similar fashion to a spatial variable to examine the validity of boundary layers in frequency and the effect of inelastic scattering on Doppler correction. First, the interior and boundary layer equations for comoving diffusion are derived with asymptotic analysis; the boundary layer equation does not have the frequency derivative associated with Doppler correction. It is inferred that frequency boundary layers are invalid in the O(U/c) comoving diffusion equation. Second, for a model problem with elastic and inelastic scattering, the Doppler correction term is shown, to leading order, to depend on the scattering redistribution function. With a frequency boundary, subscripted b, the scalings chosen are

$$c \to c/\varepsilon \quad , \tag{3.61a}$$

$$\sigma_{0,\nu_0} \to \sigma_{0,\nu_0}/\varepsilon \quad , \tag{3.61b}$$

$$\sigma_{0,\nu_0,a} \to \varepsilon\sigma_{0,\nu_0,a} \quad , \tag{3.61c}$$

$$\omega = (\nu - \nu_b)/\varepsilon^m \quad , \tag{3.61d}$$

$$q \to \varepsilon q, \tag{3.61e}$$

where ν_b is a frequency at boundary b in frequency space and q is the external or thermal source in j_{0,ν_0}. The value m is a number introduced to control the amount of variation in intensity with respect to frequency. If $\partial I_{0,\nu_0}/\partial\omega$ is O(1), then $\partial I_{0,\nu_0}/\partial\nu$ is O($1/\varepsilon^m$). Incorporating the homologous relation into the comoving transport equation and rescaling according to Eq. (3.61),

$$\frac{\varepsilon^2}{c}\frac{\partial I_{0,\nu_0}}{\partial t} + \varepsilon\hat{\Omega}_0 \cdot \nabla I_{0,\nu_0} + \sigma_{0,\nu_0} I_{0,\nu_0} - \frac{\varepsilon^{2-m}}{ct}\nu_0 \frac{\partial I_{0,\nu_0}}{\partial \omega} + \frac{\varepsilon^2}{ct}\vec{r} \cdot \nabla I_{0,\nu_0} + \frac{3\varepsilon^2}{ct} I_{0,\nu_0} = \varepsilon j_{0,\nu_0} \ , \quad (3.62)$$

and assuming isotropic elastic scattering,

$$\varepsilon j_{0,\nu_0} = \varepsilon^2 \frac{q}{4\pi} + \left(\sigma_{0,\nu_0} - \varepsilon^2 \sigma_{0,\nu_0,a}\right) \frac{1}{4\pi} \int_{4\pi} I_{0,\nu_0} d\Omega_0' \ . \quad (3.63)$$

The value, $m \in \{0, 1\}$, where $m = 0$ for an interior frequency equation and $m = 1$ for a frequency boundary layer solution. Following the prescription for space, $I_{(i,b)} = \sum_{k=0}^{\infty} I_{(i,b)}^{(k)} \varepsilon^k$, where the subscript i indicates the interior of the frequency domain and the subscript b indicates frequency within a ε-layer of ν_b. Additionally, $\lim_{\omega \to \infty} I_b = 0$; this constraint is analogous to the spatial boundary layer constraint, where the stretched variable ω is analogous to the stretched spatial variable, s, from the first asymptotic analysis.

Setting $m = 0$ and incorporating the power series in ε, Eq. (3.62) may be separated into O(ε^0), O(ε^1), and O(ε^2) equations:

$$I_i^{(0)} = \frac{\phi_i^{(0)}}{4\pi} \quad (3.64)$$

for O(ε^0),

$$I_i^{(1)} = \frac{\phi_i^{(1)}}{4\pi} - \frac{1}{4\pi}\frac{\hat{\Omega}_0}{\sigma_{0,\nu_0}} \cdot \nabla \phi_i^{(0)} \quad (3.65)$$

for O(ε^1), and

$$I_i^{(2)} = \frac{1}{4\pi}\left[\frac{q}{\sigma_{0,\nu_0}} + \phi_i^{(2)} - \frac{\sigma_{0,\nu_0,a}}{\sigma_{0,\nu_0}}\phi_i^{(0)} + \frac{\nu_0}{ct\sigma_{0,\nu_0}}\frac{\partial \phi_i^{(0)}}{\partial \nu_0} - \frac{\vec{r}}{ct\sigma_{0,\nu_0}} \cdot \nabla \phi_i^{(0)} - \frac{3}{ct\sigma_{0,\nu_0}}\phi_i^{(0)} - \frac{1}{c\sigma_{0,\nu_0}}\frac{\partial \phi_i^{(0)}}{\partial t} - \frac{\hat{\Omega}_0}{\sigma_{0,\nu_0}} \cdot \nabla\left(\phi_i^{(1)} - \frac{\hat{\Omega}_0}{\sigma_{0,\nu_0}} \cdot \nabla \phi_i^{(0)}\right)\right] \quad (3.66)$$

for O(ε^2), where Eq. (3.64) has been used in Eq. (3.65) and Eqs. (3.64) and (3.65) have been used in Eq. (3.66). The values $\phi_i^{(k)} = \int_{4\pi} I_i^{(m)} d\Omega_0$ are the ε power series coefficients for scalar intensity.

Integrating Eq. (3.66) over comoving solid angle,

$$\frac{1}{c}\frac{\partial\phi_i^{(0)}}{\partial t}-\nabla\cdot\left(\frac{1}{3\sigma_{0,\nu_0}}\nabla\phi_i^{(0)}\right)+\sigma_{0,\nu_0,a}\phi_i^{(0)}-\frac{\nu_0}{ct}\frac{\partial\phi_i^{(0)}}{\partial\nu_0}+\frac{\vec{r}}{ct}\cdot\nabla\phi_i^{(0)}+\frac{3}{ct}\phi_i^{(0)}=q\ . \tag{3.67}$$

Equation (3.67) is the correct O(U/c) comoving diffusion equation with the assumptions of homologous outflow, Eq. (3.6), and isotropic scattering in the comoving frame.

For $m=1$, the O(ε^0), O(ε^1), and O(ε^2) equations for I_b are

$$I_b^{(0)}=\frac{\phi_b^{(0)}}{4\pi} \tag{3.68}$$

for O(ε^0),

$$I_b^{(1)}=\frac{1}{4\pi}\left(\phi_b^{(1)}-\frac{\hat{\Omega}_0}{\sigma_{0,\nu_0}}\cdot\nabla\phi_b^{(0)}+\frac{\nu_b}{ct\sigma_{0,\nu_0}}\frac{\partial\phi_b^{(0)}}{\partial\omega}\right) \tag{3.69}$$

for O(ε^1), and

$$\begin{aligned}I_b^{(2)}=\frac{1}{4\pi}\Bigg[&\phi_b^{(2)}-\frac{\sigma_{0,\nu_0,a}}{\sigma_{0,\nu_0}}\phi_b^{(0)}+\frac{\nu_b}{ct\sigma_{0,\nu_0}}\frac{\partial\phi_b^{(1)}}{\partial\omega}-\frac{\vec{r}}{ct\sigma_{0,\nu_0}}\cdot\nabla\phi_b^{(0)}-\frac{3}{ct\sigma_{0,\nu_0}}\phi_b^{(0)}\\&-\frac{1}{c\sigma_{0,\nu_0}}\frac{\partial\phi_b^{(0)}}{\partial t}-\frac{\hat{\Omega}_0}{\sigma_{0,\nu_0}}\cdot\nabla\left(\phi_b^{(1)}-\frac{\hat{\Omega}_0}{\sigma_{0,\nu_0}}\cdot\nabla\phi_b^{(0)}\right)\Bigg]\end{aligned} \tag{3.70}$$

for O(ε^2), where $\phi_b^{(k)}=\int_{4\pi}I_b^{(k)}d\Omega_0$. Integrating Eq. (3.69) over solid angle, $\partial\phi_b^{(0)}/\partial\omega=0$. The O($\varepsilon^3$) solution in terms of $I_b^{(1,2,3)}$ is

$$\begin{aligned}\frac{1}{c}\frac{\partial I_b^{(1)}}{\partial t}+\hat{\Omega}_0\cdot\nabla I_b^{(2)}+\sigma_{0,\nu_0}I_b^{(3)}-\frac{\nu_b}{ct}\frac{\partial I_b^{(2)}}{\partial\omega}+\frac{\vec{r}}{ct}\cdot\nabla I_b^{(1)}+\frac{3}{ct}I_b^{(1)}&\\=\frac{\sigma_{0,\nu_0}}{4\pi}\phi_b^{(3)}-\frac{\sigma_{0,\nu_0,a}}{4\pi}\phi_b^{(1)}&\ .\end{aligned} \tag{3.71}$$

To obtain an equation for $\phi_b^{(1)}$, Eq. (3.70) may be incorporated into the second and fourth terms on the left hand side of Eq. (3.71) and the overall result may be integrated in Ω_0. Since terms that are odd in $\hat{\Omega}_0$ vanish in the integration, the result is

$$\frac{1}{c}\frac{\partial\phi_b^{(1)}}{\partial t} - \nabla\cdot\left(\frac{1}{3\sigma_{0,\nu_0}}\nabla\phi_b^{(1)}\right) + \sigma_{0,\nu_0,a}\phi_b^{(1)} - \frac{\nu_b}{ct}\frac{\partial}{\partial\omega}\left(\frac{\nu_b}{ct\sigma_{0,\nu_0}}\frac{\partial\phi_b^{(1)}}{\partial\omega}\right) + \frac{3}{ct}\phi_b^{(1)} - \frac{\nu_b}{ct}\frac{\partial\phi_b^{(2)}}{\partial\omega} + \frac{\vec{r}}{ct}\cdot\nabla\phi_b^{(1)} = 0 \ . \quad (3.72)$$

The first and fourth terms in Eq. (3.72) together resemble a diffusion equation in frequency space. Equations (3.71) and Eq. (3.72) imply

$$\frac{\partial}{\partial\omega}\left(\frac{\nu_b}{ct\sigma_{0,\nu_0}}\frac{\partial\phi_b^{(1)}}{\partial\omega}\right) = 0 \ . \quad (3.73)$$

Taking $\sigma_{0,\nu_0} = \sigma_{0,\nu_b}$, the solution of Eq. (3.73)

$$\phi_b^{(1)} = \frac{ct\sigma_{0,\nu_0}}{\nu_b}A_1\omega + A_2 \ , \quad (3.74)$$

where A_1 and A_2 are constant in ω. Since $\lim_{\omega\to\infty}\phi_b^{(1)} = 0$, so $\phi_b^{(1)} = A_1 = A_2 = 0$. Integration of Eq. (3.70) yields

$$\frac{1}{c}\frac{\partial\phi_b^{(0)}}{\partial t} - \nabla\cdot\left(\frac{1}{3\sigma_{0,\nu_0}}\nabla\phi_b^{(0)}\right) + \sigma_{0,\nu_0,a}\phi_b^{(0)} + \frac{\vec{r}}{ct}\cdot\nabla\phi_b^{(0)} + \frac{3}{ct}\phi_b^{(0)} = 0 \ . \quad (3.75)$$

Equation (3.75) indicates the leading-order boundary layer solution does not have a Doppler correction term.

Here, the analysis to obtain Eq. (3.75) is extended to a model of the transport equation with a component of inelastic scattering. Densmore [25] asymptotically analyzes the effect of treating some absorption and re-emission as instantaneous effective scattering while treating the remainder explicitly with a linear spatial distribution. To an extent, an analogy may be drawn between elastic scattering, which preserves ν_0, and IMC effective scattering, which preserves $\vec{r}$. To complete the analogy, inelastic scattering redistributes ν_0 corresponds IMC effective absorption/emission redistributes $\vec{r}$. Discussed briefly in Section 2.1.8, Densmore's analysis shows that inaccurate spatial distributions may not allow the transport equation to asymptotically converge to a correct form of the diffusion equation. With a similar construction, but treating frequency like space, the result of the following analysis is that the Doppler correction depends on the redistribution function within frequency groups.

The model equation is

$$\frac{1}{c}\frac{\partial I_{0,\nu_0}}{\partial t}+\hat{\Omega}_0\cdot\nabla I_{0,\nu_0}+\sigma_{0,\nu_0}I_{0,\nu_0}-\frac{\nu_0}{ct}\frac{\partial I_{0,\nu_0}}{\partial\nu_0}+\frac{\vec{r}}{ct}\cdot\nabla I_{0,\nu_0}+\frac{3}{ct}I_{0,\nu_0}=\frac{q}{4\pi}+$$
$$\frac{1}{4\pi}(1-\chi)\sigma_s\phi_{0,\nu_0}+\frac{1}{4\pi}\chi\sigma_s p_s(\nu_0)\phi_{0,g}\quad, \tag{3.76}$$

where $\chi\in[0,1]$ is a elastic/inelastic splitting parameter, $p_s(\nu_0)$ is a probability density function, σ_s is a frequency independent scattering opacity coefficient, and $\phi_{0,g}=\int_{\nu_b}^{\nu_t}\phi_{0,\nu_0}d\nu_0$. The value ν_t is the upper bound of the diffusive region. Constraining $\int_{\nu_b}^{\nu_t}p_s(\nu_0)d\nu_0=1$, the integral of the total scattering source term over frequency is $\sigma_s\phi_{0,g}$. Considering Eq. (3.76) implies

$$\int_{4\pi}\int_{\nu_b}^{\nu_t}\frac{\nu_0}{\nu_0'}\sigma_{0,s}(\vec{r},\nu_0'\to\nu_0,\hat{\Omega}_0'\cdot\hat{\Omega}_0)I_{0,\nu_0'}d\nu_0'd\Omega_0'=$$
$$\frac{1}{4\pi}(1-\chi)\sigma_s\phi_{0,\nu_0}+\frac{1}{4\pi}\chi\sigma_s p_s(\nu_0)\phi_{0,g}\quad, \tag{3.77}$$

the differential scattering opacity is taken to be

$$\sigma_{0,s}(\vec{r},\nu_0'\to\nu_0,\hat{\Omega}_0'\cdot\hat{\Omega}_0)=\frac{\sigma_s}{4\pi}\left[(1-\chi)\delta(\nu_0-\nu_0')+\chi\frac{\nu_0'}{\nu_0}p_s(\nu_0)\right]\quad, \tag{3.78}$$

where $\delta(\nu_0-\nu_0')$ is the Dirac delta function. The total scattering opacity is

$$\sigma_{0,\nu_0,s}=\sigma_s\left[(1-\chi)+\chi\nu_0\int_{\nu_b}^{\nu_t}\frac{p_s(\nu_0')}{\nu_0'}d\nu_0'\right]\quad. \tag{3.79}$$

The distribution

$$\tilde{p}_s(\nu_0)\equiv\left(\int_{\nu_b}^{\nu_t}\frac{p_s(\nu_0')}{\nu_0'}d\nu_0'\right)^{-1}\frac{p_s(\nu_0)}{\nu_0}\quad, \tag{3.80}$$

is shown to be the O(ε^0) and O(ε^1) frequency dependence of scalar intensity for $\nu_0\in[\nu_b,\nu_t]$. It has been assumed that p_s only redistributes frequency in $[\nu_b,\nu_t]$.

We define $\phi_{i,g}$ and $\phi_{b,g}$ as the interior and boundary scalar intensity group integrated contributions to to the diffusive range. Applying the scalings with $m = 0$, considering the interior solution, and setting $\phi_{0,g} = \sum_{k=0}^{\infty} \phi_{0,g}^{(k)}\varepsilon^k = \sum_{k=0}^{\infty}(\phi_{i,g}^{(k)} + \phi_{b,g}^{(k)})\varepsilon^k$, the O($\varepsilon^0$), O($\varepsilon^1$), and O($\varepsilon^2$) equations for intensity are

$$I_i^{(0)} = \frac{1}{4\pi}\tilde{p}_s(\nu_0)\phi_{i,g}^{(0)} \quad , \tag{3.81}$$

$$I_i^{(1)} = \frac{1}{4\pi}\tilde{p}_s(\nu_0)\left(\phi_{i,g}^{(1)} - \frac{\hat{\Omega}_0}{\sigma_{0,\nu_0,s}} \cdot \nabla\phi_{i,g}^{(0)}\right) \quad , \tag{3.82}$$

and

$$\begin{aligned} I_i^{(2)} = \frac{1}{4\pi}\Bigg[&\frac{q}{\sigma_{0,\nu_0,s}} + \frac{\sigma_s}{\sigma_{0,\nu_0,s}}[(1-\chi)\phi_i^{(2)} + \chi p_s(\nu_0)\phi_{i,g}^{(2)}] \\ &- \frac{\sigma_{0,\nu_0,a}}{\sigma_{0,\nu_0,s}}\tilde{p}_s(\nu_0)\phi_{i,g}^{(0)} + \frac{\nu_0\phi_{i,g}^{(0)}}{ct\sigma_{0,\nu_0,s}}\frac{\partial\tilde{p}_s}{\partial\nu_0} - \frac{\tilde{p}_s(\nu_0)}{ct\sigma_{0,\nu_0,s}}\vec{r}\cdot\nabla\phi_{i,g}^{(0)} \\ &-\frac{3\tilde{p}_s(\nu_0)}{ct\sigma_{0,\nu_0,s}}\phi_{i,g}^{(0)} - \frac{1}{c\sigma_{0,\nu_0,s}}\frac{\partial(\tilde{p}_s(\nu_0)\phi_{i,g}^{(0)})}{\partial t} - \frac{\tilde{p}_s(\nu_0)}{\sigma_{0,\nu_0,s}}\hat{\Omega}_0\cdot\nabla\left(\phi_{i,g}^{(1)} - \frac{\hat{\Omega}_0}{\sigma_{0,\nu_0,s}}\cdot\nabla\phi_{i,g}^{(0)}\right)\Bigg] \quad , \end{aligned} \tag{3.83}$$

respectively. The scattering profile determines the leading interior solution. For $m = 1$, the O(ε^0) and O(ε^1) equations are

$$I_b^{(0)} = \frac{1}{4\pi}\tilde{p}_s(\nu_b)\phi_{b,g}^{(0)} \quad , \tag{3.84}$$

$$I_b^{(1)} = \frac{1}{4\pi}\left(\frac{\sigma_s}{\sigma_{0,\nu_0,s}}[(1-\chi)\phi_b^{(1)} + \chi p_s(\nu_b)\phi_{b,g}^{(1)}] - \frac{\hat{\Omega}_0}{\sigma_{0,\nu_0,s}}\cdot\nabla\phi_b^{(0)} + \frac{\nu_b}{ct\sigma_{0,\nu_0,s}}\frac{\partial\phi_b^{(0)}}{\partial\omega}\right) \quad , \tag{3.85}$$

respectively, where it is assumed the inelastic probability density does not vary strongly in the boundary layer. This assumption may be expressed in terms of a Taylor expansion of $p_s(\nu)$ around ν_b at a point in the boundary layer: $p_s(\nu) = p_s(\nu_b) + \varepsilon\omega\partial p_s(\nu_b)/\partial\nu$. Since Eq. (3.84) is frequency independent, $\partial\phi_b^{(0)}/\partial\omega = 0$. Integration of Eq. (3.85) over solid angle yields

$$\phi_b^{(1)} = \tilde{p}_s(\nu_b)\phi_{b,g}^{(1)} \quad . \tag{3.86}$$

The O(ε^2) boundary layer equation is

$$I_b^{(2)} = \frac{1}{4\pi}\left[\frac{\sigma_s}{\sigma_{0,\nu_0,s}}((1-\chi)\phi_b^{(2)} + \chi p_s(\nu_b)\phi_{b,g}^{(2)}) - \frac{\sigma_{0,\nu_0,a}}{\sigma_{0,\nu_0,s}}\phi_b^{(0)} - \frac{\vec{r}}{ct\sigma_{0,\nu_0,s}}\cdot\nabla\phi_b^{(0)} - \frac{3}{ct\sigma_{0,\nu_0,s}}\phi_b^{(0)} - \frac{1}{c\sigma_{0,\nu_0,s}}\frac{\partial\phi_b^{(0)}}{\partial t} - \frac{\hat{\Omega}_0}{\sigma_{0,\nu_0,s}}\cdot\nabla\left(\phi_b^{(1)} - \frac{\hat{\Omega}_0}{\sigma_{0,\nu_0,s}}\cdot\nabla\phi_b^{(0)}\right)\right] \quad . \quad (3.87)$$

Equation (3.87) yields

$$\frac{1}{c}\frac{\partial\phi_b^{(0)}}{\partial t} - \nabla\cdot\left(\frac{1}{3\sigma_{0,\nu_0,s}}\nabla\phi_b^{(0)}\right) + \sigma_{0,\nu_0,a}\phi_b^{(0)} + \frac{\vec{r}}{ct}\cdot\nabla\phi_b^{(0)} + \frac{3}{ct}\phi_b^{(0)} = \chi\sigma_s\left(p_s(\nu_b)\phi_{b,g}^{(2)} - \frac{p_s(\nu_b)}{\tilde{p}_s(\nu_b)}\phi_b^{(2)}\right) \quad , \quad (3.88)$$

which has an inelastic scattering source from the O(ε^2) scalar flux. When $\chi = 0$, Eq. (3.88) simplifies to Eq. (3.75). Similarly to the case of elastic scattering, the leading-order boundary layer solution of the model problem with inelastic scattering does not have a Doppler correction term.

It is inferred that boundary layers, in which I_{0,ν_0} varies strongly with ν_0, do not satisfy the O(U/c) radiation diffusion for either elastic or inelastic scattering. It may be that applying the chosen ε-scaling to fully relativistic transport in optically thick media would yield leading-order Doppler correction terms. We do not provide such an analysis here.

To capture Doppler shift in multigroup, comoving diffusion Mihalas and Weibel Mihalas describe an upwind approximation for $\phi_{0,\nu_{g\pm1/2}}$ [73, p. 475]. Considering Eq. (3.88), multigroup diffusion with the upwind discretization for Doppler shift between groups may not furnish accurate results with respect to continuous-frequency transport. The multigroup, comoving diffusion equation with the upwind approximation is

$$\frac{1}{c}\frac{\partial\phi_{0,g}}{\partial t} - \nabla\cdot\left(\frac{1}{3\sigma_{0,g}}\nabla\phi_{0,g}\right) + \sigma_{0,g}\phi_{0,g} + \frac{4}{ct}\phi_{0,g} + \frac{\nu_{g+1/2}}{ct\Delta\nu_g}\phi_{0,g} + \frac{\vec{r}}{ct}\cdot\nabla\phi_{0,g} = 4\pi j_{0,g} + \frac{\nu_{g-1/2}}{ct\Delta\nu_{g-1}}\phi_{0,g-1} \quad , \quad (3.89)$$

where $\sigma_{0,g} = \sigma_{a,g} + \sigma_{s,g}$ (see Eq. (3.22)). The Doppler correction terms in Eq. (3.89) can be interpreted as "Doppler shift opacities", where sampling the value $\nu_{g+1/2}/ct\Delta\nu_g$ induces a particle to transition from group g to group $g+1$.

In `SuperNu`, frequency is tracked continuously in both IMC and DDMC. At the subgroup level, frequency redistribution is uniform in frequency. In the model equation, Eq. (3.76), uniform redistribution corresponds to

$$p_s(\nu_0) = \frac{1}{\Delta\nu_g} \quad , \tag{3.90}$$

where $\Delta\nu_g = \nu_{g-1/2} - \nu_{g+1/2} = \nu_t - \nu_b$. From Eqs. (3.80) and (3.90), $\tilde{p}_s \sim 1/\nu \sim \phi_i^{(0)}$, and

$$-\frac{\nu_0\phi_{i,g}^{(0)}}{ct}\frac{\partial\tilde{p}_s}{\partial\nu_0} = \frac{1}{ct}\phi_i^{(0)} \quad . \tag{3.91}$$

Incorporating Eq. (3.91) into Eq. (3.88) and integrating comoving frequency over $[\nu_{g+1/2}, \nu_{g-1/2}]$ yields

$$\frac{1}{c}\frac{\partial\phi_{0,g}^{(0)}}{\partial t} - \nabla\cdot\left(\frac{1}{3\sigma_{0,g}}\nabla\phi_{0,g}^{(0)}\right) + \sigma_{a,g}\phi_{0,g}^{(0)} + \frac{\vec{r}}{ct}\cdot\nabla\phi_{0,g}^{(0)} + \frac{4}{ct}\phi_{0,g}^{(0)} = q_g \quad , \tag{3.92}$$

where the second-order inelastic scattering source has been grouped into the total group source, q_g. In contrast to Eq. (3.89), Eq. (3.92) does not have terms corresponding to discrete Doppler shift. It is inferred from Eq. (3.92) that upwind Doppler group coupling in DDMC may not be sufficient to emulate continuous-frequency IMC with effective scattering that dominates the other particle processes.

In this section:

1. a new asymptotic diffusion-limit boundary condition has been derived for high-velocity cell edges,
2. the dependence of Doppler corrections on inelastic scattering has been demonstrated for a model equation.

3.1.3 Multigroup Velocity Space IMC-DDMC

The preceding asymptotic analyses provide insight into combining velocity-dependent DDMC with IMC. In this section, velocity-dependent DDMC is described. The approach is similar to that of Abdikamalov et al. [2], but with method interfacing for a Lagrangian grid and Doppler correction for continuous frequency.

Integrating over solid angle, neglecting the O(U/c) coefficient of the Lagrangian time derivative, and assuming isotropic opacity and elastic physical scattering, Eq. (3.23) becomes

$$\frac{1}{c}\frac{\partial\phi_{0,g}}{\partial t}+\frac{1}{c}\nabla\cdot(\vec{U}\phi_{0,g})+\nabla\cdot\vec{F}_{0,g}+(\mathbf{P}_{0,g}-\nu_{g-1/2}\mathbf{P}_{0,\nu_{g-1/2}}+\nu_{g+1/2}\mathbf{P}_{0,\nu_{g+1/2}}):\nabla\vec{U}$$
$$+\left[f_n\sigma_{a,g,n}+(1-\gamma_{g,n})(1-f_n)\sigma_{a,g,n}\right]\phi_{0,g}=f_n\gamma_{g,n}\sigma_{P,n}acT_n^4+\gamma_{g,n}(1-f_n)\sum_{g'\neq g}^{G_j}\sigma_{a,g',n}\phi_{0,g'} \tag{3.93}$$

where $\gamma_{g,n}=b_{0,g,n}\sigma_{a,g,n}/\sigma_{P,n}$,

$$\phi_{0,g}=\int_{4\pi}I_{0,g}d\Omega_0\ \ ,$$

$$\vec{F}_{0,g}=\int_{4\pi}\hat{\Omega}_0 I_{0,g}d\Omega_0\ \ ,$$

$$\mathbf{P}_{0,g}=\frac{1}{c}\int_{4\pi}\hat{\Omega}_0\hat{\Omega}_0 I_{0,g}d\Omega_0\ \ ,$$

$$\mathbf{P}_{0,\nu_{g\pm1/2}}=\frac{1}{c}\int_{4\pi}\hat{\Omega}_0\hat{\Omega}_0 I_{0,\nu_{g\pm1/2}}d\Omega_0\ \ ,$$

and the expression $\mathbf{W}:\mathbf{V}$ is the trace of the matrix product $\mathbf{W}\mathbf{V}^T$ [19, p. 113]. Following Abdikamalov et al. [2], Eq. (3.93) can be operator split into transport, Doppler shift, and advection-expansion components:

$$\frac{1}{c}\left(\frac{\partial\phi_{0,g}}{\partial t}\right)_{\text{Transport}}+\nabla\cdot\vec{F}_{0,g}+\left[f_n\sigma_{a,g,n}+(1-\gamma_{g,n})(1-f_n)\sigma_{a,g,n}\right]\phi_{0,g}=$$
$$f_n\gamma_{g,n}\sigma_{P,n}acT_n^4+\gamma_{g,n}(1-f_n)\sum_{g'\neq g}^{G_j}\sigma_{a,g',n}\phi_{0,g'}\ \ , \tag{3.94}$$

$$\frac{1}{c}\left(\frac{\partial\phi_{0,g}}{\partial t}\right)_{\text{Doppler}}+\mathbf{P}_{0,g}:\nabla\vec{U}=(\nu_{g-1/2}\mathbf{P}_{0,\nu_{g-1/2}}-\nu_{g+1/2}\mathbf{P}_{0,\nu_{g+1/2}}):\nabla\vec{U}\ \ , \tag{3.95}$$

and

$$\left(\frac{\partial\phi_{0,g}}{\partial t}\right)_{\text{Adv/Exp}}+\nabla\cdot(\vec{U}\phi_{0,g})=0\ \ . \tag{3.96}$$

With the same assumptions used for Eq. (3.93), multiplying Eq. (3.23) by $\hat{\Omega}_0$ and integrating over solid angle gives a first-moment equation for intensity. The analysis of Buchler [14] is applied to drop insignificant terms. With the result, the operator splitting procedure is applied to the first-moment equation to obtain [104]

$$\frac{1}{c}\left(\frac{\partial\vec{F}_{0,g}}{\partial t}\right)_{\text{Transport}}+c\nabla\cdot\mathbf{P}_{0,g}=-(\sigma_{s,g,n}+\sigma_{a,g,n})\vec{F}_{0,g}\ \ , \tag{3.97}$$

and

$$\left(\frac{\partial\vec{F}_{0,g}}{\partial t}\right)_{\text{Adv/Exp}}+\nabla\cdot(\vec{U}\vec{F}_{0,g})=0\ \ , \tag{3.98}$$

where now terms with the Fleck factor are no longer present due to comoving isotropy. Neglecting the time derivative and assuming the intensity is at most linearly anisotropic in the comoving frame, Eq. (3.97) reduces to Fick's Law,

$$\vec{F}_{0,g}=\frac{-1}{3(\sigma_{s,g,n}+\sigma_{a,g,n})}\nabla\phi_{0,g}\ \ . \tag{3.99}$$

With Eq. (3.99), Eqs. (3.94) and (3.95) become

$$\begin{aligned}\frac{1}{c}\frac{\partial\phi_{0,g}}{\partial t}-\nabla\cdot\left(\frac{1}{3\sigma_{0,g}}\nabla\phi_{0,g}\right)+\left[f_n\sigma_{a,g,n}+(1-\gamma_{g,n})(1-f_n)\sigma_{a,g,n}\right]\phi_{0,g}=\\ f_n\gamma_{g,n}\sigma_{P,n}acT_n^4+\gamma_{g,n}(1-f_n)\sum_{g'\neq g}^{G_j}\sigma_{a,g',n}\phi_{0,g'}\ \ ,\end{aligned} \tag{3.100}$$

and

$$\frac{\partial\phi_{0,g}}{\partial t}+\frac{\nabla\cdot\vec{U}}{3}\phi_{0,g}=\frac{\nabla\cdot\vec{U}}{3}(\nu_{g-1/2}\phi_{0,\nu_{g-1/2}}-\nu_{g+1/2}\phi_{0,\nu_{g+1/2}})\ \ , \tag{3.101}$$

respectively. To arrive at a DDMC equation, the spatial derivatives in Eq. (3.100) must be discretized; this will yield terms that can be interpreted as leakage opacities. Leakage opacities determine the likelihood a DDMC particle will move from one spatial cell to an adjacent cell in a grid [31, 27]. Because the form of the opacity is determined by spatial discretization, leakage opacities are dependent on grid geometry. For the numerical tests considered in Chapter 3, the spatial grid is one dimensional and spherically symmetric. With the homologous coordinate relation and discretization, interior (DDMC cell-group to DDMC cell-group) leakage opacities for 1D, spherical coordinates as

$$\sigma_{i\rightarrow i'',g} = \begin{cases} \dfrac{2U_{i-1/2}^2}{t_n^2\Delta(U^3)_i}\left(\dfrac{1}{\sigma_{0,i-1/2,g,n}^{-}\Delta U_{i-1} + \sigma_{i-1/2,g,n}^{+}\Delta U_i}\right) & , \quad i'' = i-1 \\ \\ \dfrac{2U_{i+1/2}^2}{t_n^2\Delta(U^3)_i}\left(\dfrac{1}{\sigma_{0,i+1/2,g,n}^{-}\Delta U_{i} + \sigma_{i+1/2,g,n}^{+}\Delta U_{i+1}}\right) & , \quad i'' = i+1 \end{cases} , \tag{3.102}$$

where $\Delta U_i = U_{i+1/2} - U_{i-1/2}$ is the radial velocity width, $\Delta(U^3)_i = U_{i+1/2}^3 - U_{i-1/2}^3$, and $\sigma_{0,i\pm1/2,g,n} = \sigma_{0,g,n}(r_{i\pm1/2})$, where the $+$ $(-)$ superscript indicates the remaining material properties are evaluated on the outer (inner) side of the cell edge with respect to index i. For DDMC cell-groups interfacing with IMC cell-groups, Densmore et al. [31] find both a IMC-to-DDMC transition probability and a DDMC-to-IMC leakage opacity using the asymptotic diffusion-limit boundary condition (see Section 2.1.12). For moving interfaces, the diffusion-limit boundary condition derived from the first asymptotic analysis in Section 3.1.2 may be used to obtain

$$\sigma_{b(i,i'),g} = \begin{cases} \dfrac{2U_{i-1/2}^2}{t_n\Delta(U^3)_i}\left(\dfrac{1}{\sigma_{i-1/2,g,n}^{+}t_n\Delta U_i + 2\lambda}\right) & , \quad i' = i-1 \\ \\ \dfrac{2U_{i+1/2}^2}{t_n\Delta(U^3)_i}\left(\dfrac{1}{\sigma_{i+1/2,g,n}^{-}t_n\Delta U_i + 2\lambda}\right) & , \quad i' = i+1 \end{cases} , \tag{3.103}$$

and

$$P_{b(i,i'),g}(\mu) = \begin{cases} \dfrac{4(1+3\mu/2)G_{U_{i-1/2}}(\mu)}{3\sigma^{+}_{i-1/2,g,n}t_n\Delta U_i + 6\lambda} & , \; i' = i-1 \\ \\ \dfrac{4(1+3\mu/2)G_{U_{i+1/2}}(\mu)}{3\sigma^{-}_{i+1/2,g,n}t_n\Delta U_i + 6\lambda} & , \; i' = i+1 \end{cases} \quad , \tag{3.104}$$

where $\mu = |\vec{n}\cdot\hat{\Omega}_0|$, $\sigma_{b(i,i'),g}$ is the DDMC-to-IMC interface leakage opacity from cell i to i', and $P_{b(i,i'),g}/G_U$ is the probability for IMC particles in cell i' at surface $b(i,i')$ with $\vec{n}\cdot\hat{\Omega}_{0,p} < 0$ to transition to DDMC particles in cell i. The IMC-to-DDMC probability formula is almost the same as that of Densmore et al. [31] with the exception of the singular coefficient, G_U. To solve the DDMC equations with the boundary condition from Section 3.1.2 in Monte Carlo, the term G_U may be interpreted as a factor that multiplies IMC particle weights incident on the moving DDMC surface. Equations (3.102) to (3.104) were obtained by finite volume integration of the second term on the left side of Eq. (3.100). Without specifying a particular geometry, taking the finite volume form of the entire Eq. (3.100) yields

$$\frac{1}{c}\frac{\partial\phi_{0,i,g}}{\partial t} + \left[\sum_{i''\neq i'}\sigma_{i\to i'',g} + \sigma_{b(i,i'),g} + f_{i,n}\sigma_{a,i,g,n} + (1-\gamma_{i,g,n})(1-f_{i,n})\sigma_{a,i,g,n}\right]\phi_{0,i,g} =$$
$$f_{i,n}\gamma_{i,g,n}\sigma_{P,i,n}acT^4_{i,n} + \frac{1}{V_i}\sum_{i''\neq i}V_{i''}\sigma_{i''\to i,g}\phi_{0,i'',g} + \gamma_{i,g,n}(1-f_{i,n})\sum_{g'\neq g}^{G_i}\sigma_{a,i,g',n}\phi_{0,i,g'}$$
$$+\frac{1}{V_i}\int_{A_{b(i,i')}}\int_{\hat{\Omega}_0\cdot\vec{n}<0}\int_{\nu_{g+1/2}}^{\nu_{g-1/2}}P_{b(i,i')}(|\hat{\Omega}_0\cdot\vec{n}|)|\hat{\Omega}_0\cdot\vec{n}|I_{0,g}d\nu_0 d\Omega_0 d^2\vec{r} \quad , \tag{3.105}$$

where, as in Section 2.1.14, V_i and $A_{b(i,i')}$ are the volume of cell i and the surface area shared by cells i and i', respectively. Equation (3.105) represents a DDMC cell-group surrounded by DDMC cells, indexed i'', with one adjacent cell, i', having the same group interval but with IMC. The circumstance and form of Eq. (3.105) is similar to Eq. (2.112); but Eq. (3.105) is in multigroup, without effective scattering to IMC groups, in the comoving fluid frame, and with a multiplication to particle weights implicit in the IMC-to-DDMC transmission coefficient, $P_{b(i,i')}$.

To mix IMC and DDMC over groups and interface groups at cell bounds with group boundaries that do not align, sub-indexes g_T, for IMC, and g_D, for DDMC, are introduced. The possibility of group edges that do not align between cells may be considered in calculating leakage opacities. Presented here is a generalization of the composite leakage opacity of Densmore et al. [30] for transitions to an adjacent cell, i' with transport groups indexed by g'_T and diffusion groups indexed by g'_D,

$$\tilde{\sigma}_{i\to i',g} = \left(\frac{\sum_{g'_D} b_{i,g\leftrightarrow g'_D,n}}{b_{i,g,n}}\right)\sigma_{i\to i',g} + \left(\frac{\sum_{g'_T} b_{i,g\leftrightarrow g'_T,n}}{b_{i,g,n}}\right)\sigma_{b(i,i'),g} \tag{3.106}$$

where $b_{i,g,n} = \int_{\nu_{g+1/2}}^{\nu_{g-1/2}} b_{0,\nu_0}(T_{i,n})d\nu_0$, and

$$b_{i,g\leftrightarrow g',n} = \begin{cases} \displaystyle\int_{\min([\nu_{g+1/2},\nu_{g-1/2}]\cap[\nu_{g'+1/2},\nu_{g'-1/2}])}^{\max([\nu_{g+1/2},\nu_{g-1/2}]\cap[\nu_{g'+1/2},\nu_{g'-1/2}])} b_{0,\nu_0}(T_{i,n})d\nu_0 \ , \\ [\nu_{g+1/2},\nu_{g-1/2}]\cap[\nu_{g'+1/2},\nu_{g'-1/2}] \neq \emptyset \\ \\ 0 \ , \ \ [\nu_{g+1/2},\nu_{g-1/2}]\cap[\nu_{g'+1/2},\nu_{g'-1/2}] = \emptyset \ , \end{cases} \tag{3.107}$$

where the substitution $b_{i,g\leftrightarrow g',n}$ and $b_{0,\nu_0}(T_{i,n})$ with $I_{0,g\leftrightarrow g'}$ and I_{0,ν_0}, respectively, is used for Eq. (3.108) below. If all group bounds are aligned, the method reduces in complexity to the standard multigroup approach and the set of (j,g)-transition graphs become completely reducible. If a leakage is sampled, the probability of a DDMC-to-DDMC leakage transition is $\frac{(b_{i,g\leftrightarrow g'_D,n}\sigma_{i\to i',g})}{(b_{i,g,n}\tilde{\sigma}_{i\to i',g})}$ and the probability of an DDMC to IMC leakage transition is $\frac{(b_{j,g\leftrightarrow g'_T,n}\sigma_{b(j,j'),g})}{(b_{j,g,n}\tilde{\sigma}_{j\to j',g})}$. If (j,g) is treated with IMC, then the group in the subsequent cell is determined by particle frequency in the comoving frame of the boundary. The intensity distribution at the DDMC cell interface is assumed to be well represented by the Planck function [30]. By substituting the composite leakage opacity, $\tilde{\sigma}_{i\to i',g}$, in the left side of Eq. (3.105), complementary modifications must be made to the terms on the right side; then the equation will represent radiation energy balance in a hybridized system. The hybrid

DDMC equation is

$$\begin{aligned}\frac{1}{c}\frac{\partial\phi_{0,i,g}}{\partial t} + \left(\sum_{i'}\tilde{\sigma}_{i\rightarrow i',g} + (1-\gamma_{i,g,n})(1-f_{i,n})\sigma_{a,i,g,n} + f_{i,n}\sigma_{a,i,g,n}\right)\phi_{0,i,g} = \\ f_{i,n}\gamma_{i,g,n}\sigma_{P,i,n}acT^4_{i,n} + \frac{1}{V_i}\sum_{i'}V_{i'}\sum_{g'_D}\frac{b_{i,g\leftrightarrow g'_D,n}}{b_{i,g,n}}\sigma_{i'\rightarrow i,g'_D}\phi_{0,i,g'_D} \\ + \frac{1}{V_i}\sum_{i'}\sum_{g'_T}\int_{A_{b(i,i')}}\int_{\hat{\Omega}_0\cdot\vec{n}<0}P_{b(i,i')}(|\hat{\Omega}_0\cdot\vec{n}|)|\hat{\Omega}_0\cdot\vec{n}|I_{0,g\leftrightarrow g'_T}d\Omega_0 d^2\vec{r} \\ + \frac{\gamma_{i,g,n}(1-f_{i,n})}{V_i}\sum_{g_T}\int_{V_i}\int_{4\pi}\sigma_{a,i,g_T,n}I_{0,g_T}d\Omega_0 d^3\vec{r} \\ + \gamma_{i,g,n}(1-f_{i,n})\sum_{g_D}\sigma_{a,i,g_D,n}\phi_{0,i,g_D} \quad , \qquad (3.108)\end{aligned}$$

and the hybrid Lagrangian temperature equation in differential form is

$$\begin{aligned}C_{v,i,n}\frac{DT}{Dt} = \\ f_{i,n}\left[\sum_{g_D}\sigma_{a,i,g_D,n}\phi_{0,i,g_D} + \frac{1}{V_i}\int_{V_i}\int_{4\pi}\sum_{g_T}\sigma_{a,i,g_T,n}I_{0,g_T}d\Omega_0 d^3\vec{r} - \sigma_{P,i,n}acT^4_{i,n}\right] \quad . \qquad (3.109)\end{aligned}$$

The terms in Eq. (3.108) can be interpreted as follows:

- $\frac{1}{c}\frac{\partial\phi_{0,i,g}}{\partial t}$ with the other terms on the left side determine the time evolution for each DDMC particle. The time update is $\delta t_{\text{DDMC}} = \min(\delta t, \delta t_{\text{cen}})$, where δt_{cen} is the time remaining in the time step and

$$\delta t = -\frac{1}{c}\frac{\ln(\xi)}{\sum_{i'}\tilde{\sigma}_{i\rightarrow i',g} + (1-\gamma_{i,g,n})(1-f_{i,n})\sigma_{a,i,g,n} + f_{i,n}\sigma_{a,i,g,n}} \qquad (3.110)$$

  is the time to a DDMC absorption or leakage event [31]. The form of δt comes about analogously from the stochastic solution to Beer's Law in Section 1.3.2.

- In the second term on the left side of the equation, from left to right, the opacities are the composite leakage opacities, the effective out-scattering opacity for g, and the effective absorption opacity. The effective scattering term is referred to as "out-scattering" since scattering is not simulated within DDMC groups; a trivial example is grey DDMC, in which $\gamma_{i,g,n} = 1$ and effective scattering is not directly modelled at all. If $\delta t_{\text{DDMC}} = \delta t$, then the next DDMC event can be sampled from a histogram of discrete probabilities for each opacity; for instance the probability of effective absorption in cell i and group g is

$$\frac{f_{i,n}\sigma_{a,i,g,n}}{\sum_{i'}\tilde{\sigma}_{i\rightarrow i',g}+(1-\gamma_{i,g,n})(1-f_{i,n})\sigma_{a,i,g,n}+f_{i,n}\sigma_{a,i,g,n}}.$$

- The first term on the right is the effective thermal emission source in cell-group (i, g) for time step n.
- The second term on the right is the source due to DDMC leakage from adjacent cells with groups that overlap the group g. The DDMC process accounts for this source by having particles that sample a leakage event sub-sample the target group in the adjacent cell from the composite leakage opacity formula.
- The third term on the right is analogous to the second term but for IMC transition from cells i' to group g in cell i. The IMC process accounts for this source by directly tracking IMC particle frequency through collisions and relativistic transformation; when an IMC particle, p, crosses the boundary to DDMC cell i, it is automatically in g if $\nu_{0,p} \in [\nu_{g+1/2}, \nu_{g-1/2}]$ and sampling $P_{b(i,i')}/G_U$ permits the IMC-to-DDMC transition. The weight of an IMC particle incident on cell i is multiplied by G_U if the particle is transmitted to DDMC or diffusively reflected back into the IMC region.
- The fourth term on the right side is a source due to IMC particles effectively scattering into the DDMC group, g.
- The fifth and last term on the right side of the equation is a source due to DDMC particles effectively out-scattering into group g.

When an IMC particle transitions to DDMC, the position, direction, and resolved frequency are no longer tracked with full resolution. Conversely, when a DDMC particle transitions to IMC, its position, direction and frequency must be sampled from probability distributions. If the transition occurs in a cell transition, then the IMC particle can be placed isotropically on the surface of the cell.

Otherwise, if the transition occurs in a cell's interior, then the particle can be sampled uniformly in the cell volume or with a source tilt. If the opacity is only elastic scattering, then the change in frequency from Doppler shift should match the change in particle energy from Doppler shift; hence if the frequency is known initially, then its final value should be known. Otherwise if there is an absorption opacity, then the frequency may be sampled with a subgroup distribution. DDMC is determined to be applicable to a cell-group, (i, g), if the number of mean free paths across a characteristic dimension of cell i for the opacity in group g is higher than a user-determined or heuristic threshold value, τ_D.

The two other equations from operator splitting the comoving diffusion equation must have solution techniques as well. The Doppler shift equation, Eq. (3.95), can be reduced to

$$\frac{\partial\phi_{0,g}}{\partial t} + \frac{\phi_{0,g}}{t_n} = \frac{\nu_{g-1/2}}{t_n}\phi_{0,\nu_{g-1/2}} - \frac{\nu_{g+1/2}}{t_n}\phi_{0,\nu_{g+1/2}} \ , \tag{3.111}$$

where use has been made of the homologous relation, Eq. (3.6), and Eddington's approximation, $\mathbf{P}_{0,\nu_0} = \mathbf{I}\phi_{0,\nu_0}/3c$ [19, p. 83]. Doppler shifting from the higher (lower) frequency group edge, $g - 1/2$ ($g + 1/2$), acts as a source (sink). From the homogeneous form of the equation, following Abdikamalov et al. [2], it is inferred that the change to a DDMC particle weight for a time step, n, is $E_{0,p} \rightarrow E_{0,p}e^{-\Delta t_n/t_n}$. Considering the effect of inelastic scattering on the model problem in Section 3.1.2, the following algorithm is suggested to adjust frequency for DDMC particles:

1. For each particle: redshift particle energy weight. For a homologous expansion, the energy weight is multiplied by $e^{-\Delta t_n/t_n}$.
2. For the particle's current cell and group, (i, g), determine the inelastic opacity. If only absorption, then $\sigma_{a,i,g,n}$ is the inelastic opacity.
3. Make a uniformly random sample, $\xi \in [0, 1]$.
4. If $\xi \leq \frac{\nu_{g+1/2}}{ct\Delta\nu_g}/(\frac{\nu_{g+1/2}}{ct\Delta\nu_g} + \sigma_{a,i,g,n})$, sample comoving frequency in the group then multiply comoving frequency by $e^{-\Delta t_n/t_n}$. Otherwise, do not sample or redshift comoving frequency.

The first step ensures grey outflow radiation diffusion problems are solved correctly [73, p. 474]. If

(i, g) only has elastic scattering, then $\nu_{0,p}$ is updated in the same manner as particle energy weight in IMC and DDMC. The source particle frequency is constrained to be uniform at the subgroup level; for pure elastic scattering problems, the fourth step above then should emulate the cumulative progression of redshift from elastic scattering in IMC. The fourth step heuristically mitigates frequency shift when redistribution is a strong effect. In terms of Section 3.1.2, the condition in the fourth step is similar to $\xi \leq \varepsilon$, where ε is the asymptotic parameter that scales inelastic scattering to be a dominant collision.

The remaining operator split equation to consider for IMC-DDMC is the equation for advection and expansion, Eq. (3.96). For DDMC, it is inferred from Eq. (3.96) that particles are moved along with the grid. Consequently, in velocity space, DDMC particles stay in their cell at census. For IMC, the velocity position update scheme, delineated in Section 3.1.1 must be modified to incorporate the event of an IMC particle being moved onto a DDMC cell. For an IMC particle indexed with p, the following algorithm is used:

1. Find current fluid cell i from $\vec{U}_{p,\text{old cen}}$ and expected fluid cell i' from $\vec{U}_{p,*\text{ cen}}(t_n + \alpha_2\Delta t_n + t_{\text{min}}) = \vec{U}_{p,\text{old cen}}(t_n + t_{\text{min}})$.
    (a) For the first diffusive cell i'' that passes particle p in the span of $\alpha_2\Delta t$, set particle p's velocity position to the point it would pass on the surface of i'', $\vec{U}_{p,*\text{ cen}} = \vec{U}_{p,b}$.
    (b) If there are no DDMC cells that pass p in $\alpha_2\Delta t$, then set $i = i'$ and use formula from step (1) for $\vec{U}_{p,*\text{ cen}}$.
2. IMC-DDMC: $\vec{U}_{p,*\text{ cen}} \to \vec{U}_{p,*}$
3. If p has become a DDMC particle, the position update is finished.
4. Otherwise, use $\vec{U}_{p,\text{new cen}}(t_n + \Delta t_n + t_{\text{min}}) = \vec{U}_{p,*}(t_n + \alpha_2\Delta t_n + t_{\text{min}})$ to find fluid cell i'.
    (a) For the first diffusive cell i'' that passes particle p in the span of $(1 - \alpha_2)\Delta t$, set particle p's velocity position to the point it would pass on the surface of i'', $\vec{U}_{p,\text{new cen}} = \vec{U}_{p,b}$.
    (b) If there are no DDMC cells that pass p in $(1 - \alpha_2)\Delta t$, then set $i = i'$ and use formula from step (4) for $\vec{U}_{p,\text{new cen}}$.

If a particle is placed on the spatial surface of a DDMC cell-group, then if the particle is directed into the cell it will automatically sample the diffusion-limit probability. Otherwise, if the particle is directed away from the DDMC cell, it will not be forced to transition to DDMC. This approach is conceived with a thought experiment. If a photon is in a vacuum region just outside an optically thick, expanding fluid that expands over the particle position during the advection/expansion update, then the IMC particle would be trapped and possibly destined to never escape. When the photon is directed away from the expanding fluid, or along the direction of expansion, then because it is always moving faster than the fluid it should not ever be caught and subsequently trapped.

In the preceding sections, features of the IMC-DDMC method have been discussed with emphasis on the novel aspects of the IMC-DDMC implementation in the code, `SuperNu`. In Section 3.1.4, an optimization that combines DDMC groups is described. In addition to increasing the efficiency of simple problems, this optimization, termed opacity regrouping, is found to be essential to solving the W7 Type Ia supernova model with IMC-DDMC in a reasonable span of time (<O(days)).

3.1.4 Opacity Regrouping

With inelastic opacity, a DDMC particle frequency at the subgroup level is unknown [30, 104]. Since single DDMC steps replace multiple IMC steps, if the replaced IMC steps would have included several effective scatters, then the DDMC particle after one step should have a different frequency relative to its initial value. The requirement to resample is similar to the IMC random walk scheme [36]. For multigroup DDMC, distinct DDMC groups can have particles scatter back and forth; in certain calculations this process may deteriorate code efficiency. However, there is no theory implied by the equations that precludes regrouping disjoint DDMC groups into larger groups. We extend the group-collapsed DDMC scheme of Densmore et al. [30] to allow DDMC particles to be identified with multiple, possibly non-contiguous, groups across the entire span of frequency covered by the group grid.

The process of opacity regrouping involves combining DDMC frequency intervals and properties corresponding to DDMC frequency intervals to make larger groups. This scheme was devised by Densmore et al. [30] as an approximation of an adaptive threshold frequency between grey

DDMC and multigroup IMC. Since the set of groups is divided into a DDMC set and an IMC set (see Section 3.1.3), the DDMC groups corresponding to a set of frequency intervals do not have to match the set of IMC groups corresponding to the same set of frequency intervals. Equation (3.108) accommodates adaptive grouping, unaligned groups at spatial boundaries, and opacity regrouping.

To illustrate the opacity regrouping process, we consider a subset with subindex $l \in \{1 \dots L\}$ of a resolved group structure. Groups that satisfy given regrouping criteria belong to the subset and form a group denoted $\cup_{l=1}^{L} g_l$. The union $\cup_{l=1}^{L}$ implies a union of the frequency intervals for each group index g_l. The regrouped absorption opacity is set to

$$\sigma_{a,i,\cup_l g_l,n} = \frac{\sum_{l=1}^{L} b_{i,g_l,n}\sigma_{a,i,g_l,n}}{\sum_{l=1}^{L} b_{i,g_l,n}} \quad . \tag{3.112}$$

Similarly, the regrouped leakage opacity is

$$\tilde{\sigma}_{i\to i',\cup_l g_l} = \frac{\sum_{l=1}^{L} b_{i,g_l,n}\tilde{\sigma}_{i\to i',g_l}}{\sum_{l=1}^{L} b_{i,g_l,n}} \quad . \tag{3.113}$$

Incorporating Eq. (3.106) into Eq. (3.113) yields

$$\begin{aligned} \tilde{\sigma}_{i\to i',\cup_l g_l} = \left(\sum_{l=1}^{L} b_{i,g_l,n}\right)^{-1} \times \\ \sum_{l=1}^{L}\left[\sum_{g'_D} b_{i,g_l\leftrightarrow g'_D}\sigma_{i\to i',g_l\to g'_D} + \sum_{g'_T} b_{i,g_l\leftrightarrow g'_T,n}\sigma_{b(i,i'),g_l\to g'_T}\right] \quad . \end{aligned} \tag{3.114}$$

If a leakage event from $\cup_{l=1}^{L} g_l$ is sampled, the probability of leaking to an interfacing group g'_D is $(\tilde{\sigma}_{i\to i',\cup_l g_l}\sum_{l=1}^{L} b_{i,g_l,n})^{-1}\sum_{l=1}^{L} b_{i,g_l\leftrightarrow g'_D}\sigma_{i\to i',g_l\to g'_D}$. The regrouped term responsible for the increase in efficiency over DDMC without regrouping is

$$\gamma_{i,\cup_l g_l,n} = \sum_{l=1}^{L}\gamma_{i,g_l,n} \quad , \tag{3.115}$$

which reduces overall effective scattering since a DDMC particle in g_l may no longer scatter to $g_{l'}$ if these groups are in $\cup_{l=1}^{L} g_l$. Equations (3.112)-(3.115) may be used in place of the non-opacity-regrouped (non-OR) counterparts in Eq. (3.108) to solve Eq. (3.108) for a regrouped intensity, $\phi_{0,i,\cup_l g_l}$. The values indexed by g_D in the last term on the right hand side of Eq. (3.108) correspond to DDMC groups not used to construct $\cup_{l=1}^{L} g_l$.

Regrouping opacities may cause a loss in accuracy of the distribution of the radiation field over the groups. However, the use of the Planck function in weighting the group quantities for regrouping may suffice when effective scattering is a dominant interaction. For the many of the problems described in Section 3.3, effective scattering is a dominant effect.

Similarly to τ_D, a mean-free path threshold, τ_L, is used to determine which DDMC groups are regroupable. The opacity regrouping algorithm is described as follows:

1. For each particle: find current cell and group, (i, g), and measure the inelastic collision mean free paths. For absorption, $t_n \Delta U_i \sigma_{a,i,g,n}$ is a measure of effective scattering and effective absorption mean free paths.

2. If $t_n \Delta U_i \sigma_{a,i,g,n} > \tau_L$, then search about g for neighboring groups g_l in cell i satisfying $t_n \Delta U_i \sigma_{a,i,g_l,n} > \tau_L$.

3. For the set of frequencies corresponding to $\cup_l g_l$ where $g \in \cup_l g_l$, apply Eqs. (3.112), (3.114), and (3.115).

4. Perform a DDMC step for each particle to leak into adjacent cell, effectively scatter out of group $\cup_l g_l$, get absorbed, reach census.

5. If not censused, return to first step.

To incorporate the opacity regrouping scheme into the operator split, comoving DDMC method, DDMC particles sample a resolved group after finishing the “transport” step within the time step. Consequently, for the Doppler shift step to solve Eq. (3.111), each particle has a group represented by a connected frequency interval.

For static grid problems, where $\vec{U} = 0$, IMC particles are tracked in space and relativistic corrections are removed. DDMC is only required to solve Eq. (3.108); there is no Doppler shift or implied particle advection.

3.2 Code Summary

`SuperNu` is a domain-replicated parallel, one-dimensional, Monte Carlo radiative-transfer code written in the Fortran programming language. The code implements 1D, spherically symmetric Implicit Monte Carlo (IMC) and Discrete Diffusion Monte Carlo (DDMC) for either static material or a homologous velocity field. Grid input data can be generated for certain problems by subroutines or can be read from data files. Default spatial and temporal grids are uniform and default wavelength grids are logarithmic. The spatial topology can be set to either be a simply connected sphere or a shell. A user can specify if input data for velocities, densities, temperatures, and composition are read or generated. The code runs in parallel with Message Passing Interface (MPI). Parallelization is achieved by dividing the MC particles amongst the processors. There is one master rank, or processor, dedicated to initializing the simulation, calculating opacities, and updating material properties. The master rank also transports a fraction of the particles.

The main program calls initialization subroutines and possesses the main physical time step loop. In order, for each time step, the subroutines within the time step loop: update material (excluding temperature) and grid properties including opacities, calculate the new number of source particles within a volume or at a surface, find vacant indexes in the particle array, instantiate surface particles, instantiate volume particles, propagate particles with IMC-DDMC and tally radiation energy density, calculate new material temperature, and check energy conservation (account for all particle energy losses, gains, and material coupling). The main program and subroutines have access to several modules. Each module contains variables, including derived data types, and subroutines associated with the variables in the module. There are modules for: reading and parsing input parameters; gas grid properties; reading (e.g. W7 data) or generating material structures; timing diagnostics and particle load balance; physical time step parameters; `SuperNu`-specific MPI variables and subroutines; physical constants; the particle data type and variables; reading bound-bound, bound-free, and free-free opacity data; solving material ionization state; and storing variables for analytic verifications.

For each time step, output includes: luminosity per group (erg/s), number of escaped particles per group, material temperature (K), radiation energy density (erg/cm^3), conservation error, timing data, Fleck factor values, and the number of IMC-DDMC method transitions per cell.

3.3 Numerical Results

Numerical results are described and presented to test the code, `SuperNu`. Tests include radiation transport for static material and homologously expanding fluid. For the figure legends, data from simulations with pure IMC or pure DDMC are labelled “IMC” or “DDMC,” respectively. Data from simulations applying IMC-DDMC are labelled “HMC” (hybrid Monte Carlo). Descriptions of additional labels are provided in the sections where they occur.

3.3.1 Static Grid Problems

Thermal P_1 Test

The following discussion and verification is extracted from the article by Wollaeger et al. [104]. The benchmark is a minor extension to a solution of McClarren [68] for the thermally coupled, radiative P_1 equations. The P_1 equation is an approximation to the transport equation that is valid for optically thick domains. In terms of time-dependence, in taking the zeroth and first angular moments of the transport equation, the local time derivative of the flux vector is not assumed to be negligible. Consequently, the P_1 equation is distinct from the diffusion equation. For the purpose of testing rudimentary frequency dependence, the picket-fence opacity distribution of Su and Olson [94] can be incorporated into the P_1 solution of McClarren. Su and Olson have used the picket-fence opacity to derive semi-analytic solutions to the radiation transport and diffusion equations. With some constraints on the values of the picket-fence distribution, a closed analytic solution to the P_1 equation can be obtained. Relative to transport, the P_1 solution has a slower wave speed [68]. The benchmark problem used starts at an initial time after the P_1 and transport solutions have had enough time to propagate through a 100 mean-free path domain. Thus, the spatial and temporal domains allow for good agreement between IMC, DDMC, and the P_1 solutions.

The picket-fence opacity can be thought of as the limit of a multigroup opacity distribution, over all frequency, as group sizes tend to zero. In this limit, the set of each picket frequency is dense over the positive real number line; within any frequency interval of finite width, the frequency subsets of either picket is non-empty. For a picket-fence distribution with two distinct opacity values, or two pickets, a fraction p_1 of the group intervals have opacity σ_1 while the remainder p_2 has opacity σ_2 [94]. For finite group sizes, $\Delta\nu_g$, the opacity distribution can be thought of as invariant under translation across frequency by $\Delta\nu_g$.

In the limit as $\Delta\nu_g \to 0$, the thermal emission and external source no longer vary significantly in $\Delta\nu_g$ and the P$_1$ equations can be separated by picket [94]. Consequently, the integrals of the equations for I_ν and B_ν over the dense frequency sets can be simplified to coupled group equations (or “two temperature”) [94].

Neglecting scattering, taking the zeroth and first angular moments of Eq. (1.3), and integrating the result over the set of frequencies that only yield a contribution from picket $g \in \{1, 2\}$, the thermal picket fence P$_1$ equations in planar 1D geometry are

$$\frac{1}{c}\left(\frac{\partial E_g}{\partial t} + \frac{\partial F_g}{\partial z}\right) = \sigma_g(p_g a T^4 - E_g) + p_g S \ , \tag{3.116}$$

$$\frac{1}{c}\frac{\partial F_g}{\partial t} + \frac{c}{3}\frac{\partial E_g}{\partial z} = -\sigma_g F_g \ , \tag{3.117}$$

$$\frac{C_v(T)}{c}\frac{\partial T}{\partial t} = \sum_{g'=1}^{2} \sigma_g E_g - \bar{\sigma} a T^4 \tag{3.118}$$

where z is the spatial coordinate, $E_g = \phi_g/c$ is the radiation energy density, $\bar{\sigma} = p_1\sigma_1 + p_2\sigma_2$ and S is an external source. To linearize the system of equations, it is customary to set the heat capacity proportional to the cube of temperature, $C_v(T) = a'T^3$ [68, 94]. With the non-dimensionalizations of McClarren and Su and Olson [68, 94],

$$x = \bar{\sigma} z \ , \ \ \epsilon = \frac{4a}{a'} \ , \ \ \tau = \epsilon c \bar{\sigma} t \ , \ \ w_g = \frac{\sigma_g}{\bar{\sigma}} \tag{3.119}$$

and

$$\mathcal{E}_g = \frac{E_g}{aT_r^4} \ , \ \ \mathcal{F}_g = \frac{F_g}{aT_r^4} \ , \ \ \mathcal{M} = \frac{T^4}{T_r^4} \ , \ \ Q = \frac{S}{\bar{\sigma} a T_r^4} \ , \tag{3.120}$$

where T_r is a reference temperature. The equations for the non-dimensional variables are

$$\epsilon\frac{\partial\mathcal{E}_g}{\partial\tau}+\frac{1}{c}\frac{\partial\mathcal{F}_g}{\partial x}=w_g(p_g\mathcal{M}-\mathcal{E}_g)+p_gQ \ \ , \tag{3.121}$$

$$\epsilon\frac{\partial\mathcal{F}_g}{\partial\tau}+\frac{c}{3}\frac{\partial\mathcal{E}_g}{\partial x}=-w_g\mathcal{F}_g \ \ , \tag{3.122}$$

and

$$\frac{\partial\mathcal{M}}{\partial\tau}=\sum_{g'=1}^{2}w_g\mathcal{E}_g-\mathcal{M} \ \ . \tag{3.123}$$

Taking the Laplace transform of Eqs. (3.121), (3.122), and (3.123) in time and making substitutions to remove $\mathcal{M}$, the result is two fourth-order ordinary linear differential equations for the two radiation energies over space. The coefficients of the equations are functions of s. The system can be solved numerically; in other words a numerical inverse Laplace transform of the transformed solution, $\tilde{\mathcal{E}}_g(x,s)$, may be employed. Alternatively, to leverage the analytic work of McClarren, the picket-fence distribution can be constrained so that $w_1/w_2 \ll 1$. Additionally, the opacity for $g=2$ is constrained to be dependent on the heat capacity, or

$$w_2=\epsilon \ \ . \tag{3.124}$$

Equation (3.124) does not have any physical motivation or significance but is a means of a obtaining closed-form, analytic solution of Eqs. (3.121), (3.122), and (3.123). Furthermore, the source is a Dirac delta function in space and time, $Q=\delta(x)\delta(t)$; hence the solution obtained may be used as a kernel for other source distributions [68]. The Fourier-Laplace transformed system of equations is

$$(k^2+3\epsilon^2s^2)\tilde{\tilde{\mathcal{E}}}_1=3\epsilon s\left(1-\frac{1}{\epsilon}\right) \ \ , \tag{3.125}$$

$$(k^2+3\epsilon^2s(s+2))\tilde{\tilde{\mathcal{E}}}_2=3(s+1) \ \ , \tag{3.126}$$

$$(s+1)\tilde{\tilde{\mathcal{M}}}\approx w_2\tilde{\tilde{\mathcal{E}}}_2 \ \ , \tag{3.127}$$

where double tilde indicates a Fourier-Laplace transformed quantity. Equations (3.125), (3.126), and (3.127) may be used trivially as the starting points in McClarrens derivation; the derivation is not repeated here. The solution to Eqs. (3.125), (3.126), and (3.127) are

$$\mathcal{E}_1 = \left(1 - \frac{1}{\epsilon}\right) \frac{\sqrt{3}}{2} \delta(\tau - \epsilon\sqrt{3}|x|) \ , \tag{3.128}$$

$$\mathcal{E}_2 = \frac{1}{\epsilon}\frac{\sqrt{3}}{2} e^{-\tau} \times \left[\frac{\tau I_1(\sqrt{\tau^2 - 3\epsilon^2 x^2})}{\sqrt{\tau^2 - 3\epsilon^2 x^2}} \Theta(\tau - \epsilon\sqrt{3}|x|) + I_0(\sqrt{\tau^2 - 3\epsilon^2 x^2}) \delta(\tau - \epsilon\sqrt{3}|x|) \right] \ , \tag{3.129}$$

and

$$\mathcal{M} = \frac{\sqrt{3}}{2} e^{-\tau} I_0(\sqrt{\tau^2 - 3\epsilon^2 x^2}) \Theta(\tau - \epsilon\sqrt{3}|x|) \tag{3.130}$$

where Θ is the Heaviside function, and I_0 (I_1) is the 0-order (1-order) modified Bessel function. Setting $\epsilon = 1$ yields the grey kernel solution of McClarren. Equations (3.128), (3.129) and (3.130) are P_1 solutions for planar geometry. The plane-to-point Green's function mapping may be employed to obtain the solutions in spherically symmetric coordinates [68],

$$G_{\mathrm{point}}(r, \tau) = -\frac{1}{2\pi r} \left. \frac{\partial G_{\mathrm{plane}}}{\partial x} \right|_{x=r} \ , \quad r > 0 \ , \tag{3.131}$$

where G_{point} and G_{plane} are the Green functions for 1D spherically symmetric and 1D planar geometry, respectively. For the benchmark presented here, only the material temperature kernel, Eq. (3.130), is mapped to spherical coordinates and compared to the temperature output of `SuperNu`. The spherical material temperature coordinate is

$$\mathcal{M}(r, \tau) = \frac{3\sqrt{3}}{4\pi} e^{-\tau} \epsilon^2 \frac{I_1(\sqrt{\tau^2 - 3\epsilon^2 r^2})}{\sqrt{\tau^2 - 3\epsilon^2 r^2}} \Theta(\tau - \epsilon\sqrt{3} r) + \frac{3}{4\pi} e^{-\tau} I_0(\sqrt{\tau^2 - 3\epsilon^2 r^2}) \epsilon \frac{\delta(\tau - \epsilon\sqrt{3} r)}{r} \ . \tag{3.132}$$

For the test, $\epsilon = 2$. For the numerical set-up, various cell resolutions are applied over a domain of 100 mean-free paths. The temporal domain ranges from 300 to 600 mean-free time and the time step size is fixed at three mean-free times for a total of 100 time steps. For particles, 400,000 source particles are generated per time step and 400,000 initial particles serve as the initial radiation field. With IMC, we have not discovered a way to model a source that is proportional to a Dirac delta function directly. Instead, the analytic P_1 solution is used to initialize the material temperature at a time after the initial radiation pulse. For IMC or IMC-DDMC to correctly solve the problem, radiation generated in the optically thin picket must stream out of the domain and not couple strongly to the material. Figures 7a and 7b have material temperature profiles for 15 and 50 spatial cells, respectively, along with the P_1 solution, versus the number of radial mean free paths.

By using a large number of particles per cell, a grid convergence test can be performed for the P_1 benchmark. The analytic P_1 temperature solution can be used as the exact answer in computing the error. For the domain and cell resolutions considered, the error IMC or DDMC and the P_1 solution decreases monotonically and does not appear to saturate. To remove statistical error, the minimum number of particles per cell in the spatial resolution tests is over 13,000. Figure 8 demonstrates that both IMC and IMC-DDMC achieve roughly linear convergence with the L_2 error norm.

The P_1 results indicate that DDMC computes temperature with higher fidelity at low cell resolution for this particular problem. The results verify that the IMC and IMC-DDMC implementations in `SuperNu` can produce an analytic result for static material.

Next, opacity regrouping is tested in static material for a problem with monotonic opacity dependence on frequency.

Monotonic Opacity Regrouping Test

Here, 30 groups are used to verify the code can produce results presented by Densmore et al. [30] and have opacity regrouping accelerate the IMC-DDMC calculation. The results of Densmore et al. [30] are for planar geometry; to approximate planar geometry, the domain is set as a shell with a non-zero inner radius that is large compared to the radial thickness of the domain. Apart from grid specifications, the opacity, heat capacity, boundary, and initial conditions are adapted from the

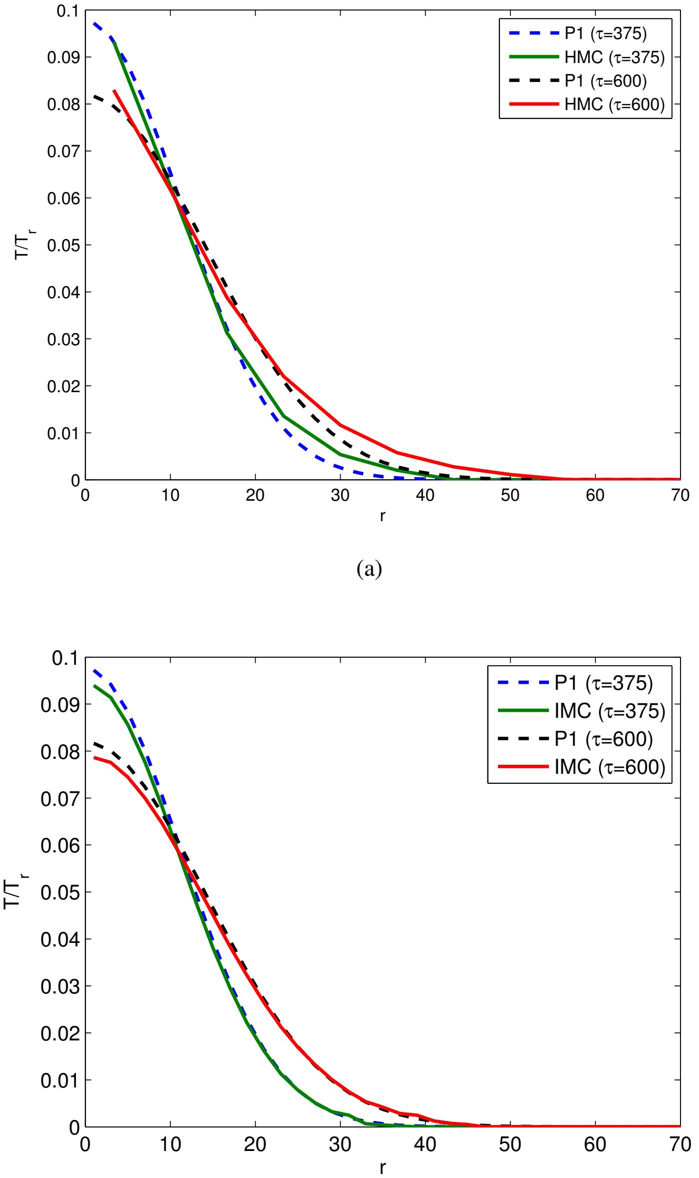

(a)

(b)

Figure 7: Solutions to the picket-fence opacity problem in Section 3.3.1. P_1 (dashed) and IMC-DDMC (solid) unitless material temperature profiles at two different (mean free) times plotted as a function of unitless radius (mean free paths). In Fig. 7a, with 15 cells, DDMC couples to the material and IMC streams. In Fig. 7b, with 50 cells, IMC is applied to both pickets.

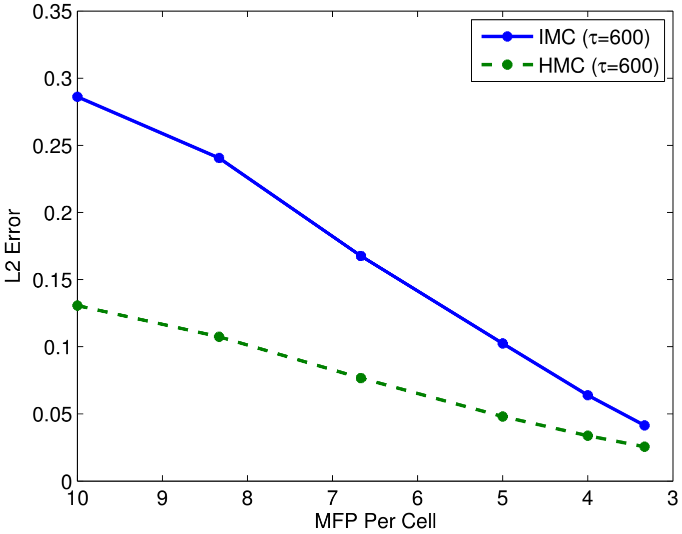

Figure 8: IMC (solid) and IMC-DDMC (dashed) L_2 temperature error relative to the P_1 solution plotted over the number of mean free paths per cell at 600 mean free times.

presentation by Densmore et al. [30].

The radial domain spans from 1×10^9 cm to 1.05×10^9 cm, the time span is 1 ns, and the wavelength grid spans 1.2398×10^{-9} to 1.2398×10^{-3} cm. The heat capacity, $C_v = 8.617343 \times 10^9$ erg/K/cm^3, and the opacity is purely absorbing [30],

$$\sigma_\nu = \sigma_{a,\nu} = \frac{\sigma_0}{\sqrt{kT}} \frac{1}{(h\nu)^3} \quad , \tag{3.133}$$

where k and h are the Boltzmann and Planck constants, respectively, and σ_0 is a constant to control optical thickness for all frequency. The grouped opacity is obtained by integrating Eq. (3.133) over frequency. The initial temperature in the domain is set uniformly to 11,604.505 K, or 1 eV. At the inner domain radius, there is an isotropic surface source at a temperature of 11,604,505 K, or 1 keV.

For the grids, there are 50 uniform spatial cells, 100 uniform time steps, and 30 logarithmic wavelength groups. Additionally, 100,000 source particles are generated per time step. For IMC-DDMC, the DDMC threshold, $\tau_D = 5$, and, for IMC-DDMC with opacity regrouping, the opacity regrouping threshold, $\tau_L = 5$. The problem is solved with pure IMC, non-opacity-regrouped (non-OR) IMC-DDMC ("UHMC"), and IMC-DDMC with opacity regrouping ("HMC"). To our knowl-

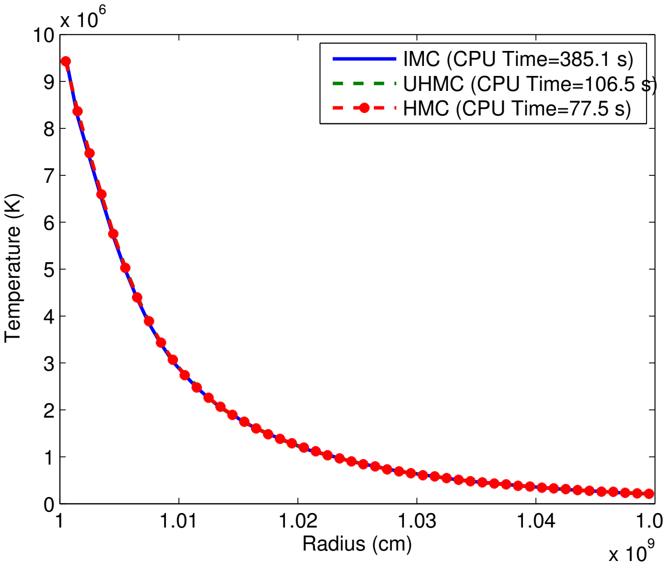

Figure 9: IMC (solid blue), non-OR IMC-DDMC (dashed green), and opacity-regrouped IMC-DDMC (dot-dashed red) material temperature versus radius for the monotonic opacity regrouping problem with $\sigma_0 = 5.32345 \times 10^{18}$ K$^{7/2}$/cm.

edge, there does not exist an analytic solution for this problem. Consequently, IMC is employed as the benchmark for the IMC-DDMC tests.

In Figs. 9, 10, and, 11, plotted are the different MC solutions with σ_0 set to 5.32345×10^{18} K$^{7/2}$/cm, 5.32345×10^{19} K$^{7/2}$/cm, and 5.32345×10^{20} K$^{7/2}$/cm, respectively. Each simulation is performed on one core; the CPU times are listed in the legends.

Increasing σ_0 increases the amount of DDMC applied over the spectrum, and in the case of opacity-regrouped IMC-DDMC, increases the amount of opacity regrouping as well. Consequently, the difference in CPU time amongst IMC, non-OR IMC-DDMC, and opacity-regrouped IMC-DDMC becomes more pronounced with increasing σ_0. For $\sigma_0 = 5.32345 \times 10^{20}$ K$^{7/2}$/cm, the speed-up with each optimization is most dramatic. Table 2 has the CPU times for each test.

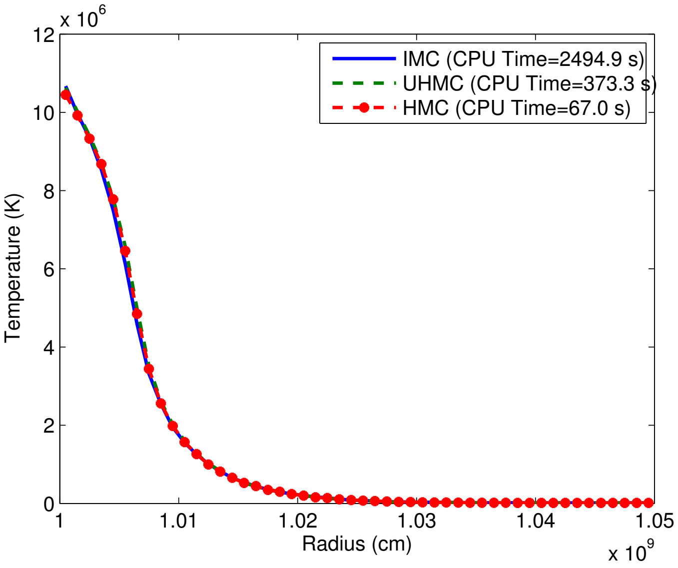

Figure 10: IMC (solid blue), non-OR IMC-DDMC (dashed green), and opacity-regrouped IMC-DDMC (dot-dashed red) material temperature versus radius for the monotonic opacity regrouping problem with $\sigma_0 = 5.32345 \times 10^{19}$ $\mathrm{K}^{7/2}$/cm.

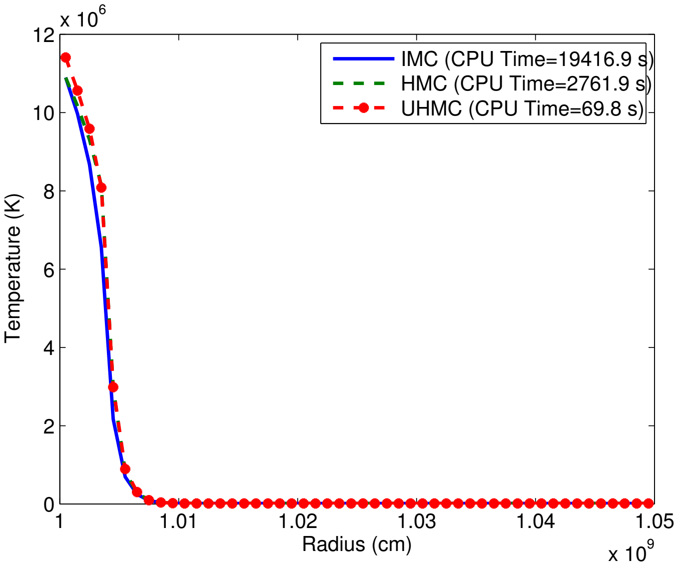

Figure 11: IMC (solid blue), non-OR IMC-DDMC (dashed green), and opacity-regrouped IMC-DDMC (dot-dashed red) material temperature versus radius for the monotonic opacity regrouping problem with $\sigma_0 = 5.32345 \times 10^{20}$ $\mathrm{K}^{7/2}$/cm.

Table 2: Monotonic Opacity Computation Times (minutes)

σ_0 (K$^{7/2}$/cm) Method	IMC	non-OR IMC-DDMC	OR IMC-DDMC
5.32345×10^{18}	6.42	1.76	1.29
5.32345×10^{19}	41.58	6.22	1.12
5.32345×10^{20}	323.62	46.03	1.16

For the tests presented, the solutions from the different methods along with the CPU times provide evidence that the methods are functioning properly.

3.3.2 Velocity-Dependent Problems

Here, a one-group quasi-manufactured solution, a two-group manufactured solution, and a ten-group step-source problem are presented in the domain of a velocity field with a maximum speed of 10^9 cm/s, or roughly 3% the speed of light. The general Method of Manufactured Solutions (MMS) is described by Oberkampf and Roy [77, p. 219]. MMS involves postulating, or manufacturing, an analytic solution, incorporating the manufactured solution into the system of equations, evaluating the additional terms that appear in the system, and incorporating the additional terms as sources in the code that solves the system. This approach has been explored for discrete ordinates transport [100] and radiation-hydrodynamics with the P_1 approximation [69].

The one-group, grey verification demonstrates the "temperature-flip" IMC pathology can occur in high-velocity outflows. The inclusion of the Gentile-Fleck factor greatly mitigates the error and prevents the radiation temperature from non-physically dropping below the material temperature in the first time step. The optimized form of the opacity derivative with respect to temperature, Eq. (3.32), is used in this test. A problem set-up for the pathology in static material is described by Gentile [42]; values for the quasi-manufactured test are adapted from the values used by Gentile. The temperature-flip represents an extreme violation of the IMC maximum principle derived by Larsen and Mercier [60] and with spatial grid effects by Wollaber et al. [101].

Both the two-group and ten-group problems are used to verify that the Doppler shift scheme, presented in Section 3.1.3 and motivated by the asymptotic analysis in the second part of Section 3.1.2, functions in the limits of elastic scattering and pure absorption with dominant effective scattering. The ten-group step source test provides evidence that the IMC-DDMC boundary condition, derived from the asymptotic analysis in the first part of Section 3.1.2, is an improvement over the static-grid, diffusion-limit boundary condition.

The multigroup step source problem is also used to provide evidence that opacity regrouping of non-contiguous groups improves computational efficiency. Moreover, for the 10-group, step source problem, the temperatures and spectrum do not seem significantly modified relative to non-OR IMC-DDMC.

One-Group Quasi-Manufactured Test

The problem is spatially independent and grey; hence the equations to be solved are

$$\frac{\partial E}{\partial t} + \frac{4}{t}E = c\sigma(T)(aT^4 - E) + S_m \ , \tag{3.134}$$

and

$$C_v\frac{\partial T}{\partial t} = c\sigma(T)(E - aT^4) \ , \tag{3.135}$$

where E is comoving radiation energy density and S_m is a manufactured source. Until the manufactured answer is given for radiation energy density, the manufactured source is unknown. The heat capacity $C_v = \rho c_v$ and the opacity is

$$\sigma(T) = \frac{\kappa\rho}{T^5} \ , \tag{3.136}$$

where c_v and κ are constants. Manufacturing the comoving radiation energy density as a constant, the time dependence of the material temperature is solved and the manufactured source can be obtained from

$$S_m = \frac{4}{t}E + C_v\frac{\partial T}{\partial t} \ , \tag{3.137}$$

where Eqs. (3.134) and (3.135) have been summed. If the material temperature increases monotonically in time, then the source, S_m, should be monotonic in time as well. Following Gentile [42], Eq. (3.135) is

$$\left(\frac{(E/a)T}{E/a-T^4}-T\right)\frac{\partial T}{\partial t}=\frac{ac\kappa}{c_v}\ \ , \tag{3.138}$$

where ρ is removed by dividing of $\sigma(T)$ by C_v. The solution of Eq. (3.138) is

$$\frac{1}{4}\sqrt{\frac{E}{a}}\ln\left(\frac{[\sqrt{E/a}+T^2][\sqrt{E/a}-T_1^2]}{[\sqrt{E/a}-T^2][\sqrt{E/a}+T_1^2]}\right)-\frac{1}{2}(T^2-T_1^2)=\frac{ac\kappa}{c_v}(t-t_1)\ \ , \tag{3.139}$$

where t_1 and T_1 are the initial time and initial material temperature, respectively.

For the data that will be used the time to equilibrium is on the order of 10^{91} seconds. The time domain of the simulations are much smaller, and it may be assumed that $T^2, T_1^2 \ll (E/a)^{1/2} = T_r^2$. Only considering early time, $t \ll 10^{91}$ s, the solution of Eq. (3.139) for material temperature is approximately

$$T(t)=T_r(e^{2ac\kappa(t-t_1)/c_v}-1)^{1/2}+T_1\ \ , \tag{3.140}$$

and the time step-integrated manufactured radiation source is approximately

$$\Delta t_n S_{m,n}=\frac{4}{t_n}E\Delta t_n+C_{v,n}(T_{n+1}-T_n)\ \ , \tag{3.141}$$

for small time steps. With the problem set-up and approximations, the manufactured source is positive-definite.

Ten spatial cells are used over a homologous outflow with a maximum speed of 10^9 cm/s. The material temperature is uniformly initialized to 116,045.05 K and the manufactured radiation temperature is set to 17,001,992.366 K. Starting from an expansion time of 2 days, the physical time span for the calculation is only a 10th of a millisecond, or $t \in [2, 2+1.1574\times10^{-9}]$ days. Both 100 and 1000 time steps are applied. The manufactured source, Eq (3.141), is uniform in space. The total mass, $M = 1\times10^{33}$ g, and the density is set to be uniform in space as well. Additionally, the fluid properties are $\kappa = 1.421\times10^{35}$ cm^{2}K^5/g, $c_v = 9.3\times10^{17}$ erg/K/g. In Fig. 12a, the time evolution of the material and radiation temperature profiles show the temperature-flip in both IMC and DDMC when the standard Fleck factor is used. In Fig. 12b, it is demonstrated that the Gentile-Fleck factor prevents the temperatures from flipping; this is true even for the larger time steps of the 100 time step test.

Because the Gentile-Fleck factor generally increases effective scattering in IMC relative to the standard Fleck factor, it is very computationally expensive to attempt modified IMC to solve this problem. Consequently, in Fig. (12b), we have only tested modified DDMC, or DDMC modified by replacing the Fleck factor with the Gentile-Fleck factor, Eq. (2.20) optimized by Eq. (3.32). The implementation of the Gentile-Fleck factor has been found to be limited in its ability to correct pathologies associated with violating the maximum principle. This can be seen in the temporal shape of the temperatures in Fig. 12b; spurious over-deposition of radiation still occurs.

Two-Group Manufactured Test

For the two-group test, the solutions are fully manufactured. This tests consists of manufacturing a source in a pure-scattering group that has radiation Doppler shift into a mixed scattering, absorbing group. The Doppler shift must occur at the correct rate for each method to balance the source for each group and sustain invariant manufactured profiles. The resulting sources for this test are also positive definite. In other words, the temperature is not derived from the manufactured radiation energy density. Instead, the radiation intensity and material temperature are manufactured as

$$I_0(r,t) = \frac{\phi_m}{4\pi} \quad , \tag{3.142a}$$

$$T(r,t) = T_m = \left(\frac{\phi_m}{ca}\right)^{1/4} \quad , \tag{3.142b}$$

respectively, where the subscript m denotes manufacturing and ϕ_m is a manufactured scalar flux. Density is uniform in space, $\rho(t) = \frac{3M}{4\pi R(t)^3}$, where $R(t)$ is the outermost radial coordinate and M is the total mass. With $g \in \{1,2\}$, the absorption opacity is

$$\sigma_{0,\nu_0,a} = \begin{cases} \kappa_g \rho(t) \quad \text{, for } g = 2 \quad , \\ \\ 0 \quad \text{, for } g = 2 \quad , \end{cases} \tag{3.143}$$

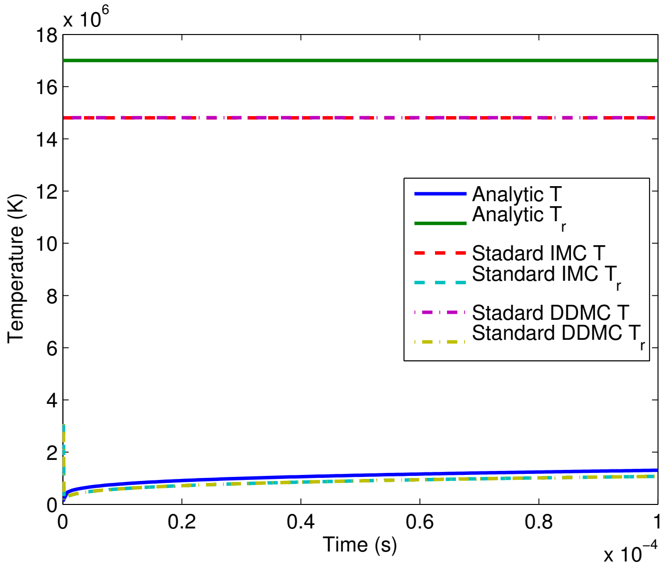

(a)

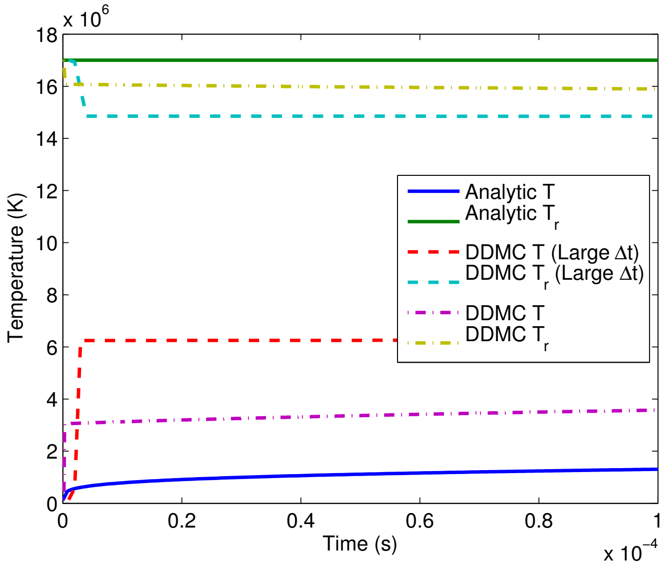

(b)

Figure 12: In Fig. 12a, manufactured (solid), standard IMC (dashed), and standard DDMC (dash-dotted) radiation temperatures (T_r) and material temperatures (T) for the quasi-manufactured problem with 1000 time steps. In Fig. 12b, manufactured (solid), modified DDMC with large time steps (dashed), and modified DDMC with small time steps. The Gentile-Fleck factor prevents the radiation and material temperatures from nearly trading places in the first time step, relative to the analytic manufactured solution.

and the scattering opacity is elastic,

$$\sigma_{0,s}(\nu_0' \to \nu_0, \hat{\Omega}_0' \cdot \hat{\Omega}_0) = \frac{\sigma_s(t)}{4\pi}\delta(\nu_0' - \nu_0) = \rho(t)\frac{\kappa_s}{4\pi}\delta(\nu_0' - \nu_0) \quad , \tag{3.144}$$

where κ_s is a constant. The frequency-resolved manufactured solution is

$$\varphi_{m,\nu_0} = \left(\frac{\sigma_s}{\sigma_g + \sigma_s}\right)\frac{\varphi_{m,s,g}}{\Delta\nu_g} + \left(\frac{\sigma_g}{\sigma_g + \sigma_s}\right)b_{\nu_0} \quad , \nu_0 \in [\nu_{g+1/2}, \nu_{g-1/2}] \quad , \tag{3.145}$$

where $I_{0,\nu_0} = I_0\varphi_{m,\nu_0}$, $\varphi_{m,s,g}$ is the uniform non-thermal contribution to g and b_{ν_0} is the normalized Planck function. For certain values of opacity, frequency group edges, and $\varphi_{m,s,g}$, the integral of φ_{ν_0} is unity.

Incorporating the manufactured solutions and opacities into the comoving transport equation and temperature update, the source terms are found to be

$$\frac{S_{m,\phi,\nu_0}}{\phi_m} = \frac{U_{\max}}{cR(t)}\left(3\varphi_{m,\nu_0} - \nu_0\frac{\partial\varphi_{m,\nu_0}}{\partial\nu_0}\right) + \sigma_g(\varphi_{m,\nu_0} - b_{\nu_0}(T_m)) \quad , \tag{3.146}$$

and

$$\frac{S_{m,T}}{\phi_m} = \sum_{g=1}^{G}\sigma_g(b_g(T_m) - \varphi_{m,g}) \quad , \tag{3.147}$$

where $U_{\max}$ is the maximum outflow speed at the outermost radius, $R(t)$, S_{m,ϕ,ν_0} is the manufactured source for the comoving transport equation, $S_{m,T}$ is the manufactured source for the temperature equation, and $\varphi_{m,g} = \int_{\nu_{g+1/2}}^{\nu_{g-1/2}}\varphi_{m,\nu_0}d\nu_0$. Integration of Eq. (3.146) over group g yields

$$\frac{S_{m,\phi,g}}{\phi_m} = \frac{U_{\max}}{cR(t)}\left(4\varphi_{m,g} - \nu_{g-1/2}\varphi_{m,\nu_{g-1/2}} + \nu_{g+1/2}\varphi_{m,\nu_{g+1/2}}\right) + \sigma_g(\varphi_{m,g} - b_g(T_m)) \tag{3.148}$$

For the test problem, $\kappa_2 = \kappa_s = 0.1$. For a particle in $g = 1$, the presence of the elastic scattering opacity and absence of the absorption opacity ensures that the frequency of the particle will change like the particle energy weight. For a DDMC particle, this implies, from the Doppler shift algorithm described in Section 3.1.3, that the frequency is always sampled uniformly from the group and multiplied by $e^{-\Delta t_n/t_n}$. The statistically converged results for both IMC and DDMC match the upwind approximation to Doppler correction for optically thick elastic scattering. Incorporating the upwind approximation for the Doppler correction terms in Eq. (3.148),

$$\frac{S_{m,\phi,1}}{\phi_m} = \frac{U_{\max}}{cR(t)}\left(4\varphi_{m,1} + \nu_{3/2}\varphi^{+}_{m,\nu_{3/2}}\right) \quad , \tag{3.149}$$

and

$$\frac{S_{m,\phi,2}}{\phi_m} = \frac{U_{\max}}{cR(t)}\left(4\varphi_{m,2} - \nu_{3/2}\varphi^{+}_{m,\nu_{3/2}}\right) + \sigma_2(\varphi_{m,2} - b_2(T_m)) \quad , \tag{3.150}$$

where quantities superscripted with $+$ are evaluated on the right side of the frequency bound. The two-group frequency grid is selected in a way that further simplifies the manufactured sources. Considering Eq. (3.145), if $\nu_{5/2} = 0$, $\varphi_{m,s,1} = \varphi_{m,s,2} = 1/2$, and integration of b_{ν_0} over $\nu_0 \in [0, \nu_{3/2}]$ is 1/2, then $\varphi_2 = b_2 = 1/2$ and the source terms become

$$\frac{S_{m,\phi,1}}{\phi_m} = \frac{U_{\max}}{cR(t)}\left(2 + \frac{1}{2}\frac{\nu_{3/2}}{\Delta\nu_1}\right) \quad , \tag{3.151}$$

$$\frac{S_{m,\phi,2}}{\phi_m} = \frac{U_{\max}}{cR(t)}\left(2 - \frac{1}{2}\frac{\nu_{3/2}}{\Delta\nu_1}\right) \quad , \tag{3.152}$$

and

$$S_{m,T} = 0 \quad . \tag{3.153}$$

Newton iteration yields $h\nu_{3/2}/kT_m \approx 3.503$ to obtain $b_2(T_m) = 1/2$. To satisfy the equilibrium of the manufactured solutions, particles generated in the high energy scattering group must redshift at the correct rate into the thermally coupled group. If the Doppler shift rate is incorrect, the effect should be discernible in the material temperature profile. In particular, the material temperature should decrease with time.

Setting $\nu_{3/2}/\Delta\nu_1 = 3$, the effect of Doppler shift on the solution should be significant. The physical specifications are: $U_{\max} = 10^9$ cm/s, $R(0) = 1.728 \times 10^{14}$ cm, $t \in [2.0, 2.1]$ days, $M = 10^{33}$ g, $C_v = 2 \times 10^7 \rho$, $T_m = 1.1602 \times 10^7$ K, and a wavelength group grid set to

$\{\lambda_{1/2}, \lambda_{3/2}, \lambda_{5/2}\} = \{2.656838745 \times 10^{-8}, 3.542 \times 10^{-8}, 1.2398 \times 10^{-3}\}$ cm.

The numerical specifications are: 10 time steps, $J = 10$ spatial cells, 400,000 source particles generated per time step, 400,000 initial particles. Tests were run for pure IMC, IMC-DDMC with IMC in the pure-scattering group, and pure DDMC. Depicted in the work of Wollaeger et al. [104], each test yields solutions that are in satisfactory agreement with the time-invariant, manufactured solutions. Figures 13a and 13b have DDMC material temperature profiles for a correct implementation of the source and for a test with the source in the pure-scattering group absent.

The manufactured source simulations depicted in Fig. 13 provide evidence that the sources yield the correct equilibrium solution with Doppler shift. Without Doppler shift from a higher-frequency source, the radiation in the thermal absorption group cannot heat the material to counteract systematic cooling due to expansion.

Ten-Group Spherical Step Source Tests

The multigroup spherical Heaviside source problem allows for non-trivial testing of the Doppler shift scheme with high effective scattering, the IMC-DDMC spatial boundary condition, and non-contiguous opacity regrouping.

The problem has a spherical step source out to $0.8U_{\max}$ of $4{\times}10^{24}/(t_n + t_{\min})^3$ erg/cm^3/s. The initial volume material temperature is 11,604,505 K and there is no initial radiation field. The opacity is absorption over 10 groups logarithmically spaced in wavelength from $1.238{\times}10^{-9}$ cm to $1.238{\times}10^{-3}$ cm. Small and large opacities alternate across the wavelength grouping; where odd groups have the larger opacity. As in previous tests, the speed $U_{\max} = 10^9$ cm/s and the total mass $M = 10^{33}$ g. Instead of uniform density, the mass is uniformly divided into each cell; given the spherical geometry, this makes a gradient in density. The density gradient affects the hybridization of the transport processes through the macroscopic opacity. The opacity is

$$\sigma_g = \begin{cases} 0.13\rho \ , \quad g = 2k-1 \\ 0.13 \times 10^{-4}\rho \ , \quad g = 2k \ . \end{cases} \tag{3.154}$$

All simulations in this section use 50 velocity cells from 0 cm/s to $U_{\max}$. For the first set of

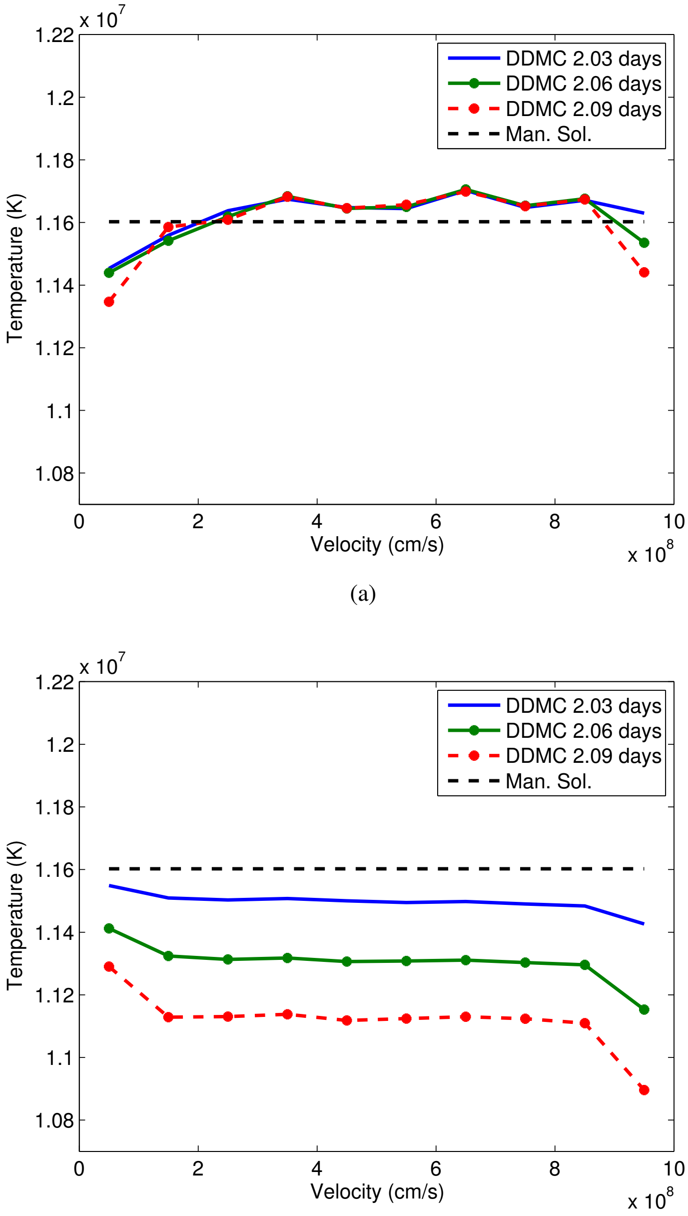

(a)

(b)

Figure 13: In Fig. 13a, manufactured (dashed) and DDMC (solid, dot-solid, and dot-dashed) material temperature at three different times plotted over the velocity grid. In Fig. 13b, the manufactured source in the pure scattering group is missing.

problems that test the moving IMC-DDMC boundary condition, 192 time steps from 2 days to 11 days are simulated. Additionally, 100,000 source particles per time step are generated. The heat capacity is estimated from the work of Pinto and Eastman [85] (see Section 2.2.2) as $C_v \approx 2 \times 10^7 \rho$ ergs/cm^3/K. The first and second boundary condition tests use $\tau_D = 3$ and $\tau_D = 10$, respectively. As a consequence of the density gradient, a "method front" is created for IMC-DDMC. An outer shell of IMC moves inward over the grid as time progresses. This phenomenon occurs in the optically thick set of groups, $g = 2k - 1$.

In Figs. 14a and 14b, depicted are simulations of the problem for $\tau_D = 3$ without and with the multiplicative term, G_U, implemented in the diffusion-limit boundary condition. The value, G_U, is anisotropic and is implemented to multiply the particle energy weights of IMC particles incident on and directed into a DDMC cell-group. In Fig. 14a, with the static-grid IMC-DDMC boundary condition, there is a discrepancy between the pure IMC result and the IMC-DDMC result at the method front at 3 and 7 days after the start time. This discrepancy propagates monotonically towards the origin as time progresses. In Fig. 14b, with the a fit of the boundary condition from Section 3.1.2, the discrepancy is mitigated.

In Fig. 15, the problem is solved for $\tau_D = 10$ mean-free paths with and without the term G_U, where G_U has $C_1 = 0.6$ and $C_2 = 1.25$. From Fig. 15, it is evident that G_U is insufficient in completely removing the error at the high-velocity IMC-DDMC method interface; this is the case even for a fit that has slightly larger C_1 than implied by the asymptotic analysis. The development and interpretation of the boundary condition is not complete, but the fit of $C_1 = 0.55$ and $C_2 = 1.25$ for G_U, along with $\tau_D \in [2, 5]$, provides a practical solution with respect to the high-velocity outflow problems tested.

Figures 16a and 16b support the Doppler shift analysis of Section 3.1.2 and consequent Doppler shift method from Section 3.1.3. Full upwind Doppler shift in DDMC groups overpredict redshift of particles out of the groups relative to IMC in Fig. 16a. The nonmonotonicity of the opacity with respect to group allows particles that are redshifted from DDMC groups to escape the domain; this reveals the coarseness of the upwind Doppler correction approximation with respect to Doppler correction in continuous frequency, pure IMC. In Fig. 16b, for this problem, agreement between

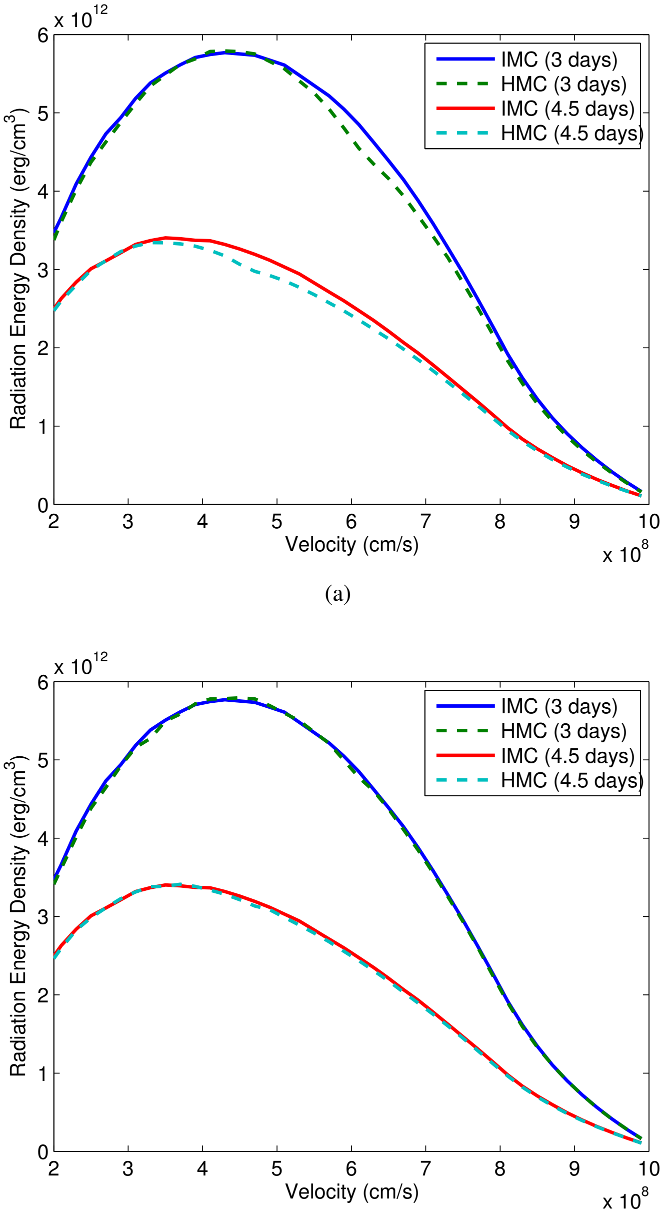

(a)

(b)

Figure 14: In Fig. 14a, radiation energy density for pure IMC (solid lines) and IMC-DDMC (dashed lines) for the step source problem with $\tau_D = 3$. In Fig. 14b, the fit of Eq. (3.57), with $C_1 = 0.55$ and $C_2 = 1.25$, is implemented for IMC-DDMC.

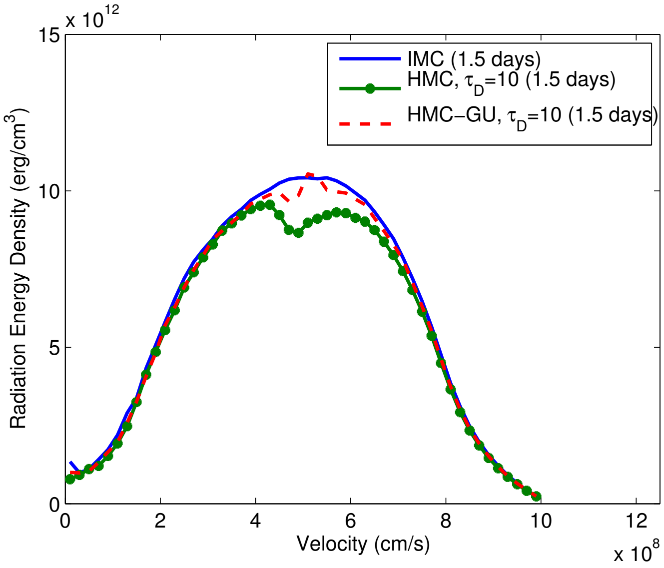

Figure 15: Radiation energy density for pure IMC (solid line), IMC-DDMC without a G_U factor (dotted solid line), and IMC-DDMC with G_U for the step source problem with $\tau_D = 10$. The fit of Eq. (3.57), with $C_1 = 0.6$ and $C_2 = 1.25$, is implemented for IMC-DDMC with G_U ("HMC-GU").

IMC and IMC-DDMC is improved by the Doppler shift method delineated in Section 3.1.3. This method emulates IMC by mitigating group coupling through redshift in the presence of strongly inelastic opacity.

For the non-contiguous opacity regrouping tests, the same step source problem is employed, but with 128 uniform time steps from day 2 to day 5 in the expansion. Additionally, a regrouping integer control parameter, g_c, is implemented to constrain the number of groups surrounding a DDMC particle that can be combined for diffusion. Figure 17 has material temperature and grouped spectra for radiation that has escaped the outflow. For this problem, the IMC-DDMC results with opacity regrouping appear to show satisfactory agreement with the non-OR results. Plotted in Fig. 18 is the L_1 error of the grouped luminosity array versus time.

The data in Fig. 18 indicate that error in the spectrum of the hybrid method, relative to IMC, increases steadily until the span of time where the outermost cells become amenable to IMC and the method front starts moving toward the origin. To test the regrouping cutoff, g_c, and demonstrate improved method performance, in Table 3 there are computation times for the step source problem

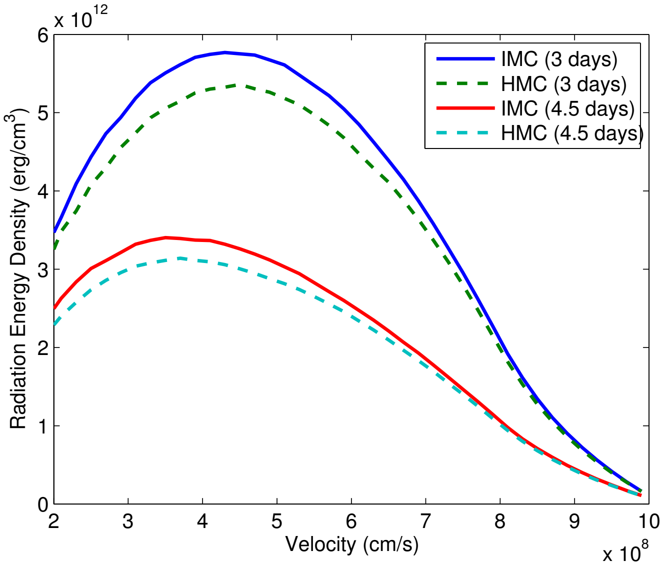

(a)

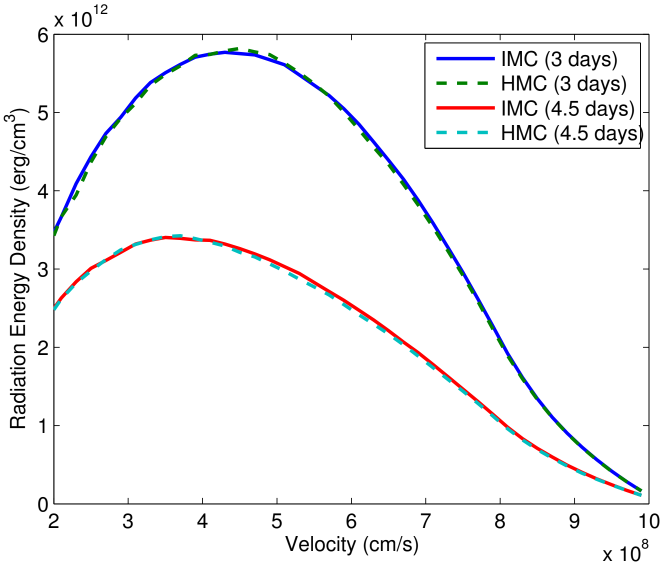

(b)

Figure 16: In Fig. 16a, radiation energy density for pure IMC (solid lines) and IMC-DDMC (dashed lines) for the step source problem with $\tau_D = 3$; IMC-DDMC uses upwind Doppler shift. In Fig. 16b, the DDMC Doppler shift algorithm from Section 3.1.3 is employed; relative to Fig. 16a, redshift from optically thick groups is mitigated since absorption/effective scattering is dominant over Doppler correction.

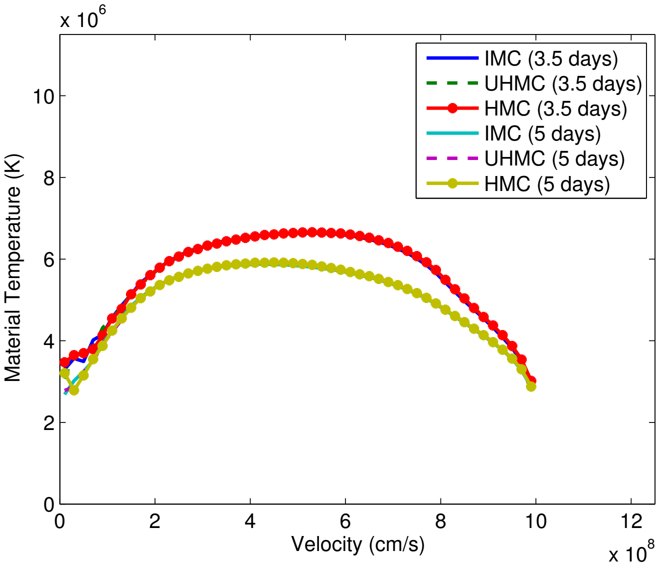

(a)

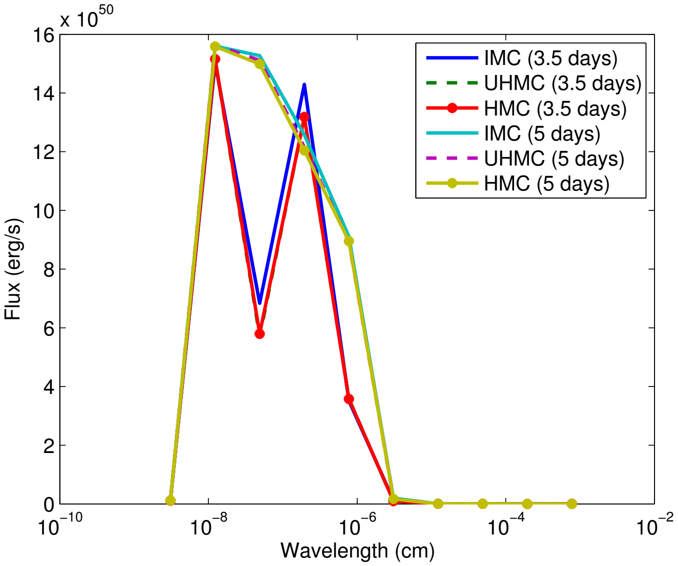

(b)

Figure 17: Material temperature, and grouped spectra of IMC (solid), non-opacity-regrouped (non-OR) IMC-DDMC (dashed, $g_c = 0$), and opacity-regrouped IMC-DDMC (dot-solid, $g_c = 10$) at 3.5 and 5 days for the spherical step source problem. In Fig. 17a, material temperature is plotted versus velocity. In Fig. 17b, grouped luminosity is plotted versus group center.

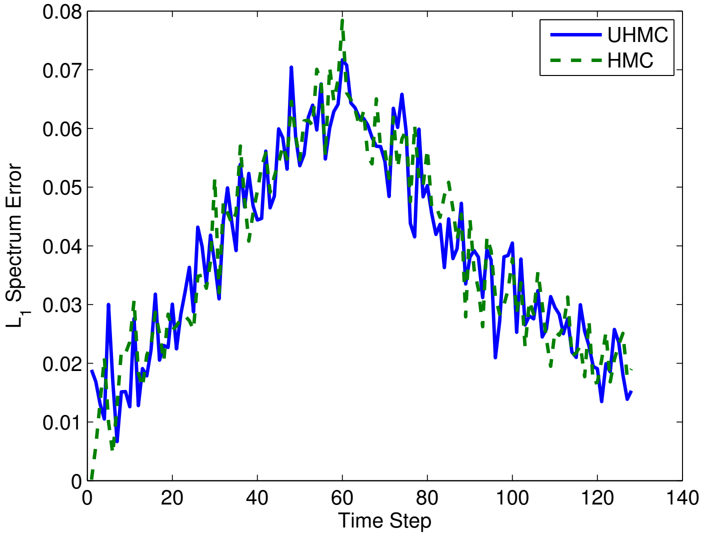

Figure 18: Non-opacity-regrouped (non-OR) IMC-DDMC (solid), and opacity regrouped IMC-DDMC (dashed) L_1 error versus time step of group spectra relative to pure IMC for radiation escaping the outermost cell of the 10 group, Heaviside source problem.

with 64 time steps from day 2 to day 3.5. The opacity is

$$\sigma_{a,g} = \begin{cases} 0.13\rho \ , \quad g = 2k-1 \\ 0.13 \times 10^{-m}\rho \ , \quad g = 2k \ , \end{cases} \tag{3.155}$$

where $m \in \{4, 7\}$. All times presented are for simulation on one core.

Table 3: Run Times for First 64 Time Steps of Heaviside Problem with $g_c \in \{0 \ldots 10\}$ with 1 Core (minutes)

Method	g_c	$m = 4$	$m = 7$
IMC	-	202.23	505.71
HMC	0	23.11	45.09
HMC	1	19.60	37.62
HMC	2	5.80	6.74
HMC	3	5.74	6.71
HMC	4	5.72	6.31
HMC	5	5.79	6.44
HMC	6	5.80	6.41
HMC	7	5.79	6.47
HMC	8	5.83	6.42
HMC	9	5.76	6.54
HMC	10	5.81	6.64

From Table 3, it is evident that non-OR IMC-DDMC improves efficiency over IMC, and regrouping only adjacent groups does not significantly improve efficiency over non-OR IMC-DDMC. However, with $g_c \geq 2$, optically thick opacities in non-contiguous groups may be combined. This apparently greatly increases the speed of IMC-DDMC. Additionally, the CPU times agree with the alternating form of the opacity in Eq. (3.155).

For IMC-DDMC with and without the opacity regrouping optimization, the Doppler shift scheme outlined in Section 3.1.3 yields satisfactory agreement with the continuous Doppler corrections of IMC for this problem. The ten-group step source problem has significant effective scattering for IMC and consequently little redshift from optically thick groups to optically thin groups.

3.3.3 W7 Model of Type Ia Supernova

For the simulations discussed and the results presented in this section, `SuperNu` is run on up to 192 cores on the Cray XE6 supercomputer Beagle at the Computation Institute of the University of Chicago.

The W7 problem of Nomoto [76] has been solved by several authors [see, e.g. [54, 56, 98]]. The SN Ia radiative transfer codes discussed in Section 2.2 have methods in place for directly treating the many lines of the ejecta. The IMC-DDMC scheme formulated in this thesis is in multigroup. Resolving line structure rigorously would in theory require storing $\sim$10,000 groups per spatial cell. In multiple dimensions, the memory overhead is much larger than in 1D. Thus, depending on computer architecture, it may not be possible to implement $\sim$10,000 groups in 2D or 3D spatial grids The primary focus of this section is on the performance and accuracy of simulations with $\sim$100 to 1000 groups. Accuracy here implies reasonable agreement with LTE results from the radiative transfer code `PHOENIX`.

IMC and IMC-DDMC data for the W7 model indicate it is very computationally expensive to use pure IMC or non-OR IMC-DDMC, relative to opacity-regrouped IMC-DDMC. For a 100 group W7 simulation with groups logarithmically spaced from 1×10^{-6} cm to 3.2×10^{-4} cm, 64 velocity cells spaced uniformly from 0 cm/s to 2.2027×10^{9} cm/s, a time domain of $t \in [40, 64]$ days post explosion with 0.25 day time steps, 250,000 initial particles, and 250,000 source particles per time step, neither IMC nor non-OR IMC-DDMC completed the simulation with 192 cores and a wall time of 40 hours each. In contrast, fully opacity-regrouped IMC-DDMC ($g_c = 100$) completed the same problem with 24 cores in 1018.9 seconds. Thus, in addition to only considering $\sim$100 to 1000 groups, the scope of the results shown in this section is narrowed further to to IMC-DDMC with opacity regrouping.

Also tested is an “opacity mix” parameter which, in conjunction with a subgroup structure for each group, linearly combines direct-averaged group opacities (Planck-type) and reciprocal-averaged group opacities (Rosseland-type). For each group, g, a subgroup index, $g_g \in \{1 \ldots G_g\}$, is used to write the opacity mixing formula. For the simulations presented, subgroups are uniform across groups. However, the main groups are logarithmically spaced unless otherwise specified.

Bound-bound (bb), bound-free (bf), and free-free (ff) transition opacities (see Section 1.1.1) populate each group. Values for bb opacities are calculated from oscillator strength data for each atomic species [57]. It is assumed that a line profile is non-zero only in the subgroup in which its line center resides [73, pp. 329-332],

$$\sigma_{a,g_g,bb} = \frac{1}{\Delta\lambda_{g_g}} \sum_s \sum_i \sum_{i'>i} \left(\frac{\pi(e^-)^2}{m_{e^-}c}\right) f_{i,i',s} \frac{\lambda^2_{i,i',s}}{c} \times \\ [\Theta(\lambda_{i,i',s} - \lambda_{g_g-1/2}) - \Theta(\lambda_{i,i',s} - \lambda_{g_g+1/2})] n_{i,s}(1 - e^{\frac{hc}{kT\lambda_{i,i',s}}}) \quad , \tag{3.156}$$

where $\sigma_{a,g_g,bb}$ is the bb contribution to subgroup g_g, $f_{i,i',s}$ is the non-dimensional oscillator strength from state i to i' of species s, $\lambda_{i,i',s}$ is the wavelength center of the line corresponding to the $i \to i'$ transition, $n_{i,s}$ is the total density of species s occupying state i, and the Θ are Heaviside step functions constraining the sum to opacity profiles centered in the subgroup. Scattering opacity is treated as elastic and isotropic; the form in the comoving frame is calculated as [19, p. 161]

$$\sigma_s = \frac{8\pi}{3} n_{\mathrm{e}^-} \left(\frac{\mathrm{e}^-}{m_{\mathrm{e}^-}c^2}\right)^2 \quad , \tag{3.157}$$

where e^- is electron charge, n_{e^-} is electron number density, and m_{e^-} is electron mass in cgs units. Mass fractions and velocity specific to the W7 problem are read from data files. The Saha-Boltzmann equations are used to obtain the excitation densities for each atom in the W7 model [73, p. 49]. The bf opacities are obtained from tables according to the prescription of Verner et al. [99] and, following Sutherland [95], the ff opacities are calculated with tabulated Gaunt factors. The total absorption opacity for subgroup g_g is $\sigma_{a,g_g} = \sigma_{a,g_g,bb} + \sigma_{a,g_g,bf} + \sigma_{a,g_g,ff}$ [73, p. 332].

Introducing the opacity mixing parameter, $\alpha_\sigma \in [0, 1]$, the opacity mix formula,

$$\sigma_{a,g} = (1 - \alpha_\sigma) \frac{1}{G_g} \sum_{g_g}^{G_g} \sigma_{a,g_g} + \frac{\alpha_\sigma G_g}{\sum_{g_g}^{G_g} 1/\sigma_{a,g_g}} \quad , \tag{3.158}$$

is applied for various values of α_σ.

For the W7 tests discussed, gamma ray energy deposition profiles and the initial material and radiation temperatures are extracted from the `PHOENIX` code [46, 47, 48, 98]. A nominal value of heat capacity of $C_v = 2.0 \times 10^7 \rho$ erg/K/cm^3 is considered. It is found that the heat capacity for this problem is unimportant since the Fleck factor is so small, $f_n \approx C_{v,n}/\alpha 4aT_n^3 c\Delta t_n \sigma_{P,n}$, division by $C_{v,n}$ of the deposition and emission terms in the material update cause the heat capacity to roughly cancel out of the equation. The heat capacity has been changed by up to a factor of 1000 without inducing significant changes to light curves.

The first problems considered have 225 and 625 groups, 20 subgroups per group, and an opacity mixing parameter $\alpha_\sigma \in \{0.0, 0.3, 0.5, 0.8, 1.0\}$. Each calculation has 64 velocity cells uniformly spaced from 0 cm/s to 2.2027×10^9 cm/s, 248 uniform time steps for $t \in [2, 64]$ days, 250,000 initial radiation particles, 250,000 source particles generated per time step, $\tau_D = \tau_L = 3$ mean free paths, and the opacity-regrouped neighborhoods span the entire set of groups ($g_c = G$). Absolute bolometric magnitudes are calculated with

$$M_{\text{bol}} = 4.74 - 2.5 \log_{10} \left(\frac{L}{3.84 \times 10^{33}} \right) \quad , \tag{3.159}$$

where L is luminosity in erg/s. The luminosities are computed by tallying lab frame particle energies escaping the domain and dividing by time step size. Figures 19a and 19b have light curve data for 225 and 625 groups, respectively. As expected, peak luminosity is earlier and brighter for opacity mixing that favors reciprocal averaging since smaller subgroup opacity values are preferentially weighted. Values of α_σ near 1 preferentially weight lower opacities in the subgrouped calculation, Eq. (3.158).

Figures 20a and 20b have spectra for 225 and 625 groups, respectively. For group resolutions $\sim$100, we find that generating 250,000 source particles per time step is adequate for statistical resolution of the spectra at times past $\sim$5-10 days post-explosion. Computation times for simulations of the problem with 225, 400, 625, and 1024 groups and different values of α_σ are in Table 4.

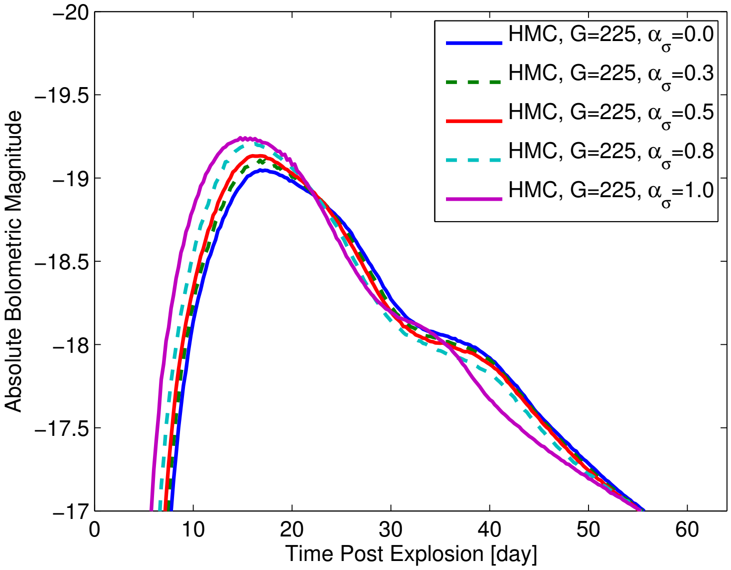

(a)

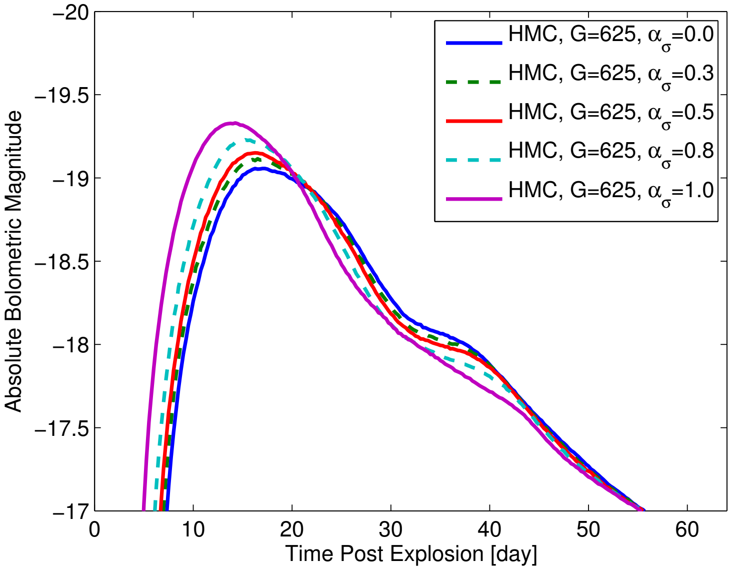

(b)

Figure 19: Opacity-regrouped IMC-DDMC W7 bolometric light curves for opacity mixing $\alpha_\sigma \in \{0.0, 0.5, 1.0\}$ (solid) and $\alpha_\sigma \in \{0.3, 0.8\}$ (dashed; so solid and dashed curves alternate versus α_σ) and a fixed number of subgroups, $G_g = 20$. In Figs. 19a, and 19b, group resolutions are $G = 225$, $G = 625$, respectively.

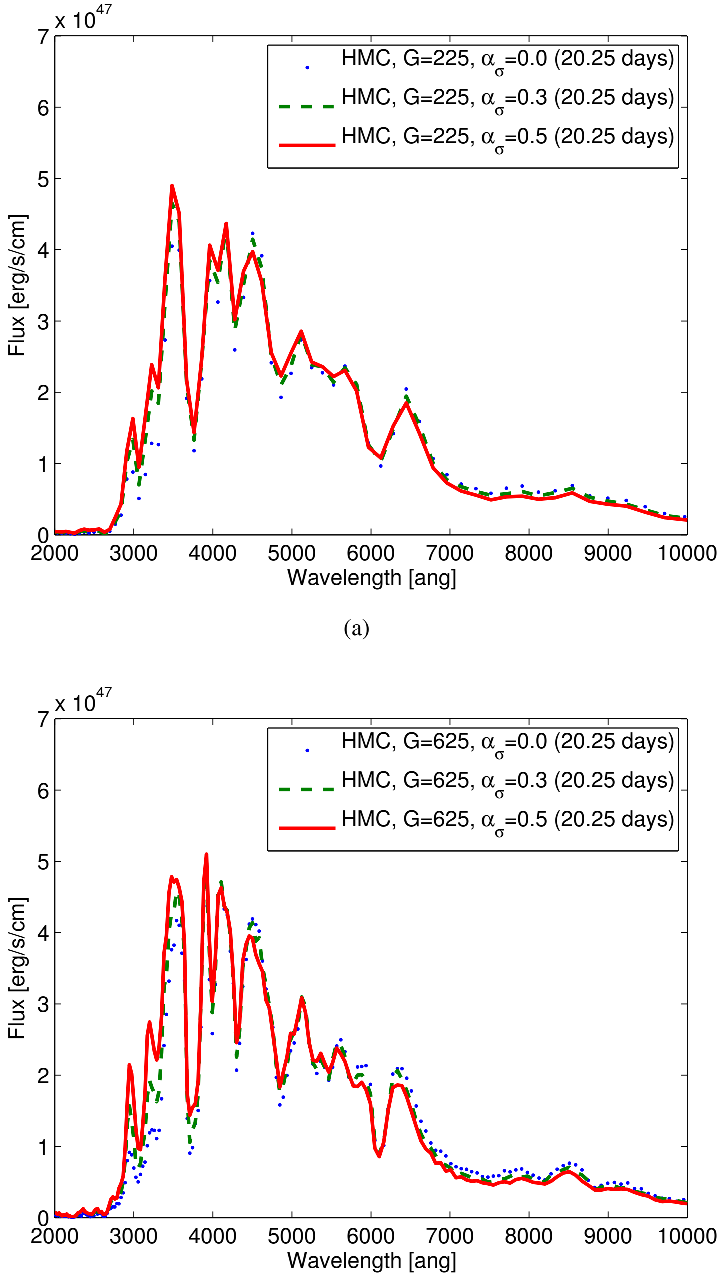

(a)

(b)

Figure 20: Opacity-regrouped IMC-DDMC W7 spectra for opacity mixing $\alpha_\sigma = 0.0, 0.3, 0.5$ (dotted, dashed, and solid, respectively) and a fixed number of subgroups, $G_g = 20$. In Figs. 20a, and 20b, group resolutions are $G = 225$, $G = 625$, respectively.

Table 4: Total Run Times for Opacity-Regrouped HMC W7 with 24 Cores (hours)

$G \setminus \alpha_\sigma$	0.0	0.3	0.5	0.8	1.0
225	0.92	0.92	0.91	0.89	0.83
400	1.33	1.32	1.32	1.28	1.21
625	1.92	1.88	1.91	1.87	1.89
1024	2.73	2.71	2.70	2.70	3.32

In Fig. 21, W7 material temperatures from IMC-DDMC with the standard Fleck factor are compared to material temperatures from IMC-DDMC applying the Gentile-Fleck factor. For the time shown of 32 days, the Gentile-Fleck factor mitigates temperature fluctuation at the outer velocities. However, the spectra are nearly identical at day 32 post-explosion; this indicates the outer cells are not important to generating the spectrum at 32 days.

For $G = 225$ and $\alpha = 0.5$, past day 25, the Gentile-Fleck factor consistently mitigates temperature fluctuations in the outer cells, relative to the standard Fleck factor.

In Fig. 22a, light curves calculated by `SuperNu` with 500 groups are plotted with light curves from the radiative transfer code, `PHOENIX`. `PHOENIX` is run both in standard high-resolution form, with 30,000 wavelength points, and with a 500 group scheme for further control in comparisons. For multigroup, both codes have $\alpha_\sigma = 0$. The light curve from `SuperNu` is systematically dimmer by roughly 10% than the light curve from `PHOENIX` for multiple time step and group resolutions. In Fig. 22b, at day 20 post-explosion, the spectrum of 500-group IMC-DDMC appears to agree well, in shape, with the high-resolution spectrum of `PHOENIX`.

Lastly reported are findings from preliminary W7 SN Ia error convergence tests. The errors are computed with the raw luminosity data in erg/s. The convergence variables are wavelength, space, and time; thus group, cell, and time step numbers are changed. Temporal grid convergence results average the error over the coarse time steps. Because the present set of simulation results do not contain pure IMC, luminosity errors are calculated with respect to the luminosity from the most resolved IMC-DDMC simulation. The highest resolution simulation has 1024 groups, 256 cells, and 992 time steps with the wavelength, velocity, and time domains unchanged from the prior tests.

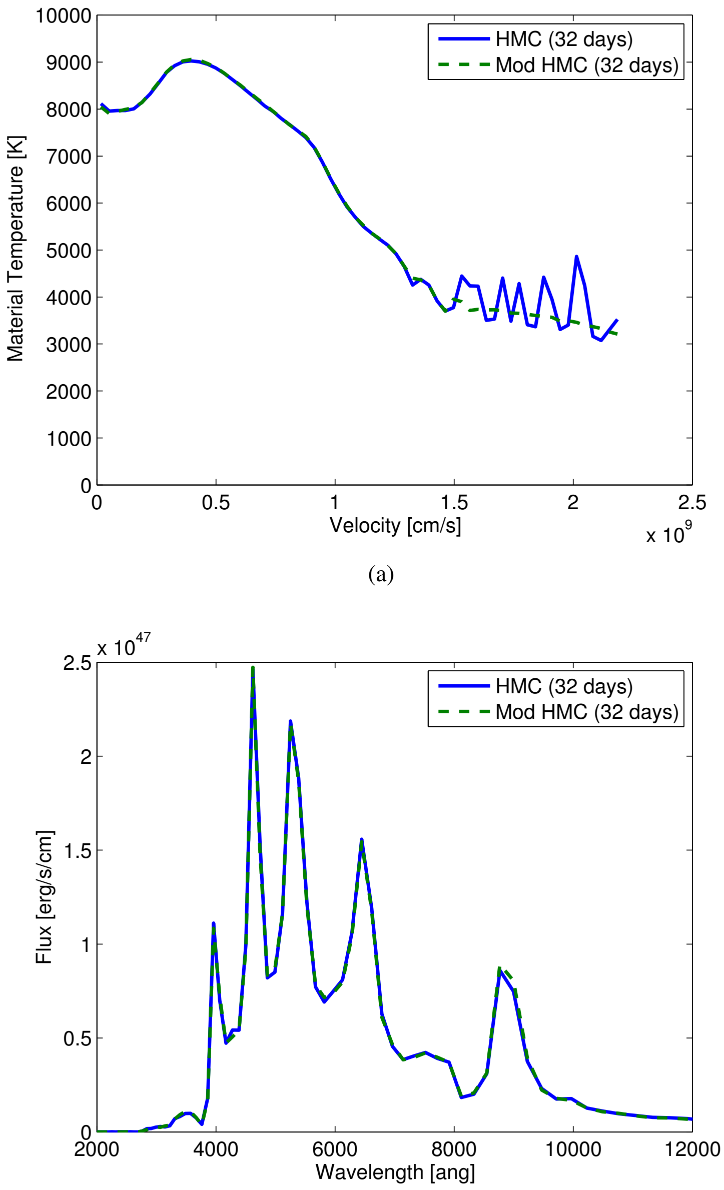

(a)

(b)

Figure 21: IMC-DDMC (solid) and Gentile-Fleck factor modified IMC-DDMC (dashed) material temperatures and spectra at day 32 post-explosion with $G = 225$ and $\alpha_\sigma = 0.5$.

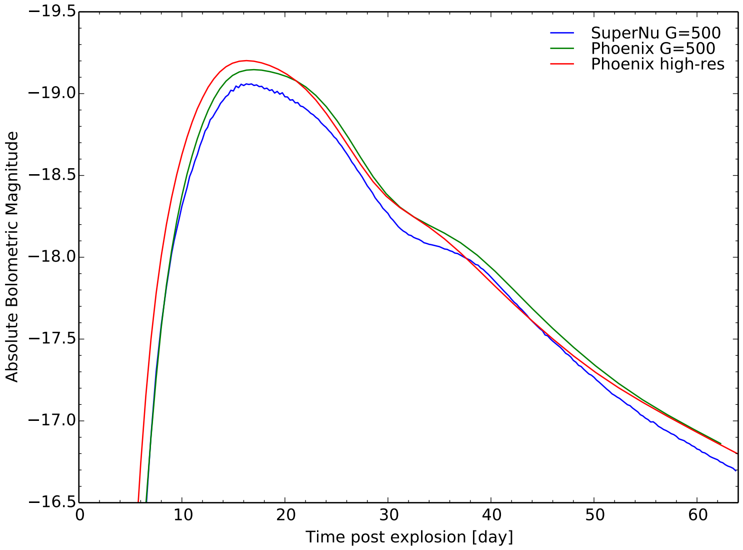

(a)

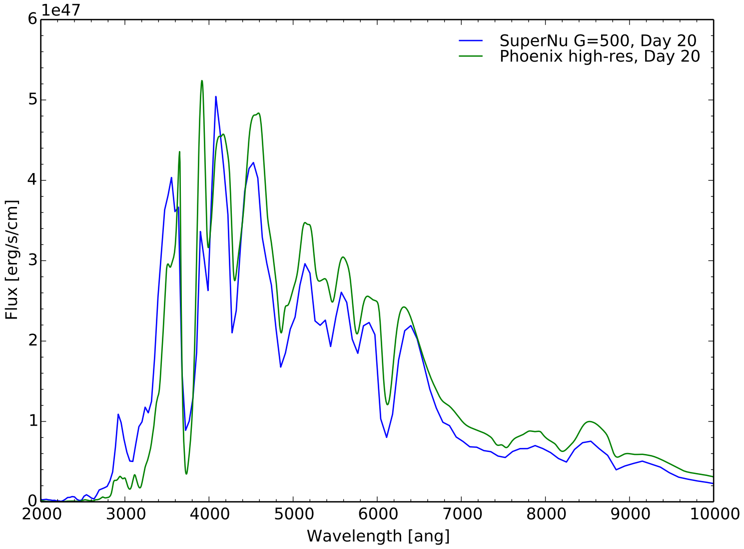

(b)

Figure 22: In Fig. 22a, bolometric light curves for `SuperNu` with 500 groups (blue), multigroup `PHOENIX` with 500 groups (green), and standard `PHOENIX` (red). In Fig. 22b, spectra at day 20 for `SuperNu` with 500 groups (blue) and standard, or high-resolution, `PHOENIX` (green).

All time and velocity grids are uniform and all wavelength grids are logarithmic. Additionally, $\alpha_\sigma = 0$ for all simulations. The mean-free path thresholds are unchanged as well, $\tau_L = \tau_D = 3$. For the wavelength convergence test, the simulations have 225, 400, and 625 groups; each has 256 cells and 992 time steps. For the spatial convergence test, the simulations have 32, 64, and 128 cells; each has 992 time steps and 1024 groups. For the temporal convergence test, the simulations have 124, 248, and 496 time steps; each has 1024 groups and 256 cells. All simulations have 2,000,000 source particles generated per time step. On 192 cores, the highest resolution test took 46.44 hours.

These convergence tests have some complicating factors. Firstly, the most resolved W7 simulation (1024 groups, 256 cells, 992 time steps) is not fully converged. In addition to not having an absolute convergence limit, the validity of Eq. (3.156) diminishes with higher group resolution since lines are not actually fully contained in groups or subgroups. Secondly, an increase in the number of: groups changes the opacity profile and the amount of opacity regrouping, cells increases the number of IMC particles, and time steps changes the amount of IMC particle position displacement in velocity space in between transport steps. Despite the complexities, for the grid resolutions tested, the data shown in Figs. 23, 24, and 25 show monotonic convergence towards the highest resolution data, throughout the time span, in wavelength, space, and time, respectively. In each case, increasing the number of grid points makes the light curve rise earlier and peak somewhat brighter.

With higher resolution in any of the three independent variables, the early rise in luminosity shifts to earlier times and consequently induces large error before peak luminosity. Near peak luminosity, around day 20 post explosion, the least resolved luminosity for each resolution test appears to be roughly 2% lower than that of the high resolution benchmark. The convergence data, along with data comparisons with the `PHOENIX` radiative-transfer code, indicate that the IMC-DDMC method can accurately simulate radiation transport in Type Ia supernovae.

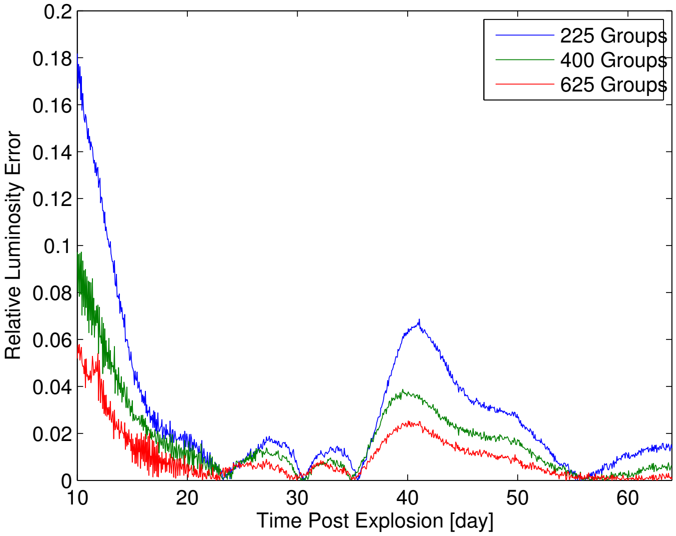

Figure 23: W7 SN Ia luminosity error versus time for 225 (blue), 400 (green), and 625 (red) groups relative to the 1024 group test. The spatial and temporal grids have 256 cells and 992 time steps, respectively, in each simulation.

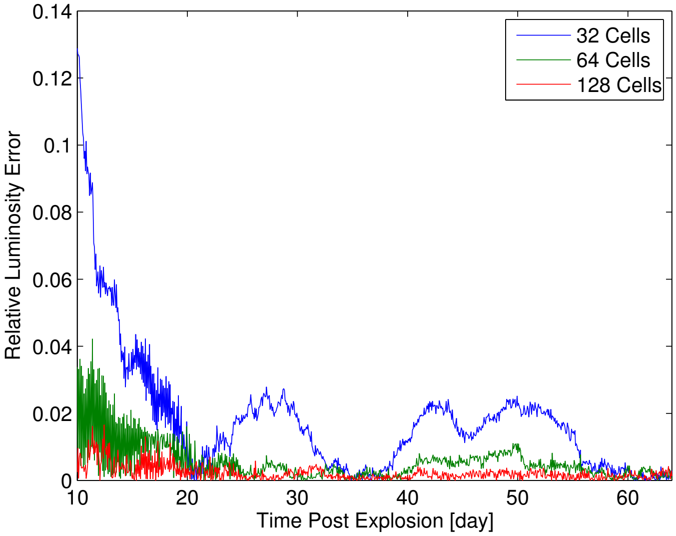

Figure 24: W7 SN Ia luminosity error versus time for 32 (blue), 64 (green), and 128 (red) cells relative to the 256 cell test. The wavelength and temporal grids have 1024 groups and 992 time steps, respectively, in each simulation.

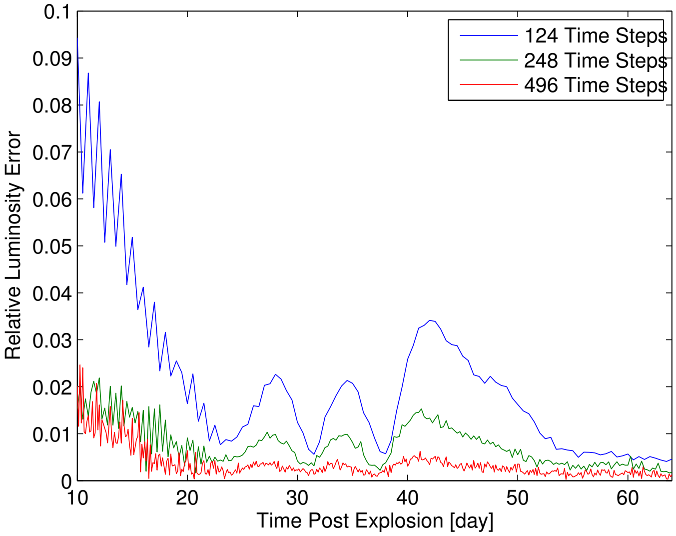

Figure 25: W7 SN Ia luminosity error versus time for 124 (blue), 248 (green), and 496 (red) time steps relative to the 992 time step test. The spatial and wavelength grids have 256 cells and 1024 groups, respectively, in each simulation.

4 Conclusions

The IMC-DDMC radiative-transfer code, `SuperNu`, has been developed to solve a variety of transport problems and, in particular, the one dimensional W7 model of the Type Ia supernovae. The effort commensurate to the making of this thesis was focused in formulating IMC and DDMC to function in a high-velocity outflow and writing an efficient code to execute the resulting method. The resulting scheme has the prescription of Abdikamalov et al. [2] for operator splitting the comoving diffusion equation, but with an additional algorithm for advecting IMC particles through velocity space. The formulation included the development of a diffusion-limit boundary condition for moving hybrid-method interfaces, a redshift scheme in DDMC that can emulates continuous Doppler shift in IMC, and a generalization of the DDMC opacity regrouping scheme of Densmore et al. [30] to non-contiguous groups. Both non-contiguous opacity regrouping and continuous Doppler shifting are found to be necessary to computing efficient and accurate W7 spectra for group numbers of O(100)-O(1000). The ability to use low group numbers to obtain accurate spectra is promising to mitigating memory overhead in extension to multiple spatial dimensions.

With the numerical results presented in Section 3.3, the novel features of the code are benchmarked against analytic solutions and tested further with simple problems having analytic opacity. Using a manufactured source with two groups and a step source with ten groups (Section 3.3.2), the DDMC Doppler shift scheme from Section 3.1.3 demonstrates agreement to the manufactured solution and to IMC in both the limits of purely elastic scattering and high effective scattering. The Doppler shift scheme is motivated by the second asymptotic analysis in Section 3.1.2. The density gradient in the step source problem can induce a non-physical dip in the IMC-DDMC radiation energy density solution at the spatial interface between IMC and DDMC for the static-grid, asymptotic diffusion-limit boundary condition. In Section 3.1.2, the first asymptotic analysis motivates a new boundary condition that has a multiplicative factor on particle weights. The new boundary condition mitigates the non-physical dip in radiation energy density for the step source problem. With a static grid, monotonic opacity test in Section 3.3.1 and, again, the high-velocity, ten-group, step source problem in Section 3.3.2, the opacity regrouping optimization, described in Section 3.1.4, is seen to greatly increase simulation speed.

4.1 Future Work

The interest in pursuing IMC-DDMC to solve the radiative transfer equations in Type Ia supernovae comes from the possibility of solving the multidimensional problem efficiently and accurately. Certain progenitor models have spatial asymmetry; having the capability to generate light curves and spectra from asymmetric progenitors requires the transport code to be multidimensional, or have multidimensional capabilities. An important objective to extending to two or three spatial dimensions is to minimize the amount of memory required by processors to advance particles. In addition to absorption and scattering, DDMC requires leakage opacities or probabilities during particle propagation; this must be implemented carefully in multiple dimensions to not over-tax memory resources.

The homologous outflow is a very simplified form of hydrodynamics. More realistic hydrodynamics must be implemented in `SuperNu` to be able to solve the fully coupled radiation hydrodynamics equations. In multiple dimensions, non-orthogonal meshes cause DDMC to acquire negative leakage opacities; this must be taken into consideration for a Lagrangian IMC-DDMC radiation hydrodynamics code.

References

[1] 2012. Obtained from http://www.fusionfuture.org.

[2] E. Abdikamalov, A. Burrows, C. D. Ott, F. Loffler, E. O'Connor, J. C. Dolence, and E. Schnetter. A new Monte Carlo method for time-dependent neutrino radiation transport. *The Astrophysical Journal*, 755:111, 2012.

[3] M. L. Adams. Discontinuous finite element transport solutions in thick diffusive problems. *Nuclear Science and Engineering*, 137, 2001.

[4] S. Atzeni and J. M. ter Vehn. *The Physics of Inertial Fusion*. Oxford University Press, 2004.

[5] E. Baron and P. H. Hauschildt. A 3D radiative transfer framework. II. Line transfer problems. *Astronomy & Astrophysics*, 468:255–261, June 2007.

[6] G. I. Bell and S. Glasstone. *Nuclear Reactor Theory*. Robert E. Krieger Publishing Company, 1979.

[7] J. S. Bloom, D. Kasen, K. J. Shen, P. E. Nugent, N. R. Butler, M. L. Graham, D. A. Howell, U. Kolb, S. Holmes, C. A. Haswell, V. Burwitz, J. Rodriguez, and M. Sullivan. A compact degenerate primary-star progenitor of SN 2011fe. *Astrophysical Journal, Letters*, 744:L17, 2012.

[8] T. Booth. Exponential convergence on a continuous Monte Carlo transport problem. *Nuclear Science and Engineering*, 127:338, 1997.

[9] D. Branch. Type Ia supernovae and the Hubble Constant. *Annual Review of Astronomy and Astrophysics*, 36:17, 1998.

[10] D. Branch and A. Khokhlov. Type Ia supernovae: observations, modeling, distances. *Physics Reports*, 256:53, 1995.

[11] E. D. Brooks. Symbolic Implicit Monte Carlo. *Journal of Computational Physics*, 83, 1989.

[12] E. D. Brooks, A. Szőke, and J. D. L. Peterson. Piecewise linear discretization of Symbolic Implicit Monte Carlo radiation transport in the difference formulation. *Journal of Computational Physics*, 220:471, 2006.

[13] F. B. Brown and W. R. Martin. Direct sampling of Monte Carlo flight paths in media with continuously varying cross-sections. In *Nuclear Mathematical and Computational Science, ANS Mathematics & Computation Topical Meeting*, 2003.

[14] J. R. Buchler. Radiative transfer in the fluid frame. *Journal of Quantitative Spectroscopy and Radiative Transfer*, 30:395, 1983.

[15] A. C. Calder, B. Fryxell, T. Plewa, R. Rosner, L. J. Dursi, V. G. Weirs, T. Dupont, H. F. Robey, J. O. Kane, B. A. Remington, R. P. Drake, G. Dimonte, M. Zingale, F. X. Timmes, K. Olson, P. Ricker, P. MacNeice, and H. M. Tufo. On validating an astrophysical simulation code. *Astrophysical Journal, Supplement*, 143:201–229, 2002.

[16] A. C. Calder, T. Plewa, N. Vladimirova, D. Q. Lamb, and J. W. Truran. Type Ia supernovae: An asymmetric deflagration model. *Astrophysical Journal, Letters*, 2004.

[17] L. L. Carter and C. A. Forest. Nonlinear radiation transport simulation with an implicit Monte Carlo method. LA-5038, Los Alamos National Laboratory, 1973.

[18] K. M. Case. Elementary solutions of the transport equation and their applications. *Annals of Physics*, 9:1, 1960.

[19] J. I. Castor. *Radiation Hydrodynamics*. Cambridge University Press, 2004.

[20] S. Chandrasekhar. *Radiative Transfer*. Dover Publications, Inc., 1960.

[21] F. F. Chen. *Plasma Physics and Controlled Fusion, 2nd Ed.* Springer, New York, 1983.

[22] M. A. Cleveland, N. A. Gentile, and T. S. Palmer. An extension of implicit Monte Carlo diffusion: Multigroup and the difference formulation. *Journal of Computational Physics*, 229:5707, 2010.

[23] J. F. Clouet and G. Samba. Asymptotic diffusion limit of the symbolic Monte Carlo method for the transport equation. *Journal of Computational Physics*, 195:293, 2004.

[24] P. Colella and P. R. Woodward. The piecwise parabolic method (PPM) for gas-dynamical simulations. *Journal of Computational Physics*, 54:174, 1984.

[25] J. D. Densmore. Asymptotic analysis of the spatial discretization of radiation absorption and re-emission in Implicit Monte Carlo. *Journal of Computational Physics*, 230:1116, 2011.

[26] J. D. Densmore, G. Davidson, and D. B. Carrington. Emissivity of discretized diffusion problems. *Annals of Nuclear Energy*, 33:583, 2006.

[27] J. D. Densmore, T. M. Evans, and M. W. Buksas. A hybrid transport-diffusion algorithm for Monte Carlo radiation-transport simulations on adaptive-refinement meshes in xy geometry. *Nuclear Science and Engineering*, 159:1, 2008.

[28] J. D. Densmore and E. W. Larsen. Asymptotic equilibrium diffusion analysis of time-dependent Monte Carlo methods for grey radiative transfer. *Journal of Computational Physics*, 199:175, 2004.

[29] J. D. Densmore, K. G. Thompson, and T. J. Urbatsch. Discrete Diffusion Monte Carlo for frequency-dependent radiative transfer. In *International Conference on Mathematics and Computational Methods Applied to Nuclear Science & Engineering*, 2011.

[30] J. D. Densmore, K. G. Thompson, and T. J. Urbatsch. A hybrid transport-diffusion Monte Carlo method for frequency-dependent radiative-transfer simulations. *Journal of Computational Physics*, 231:6925, 2012.

[31] J. D. Densmore, T. J. Urbatsch, T. M. Evans, and M. W. Buksas. A hybrid transport-diffusion method for Monte Carlo radiative-transfer simulations. *Journal of Computational Physics*, 222:485, 2007.

[32] R. Diehl and F. X. Timmes. Gamma-ray line emission from radioactive isotopes in stars and galaxies. *Publications of the Astronomical Society of the Pacific*, 110:637, 1998.

[33] B. D. Esham, 2007. Obtained from http://en.wikipedia.org/wiki/Inertial_confinement_fusion.

[34] T. M. Evans, S. W. Mosher, S. R. Slattery, and S. P. Hamilton. A Monte Carlo synthetic-acceleration method for solving the thermal radiation diffusion equation. *Journal of Computational Physics*, 258:338, 2014.

[35] T. M. Evans, T. J. Urbatsch, H. Lichtenstein, and J. E. Morel. A residual Monte Carlo method for discrete thermal radiative diffusion. *Journal of Computational Physics*, 189:539, 2003.

[36] J. A. Fleck, Jr. and E. H. Canfield. A random walk procedure for improving the computational efficiency of the Implicit Monte Carlo method for nonlinear radiation transport. *Journal of Computational Physics*, 54:508, 1984.

[37] J. A. Fleck, Jr. and J. D. Cummings. An implicit Monte Carlo scheme for calculating time and frequency dependent radiation transport. *Journal of Computational Physics*, 8:313, 1971.

[38] B. Fryxell, K. Olson, P. Ricker, F. X. Timmes, M. Zingale, D. Q. Lamb, P. MacNeice, R. Rosner, J. W. Truran, and H. Tufo. FLASH: An Adaptive Mesh Hydrodynamics Code for Modeling Astrophysical Thermonuclear Flashes. *Astrophysical Journal, Supplement*, 131:273–334, Nov. 2000.

[39] V. N. Gamezo, A. M. Khokhlov, E. S. Oran, A. Y. Chtchelkanova, and R. O. Rosenberg. Thermonuclear supernovae: simulations of the deflagration stage and their implications. *Science*, 299:77, 2003.

[40] N. A. Gentile. Implicit Monte Carlo Diffusion - an acceleration method for Monte Carlo time-dependent radiative transfer simulations. *Journal of Computational Physics*, 172:543, 2001.

[41] N. A. Gentile. A comparison of various temporal discretization schemes for infinite media radiation transport. In *Transactions of the American Nuclear Society*, 2007.

[42] N. A. Gentile. Including the effects of temperature-dependent opacities in the implicit Monte Carlo algorithm. *Journal of Computational Physics*, 230, 2011.

[43] D. A. Gurnett and A. Bhattacharjee. *Introduction to Plasma Physics*. Cambridge University Press, 2005.

[44] G. J. Habetler and B. J. Matkowsky. Uniform asymptotic expansions in transport theory with small mean free paths, and the diffusion approximation. *Journal of Mathematical Physics*, 16:846, 1975.

[45] F. Hang and S. Jiang. Generalized poincaré-bertrand formula on a hypersurface. *Applied Compututaional Harmonic Analysis*, 27, 2009.

[46] P. H. Hauschildt. A fast operator perturbation method for the solution of the special relativistic equation of radiative transfer in spherical symmetry. *Journal of Quantitative Spectroscopy and Radiative Transfer*, 47:433, 1992.

[47] P. H. Hauschildt and E. Baron. Numerical solution of the expanding stellar atmosphere problem. *Journal of Computational and Applied Mathematics*, 109, 1999.

[48] P. H. Hauschildt and E. Baron. Improved discretization of the wavelength derivative term in CMF operator splitting numerical radiative transfer. *Astronomy & Astrophysics*, 417:317–324, Apr. 2004.

[49] P. H. Hauschildt and R. Wehrse. Solution of special relativistic equation of radiation transfer in rapidly expanding spherical shells. *Journal of Quantitative Spectroscopy and Radiative Transfer*, 46, 1991.

[50] D. L. Henderson and C. W. Maynard. Time-dependent single-collision kernels for integral transport theory. *Nuclear Science and Engineering*, 102:172, 1989.

[51] D. L. Henderson and C. W. Maynard. Time-dependent first-flight leakage rates for the general case of a two-region spherical medium. *Annals of Nuclear Energy*, 18:365, 1991.

[52] W. Hillebrandt and J. Niemeyer. Type Ia supernova explosion models. *Annual Review of Astronomy and Astrophysics*, 38:191, 2000.

[53] J. D. Jackson. *Classical Electrodynamics, 3rd Ed.* John Wiley & Sons, Inc., 1999.

[54] D. Kasen, R. C. Thomas, and P. Nugent. Time-dependent Monte Carlo radiative transfer calculations for three-dimensional supernova spectra, light curves and polarization. *The Astrophysical Journal*, 651:366, 2006.

[55] K. S. Krane. *Introductory Nuclear Physics*. John Wiley & Sons, Inc., 1988.

[56] M. Kromer and S. A. Sim. Time-dependent three-dimensional spectrum synthesis for Type Ia supernovae. *Monthly Notices of the Royal Astronomical Society*, 398, 2009.

[57] R. L. Kurucz, 1994.

[58] E. W. Larsen and G. J. Habetler. A functional-analytic derivation of case's full and half-range formulas. *Communications on Pure and Applied Mathematics*, 26:525, 1973.

[59] E. W. Larsen and J. B. Keller. Asymptotic solution of neutron transport problems for small mean free paths. *Journal of Mathematical Physics*, 15:75, 1974.

[60] E. W. Larsen and B. Mercier. Analysis of a Monte Carlo method for nonlinear radiative transfer. *Journal of Computational Physics*, 71, 1987.

[61] E. W. Larsen, J. E. Morel, and W. F. Miller, Jr. Asymptotic solutions of numerical transport problems in optically thick, diffusive regimes. *Journal of Computational Physics*, 69:283, 1987.

[62] E. E. Lewis and W. F. Miller, Jr. *Computational Methods of Neutron Transport*. American Nuclear Society, 1993.

[63] M. Long, G. C. Jordan, IV, D. R. van Rossum, B. Diemer, C. Graziani, R. Kessler, B. Meyer, P. Rich, and D. Q. Lamb. Three-dimensional Simulations of Pure Deflagration Models for Thermonuclear Supernovae. *ArXiv e-prints*, July 2013.

[64] G. Longoni and A. Haghighat. Developement of new quadrature sets with the ”Ordinate Splitting” technique. In *ANS Mathematics & Computing Conference*, 2001.

[65] R. B. Lowrie, D. Mihalas, and J. E. Morel. Comoving-frame radiation transport for nonrelativistic fluid velocities. *Journal of Quantitative Spectroscopy and Radiative Transfer*, 69:291, 2001.

[66] L. B. Lucy. Monte Carlo techniques for time-dependent radiative transfer in 3-d supernovae. *Astronomy & Astrophysics*, 429:19, 2005.

[67] F. Malvagi and G. C. Pomraning. Initial and boundary conditions for diffusive linear transport problems. *Journal of Mathematical Physics*, 32:805, 1991.

[68] R. G. McClarren, J. P. Holloway, and T. A. Brunner. Analytic P_1 solutions for time-dependent, thermal radiative transfer in several geometries. *Journal of Quantitative Spectroscopy and Radiative Transfer*, 109:389, 2008.

[69] R. G. McClarren, R. B. Lowrie, A. K. Prinja, and J. E. Morel. Manufactured solutions for the P_1 radiation-hydrodynamics equations. *Journal of Quantitative Spectroscopy and Radiative Transfer*, 109:2590, 2008.

[70] R. G. McClarren and T. J. Urbatsch. A modified implicit Monte Carlo method for time-dependent radiative transfer with adaptive material coupling. *Journal of Computational Physics*, 228:5669, 2009.

[71] R. G. McClarren and T. J. Urbatsch. An Implicit Monte Carlo method based on BDF-2 time integration for simulating nonlinear radiative transfer. In *Transactions of the American Nuclear Society*, 2012.

[72] M. S. McKinley, E. D. Brooks, and A. Szőke. Comparison of implicit and symbolic implicit Monte Carlo line transport with frequency weight vector extension. *Journal of Computational Physics*, 189:330, 2003.

[73] D. Mihalas and B. W. Mihalas. *Foundations of Radiation Hydrodynamics*. Oxford University Press, 1984.

[74] J. V. Narlikar. *An Introduction to Cosmology, 3rd Ed.* Cambridge University Press, 2002.

[75] T. N’Kaoua. Solution of the nonlinear radiative transfer equations by a fully implicit matrix Monte Carlo method coupled with the Rosseland diffusion equation via domain decomposition. *SIAM Journal on Scientific and Statistical Computing*, 12:505, 1991.

[76] K. Nomoto, F. Thielemann, and K. Yokoi. Accreting white dwarf models for type I supernovae. *The Astrophysical Journal*, 286:644, 1984.

[77] W. L. Oberkampf and C. J. Roy. *Verification and Validation in Scientific Computing*. Cambridge University Press, 2010.

[78] G. L. Olson and P. B. Kunasz. Short characteristic solution of the non-LTE line transfer problem by operator perturbation-I. the one-dimensional plabar slab. *Journal of Quantitative Spectroscopy and Radiative Transfer*, 38, 1987.

[79] K. R. Olson and D. L. Henderson. Numerical benchmark solutions for time-dependent neutral particle transport in one-dimensional homogeneous media using integral transport. *Annals of Nuclear Energy*, 31:1495, 2004.

[80] S. Perlmutter. Supernovae, dark energy, and the accelerating universe. *Physics Today*, page 53, 2003.

[81] S. Perlmutter, G. Aldering, G. Goldhaber, R. A. Knop, P. Nugent, P. G. Castro, S. Deustua, S. Fabbro, A. Goobar, D. E. Groom, I. M. Hook, A. G. Kim, M. Y. Kim, J. C. Lee, N. J. Nunes, R. Pain, C. R. Pennypacker, R. Quimby, C. Lidman, R. S. Ellis, M. Irwin, R. G. McMahon, P. Ruiz-Lapuente, N. Walton, B. Schaefer, B. J. Boyle, A. V. Filippenko, T. Matheson, A. S. Fruchter, N. Panagia, H. J. M. Newberg, W. J. Couch, and Supernova Cosmology Project. Measurements of Omega and Lambda from 42 High-Redshift Supernovae. *The Astrophysical Journal*, 517:565–586, June 1999.

[82] S. Perlmutter, S. Gabi, G. Goldhaber, A. Goobar, D. E. Groom, I. M. Hook, A. G. Kim, M. Y. Kim, J. C. Lee, R. Pain, C. R. Pennypacker, I. A. Small, R. S. Ellis, R. G. McMahon, B. J. Boyle, P. S. Bunclark, D. Carter, M. J. Irwin, K. Glazebrook, H. J. M. Newberg, A. V. Filippenko, T. Matheson, M. Dopita, and W. J. Couch. Measurements of the cosmological parameters and from the first seven supernovae at z 0.35. *The Astrophysical Journal*, 483(2):565, 1997.

[83] A. Petschek. *Supernovae*. Springer-Verlag, 1990.

[84] M. M. Phillips. The absolute magnitudes of Type IA supernovae. *Astrophysical Journal, Letters*, 413:L105–L108, Aug. 1993.

[85] P. A. Pinto and R. G. Eastman. The physics of type Ia supernova light curves. I. Analytic results and time dependence. *The Astrophysical Journal*, 530:744, 2000.

[86] G. C. Pomraning. *The Equations of Radiation Hydrodynamics*. Pergamon Press, 1973.

[87] P. Preuss, 2005. Obtained from http://www2.lbl.gov.

[88] Y. P. Pskovskii. Light curves, color curves, and expansion velocity of Type I supernovae as functions of the rate of brightness decline. *Soviet Astronomy*, 21:675, 1977.

[89] G. Reinhardt. *Quantum Electrodynamics*. Springer-Verlag, 1994.

[90] A. G. Riess, A. V. Filippenko, P. Challis, A. Clocchiatti, A. Diercks, P. M. Garnavich, R. L. Gilliland, C. J. Hogan, S. Jha, R. P. Kirshner, B. Leibundgut, M. M. Phillips, D. Reiss, B. P. Schmidt, R. A. Schommer, R. C. Smith, J. Spyromilio, C. Stubbs, N. B. Suntzeff, and J. Tonry. Observational Evidence from Supernovae for an Accelerating Universe and a Cosmological Constant. *The Astronomical Journal*, 116:1009–1038, Sept. 1998.

[91] C. Scannapieco, P. B. Tissera, S. D. M. White, and V. Springel. Effects of supernova feedback on the formation of galaxy discs. *Monthly Notices of the Royal Astronomical Society*, 389, 2008.

[92] I. R. Seitenzahl, F. Ciaraldi-Schoolmann, F. K. Ropke, M. Fink, W. Hillebrandt, M. Kromer, R. Pakmor, A. J. Ruiter, S. A. Sim, and S. Taubenberger. Three-dimensional delayed-detonation models with nucleosynthesis for type Ia supernovae. *Monthly Notices of the Royal Astronomical Society*, 429:1156, 2013.

[93] R. P. Smedley-Stevenson and R. G. McClarren. Asymptotic diffusion limit of cell temperature discretisation schemes for thermal radiation transport. *Journal of Computational Physics*, 2013.

[94] B. Su and G. L. Olson. Non-grey benchmark results for two temperature non-equilibrium radiative transfer. *Journal of Quantitative Spectroscopy and Radiative Transfer*, 62:279, 1999.

[95] R. S. Sutherland. Accurate free-free Gaunt factors for astrophysical plasmas. *Monthly Notices of the Royal Astronomical Society*, 300:321, 1998.

[96] A. Szőke and E. D. Brooks. The transport equation in optically thick media. *Journal of Quantitative Spectroscopy and Radiative Transfer*, 91:95, 2005.

[97] T. J. Urbatsch, J. E. Morel, and J. C. Gulick. Monte Carlo solution of a spatially-discrete transport equation, part i: Transport. In *Proc. Int. Conf. Mathematics and Computation, Reactor Physics, and Environment Analysis in Nuclear Applications*, 1999.

[98] D. R. van Rossum. Radiation Energy Balance Method for Calculating the Time Evolution of Type Ia Supernovae during the Post-explosion Phase. *The Astrophysical Journal*, 756:31, Sept. 2012.

[99] D. A. Verner, G. J. Ferland, K. T. Korista, and D. G. Yakovlev. Atomic data for astrophysics. ii. new analytic FITS for photoionization cross sections of atoms and ions. *The Astrophysical Journal*, 465:487, 1996.

[100] J. S. Warsa and J. D. Densmore. Manufactured solutions in the thick diffusion limit. *Nuclear Science and Engineering*, 166:36, 2010.

[101] A. B. Wollaber, E. W. Larsen, and J. D. Densmore. A discrete maximum principle for the Implicit Monte Carlo equations. *Nuclear Science and Engineering*, 173:259, 2013.

[102] R. T. Wollaeger and J. D. Densmore. A residual monte carlo method for spatially discrete, angularly continuous radiation transport. In *American Nuclear Society Annual Meeting*, 2012.

[103] R. T. Wollaeger and D. R. van Rossum. Radiation transport for explosive outflows: opacity regrouping. Submitted to the Astrophysical Journal, Supplement, 2014.

[104] R. T. Wollaeger, D. R. van Rossum, C. Graziani, S. M. Couch, G. C. Jordan, D. Q. Lamb, and G. A. Moses. Radiation transport for explosive outflows: a multigroup hybrid Monte Carlo method. *Astrophysical Journal, Supplement*, 209, 2013.